University of Canterbury
Department of Mathematics and Statistics

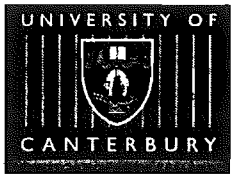

Mathematical models of pituitary corticotrophs and perifusion experiments

---

A thesis submitted in partial fulfilment
of the requirements for
the Degree of
Doctor of Philosophy in Mathematics
at the
University of Canterbury
by

Paul Shorten

Supervisor: Assoc. Prof. David Wall
Assoc. Supervisor: Assoc. Prof. Bruce Robson
2000

Abstract

It is well known that stress is an unavoidable and potentially harmful fact of life. Indeed mental stress is becoming recognised as a predominant factor behind many illnesses and deaths in industrialised nations. However it is also true that stress hormones, which mediate our physical response to stress, are essential to allow us to meet physical challenges. In times of physical stress they stimulate the heart, increase respiration, shunt blood from internal organs and skin to skeletal muscle, decrease pain, and have a host of other actions that contribute to our ability to engage in sustained physical activity. It is apparent that a better understanding of how the body copes with stress may lead to an improved means of controlling its effects, both in the medical context, such as during infections and operations, and in psychological and social situations.

Corticotropin releasing hormone (CRH) is one of the major regulatory hormones linked with the neuroendocrine response to stress. Secreted from CRH-neurons in the hypothalamus, CRH travels to the anterior pituitary, stimulating the secretion of adrenocorticotropic hormone (ACTH) from the corticotroph cell population. Secreted ACTH then initiates the release of adrenal glucocorticoids, which help the body reduce the metabolic demands of stress.

Pituitary corticotroph cells generate repetitive action potentials and associated Ca^{2+} transients in response to CRH. There is indirect evidence suggesting that CRH modulates the voltage sensitivity of the L-type Ca^{2+} channels embedded in the plasma membrane. A Hodgkin–Huxley type model of this process is constructed which provides insight into the action potential firing frequency, membrane excitability, and bursting activity.

Information transfer in a number of endocrine systems occurs through rapid modulation of hormone levels in concentration pulses. The temporal architecture of the endocrine glandular signaling process is believed to convey important biochemical information to the target tissue, and also represents a signature of the responsive endocrine cells. Therefore to understand the endocrine glandular physiology, the time domain structure of hormone release is required.

The perifusion apparatus has been used to investigate the hormone stimulated release of hormones. In this system, a liquid medium flowing at a constant rate flows through a pipe over cells, releasing a substance in response to a stimulus in the flowing medium. The temporal concentration profile of this released substance is then measured at some downstream location. However the major drawback of the perifusion system derives from dispersion, molecular diffusion, and mixing of the hormones in the tubing, generating a distortion in the experimentally observed hormone concentration profile. A comprehensive model of the shear dispersion, mixing, and diffusion associated with the mass transport of a material concentration down a pipe is constructed. Computationally efficient mathematical strategies to the concentration deconvolution problem are constructed, allowing an improved interpretation of the underlying secretory events.

Acknowledgements

First and foremost, I thank my supervisor Professor David Wall. David was a great source of inspiration, motivation and most of all a fun guy. I have fond memories of late afternoon blackboard sessions and yearly Hurunui excursions. Thanks also to Dr Andrew LeBeau, who taught me a great deal during the first year of my studies, and to Professor's Bruce Robson and Alan McKinnon for many fruitful discussions on pituitary corticotrophs. Thanks to Marg Evans and Drusilla Mason for helpful discussions and data from their perifusion systems. I was indeed fortunate to have such a splendid group of mentors to foster my interest in biomathematics during my study. Sincere thanks also to anonymous journal reviewers for their valuable comments and suggestions.

Thanks to the mathematics department and all the postgraduate students for creating an enjoyable atmosphere and learning environment. Special thanks to Andy for showing me the odd judo move, to Jon for keeping my soccer skills up to scratch, and to Chris for being a cricket sensation.

This thesis was completed with the help of a University of Canterbury Doctoral Scholarship and a Marsden Grant from the Royal Society of New Zealand. Thank-you also to the New Zealand Mathematics Society for conference travel assistance.

A final thanks to my parents, for providing me with the opportunities that have lead to the writing of this thesis, and to Mami for keeping me motivated.

Preface

Pituitary corticotroph cells generate repetitive action potentials and associated Ca^{2+} transients in response to the agonist CRH. The mechanisms of action potential generation are not well characterised. There is indirect evidence suggesting that the agonist, by way of complex intracellular mechanisms, modulates the voltage sensitivity of the L-type Ca^{2+} channels embedded in the plasma membrane. A Hodgkin–Huxley type model of this process is constructed in Chapter 2, which indicates that an increase in the L-type Ca^{2+} current is sufficient to generate repetitive action potentials. The model also provides insight into action potential firing frequency and membrane excitability.

Other major hormones influencing ACTH secretion are arginine vasopressin (AVP) and cortisol. A model of the AVP-activated intracellular inositol triphosphate signaling pathway is constructed in Chapter 5, which provides insight into the stimulus secretion pathway. This model exhibits the experimentally observed concentration dependent step, spike/plateau, oscillating plateau, and sinusoidal $[Ca^{2+}]_i$ responses. The oscillations are due to the $[Ca^{2+}]_i$ regulation of the binding of inositol triphosphate to its receptor. The model also displays the oscillating hyperpolarization and $[Ca^{2+}]_i$ plateau that are observed experimentally.

The spatio-temporal patterns in cytosolic Ca^{2+}, generated by the subtle interplay between cellular Ca^{2+} sources and removal mechanisms, is an integral part of the exocytotic pathway. The study of the mechanisms in which a cell controls its Ca^{2+} concentration and membrane electrical activity provides insight into the stimulus secretion pathway. The roles of the endoplasmic reticulum, an intracellular organelle responsible for Ca^{2+} homeostasis and the spatial patterns in Ca^{2+} is studied in detail in Chapters 2 and 3.

CRH is also believed to inhibit an inwardly rectifying K^+ current, and this effect is investigated in Chapter 4. A CRH-induced inhibition of the model inwardly rectifying K^+ current increases the action potential firing frequency and membrane excitability in agreement with experimental observations.

Many cell types exhibit bursting activity, characterised by alternating phases of near steady state behaviour and trains of rapid spike-like oscillations. The model exhibits experimentally observed bursting behaviour, where the depolarization spike is followed by small oscillations in

the membrane potential. The different model bursting modes are all modulated by the slow increase in $[Ca^{2+}]_i$, and are examined in Chapter 4. The model also exhibits a new mode of bursting indirectly driven by slow modulation of the endoplasmic reticulum Ca^{2+} concentration. Transitions between these bursting modes are investigated and similar modes of bursting in other Hodgkin–Huxley models are examined in Chapter 3.

The perifusion apparatus has been used to investigate the hormone stimulated release of hormones. In this system, a liquid medium flowing at a constant rate flows through a pipe over cells, releasing a substance in response to a stimulus in the flowing medium. The temporal concentration profile of this released substance is then measured at some downstream location. However the major drawback of the perifusion system derives from dispersion, molecular diffusion, and mixing of the hormones in the tubing, generating a distortion in the experimentally observed hormone concentration profile. A comprehensive model of the mass transport of the material concentration in the perifusion system is constructed in Chapter 10. Although the direct problem of the prediction of elution concentration has been considered, very little research has addressed associated inverse problems. Computationally efficient mathematical strategies to the concentration deconvolution problem are constructed, allowing an improved interpretation of the underlying secretory events.

In experiments associated with stress-levels in horses, a cannula tube is inserted *in vivo* to sample blood secreted near the pituitary, allowing the cells to be monitored in their natural environment. However the flow of blood does not behave in a Newtonian manner. Inverse problems associated with the mass transport of a material concentration down a pipe where the flowing non-Newtonian medium has a two-dimensional velocity profile are examined in Chapter 9. The inverse problem of estimation of a temporally varying concentration at one end of a pipe, from measurement of the cross-sectional average concentration at the opposite end, is solved in Chapter 7. The problem of determining the two-dimensional fluid velocity profile from temporally varying cross-sectional average concentration measurements at upstream and downstream locations is also solved in Chapter 8. These inverse problems are ill-posed deconvolution problems.

The interesting mathematical problem of signal reconstruction after transmission through an advective and diffusive medium is examined in detail in Chapter 11. By considering more generalised mass transport processes that ensure finite mass propagation speeds, wave splitting and invariant imbedding techniques can be applied to inverse problems associated with parabolic mass transport processes. This enables a stable equation to be utilised in reconstructing the interior boundary condition; so providing a regularized solution to the inverse problem. The transformation of the associated parabolic partial differential equation, by way of singular perturbation, to a hyperbolic one, yields valuable theoretical insight into this and other related problems.

During my studies the following papers have been prepared:

Most of Chapter 2 appeared in the research report "A role of the endoplasmic reticulum in a mathematical model of corticotroph action potentials", *University of Canterbury, New Zealand*, number 173, 1999, (pages 1–21). This work was co-authored with A.P. LeBeau, A.B. Robson, A.E. McKinnon and D.J.N. Wall.

Most of Chapter 3 appeared in the paper "A Hodgkin–Huxley model exhibiting bursting oscillations", published in the *Bulletin of Mathematical Biology*, volume 62, 2000, (pages 695–715). This work was co-authored with D.J.N. Wall.

Most of Chapter 4 appeared in the paper "CRH-induced electrical activity and calcium signalling in pituitary corticotrophs", published in the *Journal of theoretical Biology*, volume 206, 2000, (pages 395-405). This work was co-authored with A.B. Robson, A.E. McKinnon and D.J.N. Wall.

Most of Chapter 5 appeared in the paper "AVP-induced calcium signalling in pituitary corticotrophs", submitted to the *Journal of theoretical Biology.* This work was co-authored with D.J.N. Wall.

Most of Chapter 7 appeared in the paper "Signal restoration for a mass transport problem involving shear dispersion", published in *Inverse Problems*, volume 14, 1998, (pages 1021–1032). This work was co-authored with D.J.N. Wall.

Most of Chapter 8 appeared in the paper "Fluid velocity profile reconstruction for non-Newtonian shear dispersive flow", submitted to the *Journal of Applied Mathematics and Decision Sciences.* This work was co-authored with D.J.N. Wall.

Most of Chapters 9 and 10 appeared in the paper "A model of dispersion in perifusion systems", submitted to *The Journal of Theoretical Medicine.* This work was co-authored with D.J.N. Wall.

The introductory Chapters 1 and 6, Sections 2.2, 5.2, and Appendices A and B contain no original material, and each chapter includes a discussion section that outlines possible future work.

Contents

Glossary

Cellular and bifurcation terminology

Symbol	Definition
ER	endoplasmic reticulum
V	potential difference
$[Ca^{2+}]_i$	intracellular calcium concentration
$[Ca^{2+}]_{er}$	endoplasmic reticulum concentration
ACTH	adrenocorticotropic hormone, also known as corticotropin
AVP	arginine vasopressin, also known as antidiuretic hormone (ADH)
CRH	corticotropin releasing hormone, also known as CRF
cAMP	adenosine 3',5'-cyclic monophosphate
IP_3	inositol 1,4,5-triphosphate
IP_3R	IP_3 receptor
PKA	protein kinase A
PKC	protein kinase C
PLC	phospholipase C
DAG	diacylglycerol
VSCC	voltage sensitive Ca^{2+} channels
PDE	phosphodiesterase
ODE	ordinary differential equation
PDE	partial differential equation
SNP	saddle node of periodics bifurcation
HB	Hopf bifurcation
TB	torus bifurcation
F	subcritical flip (period doubling) bifurcation
BB	Bautin bifurcation
CP	cusp of periodics bifurcation
SN	saddle-node bifurcation
BT	Bogdanov-Takens bifurcation
HC	homoclinic bifurcation
SNHC	saddle-node-homoclinic bifurcation

Perifusion modeling symbols

Symbol	Definition
PES	pituitary effluent sampling
v_m	maximum fluid velocity
ℓ	pipe length
a	minimum fluid travel time (ℓ/v_m)
R	pipe radius
$v(r)$	fluid velocity profile
$\bar{v}$	average fluid velocity
$c_0(t)$	input concentration profile
$Q(t)$	downstream cross-sectional average concentration profile
n	flow index
H	Heaviside function
D	diffusion coefficient
Pe	Péclet number
N_R	Reynolds number
δ	mollification radius
$\mathrm{L}^2[\mathrm{a},\mathrm{b}]$	the Hilbert space of square integrable functions
$\mathrm{C}^s[\mathrm{a},\mathrm{b}]$	space of s-th order continuously differentiable functions
$\mathrm{H}^s[\mathrm{a},\mathrm{b}]$	Sobolev space of order s
κ^2	fluid diffusivity
τ	relaxation time
ν^2	mass flux wave slowness ($\kappa^{-2}\tau$)

Chapter 1

Introduction to pituitary corticotroph cells

The endocrine system is a highly complex communication network that along with the nervous system is responsible for maintaining the body's closely regulated internal environment. However, the control mechanisms used by the nervous and endocrine systems are very different. The endocrine[1] system consists of organs, tissues and cells which secrete hormones into the blood stream, substances that control a considerable number of bodily functions. These organs are very small and scattered throughout the body. The endocrine system interacts with many different parts of the body including the skeletal, muscular, nervous, immune, reproductive, digestive, lymphatic, urinary, and respiratory systems. Hormones are produced in different areas of the body, including the hypothalamus, pituitary, thyroid gland, pineal gland, pancreas, kidneys, heart, and adrenal gland. Hormones travel to other parts of the body triggering specific target cells to change their activity. Thus in contrast with the nervous system there is significant time delay in the response of the target cells. Each hormone generates a different response; the hormone may trigger the target cell to contract, reproduce, regulate growth, change it's membrane potential, excrete another hormone, or stimulate intracellular synthesis of enzymes and proteins. Target cells have receptors, so the specificity of hormonal action is determined by the target cells rather than the hormone itself. Because receptors can be linked to different intracellular messenger systems, different cells may respond differently, if at all, to the same hormone. The degree of target cell activation is determined by the concentration of the hormone, the receptor affinity, and the number of receptors.

Hormones may be generated in a constant, periodic, or pseudo-random fashion. The amount of hormone present in the bloodstream is determined by a number of complex feedback loops, involving different types of cells. Hormones are normally metabolised quickly, so that target cells

[1]The Latin translation is to secrete within.

remain sensitive to changing levels of hormone. However target cell desensitisation can occur after prolonged elevated stimulation by the hormone.

The pituitary gland is located in a cavity at the base of the skull below the hypothalamus. The infundibulum connects the hypothalamus to the pituitary, which in humans has a diameter of less than 1 cm. Hormone secretion from the pituitary is primarily controlled by the hypothalamus, which largely consists of neurons. The pituitary consists of two regions, the anterior pituitary and the posterior pituitary. Neurosecretory cells in the hypothalamus are connected to the posterior pituitary by hormone transporting axons. Although hormones are not produced in the posterior pituitary, hormones synthesised in the hypothalamus are stored there prior to being released into the bloodstream. Cells in the anterior pituitary receive hormones through the hypothalmo-pituitary portal system from the hypothalamus. These cells then synthesise and secrete further hormones. A schematic diagram of the pituitary is shown in Figure 1.1.

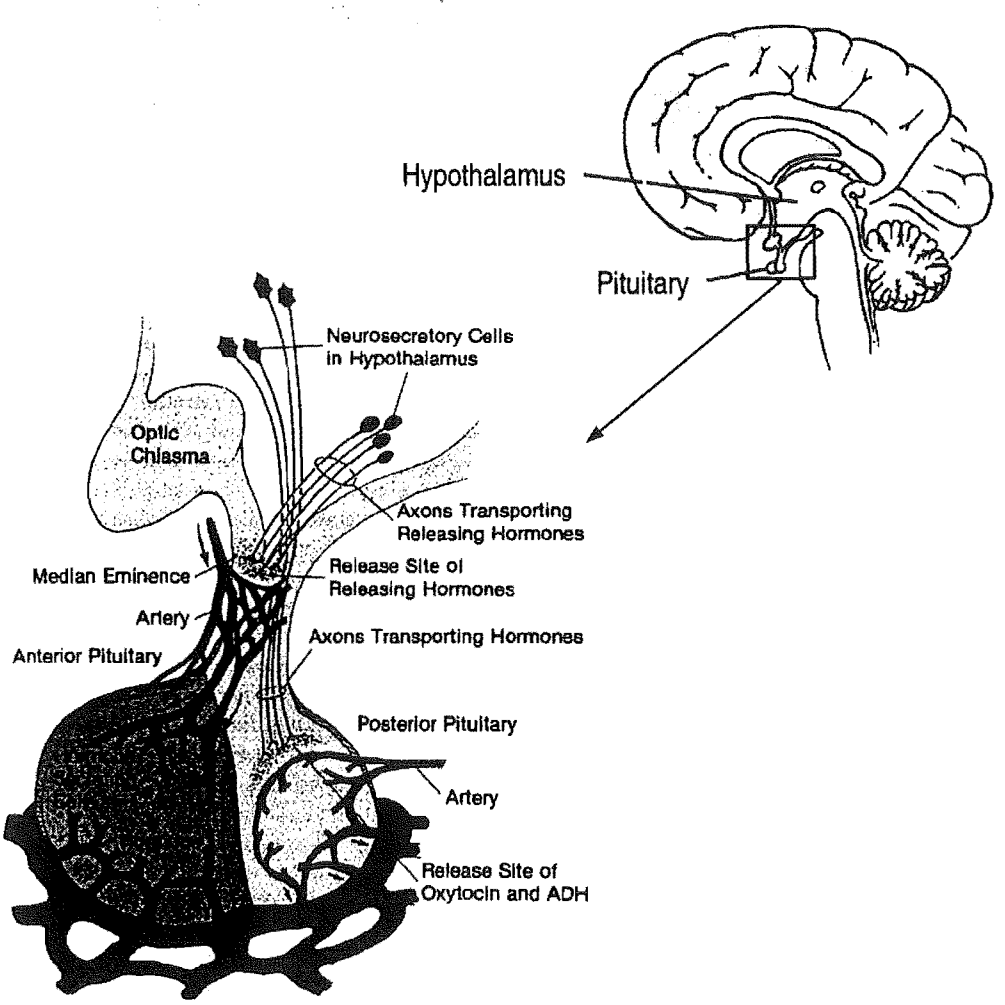

Figure 1.1: Schematic diagram of the pituitary. Figure from Wessells and Hopson (1988), p919.

Corticotropin releasing hormone (CRH) is one of the major regulatory hormones linked with the neuroendocrine response to stress including hypoglycemia, inflammation, and hemorrhage. Secreted from CRH-neurons in the paraventricular nucleus of the hypothalamus in the lower part of the brain, CRH travels through the hypothalmo-pituitary portal system to the anterior pituitary, stimulating the secretion of adrenocorticotropic hormone (ACTH) from the corticotroph cell population. The release of CRH from the paraventricular nucleus of the hypothalamus is regulated by several neurotransmitters, including acetylcholine, catecholamines, and serotonin (Jones and Gillham, 1988; Westlund et al., 1985).

Corticotroph cells constitute 3–15% of the cells in the anterior pituitary (Westlund et al., 1985), which also contains gonadotrophs, lactotrophs, somatotrophs and thyrotrophs. Corticotrophs synthesize a common precursor protein called pro-opiomelanocortins (POMC), which is divided into (ACTH), β-lipotropin, and small quantities of β-endorphins (King and Baertschi, 1990). These peptides are stored in vesicles within the corticotroph cell, and are secreted via exocytosis upon stimulation by CRH.

Secreted ACTH then travels to the adrenal glands located above the kidneys. ACTH is essential in the conversion of cholesterol into Δ^5-pregnenolone, thus stimulating the release of glucocorticoids from the adrenal cortex, which help cells in the body reduce the metabolic demands of stress. In mammals the predominant glucocorticoid is cortisol. Glucocorticoids are involved in the breakdown of proteins and carbohydrates into glucose. In particular, gluconeogenesis activity in the liver helps maintain blood glucose levels. There is also an increase in fatty acids and amino acids in the blood. Glucocorticoids also increase blood circulation ensuring that the glucose, fatty acids, and amino acids are quickly distributed to cells. Glucocorticoids also help maintain blood volume by preventing the transport of water into cells. These glucocorticoids also provide a negative feedback mechanism, inhibiting CRH secretion in the hypothalamus (Keller-Wood and Dallman, 1984) and ACTH synthesis and secretion in the pituitary (Lundblad and Roberts, 1988).

Other hormones influencing ACTH secretion are arginine vasopressin (AVP), and oxytocin (OXT). At high concentrations AVP stimulates blood vessels to constrict causing an elevation in blood pressure. AVP is also known as antidiuretic hormone (ADH) due to its water conservation role in the kidney. Oxytocin is primarily important during pregnancy and nursing. The release of ACTH is synergistic with respect to AVP and CRH, that is together they produce a greater effect than the sum of their effects acting alone. These hormones and their associated intracellular messenger system will be discussed in more detail in Chapter 5.

The agonist CRH, by way of complex intracellular mechanisms, modulates voltage sensitive Ca^{2+} channels embedded in the plasma membrane. The resulting potentiation of these Ca^{2+} channels induces a membrane depolarization, that generates action potentials in quiescent corti-

cotrophs, and enhances action potential frequency in spontaneously active corticotrophs. Associated with the action potentials are Ca^{2+} transients, which are generated by Ca^{2+} influx via Ca^{2+} channels and efflux via plasma membrane Ca^{2+}-ATPases.

Ca^{2+} is critically important for a vast array of cellular functions, playing a major role in muscle mechanics, cardiac electrophysiology, bursting oscillations, adaption in photoreceptors, gene expression, egg fertilisation, wound healing, and hormone secretion. The spatio-temporal patterns in cytosolic Ca^{2+}, generated by the subtle interplay between cellular Ca^{2+} sources and removal mechanisms, are believed to be an integral part of the exocytotic pathway. For this reason the study of the mechanisms in which a cell controls its Ca^{2+} concentration and membrane electrical activity provides insight into the stimulus secretion pathway.

ACTH secretion is believed to be closely associated with $[Ca^{2+}]_i$, and thus bursts of ACTH result from the Ca^{2+} transients. This may maximise the secretory output while avoiding the toxic effects of a sustained rise in $[Ca^{2+}]_i$.

Changing hormone levels are also believed to initiate the process of birth. In order for birth to be timely, the fetal pituitary must secrete ACTH, which stimulates the fetal adrenal gland to secrete glucocorticoids. These compounds then signal maternal cells in the placenta to manufacture and secrete prostaglandins, derivatives of fatty acids, which are powerful stimulators of uterine-muscle contractions. A better understanding of the maternal hormone changes prior to birth may allow the prediction of a premature birth.

Stress and sleep-wake patterns influence ACTH secretion. ACTH and corresponding cortisol secretions are highest when we wake, and lowest as we go to sleep. A change in sleep patterns eventually leads to a change in ACTH rhythms. Jet lag is now a common problem facing modern travellers. A greater understanding of ACTH patterns and the associated body bio-rhythms may help alleviate sudden time-zone changes.

1.1 Membrane electrophysiology

Because of the complex nature of biological phenomena it is useful to construct mathematical models to provide insight, show how a process works, and then predict what may follow. A Hodgkin-Huxley type mathematical model investigating corticotropic plasma membrane electrical activity and associated intracellular Ca^{2+} mechanisms in response to the agonist CRH provides insight into the stimulus secretion pathway. The evolving process of model construction and comparison with experimental data allows a deeper understanding of the fundamental biological mechanisms involved. We now discuss some elementary background membrane electrophysiology.

All cells are bounded by a plasma membrane, a dynamic barrier about 5 nm thick that governs the flow of material into and out of the cell. Cells continually consume energy in their battle

against the second law of thermodynamics to create a highly organised cytoplasmic environment. Plasma membranes are composed of a variety of different proteins dispersed throughout a phospholipid bilayer. The lipid bilayer is arranged with the hydrophilic ends of phospholipid molecules directed away from the membrane, creating a semi-waterproof membrane. Membranes are fluid structures, and some of these proteins are able to travel throughout the membrane by molecular diffusion. Other proteins may be attached to the cytoskeleton or other proteins, thus restricting their movements. The lipid bilayer is largely impermeable, although proteins in the membrane allow information and certain substances to traverse it. Intracellular organelles are also surrounded by phospholipid bilayers, although their composition is slightly different.

The intracellular and extracellular fluids are largely water, containing small quantities of ions, proteins, sugars and other substances. The cell plasma membrane acts as a selective, semipermeable barrier that maintains concentration differences in ions and proteins such as Na^+, K^+, Cl^-, glucose, and Ca^{2+}. Typical cellular ionic concentration differences are shown in Figure 1.2. Cells expedite large amounts of energy in maintaining these concentration differences to control their volume, and significant deviations can result in cell death. Because the phospholipid bilayer

Intracellular	Extracellular
$Na^+ = 12$ mM	$Na^+ = 150$ mM
$K^+ = 140$ mM	$K^+ = 5.6$ mM
$Ca^{2+} = 0.1$ μM	$Ca^{2+} = 2$ mM

Figure 1.2: Typical cellular ionic concentration differences.

is charged, it is difficult for polar proteins or ions to traverse the plasma membrane. However certain materials such as steroid hormones lack surface charge and don't interact with water, and are thus lipid soluble. These materials therefore can cross the plasma membrane via molecular diffusion. However small non-lipid soluble materials such as water are able to traverse the plasma membrane through pores, protein lined holes in the bilipid layer.

Other materials can cross the plasma membrane in more sophisticated ways. Dispersed in the bilayer are protein lined pores, called carrier proteins or channels, which allow the passage of specific molecules. Some of these channels transport ions passively down concentration gradients and others transport ions against concentration gradients, thus requiring energy. The control of these channels is crucial to cellular function. Fuelled by ATP's energy, carrier proteins undergo conformational changes allowing the binding, transport and release of specific materials. The pump enzymes that catalyze this process are called ATPases. The binding affinity of the channel can also change with the conformational change in the channel, accelerating the transport

of material. Pumping molecules against concentration gradients is a costly process, consuming significant quantities of a cells primary fuel, ATP. There are different types of channels, some transport different ions in opposite directions (antiports), and others transport more than one material through the membrane (symports).

Differences in ionic concentrations generates an electric field across the plasma membrane, which drive ionic currents. The flow of ions across the plasma membrane is also driven by concentration gradients. The contribution from the electric field is given by Planck's equation, and the contribution from the concentration gradient is given by Fick's Law, thus giving the Nernst-Planck flux equation for the current density J as

$$J = -D(\nabla c + \frac{zF}{RT} c \nabla \phi), \tag{1.1.1}$$

where c is the ionic concentration, D is the molecular diffusion coefficient, z is the valence of the ion, F is Faraday's constant, R is the universal gas constant, T is the absolute temperature, and ϕ is the electric potential. If the flow of ions and the electric field are assumed to be transverse to the membrane then (1.1.1) reduces to

$$J = -D\left(\frac{dc}{dx} + \frac{zF}{RT} c \frac{d\phi}{dx}\right), \tag{1.1.2}$$

where x is the coordinate transverse to the membrane. Secondly, if the electric field through the membrane is assumed to be constant then

$$\frac{d\phi}{dx} = -V/L, \tag{1.1.3}$$

where V is the transmembrane potential, and L is the thickness of the semipermeable membrane (Keener and Sneyd, 1998). If c_i and c_e are the intracellular and extracellular concentrations of the ion S, then $c(0) = c_i$ and $c(L) = c_e$. The linear first order ordinary differential equation (1.1.2), with (1.1.3) and $c(0) = c_i$, is then easily solved for the concentration c (Keener and Sneyd, 1998) yielding

$$c(x) = \frac{JLRT}{zFDV}\left(e^{(zFVx/RTL)} - 1\right) + c_i e^{(zFVx/RTL)}. \tag{1.1.4}$$

The extra boundary condition $c(L) = c_e$ is satisfied when

$$J_S = \frac{zFDV}{LRT} \frac{c_i - c_e e^{-zFV/RT}}{1 - e^{-zFV/RT}}, \tag{1.1.5}$$

the GHK driving force equation for the net flux density J_S.

There is no net flow of the ion S when $J_S = 0$. From (1.1.5) this occurs at the Nernst equilibrium potential or reversal potential

$$V_S = \phi_i - \phi_e = \frac{RT}{zF} \ln\left(\frac{c_e}{c_i}\right), \tag{1.1.6}$$

where ϕ_i and ϕ_e are the intracellular and extracellular electric potentials. For example in quiescent corticotrophs $V_{Ca} = +123.8$ mV and $V_K = -80.5$ mV. Although we have used the constant electric field approximation (1.1.3) along with the assumption that the flow of ions and the electric field are transverse to the membrane in our derivation of the Nernst equilibrium potential, (1.1.6) can also be derived under more general conditions using chemical equilibrium thermodynamics (Denbigh, 1971).

Another important property of channels is there ability to open or close is response to changes in membrane potential. Channels with this property are called voltage gated channels. The current through a channel can be expressed simply as

$$I = g(V,t)\Phi(V), \tag{1.1.7}$$

where $g(V,t)$ is the probability that the channel is open and $\Phi(V)$ is the current-voltage relationship for an open channel. The functional form of $\Phi(V)$ is in general highly nonlinear. A simple but useful choice of $\Phi(V)$ is the current obtained from the GHK driving force equation. The simplest channel model assumes that the channel can be either open or closed, where $\alpha(V)$ is the rate that a closed channel opens and $\beta(V)$ is the rate that open channels close. By assuming the receptor states are governed by the law of mass action kinetics, it then follows that

$$\frac{dg(V,t)}{dt} = \alpha(V)(1 - g(V,t)) - \beta(V)g(V,t). \tag{1.1.8}$$

This differential equation can be expressed in the more standard form

$$\tau_g(V)\frac{dg(V,t)}{dt} = g_\infty(V) - g. \tag{1.1.9}$$

For fixed V this implies that $g(V,t)$ approaches a steady state, $g_\infty(V)$, at a rate determined by the time constant $\tau_g(V)$.

We have seen that the cell separates charge, and thus can be viewed as a capacitor. The plasma membrane can be modeled as the equivalent electrical circuit shown in Figure 1.3. Hence

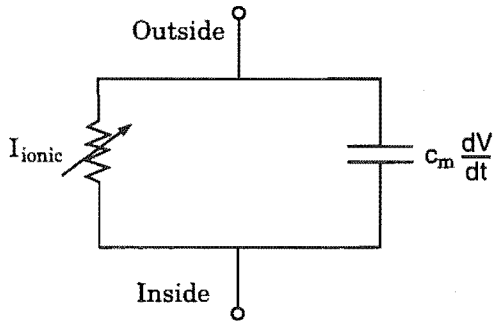

Figure 1.3: Cell equivalent circuit

current can flow through the plasma membrane as a capacitative current, or as an ionic current

through ionic channels. Thus current balance implies that

$$c_m \frac{dV}{dt} + I_{ionic} = 0, \tag{1.1.10}$$

where c_m is the cell capacitance. The capacitance of cell membranes is usually 1 $\mu\text{F} \cdot \text{cm}^{-2}$. The specific form of I_{ionic} is dependent on the ionic channels present in the plasma membrane. The model representation of the ionic currents in the corticotroph cell are discussed in Chapter 2.

Chapter 2

A role of the endoplasmic reticulum in a mathematical model of corticotroph action potentials

2.1 Introduction

CRH is one of the major regulatory hormones linked with the neuroendocrine response to stress (Rivier and Vale, 1983b; Gibbs, 1985; Jones and Gillham, 1988). Secreted from CRH-neurons in the paraventricular nucleus of the hypothalamus, CRH travels through the hypothalmo-pituitary portal system to the anterior pituitary (Merchenthaler et al., 1984; Plotsky et al., 1985; Whitnall et al., 1985; Plotsky and Sawchenko, 1987), stimulating the secretion of adrenocorticotropic hormone (ACTH) from the corticotroph cell population (Antoni, 1986; Rivier and Plotsky, 1986; Jones and Gillham, 1988). Secreted ACTH then initiates the release of adrenal glucocorticoids, which help the body reduce the metabolic demands of stress. These glucocorticoids also provide a negative feedback mechanism, inhibiting the secretory process at the pituitary and hypothalamus (Bilezikjian and Vale, 1983; Keller-Wood and Dallman, 1984; Widmaier and Dallman, 1984).

The intracellular mechanisms underlying the control of ACTH secretion in response to CRH have been only partially characterised. However CRH is known to activate the adenosine 3',5'-cyclic monophosphate (cAMP) dependent protein kinase A (PKA) pathway (Labrie et al., 1982; Aguilera et al., 1983; Reisine et al., 1986; Kuryshev et al., 1995a). The phosphorylation targets for PKA in corticotrophs have not been identified, however PKA is known to phosphorylate L-type voltage dependent Ca^{2+} channels (Mundiña-Weilenmann et al., 1991; Hille, 1992; Sculptoreanu et al., 1993). CRH also induces a membrane depolarization (Mollard et al., 1987), which is associated with the generation of action potentials in quiescent corticotrophs, and the enhancement

of action potential frequency in spontaneously active corticotrophs (Guérineau et al., 1991; Kuryshev et al., 1996). Associated with the action potentials are Ca^{2+} transients, predominately, if not totally, arising due to Ca^{2+} influx via L-type Ca^{2+} channels (Kuryshev et al., 1996). H-89, an inhibitor of PKA, significantly attenuates CRH-induced action potentials (Kuryshev et al., 1995a), demonstrating a major role for PKA in mediating the changes in electrical excitability and Ca^{2+}-mobilising actions of CRH. There is thus indirect evidence supporting the hypothesis of a CRH-induced PKA-dependent phosphorylation of the L-type Ca^{2+} channels (LeBeau et al., 1997), resulting in action potentials, and Ca^{2+} transients. A schematic diagram of this pathway is shown in Figure 2.1. The model introduced in LeBeau et al. (1997) is central to our discussion;

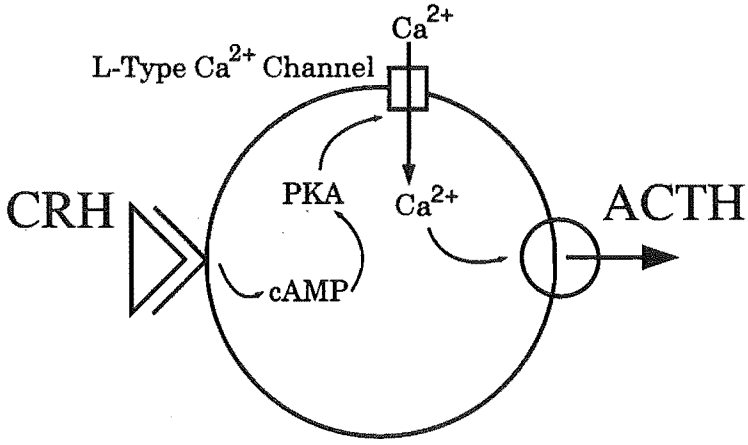

Figure 2.1: Schematic representation of the intracellular mechanisms that lead to action potentials, $[Ca^{2+}]_i$ transients, and ACTH secretion in corticotroph cells. Indirect evidence supports the hypothesis of a CRH-induced PKA-dependent phosphorylation of the L-type Ca^{2+} channels, resulting in action potentials and Ca^{2+} transients.

we henceforth denote it by (I).

Ca^{2+} has been well established as an important intracellular trigger for hormone secretion (Tsien and Tsien, 1990; Clapham, 1995a). The spatio-temporal patterns in cytosolic Ca^{2+}, generated by the subtle interplay between cellular Ca^{2+} sources and removal mechanisms, are believed to be an integral part of the exocytotic pathway (Meyer and Stryer, 1991). For this reason the study of Ca^{2+} transport and cell electrical activity provides insight into the stimulus secretion pathway. A mathematical model of the major plasma membrane ionic currents and the associated intracellular Ca^{2+} dynamics identified in corticotrophs has previously been constructed (I). For model simplicity, it was assumed that the intracellular free Ca^{2+} concentration ($[Ca^{2+}]_i$) was spatially uniform, and instantly mixed. The endoplasmic reticulum (ER) Ca^{2+} storage capacity was assumed to be large, and the amount of Ca^{2+} stored in the ER was assumed to vary negligibly during action potentials. It was found that an increase in the L-type current was sufficient to gen-

erate repetitive action potentials from a previously resting state of the model. The increase in the L-type current could be elicited by either a shift in the voltage dependence of the current to more negative potentials, or by an increase in the conductance. In this chapter we extend the model in (I) by including two new components. Firstly, we allow bidirectional Ca^{2+} transport between the cytosol and a finite, dynamic ER store. Secondly, along with other workers (Atri et al., 1993; Li et al., 1997), because the Ca^{2+}-sensing components of the cell have both different sensitivities to Ca^{2+} and different spatial locations, we consider spatially varying Ca^{2+}. We investigate what effects these two changes have on the model dynamics.

2.2 The original model

The original model (I) is of Hodgkin–Huxley form (Hodgkin and Huxley, 1952), and consists of six coupled ordinary differential equations. The model description is similar to the models of Li et al. (1995, 1997), which investigated electrical activity in pituitary gonadotroph cells. Four ionic currents are included in the corticotroph model: 1) a high voltage threshold dihydropyridine sensitive L-type Ca^{2+} current ($I_{\mathrm{Ca-L}}$), responsible for most of the inward Ca^{2+} current during an action potential; 2) a low voltage threshold rapidly inactivating T-type voltage sensitive Ca^{2+} current ($I_{\mathrm{Ca-T}}$); 3) a voltage-sensitive K^+ current ($I_{\mathrm{K-DR}}$), predominantly responsible for the action potential repolarization; and 4) a Ca^{2+}-activated K^+ current ($I_{\mathrm{K-Ca}}$). A leak current (I_{Leak}) represents all other ionic current contributions not specifically described. These model ionic currents are constructed from electrophysiological measurements in corticotrophs (I). It follows from (1.1.10) that the potential difference (V) across the plasma membrane for the corticotroph model satisfies

$$c_{\mathrm{m}}\frac{dV}{dt} = -(I_{\mathrm{Ca-L}} + I_{\mathrm{Ca-T}} + I_{\mathrm{K-DR}} + I_{\mathrm{K-Ca}} + I_{\mathrm{Leak}}), \tag{2.2.1}$$

where c_{m} is the cell surface membrane capacitance (see Table 2.1 for parameter values).

The voltage-dependent currents ($I_{\mathrm{Ca-L}}$, $I_{\mathrm{Ca-T}}$, and $I_{\mathrm{K-DR}}$) are described by the product of their macroscopic conductances, one or more voltage-dependent activation/inactivation gating variables, and a driving force specific for each ion (I). The ionic current through the L-type Ca^{2+} channel is

$$I_{\mathrm{Ca-L}} = g_{\mathrm{Ca-L}} m_{\mathrm{L}}^2 J_{\mathrm{Ca}}, \tag{2.2.2}$$

where g_{Ca-L} is the channel conductance, m_L is the voltage-dependent activation variable, which represents the fraction of current flow for a given membrane potential, and J_{Ca} is the driving force for Ca^{2+} given by equation (1.1.5). Negligible channel inactivation occurs during each action potential (Guérineau et al., 1991), so it is not necessary to include an inactivation variable for this current.

The T-type Ca^{2+} channel is defined similarly to the L-type current:

$$I_{\mathrm{Ca-T}} = g_{\mathrm{Ca-T}} m_{\mathrm{T}}^2 h_{\mathrm{T}} J_{\mathrm{Ca}}, \tag{2.2.3}$$

where m_{T} is the corresponding voltage-dependent gating variable, and an inactivation gating variable (h_{T}) is included.

$I_{\mathrm{K-DR}}$, the voltage-sensitive K^+ current is given by

$$I_{\mathrm{K-DR}} = g_{\mathrm{K-DR}} n J_{\mathrm{K}}, \tag{2.2.4}$$

where the activation variable appears linearly (Li et al., 1995), and J_{K} is the GHK driving force for K^+.

Corticotrophs exhibit both large conductance (BK-type) (Shipston et al., 1996) and small conductance, apamin-sensitive (SK-type) (Corcuff et al., 1993) Ca^{2+}-activated K^+ conductances. Neither of these channels has been particularly well characterised in corticotrophs. Hence a lumped Ca^{2+}-activated K^+ current ($I_{\mathrm{K-Ca}}$) that does not exhibit voltage-sensitivity is included:

$$I_{\mathrm{K-Ca}} = g_{\mathrm{K-Ca}} \frac{[\mathrm{Ca}^{2+}]_{\mathrm{i}}^{\,4}}{[\mathrm{Ca}^{2+}]_{\mathrm{i}}^{\,4} + K_{\mathrm{c}}^{\,4}} J_{\mathrm{K}}, \tag{2.2.5}$$

where K_{c} is the half-maximally activating $[Ca^{2+}]_{\mathrm{i}}$.

The leakage current (I_{Leak}) is given by the ohmic relationship

$$I_{\mathrm{Leak}} = g_L (V - V_L), \tag{2.2.6}$$

which reflects the effects of the ionic currents not included in the model. The reversal potential of the current (V_L) has a value of -67 mV, close to the Nernst potential for K^+, reflecting the fact that K^+ conductances are the major component of the remaining membrane current.

The activation variables satisfy equation (1.1.9), where g stands for m_L, m_T, h_T, or n. This equation describes how each activation variable relaxes to its voltage-dependent steady-state (g_∞), following a particular time course (τ_g). The steady states g_∞, for m_L, m_T, and n are sigmoidal relationships [1] given by

$$g_\infty = \frac{1}{1 + \exp\left[(V_g - V)/k_g\right]}, \tag{2.2.7}$$

which gives values between 0 (no activation) and 1 (fully activated). V_g is the voltage at which the current is half maximally activated, and k_g is the steepness of the curve. The steady-state inactivation of the T-type channel, $h_{\mathrm{T}\infty}$, is a reverse sigmoidal function:

$$h_{\mathrm{T}\infty} = \frac{1}{1 + \exp\left[(V - V_{\mathrm{h_T}})/k_{\mathrm{h_T}}\right]}. \tag{2.2.8}$$

[1] Also known as Boltzmann functions.

The time constants for m_L and m_T are given by

$$\tau_x(V) = \frac{\bar{\tau}_x}{\exp\left[(V - V_\tau)/k_\tau\right] + 2\exp\left[2(V_\tau - V)/k_\tau\right]}, \tag{2.2.9}$$

and the time constants for h_T and n are voltage independent (Li et al., 1995).

There is evidence suggesting the existence of other channel types in corticotrophs, including: 1) TTX-sensitive Na^+ channels which do not appear to play a major role in corticotroph action potential generation, Ca^{2+} responses (Kuryshev et al., 1996) or ACTH secretion (Halili-Manabat et al., 1995); 2) P-type Ca^{2+} channels, contributing to the regulation of firing frequency (Kuryshev et al., 1995b; Kuryshev et al., 1996); 3) an inward rectifier K^+ current (Kuryshev et al., 1997), contributing to the maintenance of the resting membrane potential; and 4) a nonselective cation current (Takano et al., 1996). However these channels are not well characterised in corticotrophs and it is not clear what roles they might perform. Thus a description of these other channels is not included in the model presented in this chapter. Parameter values obtained from experimental data (Mollard et al., 1987; Marchetti et al., 1987; Guérineau et al., 1991; Kuryshev et al., 1995b) are given in Table 2.1.

The model in (I) also included simple Ca^{2+} handling mechanisms. For model simplicity, it was assumed that the intracellular free Ca^{2+} concentration ($[Ca^{2+}]_i$) was spatially uniform, and instantly mixed. The ER Ca^{2+} storage capacity was assumed to be large, and the amount of Ca^{2+} stored in the ER was assumed to vary negligibly during action potentials. A more general model of corticotroph Ca^{2+} handling mechanisms is investigated in the next section.

2.3 The ER model

The ER Ca^{2+} store performs a number of important cellular functions, including cellular Ca^{2+} homeostasis and protein synthesis (Alberts et al., 1983, p335). In this section the model in (I), outlined in Section 2.2, is extended to include bidirectional Ca^{2+} transport between the cytosolic and ER compartments. This allows Ca^{2+} that has been sequestered by the ER to be released back into the cytosol, a feature that was not incorporated into (I).

2.3.1 The model

The cell is modeled as a spherical body, bounded by a plasma membrane containing Ca^{2+}-ATPase pumps and various ionic currents as outlined above. A schematic diagram of the various ionic transport processes is shown in Figure 2.2. It is assumed that the ER is distributed homogeneously throughout the cell, and shares the intracellular volume with the cytosol. The ER and cytosolic compartments are of different volumes V_{er} and V_c respectively, where the ER is assumed to fill 15% of the cell volume (Alberts et al., 1983, p320).

Parameter	Definition	Value	Source
c_m	Cell membrane capacitance	7 pF	$1\mu F \cdot cm^{-2} \cdot A_{cell}$
d_{cell}	Cell diameter	15 μm	(I)
V_{cell}	Cell volume	1.77 pL	$1/6\pi {d_{cell}}^3$
V_c	Cytosolic volume	0.85 V_{cell}	(Alberts et al., 1983)
V_{er}	ER volume	0.15 V_{cell}	(Alberts et al., 1983)
A_{cell}	Cell surface area	707 μm^2	$\pi {d_{cell}}^2$
f_{cyt}	Cytosolic Ca^{2+} buffering factor	0.01	(Neher and Augustine, 1992)
f_{er}	ER Ca^{2+} buffering factor	0.0025	(Li et al., 1997)
α	Ca^{2+} current to flux density conversion factor	0.0074 $\mu M \cdot \mu m \cdot ms^{-1} \cdot pA^{-1}$	$1/(z_{Ca} F A_{cell})$
β	Ratio of cell surface area to cytosolic volume	0.47 μm^{-1}	A_{cell}/V_c
P	ER permeability	0.0012 pL $\cdot$ ms^{-1}	This chapter
ν_{er}	Maximum ER Ca^{2+}-ATPase current	0.05 $\mu M \cdot pL \cdot ms^{-1}$	This chapter
K_{er}	$[Ca^{2+}]_i$ for half maximal pump activity	0.2 μM	(Li et al., 1997)
ν_p	Maximum plasma membrane Ca^{2+}-ATPase flux	0.05 $\mu M \cdot \mu m \cdot ms^{-1}$	(I)
K_p	$[Ca^{2+}]_i$ for half maximal pump activity	0.08 μM	(I)
V_{m_L}	L-type Ca^{2+} channel midpoint factor	-12 mV	(Kuryshev et al., 1995b)
D_c	Cytosolic Ca^{2+} diffusion coefficient	20 $\mu m^2 \cdot s^{-1}$	(Wagner and Keizer, 1994)
D_{er}	ER Ca^{2+} diffusion coefficient	5 $\mu m^2 \cdot s^{-1}$	(Li et al., 1997)
$[Ca^{2+}]_e$	Extracellular $[Ca^{2+}]$	20 mM	(Guérineau et al., 1991)
$[K^+]_e$	Extracellular $[K^+]$	5.6 mM	(Guérineau et al., 1991)
$[K^+]_i$	Intracellular $[K^+]$	140 mM	(Li et al., 1995)
g_L	Leak conductance	0.3 nS	(I)
$g_{Ca\text{-}L}$	L-type conductance	9 nS $\cdot$ mM^{-1}	(Guérineau et al., 1991)
$g_{Ca\text{-}T}$	T-type conductance	10 nS $\cdot$ mM^{-1}	(Guérineau et al., 1991)
$g_{K\text{-}DR}$	K-DR conductance	0.1 nS $\cdot$ mM^{-1}	(Mollard et al., 1987)
$g_{K\text{-}Ca}$	K-Ca conductance	0.09 nS $\cdot$ mM^{-1}	(Mollard et al., 1987)
K_c	$[Ca^{2+}]_i$ for half maximal K-Ca activation	0.4 μM	(I)
V_{m_T}	Midpoint T-type Ca^{2+} channel activation	-30 mV	(Guérineau et al., 1991)
V_L	Leak current reversal potential	-67 mV	(I)
V_τ	Midpoint of time factor	-60 mV	(Li et al., 1995)
V_n	Midpoint K-DR channel activation	-20 mV	(Mollard et al., 1987)
V_{h_T}	Midpoint T-type Ca^{2+} channel inactivation	-57 mV	(Guérineau et al., 1991)
k_{m_L}	Slope factor for L-type Ca^{2+} channel activation	12 mV	(Kuryshev et al., 1995b)
k_{m_T}	Slope factor for T-type Ca^{2+} channel activation	10.5 mV	(Guérineau et al., 1991)
k_{h_T}	Slope factor for T-type Ca^{2+} channel inactivation	5 mV	(Guérineau et al., 1991)
k_n	Slope factor for K-DR activation	4.5 mV	(Mollard et al., 1987)
k_τ	Slope factor for time factor	22 mV	(Li et al., 1995)
$\bar{\tau}_{m_L}$	L-type Ca^{2+} channel activation time constant	27 ms	(Kuryshev et al., 1995b)
$\bar{\tau}_{m_T}$	T-type Ca^{2+} channel activation time constant	10 ms	(Li et al., 1995)
τ_{h_T}	T-type Ca^{2+} channel inactivation time constant	15 ms	(Li et al., 1995)
τ_n	K-DR activation time constant	20 ms	(I)

Table 2.1: Table of relevant model parameters.

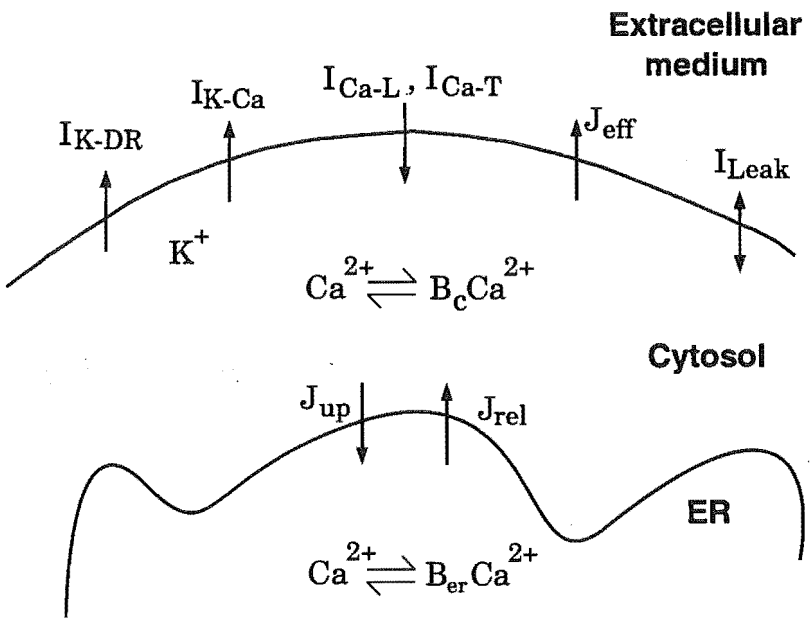

Figure 2.2: Schematic diagram of the ionic pathways included in the model. Three compartments are distinguished, the cytosol, the ER, and the extracellular medium. Bold arrows indicate the various channels and pumps. Within the ER and cytosolic compartments, significant portions of Ca^{2+} are bound to buffers, denoted by B_{er} and B_c respectively. Four ionic currents are included in the model: an L-type voltage sensitive Ca^{2+} current I_{Ca-L}, a fast inactivating T-type voltage sensitive Ca^{2+} current I_{Ca-T}, a voltage-sensitive K^+ current I_{K-DR}, and a non-voltage sensitive Ca^{2+}-activated K^+ current I_{K-Ca}. The remaining leak current I_{Leak} represents all other ionic current contributions. Also indicated are the plasma membrane and ER Ca^{2+}-ATPase pumps, J_{eff} and J_{up} respectively, along with an ER Ca^{2+} leakage term J_{rel}.

The compartments also have different buffering kinetics, (Li et al., 1997) given by f_{er} and f_{cyt}, the fraction of unbuffered Ca^{2+} in the respective volumes. This fraction is dependent on the concentration of buffer sites, their individual binding kinetics, and the $[Ca^{2+}]$ in the corresponding compartment (Wagner and Keizer, 1994). The precise nature of these Ca^{2+} buffers, each with unique binding kinetics is as yet undetermined, hence the model of Ca^{2+} buffering is simple. Assuming that the Ca^{2+} buffer concentration is suitably large relative to the $[Ca^{2+}]$ in the respective compartments (Jafri and Keizer, 1995), and the buffer kinetics are fast and in equilibrium at all times, it follows that the functional dependence of f_{er} and f_{cyt} on $[Ca^{2+}]$ will be weak, and can thus be treated as constant. In the cytosol, approximately 99% of Ca^{2+} is bound to buffers (Neher and Augustine, 1992; Tse et al., 1994), hence $f_{cyt} = 0.01$. The buffering of Ca^{2+} in the ER is assumed to be four times greater than in the cytosol (Li et al., 1997), hence $f_{er} = 0.0025$. (See Table 2.1)

There is no evidence to suggest that CRH, by means of a secondary messenger, directly induces the release of Ca^{2+} from the ER. Therefore, assuming the diffusive surface flux across the ER membrane is described by Fick's law, the leak current from the ER can be described by

$$J_{rel} = P([Ca^{2+}]_{er} - [Ca^{2+}]_i), \tag{2.3.1}$$

where P is the ER membrane leak permeability, $[Ca^{2+}]_{er}$ is the concentration of free Ca^{2+} in the ER, and $[Ca^{2+}]_i$ is the concentration of free Ca^{2+} in the cytosol. Ca^{2+}-ATPase pumps are located on the surface of the ER membrane, allowing the cell to remove cytosolic Ca^{2+}. The uptake of Ca^{2+} into the ER is described by Michaelis–Menten kinetics (Lytton et al., 1992)

$$J_{up} = \frac{\nu_{er}[Ca^{2+}]_i^{\,2}}{[Ca^{2+}]_i^{\,2} + {K_{er}}^2}, \tag{2.3.2}$$

where ν_{er} is the maximum pump rate and K_{er} is the $[Ca^{2+}]_i$ for half maximal pump activity.

Ca^{2+} influx through voltage sensitive Ca^{2+} channels (J_{in}), and efflux via the plasma membrane Ca^{2+}-ATPase pump (J_{eff}) are given by

$$J_{in} = -\alpha(I_{Ca-L} + I_{Ca-T}), \tag{2.3.3}$$

$$J_{eff} = \frac{\nu_p[Ca^{2+}]_i^{\,2}}{[Ca^{2+}]_i^{\,2} + {K_p}^2}, \tag{2.3.4}$$

respectively (I), where α converts a Ca^{2+} ionic current into a Ca^{2+} flux density, ν_p is the maximum pump rate, and K_p is the $[Ca^{2+}]_i$ for which the pump is half-maximally activated (see Table 2.1).

Because of Ca^{2+} buffering the current ($J_{rel} - J_{up}$), representing the Ca^{2+} exchange across the ER membrane, must be multiplied by f_{cyt}/V_c to produce the rate of concentration accumulation

in the cytosol [2]. The differential equation for $[Ca^{2+}]_i$ is then given by

$$\frac{d[Ca^{2+}]_i}{dt} = \frac{f_{cyt}}{V_c}(J_{rel} - J_{up}) + f_{cyt}\beta(J_{in} - J_{eff}), \tag{2.3.5}$$

where β is the ratio of cell surface area to cytosolic volume, relating ionic fluxes in the plasma membrane to the rate of intracellular concentration accumulation. The differential equation for the ER dynamics is similar to (2.3.5), but the ER is assumed not to interact directly with the extracellular medium, and the rate of concentration accumulation in the ER is now moderated by the factor f_{er}/V_{er} so yielding

$$\frac{d[Ca^{2+}]_{er}}{dt} = -\frac{f_{er}}{V_{er}}(J_{rel} - J_{up}). \tag{2.3.6}$$

The value for $[Ca^{2+}]_{er}$ at rest has not been determined, but a lower bound estimate can be obtained from previously published experimental data. The agonist arginine vasopressin is thought to induce intracellular inositol triphosphate (IP_3) production which binds to receptors located on the ER membrane and causes release of stored Ca^{2+} from the ER (Won and Orth, 1995). Single cell measurements of Ca^{2+} have shown that arginine vasopressin can generate a transient $[Ca^{2+}]_i$ response of up to 3 μM (Corcuff et al., 1993). By use of the values for the relative volumes and buffering capacities (see Table 1), this gives a lower estimate for the resting $[Ca^{2+}]_{er}$ of 6–10 μM. At equilibrium there will be no net Ca^{2+} exchange between the cytosol and the ER. This allows us to find, using equations (2.3.1) and (2.3.2), a linear functional relationship between ν_{er} and P. A leak permeability of $P = 0.0012$ pL $\cdot$ ms^{-1} then indicates that $\nu_{er} = 0.05$ μM $\cdot$ pL $\cdot$ ms^{-1}.

2.3.2 Numerical methods

The system of seven ordinary differential equations (equations (2.2.1), (2.3.5), (2.3.6), and the four gating variable equations (1.1.9) for m_L, m_T, h_T, and n) were solved using a stiff system solver in the numerical package XPPAUT(3.0) [3]. Bifurcation diagrams were computed using AUTO (Doedel, 1981), as incorporated in XPPAUT.

2.3.3 Model behaviour

Experimentally, application of cAMP has been shown to increase the whole-cell Ca^{2+} current in corticotroph tumor cells (Luini et al., 1985). It has been shown in (I) that such an increase in the current can be generated either by an increase in the macroscopic conductance or by a shift in the voltage-sensitivity of the L-type Ca^{2+} current to more hyperpolarised potentials, the latter effect

[2] It should be noted that $(J_{rel} - J_{up})$ is an ionic current whereas $(J_{in} - J_{eff})$ is an ionic surface flux, thus ν_{er} and ν_p have different units.

[3] Written by Bard Ermentrout, and available at ftp.math.pitt.edu/pub/bardware.

having experimental support from other cell-types (Nargeot et al., 1983; Mundiña-Weilenmann et al., 1991; Sculptoreanu et al., 1993). In the model, both effects led to the generation of repetitively firing action potentials. At present, it would seem that neither the currently available experimental data, nor the model, can resolve which, if any, of these mechanisms genuinely underlies action potential generation in response to CRH. Previously in (I) a shift in the voltage-dependence of the L-type Ca^{2+} current was arbitrarily chosen but an increase in the macroscopic conductance always produced very similar results. We continue with the same choice in the following analysis. The model parameter that controls the voltage-sensitivity of the L-type current is V_{m_L} (as described in Section 2.2). Analysis of experimental data suggested a control V_{m_L} value of -12 mV under rest conditions, and a negative shift of 6–8 mV was typically used to generate action potentials (I).

With the addition of more realistic Ca^{2+} handling in the ER model, described by (2.2.1)–(2.3.6) above, we compare its behaviour with the original model (I). The ER model resting state is similar to that in the original model; at equilibrium the $[Ca^{2+}]_i$ is 0.12 μM, $[Ca^{2+}]_{er}$ is 10.8 μM and the plasma membrane potential difference V is -56.1 mV. At equilibrium in the original model the $[Ca^{2+}]_i$ is 0.1 μM, with a plasma membrane potential difference of -54.8 mV. Figure 2.3 compares ER model simulations (—) with those from the original model (– – –), in which the voltage dependence of the L-type Ca^{2+} current activation is shifted to more negative potentials by changing V_{m_L} from -12 mV to -18 mV. This generates action potentials, and associated $[Ca^{2+}]_i$ transients in both models. The period of oscillations in both models is dependent on the rate of clearance of Ca^{2+} from the cytosol (i.e., due to the gradual removal of the hyperpolarizing influence of the Ca^{2+}-activated K^+ current). The choice of parameters governing bidirectional flow of Ca^{2+} between the cytosol and ER results approximately in a 50% increase in the period of oscillations compared with the original model. However, the characteristics of the action potentials and $[Ca^{2+}]_i$ transients in the ER model are similar to those in the original model. The slower period is actually more consistent with experimentally observed activity (Guérineau et al., 1991; Kuryshev et al., 1996). The model $[Ca^{2+}]_i$ profiles display kinetic features similar to the experimental data (Guérineau et al., 1991), such as a rapid rising phase, and a slower falling phase where $[Ca^{2+}]_i$ falls most of the way back to its basal value before the next action potential. The action potentials display typical experimentally observed features, such as a rapid upstroke, a rapid downstroke which overshoots the resting potential, and a slow ramping hyperpolarization, leading to the firing of the next action potential (see Figure 4.3).

During the train of action potentials in the ER model, $[Ca^{2+}]_{er}$ slowly increases (Figure 2.3 C), as the ER sequesters Ca^{2+} and therefore acts to buffer the $[Ca^{2+}]_i$. If only a single transient were generated, the additional ER Ca^{2+} would be returned to the cytosol, and eventually removed from

the cell altogether to recover cellular $[Ca^{2+}]$ homeostasis. However, Figure 2.3 C shows that with repetitive action potential activity, $[Ca^{2+}]_{er}$ builds up as each transient contributes additional Ca^{2+} to the cytosol.

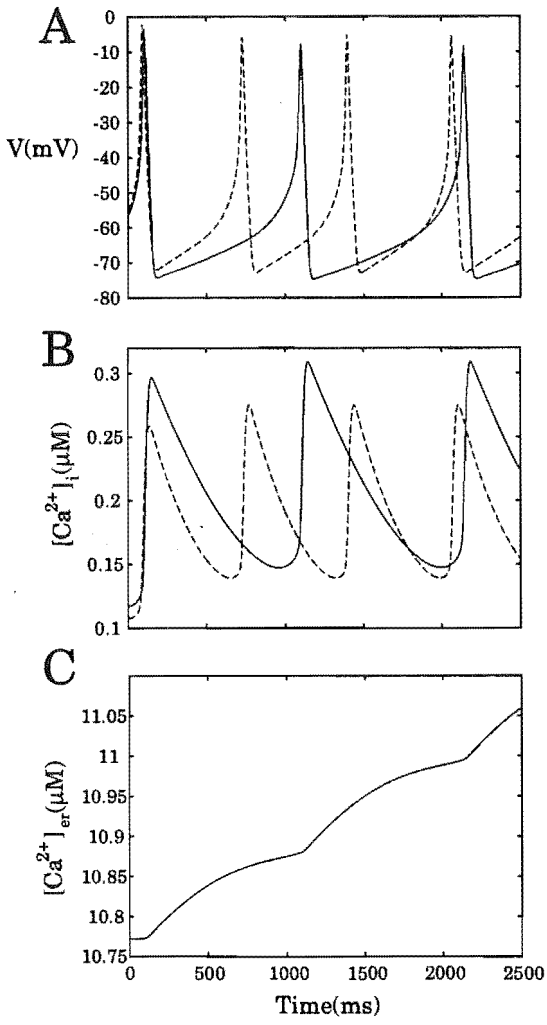

Figure 2.3: Comparison of the oscillatory phenomena in the ER model (—) with the original model (– – –). Indirect evidence supports a CRH-induced phosphorylation of the L-type Ca^{2+} channels, resulting in action potentials and Ca^{2+} transients. This phosphorylation is modeled by left-shifting the voltage dependence of the L-type Ca^{2+} current, V_{m_L}, from -12 mV to -18 mV, generating (A) action potentials, (B) $[Ca^{2+}]_i$ transients, and (C) a slow $[Ca^{2+}]_{er}$ increase.

The ER model behaves in a similar fashion to the original model for short periods of time. However an interesting behaviour is exhibited when the ER model is viewed over a longer period of time. Figure 2.4 shows a model simulation over 70 s, where a negative shift in the voltage dependence of the L-type Ca^{2+} current from -12 mV to -18 mV generates action potentials, and associated $[Ca^{2+}]_i$ transients. During $[Ca^{2+}]_i$ oscillations, $[Ca^{2+}]_{er}$ rises slowly to approximately 15.8 μM after 70 s (Figure 2.4 C). Coupled to the buildup in $[Ca^{2+}]_{er}$ is a gradual rise in the average

$[Ca^{2+}]_i$ (i.e., averaged over the course of a transient) and a slight decrease in the amplitude and frequency of $[Ca^{2+}]_i$ oscillations. The slow but steady rise in $[Ca^{2+}]_i$ results from an enhanced leak from the ER and leads to a gradual increase in the average activation of I_{K-Ca}. This in turn has a subtle inhibitory effect on the regeneration of action potentials. The action potential peaks decrease until after 60 s enough feedback is present to significantly reduce the action potentials, resulting in small amplitude V oscillations (< 20 mV amplitude and decreasing).

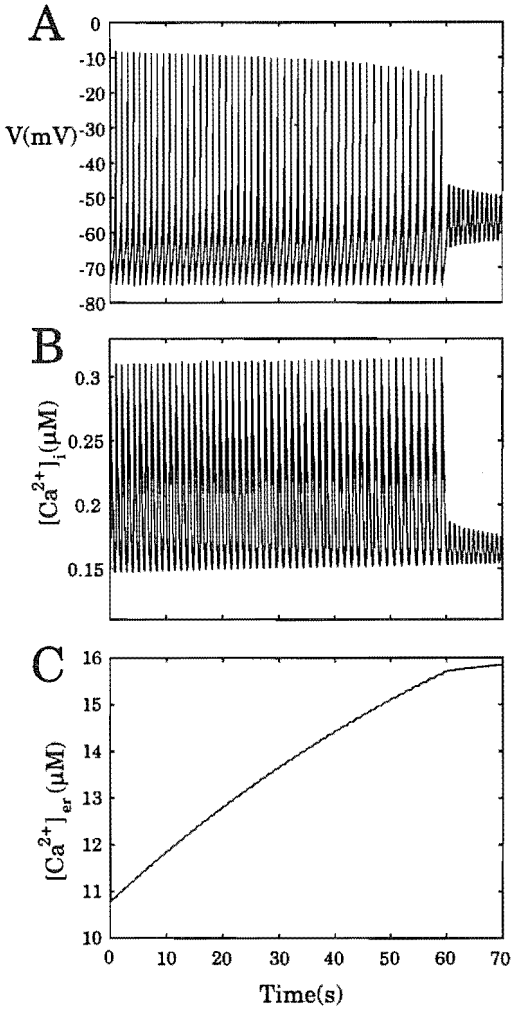

Figure 2.4: (A) ER model action potentials on a longer time scale to that of Figure 2.3, generated by left-shifting the voltage dependence of the L-type Ca^{2+} current, V_{m_L}, from -12 mV to -18 mV. (B) There is a gradual rise in the $[Ca^{2+}]_i$, which increasingly activates the I_{K-Ca} current, inhibiting the action potentials. The action potential peaks decrease, until after 60 s enough feedback is present to significantly reduce the action potentials, resulting in small amplitude oscillations. (C) Coupled to the rise in $[Ca^{2+}]_i$ is a buildup of $[Ca^{2+}]_{er}$.

The oscillations in Figure 2.4 A & B are more easily analysed if we plot how V and $[Ca^{2+}]_i$ change together over time (Figure 2.5). The system starts from the point indicated by the $\star$,

representing the model quiescent state. Time is represented by the line, progressing as both V and $[Ca^{2+}]_i$ change in value. From the quiescent state, both V and $[Ca^{2+}]_i$ start to increase. V soon peaks just below 0 mV, and then starts to repolarize as $[Ca^{2+}]_i$ increases further. Note that $[Ca^{2+}]_i$ increases greatly during the repolarization phase, because although the L-type Ca^{2+} current is being shut off as V falls, the driving force for Ca^{2+} is increasing. When V reaches its minimum value of -72 mV, the rise in $[Ca^{2+}]_i$ is complete, and V slowly ramps up as $[Ca^{2+}]_i$ falls. This represents the interspike interval. When V reaches about -60 mV, the next spike is initiated. Note that after the initial spike, the next several spikes follow a similar, but not identical, path. Viewed over a time period of up to about 10 s, the action potentials appear to be stable, but Figure 2.5 shows that each oscillation has a slightly larger average $[Ca^{2+}]_i$ value (i.e., average throughout one $[Ca^{2+}]_i$ transient cycle). This is because $[Ca^{2+}]_{er}$ is slowly rising (Figure 2.4 C), and therefore J_{rel} is also slowly rising, releasing more Ca^{2+} during each oscillation. This in turn progressively increases the activation of the Ca^{2+}-activated K^+ channel, which affects the balance between the inward and outward currents that underlie the regeneration of action potentials. When $[Ca^{2+}]_{er}$, and thus the average $[Ca^{2+}]_i$ increase sufficiently, there is too much I_{K-Ca} current for another action potential to be generated. Instead small amplitude V oscillations occur (< 20 mV amplitude and decreasing). Ultimately stable oscillations are achieved, which have a V amplitude of 5 mV. Note that this effect (abolition of action potential activity) occurs due to a very minor increase in $[Ca^{2+}]_i$, demonstrating the subtle interplay between the ER filling state and the plasma membrane electrical activity. Further, this effect shows that the ER can potentially play an important signaling role despite an initial appearance that it plays only a passive, buffering function during CRH-induced activity.

Experimental observations have shown that action potentials in response to application of CRH can persist for at least 15 min (Kuryshev et al., 1995a; Ritchie et al., 1996), indicating that the loss of action potentials observed in the ER model does not reflect a genuine physiological effect. However, it does seem physiologically reasonable that the ER should take up Ca^{2+} during repetitive $[Ca^{2+}]_i$ generation, which is the underlying cause of the model effect observed. This leads us to the question of how the cell avoids this model response when it would seem to have all the elements from which such an effect could arise. Obviously the model is a much simplified representation of the cells themselves, and the cells may have sophisticated mechanisms to prevent such an effect from occurring. However, within the confines of the model as it currently exists, we now investigate ways in which action potential activity can be maintained despite a filling ER.

To see if the loss of action potential activity could be prevented, we now examine the effects of changing various parameters in the ER model. If the maximum plasma membrane Ca^{2+} pump rate, ν_p, is increased from 0.04 $\mu M \cdot \mu m \cdot ms^{-1}$ to 0.05 $\mu M \cdot \mu m \cdot ms^{-1}$ then, during repetitive

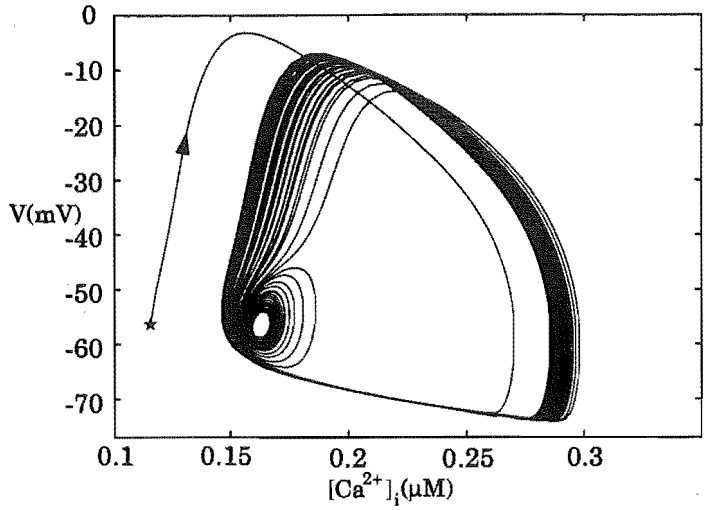

Figure 2.5: A left-shift in the voltage dependence of the L-type Ca^{2+} current V_{m_L} from -12 mV to -18 mV generates action potentials and associated $[Ca^{2+}]_i$ transients. The relationship between V and $[Ca^{2+}]_i$ during the oscillations is shown. The system starts from the previously quiescent state $\star$. The cycles move slowly to the right, indicating the gradual rise in $[Ca^{2+}]_i$. Ultimately stable oscillations are achieved, which have a V amplitude of 5 mV.

action potential activity, $[Ca^{2+}]_{er}$ still rises but reaches a new, elevated, stable value of about 20 μM without abolishing action potentials. The increased activity of the plasma membrane Ca^{2+} pump is able to prevent $[Ca^{2+}]_i$ from increasing to the level necessary to activate I_{K-Ca} and abolish action potential activity. The increase in the maximum pump rate is small and entirely reasonable, and in fact changes the resting (i.e., prior to the shift of V_{m_L}) membrane potential and $[Ca^{2+}]_i$ to -54.1 mV and 0.1 μM, respectively, values that are very similar to those from the original model.

Therefore a small and reasonable change in a single parameter can prevent the loss of action potentials, and in fact, appears to bring the ER model more into line with the original model (see below for further comparison). However, it seems unlikely that the cells would exist in a situation where a small perturbation in the level of expression of the plasma membrane Ca^{2+} pump (the cellular equivalent of reducing the maximum pump rate in the model) might lead to an inability to generate sustained firing of action potentials (as would happen in the model, if the maximum pump rate were reduced back to the original value of 0.4 $\mu M \cdot \mu m \cdot ms^{-1}$). The cell may therefore employ additional mechanisms to avoid, or at least reduce the possibility of, moving into a regime where repetitive firing would be compromised.

One well documented experimental observation in corticotrophs is a small depolarization, induced by CRH, which occurs prior to, and apparently independent of, firing of action potentials (Mollard et al., 1987; Kuryshev et al., 1995a; Kuryshev et al., 1996). These reports indicate

that the depolarization is due to the reduction in a K^+ current. This current has recently been identified as an inward rectifier (Kuryshev et al., 1997), that is active at rest and its activity is reduced by CRH. Although no clear role for this effect has been determined, it could result in an increase in membrane excitability. This effect has previously been simulated and it was found that it did increase membrane excitability, but was not obligatory for action potential generation (I).

We now re-analyse the effect of a reduction in the K^+ current that is active at rest by reducing the conductance of the leak current. The inward rectifier current is believed to be a major component of the leak current, and this current is investigated in more detail in Chapter 4. With the maximum rate of the plasma membrane Ca^{2+} pump set to the original value of 0.04 $\mu M \cdot \mu m \cdot ms^{-1}$, a reduction of the leak conductance prevented the abolition of action potentials during sustained electrical activity. Therefore these results suggest that an integrated response to CRH (i.e., activation of the L-type Ca^{2+} current and inhibition of the inward rectifier, amongst other effects) may be employed to ensure that the cell is able to provide a sustained response for as long as it may be required.

Using the change in the maximum pump rate from 0.04 $\mu M \cdot \mu m \cdot ms^{-1}$ to 0.05 $\mu M \cdot \mu m \cdot ms^{-1}$, a 6 mV negative shift in the voltage-sensitivity parameter V_{m_L} generates sustained action potentials in the ER model, indicating that action potential generation occurs in the same way as it does for the original model. However to determine this with confidence and to investigate in more depth the behaviour of the system we subject the ER model to an analysis in which the behaviour is determined for V_{m_L} values that should encompass the physiologically relevant range. This is termed a bifurcation analysis, and is shown in Figure 2.6 A, along with the bifurcation diagram for the original model (I) (Figure 2.6 B). The resting, stable state of the model occurs at the right-hand side of the figures, at $V_{m_L} = -12$ mV, where the membrane potential is approximately -55 mV. As V_{m_L} is made progressively more negative the model retains stability (in electrophysiological terms the cell remains in its quiescent state) until $V_{m_L} = -17.72$ mV, a bifurcation point, whereupon action potentials emerge and the steady-state solution becomes unstable (- - -). The maximum and minimum values of the initially unstable periodic solution are indicated by the two branches extending from the bifurcation point ($\cdots$). These two branches arch backwards, and when the amplitude of the periodic solution reaches approximately 55 mV, the periodic solution becomes stable (—), i.e., repetitive action potentials are generated. The almost perpendicular arching of the unstable branches from the bifurcation point with respect to the steady state solution indicates that as observed experimentally, the repetitive model action potentials are generated in an all-or-none manner. As V_{m_L} is further decreased the amplitude of the periodic solution increases more slowly. A slightly larger shift in V_{m_L} is required to generate action potentials in

the ER model than in the original model, indicating that the ER model is slightly less excitable. This difference in model excitability is reflected in the bifurcation diagrams (Figure 2.6), where the branching at the bifurcation point occurs at a more negative value of V_{m_L} for the ER model. Overall, the behaviours of the original and ER models are very similar with respect to action potential generation.

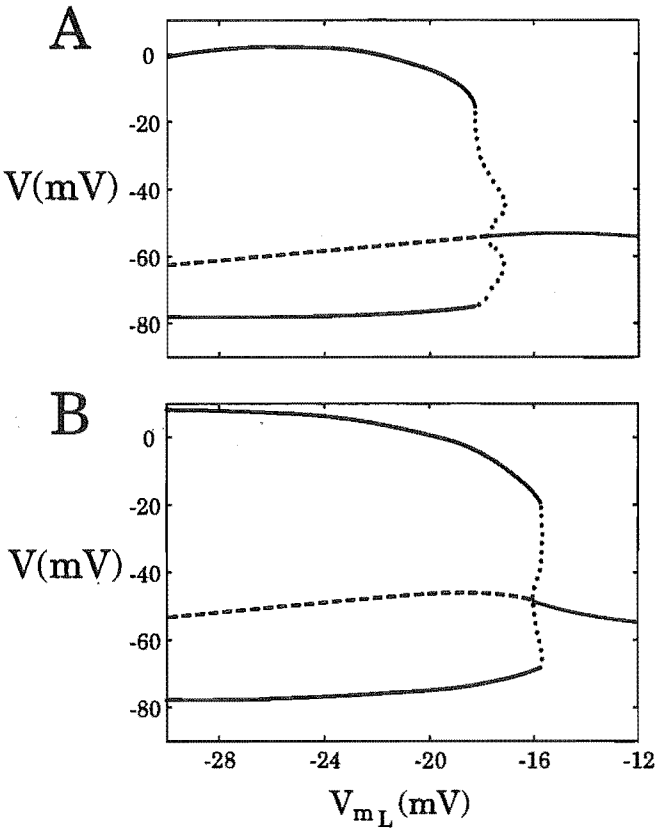

Figure 2.6: A comparison of the long term behaviour of the models for a range of V_{m_L} values: (A) The modified ER model, with a 25% larger plasma membrane pump rate $\nu_p = 0.05\ \mu M \cdot \mu m \cdot ms^{-1}$, and (B) the original model. This is termed a bifurcation analysis, and the upper and lower solid lines represent the max/min amplitude of the action potentials. A slightly larger shift in V_{m_L} is required to generate action potentials in the ER model than in the original model, indicating that the corticotroph cell model including the ER component is slightly less excitable.

2.4 The spatio-temporal calcium model

The spatio-temporal patterns in $[Ca^{2+}]_i$, generated by the subtle interplay between cellular Ca^{2+} sources and removal mechanisms, are a common mechanism of transmitting hormonal signals intracellularly (Meyer and Stryer, 1991). Because the Ca^{2+}-sensing components of the cell have both different sensitivities to Ca^{2+} and different spatial locations, we now consider the inclusion

of spatial variation in the intracellular $[Ca^{2+}]$. This structural change in the model is introduced because it is believed to be an integral part of the exocytotic pathway, and may be important in the plasma membrane electrics (Meyer and Stryer, 1991). The spatial distribution of $[Ca^{2+}]_i$ is important in *Xenopus laevis* oocytes (Atri et al., 1993), and was considered in a model of gonadotrophs (Li et al., 1997). Consequently spatial variation is now incorporated in the model description of cytosolic and endoplasmic $[Ca^{2+}]$. The cell is modeled as a spherical body, bounded by a plasma membrane, and the ER is assumed to be distributed homogeneously throughout the cell sharing the intracellular volume with the cytosol. Furthermore, the distribution of pumps, channels and leaks is assumed to be uniform. The effects of cellular pump distribution on excitable cell electrical activity is not addressed here (see Sneyd and Sherratt, (1997) for a discussion of $[Ca^{2+}]_i$ wave propagation in inhomogeneous media).

2.4.1 The model

The partial differential equation governing $[Ca^{2+}]_i$ transport can be written as

$$\frac{\partial [Ca^{2+}]_i}{\partial t} = D_c \nabla^2 [Ca^{2+}]_i + \frac{f_{cyt}}{V_c}(J_{rel} - J_{up}), \tag{2.4.1}$$

where D_c is the effective diffusion coefficient for cytosolic Ca^{2+} and ∇^2 is the Laplacian operator, which under spherical symmetry has the form $r^{-2}\partial_r(r^2\partial_r)$. This equation is similar to (2.3.5). Again $\frac{f_{cyt}}{V_c}(J_{rel} - J_{up})$ represents the ionic transfer from the ER into the cytosol, and the term $D_c\nabla^2[Ca^{2+}]_i$ represents Ca^{2+} diffusion within the cytosol. It is important to observe that D_c is a function of the concentration of Ca^{2+} buffer sites, the buffering kinetics, and the $[Ca^{2+}]_i$. When the $[Ca^{2+}]_i$ is high, the Ca^{2+} buffers become saturated and the diffusion of Ca^{2+} is less impeded than for low $[Ca^{2+}]_i$. For $[Ca^{2+}]_i < 1.0$ μM, D_c can be assumed to have a constant value of 20 $\mu m^2 \cdot s^{-1}$ (Wagner and Keizer, 1994). The boundary condition for equation (2.4.1), is described by the flux condition

$$D_c \frac{\partial [Ca^{2+}]_i}{\partial r}\bigg|_{r=d_{cell}/2} = f_{cyt}(J_{in} - J_{eff}), \tag{2.4.2}$$

where $d_{cell} = 15$ μm, is the cell diameter. The construction of this boundary condition assumes that the Ca^{2+} flux near the plasma membrane is governed by Fick's law. The fraction of unbuffered cytosolic Ca^{2+}, f_{cyt}, near the plasma membrane is likely to be larger than 1%, and the Ca^{2+} diffusion coefficient near the plasma membrane is also likely to be nearer the unbuffered Ca^{2+} diffusion coefficient. However this detail is not incorporated in the model. The ER dynamics are defined through an equation similar to (2.4.1), but the rate of concentration accumulation is now moderated by the factor f_{er}/V_{er}, so yielding

$$\frac{\partial [Ca^{2+}]_{er}}{\partial t} = D_{er}\nabla^2 [Ca^{2+}]_{er} - \frac{f_{er}}{V_{er}}(J_{rel} - J_{up}), \tag{2.4.3}$$

where D_{er} is the effective diffusion coefficient for ER Ca^{2+}. Because the concentration of Ca^{2+} buffer sites in the ER is several orders of magnitude larger than in the cytosol (Allbritton et al., 1992), it is expected that $D_{er} < D_c$. Interestingly, because the cell does not generate large $[Ca^{2+}]_{er}$ gradients and the ER predominantly acts as a Ca^{2+} storage facility rather than a source of Ca^{2+}, the value of D_{er} (see Table 2.1) has very little effect on the model behaviour. It is assumed that the ER does not interact directly with the extracellular medium, i.e.,

$$D_{er}\frac{\partial[Ca^{2+}]_{er}}{\partial r}\bigg|_{r=d_{cell}/2} = 0. \tag{2.4.4}$$

The model assumes for simplicity that all Ca^{2+} buffers are immobile. It is important to note that the existence of even small amounts of mobile buffer alters the mass transport equations, introducing an extra non-diffusive term (Wagner and Keizer, 1994) into (2.4.1) and (2.4.3). However a model including this extra complexity is not presented here.

2.4.2 Numerical methods

The system of partial differential equations ((2.4.1)–(2.4.4)), equation (2.2.1) and the four channel gating variable equations (1.1.9), were solved by the method of lines (Schiesser, 1994) using a stiff system solver in the numerical package XPPAUT(3.0). Various discretisations of the partial differential equations, ranging from coarse (5 shells of equal thickness) to fine (100 shells) were implemented. The figures in this chapter were generated using a model discretisation of 20 shells, allowing sufficient accuracy without excessive computation.

2.4.3 The model behaviour

As more realistic Ca^{2+} handling has been incorporated in the model, the mechanisms of action potential generation established previously require verifying. The inclusion of spatial variation in the intracellular $[Ca^{2+}]$ into the model does not affect the equilibrium state; at rest the $[Ca^{2+}]_i = 0.1$ μM, $[Ca^{2+}]_{er} = 8.48$ μM and the membrane potential $V = -54.1$ mV. As before, to simulate the proposed PKA-induced shift in the voltage sensitivity of the L-type current, we left-shift V_{m_L}, the voltage at which the L-type current is half-maximally activated. This left-shift in V_{m_L} from -12 mV to -18 mV generates action potentials, with associated $[Ca^{2+}]_i$ transients (Figure 2.7). The action potentials (—) exhibit a similar form when compared with those from the ER model (– – –), with a decrease in both the period and the amplitude of oscillation. $[Ca^{2+}]_i$ transients near the plasma membrane (—), and at the cell centre (– — –), display faster and slower falling phases respectively when compared with $[Ca^{2+}]_i$ transients in the ER model (– – –). Both models exhibit a slow $[Ca^{2+}]_{er}$ increase. The similarity of the bifurcation diagrams (not shown)

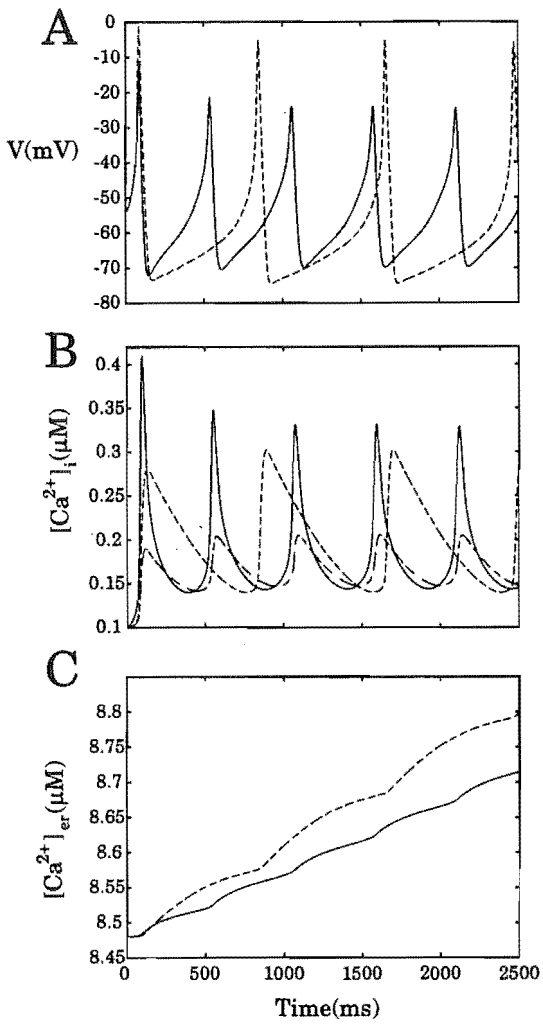

Figure 2.7: Comparison of the action potentials and $[Ca^{2+}]_i$ transients for the spatio-temporal Ca^{2+} model, and the modified ER model with $\nu_p = 0.05\ \mu M \cdot \mu m \cdot ms^{-1}$. (A) A left-shift in the voltage dependence of the L-type Ca^{2+} current, V_{m_L}, from -12 mV to -18 mV generates action potentials in the spatio-temporal Ca^{2+} model (—), which display similar kinetic features to those in the ER model (- - -). (B) $[Ca^{2+}]_i$ transients near the plasma membrane (—), and at the cell centre (- — -), display faster and slower falling phases respectively when compared with $[Ca^{2+}]_i$ transients in the ER model (- - -). (C) The ER model (- - -) exhibits a faster $[Ca^{2+}]_{er}$ increase than the spatio-temporal Ca^{2+} model (—).

for the spatio-temporal Ca^{2+} model and the ER model indicates that the characteristics of action potential generation are similar.

The cytosolic Ca^{2+} diffusive flux is small relative to the average Ca^{2+} flux through the plasma membrane during an action potential. Hence there exists a high $[Ca^{2+}]_i$ gradient within the cell. $[Ca^{2+}]_i$ levels near the plasma membrane are typically higher than average $[Ca^{2+}]_i$ levels (Figure 2.8). The combination of the high $[Ca^{2+}]_i$ gradient, and Ca^{2+} diffusion, generates diffusive $[Ca^{2+}]_i$ waves traveling from the cell boundary to the cell centre (Figure 2.8). Due to Ca^{2+} buffering and Ca^{2+} uptake by the ER, these diffusive waves undergo severe damping as they travel toward the centre of the cell. The Ca^{2+} waves can also be visualised in Figure 2.9. The plasma

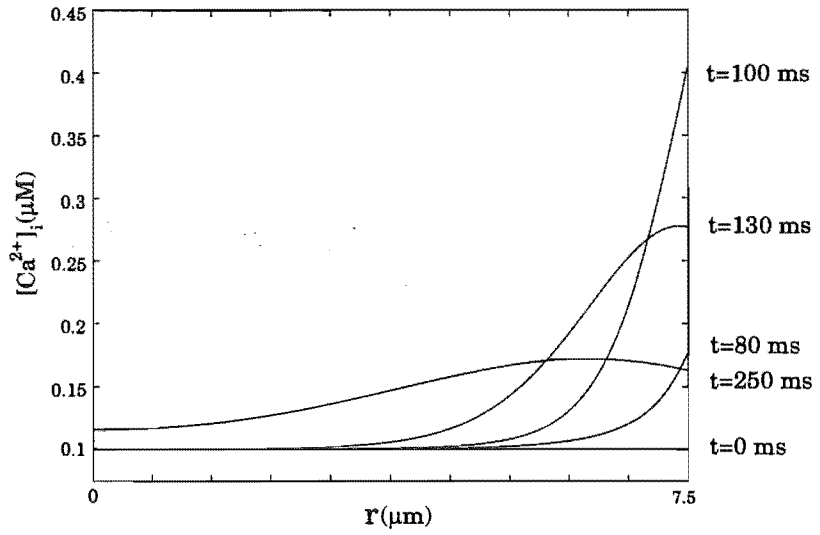

Figure 2.8: The spatial distribution of $[Ca^{2+}]_i$ during an action potential, at times 0, 80, 100, 130, and 250 ms. The horizontal coordinate r denotes the radial distance from the cell centre ($r = 0$) to the plasma membrane ($r = 7.5$ μm). The diffusive $[Ca^{2+}]_i$ wave traveling from the cell boundary to the cell centre is highly damped, due to Ca^{2+} buffering and ER Ca^{2+} uptake.

membrane action potentials, diffusive $[Ca^{2+}]_i$ waves, and $[Ca^{2+}]_i$ gradient are all distinguishable in this diagram. This $[Ca^{2+}]_i$ gradient does not significantly affect the generation of action potentials so that at present the simple lumped cytosolic Ca^{2+} description seems sufficient to explain plasma membrane electrical activity. The ordinary differential equation model description is also more convenient to use and easier to understand.

2.5 Proposed experiment to test model predictions

Both the ER model and the spatio-temporal model predict a considerable rise in $[Ca^{2+}]_{er}$ during repetitive action potential activity and that this, in principle, could signal back to the plasma membrane and influence electrical activity. The extent of the rise in $[Ca^{2+}]_{er}$ would be an impor-

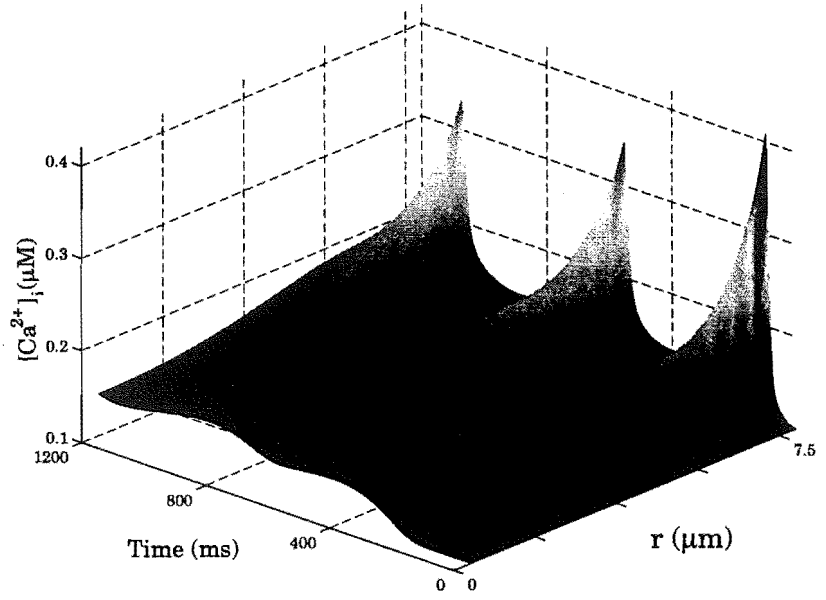

Figure 2.9: The spatial distribution of $[Ca^{2+}]_i$ during action potentials. The coordinate r denotes the radial distance from the cell centre ($r = 0$) to the plasma membrane ($r = 7.5$ μm).

tant determinant of the level of influence of such a signal, and is therefore an important factor to consider. In this section a simple experiment that could be used to measure this factor is proposed and simulated.

ER Ca^{2+} can be released into the cytosol by Ca^{2+} ionophores such as A23187 and ionomycin (Iono) (Corcuff et al., 1993; Won and Orth, 1995), and Ca^{2+} uptake into the ER can be inhibited by thapsigargin, an ER Ca^{2+}-ATPase inhibitor. To measure the amount of sequestered ER Ca^{2+} following CRH-induced activity, Iono could be applied, and the level of $[Ca^{2+}]_i$ compared with the same treatment without prior exposure to CRH. The results of this experiment simulated with the ER model are shown in Figure 2.10, where a 40 s CRH application is elicited by a change in V_{m_L} from -12 mV to -18 mV, and the application of Iono is mimicked by a tenfold increase in the ER leak permeability P. As can be seen, there is a greater release of stored Ca^{2+} in the CRH-treated case. Some indication of the rate of Ca^{2+} accumulation in the ER could be obtained by varying the period of exposure to CRH. Although this is a simple experiment, the results of its execution would be valuable for testing the model predictions and for providing information on the role of the ER during action potential activity.

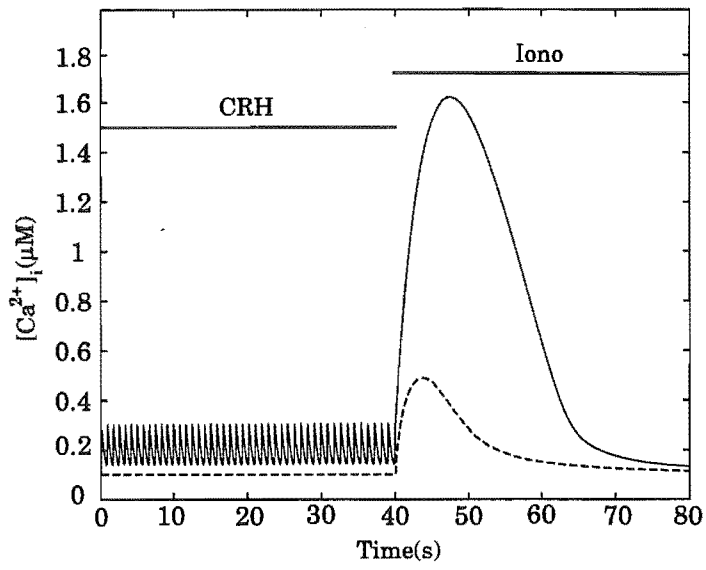

Figure 2.10: The magnitude of $[Ca^{2+}]_{er}$ increase during CRH application is undetermined. Application of an ionophore such as ionomycin (Iono) after an application of CRH would indicate the amount of Ca^{2+} sequestered by the ER during CRH application. A 40 s CRH application is elicited by a change in V_{m_L} from -12 mV to -18 mV, and is followed by an application of ionomycin(—), mimicked by a tenfold increase in the ER leak permeability P. The degree of ER Ca^{2+} uptake is apparent from a comparison with cells subjected to only ionomycin (- - -).

2.6 Discussion

To investigate mechanisms by which CRH induces membrane electrical activity, we described in this chapter an extension to the model of corticotroph electrical activity in (I), by investigating more realistic intracellular Ca^{2+} mechanisms (addition of a distinct ER compartment allowing bidirectional exchange of Ca^{2+} with the cytosol) and the resulting effects on the model dynamics. This model indicated that an increase in the L-type Ca^{2+} current is sufficient to initiate repetitive action potentials from a previous quiescent model state. It must be emphasized that the hypothesis of action potential generation via a PKA-induced enhancement of the L-type Ca^{2+} current remains valid in the more physiological model. Experimental investigation is necessary to determine whether the PKA enhancement of the L-type Ca^{2+} current occurs by an increase in the macroscopic current of the L-type channel, or by inducing a left-shift in the voltage sensitivity of the L-type channel. Reports from other cell types have indicated that PKA can induce a left-shift of 6–10 mV in the voltage sensitivity of the L-type current. Shifts within this experimentally observable range induced repetitive model action potentials in an all-or-none manner as observed experimentally.

During repetitive action potential activity, the ER sequesters Ca^{2+} and therefore acts as a

buffer for $[Ca^{2+}]_i$. However, for the original parameter choices and Ca^{2+} exchange mechanisms action potential activity was eventually lost due to excessive feedback release of Ca^{2+} from the ER causing an increase in the activity of I_{K-Ca}, which in turn reduced membrane excitability sufficiently to prevent further action potential generation. This is not believed to be a response normally found in corticotrophs, and the effect can be eliminated by small and reasonable parameter changes. However the underlying mechanisms seem valid and so there would appear to be some risk to the cells that they could not faithfully generate a sustained cellular response to CRH exposure. This suggests that corticotrophs employ strategies to prevent such an effect from occurring. The potential role of CRH-induced reduction of an inward rectifier K^+ current was tested, an effect observed experimentally by Kuryshev et al., 1997. This was achieved by reducing the conductance of the model leak current, and it was found that this change prevented the loss of action potential activity. This reduction in the inward rectifier K^+ current may represent one of many strategies employed by corticotrophs to ensure a sustained cellular response to CRH.

The spatial distribution of Ca^{2+} is important in other cell types. Consequently spatial variation was incorporated in the cytosolic and endoplasmic Ca^{2+} in the model. The resulting model action potentials and Ca^{2+} transients exhibit a similar form when compared with the previous models. Model $[Ca^{2+}]_i$ levels near the plasma membrane were typically higher than average $[Ca^{2+}]_i$ levels. This high $[Ca^{2+}]_i$ gradient, combined with Ca^{2+} diffusion, generates highly damped diffusive $[Ca^{2+}]_i$ waves traveling from the cell boundary to the cell centre. This $[Ca^{2+}]_i$ gradient did not have a significant impact on the generation of action potentials, so at present the simple lumped cytosolic Ca^{2+} description is sufficient to explain plasma membrane electrical activity. However the spatial variation in Ca^{2+} may be important in modeling aspects of the secretion process. The simple lumped cytosolic Ca^{2+} model description is also more convenient to use and easier to understand.

Chapter 3

Bursting in a model of corticotroph electrical activity

3.1 Introduction

In certain parameter regimes, the Hodgkin–Huxley type mathematical model constructed in Chapter 2 exhibits a novel form of bursting behaviour. Many cell types exhibit bursting activity, characterised by alternating phases of near steady state behaviour and trains of rapid spike-like oscillations. The basic idea is that these slow processes modulate the faster spike generating dynamics. The bursting in the model is due to the existence of a fast time scale associated with the membrane action potentials and a slow time scale associated with the slow modulation of the endoplasmic reticulum (ER) Ca^{2+} concentration. In this chapter we investigate this bursting where the quiescent state is a small amplitude ("subthreshold") limit cycle attractor and the spiking state is a limit cycle attractor. In order to perform a mathematical analysis of this bursting behaviour, a reduced version of this model is studied which also exhibits topologically similar types of bursting behaviour in certain parameter regimes.

Although pituitary corticotrophs do not seem to exhibit these modes of bursting this interesting type of bursting hasn't been observed in Hodgkin–Huxley type models and warrants further study. Some corticotrophs exhibit other modes of bursting where the depolarization spike is followed by small oscillations in the membrane potential (Kuryshev et al., 1996; Kuryshev et al., 1997; Adler et al., 1983). These modes of bursting are exhibited in the model and the behaviour and underlying mechanisms are investigated in Chapter 4.

The bursting process is driven by the slow modulation of the endoplasmic reticulum Ca^{2+} concentration ($[Ca^{2+}]_{er}$), giving rise to a slow component in $[Ca^{2+}]_i$. This slow component in $[Ca^{2+}]_i$ gives rise to the electrical bursting via a Ca^{2+}-activated K^+ current. This store operated burst modulation mechanism has also been observed in other Hodgkin–Huxley type models (Chay,

1997; Gall and Susa, 1999), and this mechanism is analysed from a bifurcation perspective.

There has been much interest in bursting oscillations in electrophysiological systems based on slowly varying dynamical systems (Rinzel, 1987; Bertram et al., 1995; de Vries, 1998). There are two time scales identified in the model; a fast time scale associated with membrane action potentials, and a slow time scale associated with the gradual increase in $[Ca^{2+}]_{er}$. This slow time scale allows us to interpret the model as a fast system evolving through a slow subsystem. Thus by treating the slow variable as a fixed parameter the system can be regarded as a family of vector fields. This allows the use of tools from bifurcation theory to investigate the different modes of bursting in the model.

The first formal classification of bursting is due to Rinzel (1987) who classified the "parabolic", "elliptic", and "square-wave" modes of bursting. Bertram et al. (1995) suggested using Roman numerals to identify the different modes, and they introduced the Type IV burster. Further classification was also carried out by Rush and Rinzel (1994) and de Vries (1998) who suggested the addition of the "triangular" and Type V burster respectively. However the current naming scheme is misleading and is becoming unmanageable as the number of classified modes increases. A more self-explanatory comprehensive naming scheme suggested by Izhikevich (2000) is to name the bursting mode after the two bifurcations involved. Thus for example the well known "elliptic" (Type III) burster is a "subHopf/fold cycle" burster because the rest state disappears in a subcritical Hopf bifurcation and the limit cycle attractor disappears in a fold limit cycle bifurcation. All of the aforementioned bursters are termed point–cycle bursters due to the fact that the quiescent state is a stable equilibrium and the spiking state is a limit cycle attractor. In this chapter a novel form of bursting due to bistability between two periodic solutions is investigated. This is termed a cycle-cycle burster. Due to the bifurcations involved, this topological type of bursting is named "fold cycle/fold cycle" bursting (Izhikevich, 2000). Because the fast spiking subsystem is two-dimensional the burster is termed planar by Izhikevich (2000) .

The model bursting is similar to a mode of cycle–cycle bursting exhibited in the neuron model of Wang (1993). However in that model the bursting is modulated by the slow inactivation kinetics of a K^+ current. A bifurcation analysis with respect to this inactivation variable reveals the model bistability. This shows the subthreshold limit cycle disappears in a fold cycle bifurcation and the spiking limit cycle attractor disappears in a subcritical flip (period doubling) bifurcation. This mode is termed a "fold cycle/flip" burster (Izhikevich, 2000).

The broad classification scheme of Izhikevich (2000) is theoretical in the sense that many of the 120 bursting modes have yet to be observed in conductance based models. The "fold cycle/fold cycle" and "fold cycle/flip" bursters identified in this chapter have not previously been observed in Hodgkin–Huxley type models. An interesting open problem is whether conductance based models

of the Hodgkin–Huxley type impose restrictions on the possible bifurcations and hence the type of bursters (Izhikevich, 2000).

3.2 The model

The model is of Hodgkin–Huxley form (Hodgkin and Huxley, 1952), and consists of seven coupled ordinary differential equations. The model equations and parameters are presented in Chapter 2, and the equations are reproduced in the Appendix. Four ionic currents are included in the model: 1) a high-voltage threshold dihydropyridine-sensitive L-type Ca^{2+} current (I_{Ca-L}), responsible for most of the inward Ca^{2+} current during an action potential; 2) a low-voltage threshold rapidly inactivating T-type voltage-sensitive Ca^{2+} current (I_{Ca-T}); 3) a voltage-sensitive K^+ current (I_{K-DR}), predominantly responsible for the action potential repolarization; and 4) a Ca^{2+}-activated K^+ current (I_{K-Ca}), essential in the bursting behaviour. The remaining leak current (I_{Leak}) represents all other ionic current contributions not specifically described. The model descriptions of these ionic currents is described in Section 2.2.

Ca^{2+} transport is crucial for action potential generation in corticotrophs, and the model includes equations for the intracellular Ca^{2+} concentration ($[Ca^{2+}]_i$) and the ER Ca^{2+} concentration. The ER performs a number of important cellular functions, including cellular Ca^{2+} homeostasis and protein synthesis (Alberts et al., 1983, p335). A schematic diagram of the ionic transport processes is shown in Figure 2.2.

The bursting type behaviour we discuss and analyse in this chapter is exhibited in the full seven variable model presented in Chapter 2 and simpler models containing a smaller number of variables, albeit with slightly different parameter values. The reduction in the number of model variables utilises the fact that the channel gating variables m_L, h_T and m_T present in the I_{Ca-L} and I_{Ca-T} channel currents (see the Appendix) remain very close to their steady state values during an action potential, that is they are fast variables and can be removed and set to their steady state values. This produces a four variable model, which has been previously discussed in the context of action potential generation and excitability (LeBeau et al., 1998). However for ease of explanation we eliminate another variable from the model. The fourth gating variable n, present in the I_{K-DR} channel current (see the Appendix), is not as fast as the membrane potential difference (V). However to aid in the visualisation of the model we set n to its steady state value to obtain the three variable model governed by the equations in Table 3.1. This change does not significantly change the model dynamics. This model system was solved using a stiff system solver in the numerical package XPPAUT(3.0) [1]. Bifurcation diagrams were computed using AUTO (Doedel, 1981), as incorporated in XPPAUT.

[1] Written by Bard Ermentrout, and available at ftp.math.pitt.edu/pub/bardware.

$$
\begin{aligned}
c_{\mathrm{m}}\frac{dV}{dt} &= -(I_{\mathrm{Ca-L}} + I_{\mathrm{Ca-T}} + I_{\mathrm{K-DR}} + I_{\mathrm{K-Ca}} + I_{\mathrm{Leak}}),\\
\frac{d[\mathrm{Ca}^{2+}]_{\mathrm{i}}}{dt} &= \frac{f_{\mathrm{cyt}}}{V_{\mathrm{c}}}(J_{\mathrm{rel}} - J_{\mathrm{up}}) + f_{\mathrm{cyt}}\beta(J_{\mathrm{in}} - J_{\mathrm{eff}}),\\
\frac{d[\mathrm{Ca}^{2+}]_{\mathrm{er}}}{dt} &= -\frac{f_{\mathrm{er}}}{V_{\mathrm{er}}}(J_{\mathrm{rel}} - J_{\mathrm{up}}),\\
g &= g_{\infty}(V), \quad g \in \{m_{\mathrm{L}}, m_{\mathrm{T}}, h_{\mathrm{T}}, n\},
\end{aligned}
$$

Table 3.1: Reduced three-variable model equations.

3.3 The model bursting

The bursting behaviour in the three variable model is shown in Figure 3.1 A. There is one change to the model parameter set in Table 2.1 with $\nu_{\mathrm{p}} = 0.045\ \mu\mathrm{M}\cdot\mu\mathrm{m}\cdot\mathrm{ms}^{-1}$. The quiescent state is a small amplitude ("subthreshold") limit cycle attractor and the spiking state is a limit cycle attractor. Due to the bistability between two periodic solutions this is termed a cycle-cycle burster (Izhikevich, 2000). The silent and active phases of the bursts are associated with increasing and decreasing $[\mathrm{Ca}^{2+}]_{\mathrm{er}}$ respectively (Figure 3.1 C).

During the spiking train of action potentials $[\mathrm{Ca}^{2+}]_{\mathrm{er}}$ slowly increases as the ER sequesters Ca^{2+} and therefore acts to buffer the $[\mathrm{Ca}^{2+}]_{\mathrm{i}}$ (Figure 3.1 C). If only a single $[\mathrm{Ca}^{2+}]_{\mathrm{i}}$ transient was generated, the additional ER Ca^{2+} would be returned to the cytosol, and eventually removed from the cell altogether to recover cellular $[\mathrm{Ca}^{2+}]$ homeostasis. However, Figure 3.1 C shows that with each successive action potential, $[\mathrm{Ca}^{2+}]_{\mathrm{er}}$ builds up as each transient contributes additional Ca^{2+} to the cytosol via the L-type Ca^{2+} current. $[\mathrm{Ca}^{2+}]_{\mathrm{er}}$ increases until $[\mathrm{Ca}^{2+}]_{\mathrm{er}} = 17.8\ \mu\mathrm{M}$, where the limit cycle disappears and $[\mathrm{Ca}^{2+}]_{\mathrm{er}}$ begins to decrease. The trajectory is then attracted towards the smaller stable subthreshold quiescent state. $[\mathrm{Ca}^{2+}]_{\mathrm{er}}$ decreases until $[\mathrm{Ca}^{2+}]_{\mathrm{er}} = 17.3\ \mu\mathrm{M}$, where the small periodic orbit disappears, and the trajectory is attracted back towards the spiking state. The process of moving between the two stable periodic solutions then repeats, and "fold cycle/fold cycle" bursting behaviour is obtained. The "fold cycle/fold cycle" bursting can be visualised as a flow on a two-dimensional invariant torus in V-$[\mathrm{Ca}^{2+}]_{\mathrm{i}}$-$[\mathrm{Ca}^{2+}]_{\mathrm{er}}$ phase space (Hale and Kocak, 1991), with the silent and active phases of the bursts associated with flow on the inner and outer surfaces of the torus, respectively.

The $[\mathrm{Ca}^{2+}]_{\mathrm{i}}$ transients mimic the voltage bursting response (Figure 3.1 B). Coupled to the increase in $[\mathrm{Ca}^{2+}]_{\mathrm{er}}$ during the spiking phase is a slight rise in the average $[\mathrm{Ca}^{2+}]_{\mathrm{i}}$ (i.e., averaged over the course of a transient) The small rise in $[\mathrm{Ca}^{2+}]_{\mathrm{i}}$ results from an enhanced Ca^{2+} leak current from the ER and leads to a gradual increase in the average activation of $I_{\mathrm{K-Ca}}$. This in turn has a subtle inhibitory effect on the regeneration of action potentials. During the spiking phase the

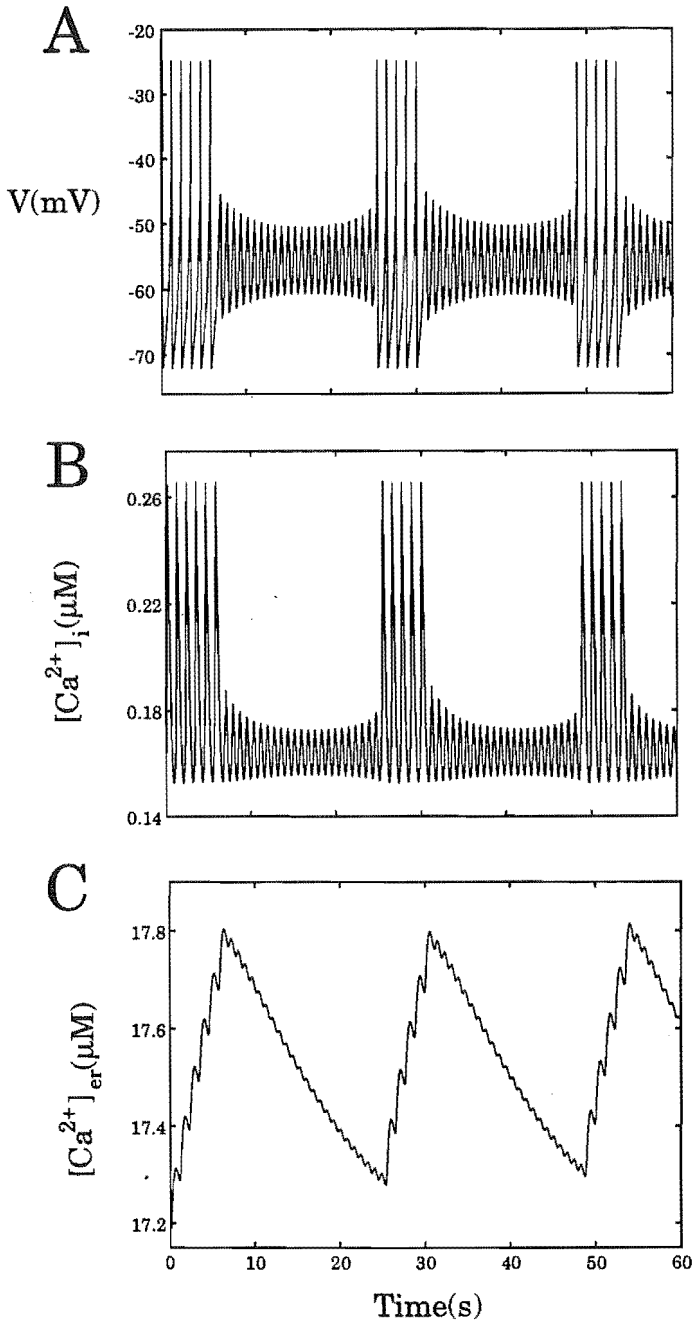

Figure 3.1: (A) Model "Fold cycle/fold cycle" bursting due to bistability between the two stable periodic solutions ($\nu_p = 0.045\ \mu M \cdot \mu m \cdot ms^{-1}$). To allow the individual action potentials to be resolvable on the scale illustrated, the ER Ca^{2+} buffering factor is increased from $f_{er} = 0.0025$ to $f_{er} = 0.01$. (B) Coupled to the voltage bursting response are $[Ca^{2+}]_i$ transients. (C) During the active and silent phases of the bursts $[Ca^{2+}]_{er}$ increases and decreases respectively.

action potential peaks slightly decrease until enough feedback is present to significantly reduce the action potentials, resulting in small amplitude oscillations. To allow the individual action potentials to be resolvable on the scale illustrated, the ER Ca^{2+} buffering factor is increased from $f_{er} = 0.0025$ to $f_{er} = 0.01$. This reduction in the ER Ca^{2+} buffering allows $[Ca^{2+}]_{er}$ to change more rapidly and has little effect on the dynamics under consideration.

The bursting is modulated by a very minor increase in $[Ca^{2+}]_i$, demonstrating the delicate interplay between the ER filling state and the plasma membrane electrical activity. This store operated burst modulation mechanism has also been observed in other Hodgkin–Huxley type models (Chay, 1997; Gall and Susa, 1999). Further, this effect shows that the ER could potentially play an important signaling role despite an initial appearance that it plays only a passive, buffering function during CRH-induced activity.

3.4 One parameter bifurcation analysis

Now we consider a fast-slow decomposition of the system of equations based on the pioneering work of Rinzel (1985, 1986, 1987) . This decomposition is justifiable since the spiking time scale is significantly smaller than the time scale of modulation. As illustrated in Figure 3.1, it is evident that V and $[Ca^{2+}]_i$ are the fast variables, and $[Ca^{2+}]_{er}$ is the slow variable. By treating the slow variable $[Ca^{2+}]_{er}$ as a fixed parameter the model can be interpreted as a family of vector fields, with the slow variable dynamics allowing the fast system to evolve through this family.

The sequence of model behaviour is illustrated by showing trajectories in $[Ca^{2+}]_i$-V phase space instead of temporal plots. If the slow variable $[Ca^{2+}]_{er}$ is fixed at 17 μM then the model exhibits stable action potentials as shown by the stable periodic orbit (—) in Figure 3.2 A. Increasing $[Ca^{2+}]_{er}$ to 17.6 μM changes the model behaviour. In addition to the large stable periodic orbit a smaller stable oscillation has emerged as shown in Figure 3.2 B. In between these two stable periodic solutions lies an unstable periodic orbit (– – –). This unstable periodic orbit specifies the regions of attraction of the two periodic solutions. If $[Ca^{2+}]_{er}$ is further increased the model behaviour changes again. Figure 3.2 C indicates the model behaviour when $[Ca^{2+}]_{er} = 18$ μM. The large periodic orbit has coalesced with the unstable periodic orbit and disappeared. All trajectories are now attracted onto the smaller stable periodic orbit. If $[Ca^{2+}]_{er}$ is further increased to $[Ca^{2+}]_{er} = 19$ μM, then the small stable periodic solution has disappeared, and all trajectories are attracted onto a stable steady state solution (Figure 3.2 D). The sequence of $[Ca^{2+}]_{er}$ values chosen above are not values for which bifurcations occur.

The visualisation of the vector field is useful in understanding the model behaviour. This is the reason we make the reduction to the three variable model. The nullclines are helpful in understanding action potential generation, and are shown with $[Ca^{2+}]_{er}$ fixed at 17 μM in

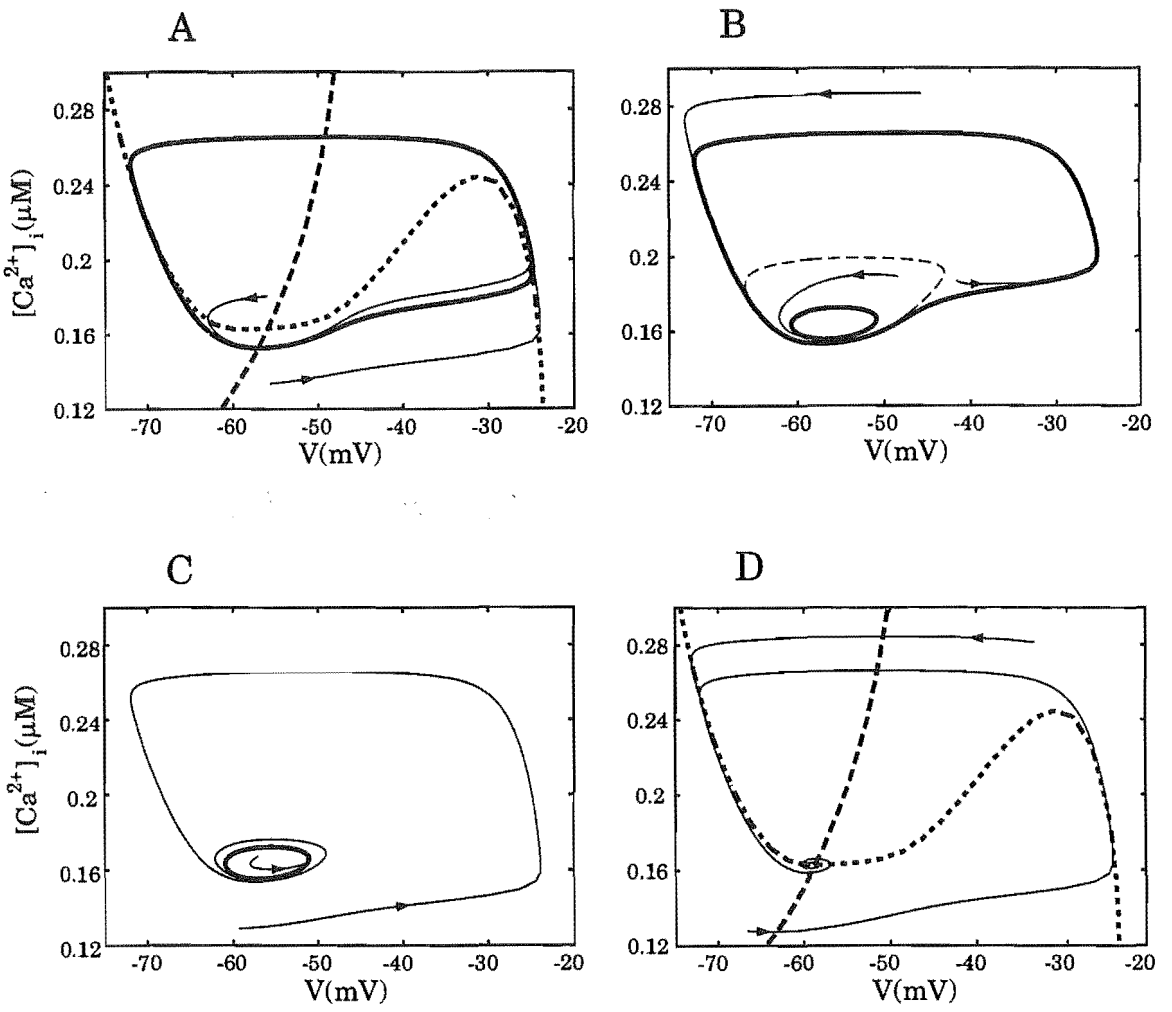

Figure 3.2: Sequence of model situations as $[Ca^{2+}]_{er}$ increases. (A) For $[Ca^{2+}]_{er} = 17$ μM the model exhibits stable action potentials (—). The S-shaped V nullcline (· · ·) and the $[Ca^{2+}]_i$ nullcline (– – –) indicate that V is a faster variable than $[Ca^{2+}]_i$. Directed arrows represent trajectories. (B) For $[Ca^{2+}]_{er} = 17.6$ μM a small stable oscillation has emerged that is surrounded by an unstable periodic orbit (– – –). (C) The larger periodic orbit has coalesced with the unstable periodic orbit and disappeared when $[Ca^{2+}]_{er} = 18$ μM. (D) When $[Ca^{2+}]_{er} = 19$ μM the small stable periodic solution has disappeared and is replaced by a single stable steady state.

Figure 3.2 A. The S-shaped V nullcline ($\cdots$) is not a function of $[Ca^{2+}]_{er}$, and hence is simple to visualise in V-$[Ca^{2+}]_i$-$[Ca^{2+}]_{er}$ phase space. However the $[Ca^{2+}]_i$ nullcline ($- - -$) is a function of $[Ca^{2+}]_{er}$, and moves gradually up and to the left with increasing $[Ca^{2+}]_{er}$ (see Figure 3.2 D). Because the change in this nullcline is subtle the $[Ca^{2+}]_i$ null-surface is also easily visualised in V-$[Ca^{2+}]_i$-$[Ca^{2+}]_{er}$ phase space. Superimposed in Figure 3.2 A is the orbit of a typical action potential (—) in the V-$[Ca^{2+}]_i$ phase plane. Notice that the orbit is heavily attracted onto the S-shaped V nullcline, indicating that V is a faster variable than $[Ca^{2+}]_i$.

To summarise the sequence of phase portraits shown in Figure 3.2 a bifurcation analysis of the model with respect to the slow variable $[Ca^{2+}]_{er}$ is shown in Figure 3.3 A. This bifurcation structure is called the slow manifold. For $[Ca^{2+}]_{er} < 17.46$ μM the model only exhibits stable action potentials (—), with an amplitude of about 50 mV. However for $17.46 \leq [Ca^{2+}]_{er} < 17.76$ μM the model exhibits bistability due to the emergence of a small stable solution from a saddle node of periodics bifurcation (SNP). A SNP bifurcation is also called a fold bifurcation of limit cycles or a fold cycle, the term used in our classification of bursting. The unstable periodic orbit ($- - -$) denotes the regions of attraction of the two periodic orbits. For $17.76 \leq [Ca^{2+}]_{er} < 18.29$ μM only small oscillations are exhibited due to the disappearance of the action potentials through another SNP bifurcation. For $[Ca^{2+}]_{er} \geq 18.29$ μM the small oscillations disappear in a supercritical Hopf bifurcation (HB) and the previous unstable steady state ($- - -$) becomes stable (—). The interesting feature of this diagram is the bistability between two stable periodic solutions for $[Ca^{2+}]_{er}$ between the two SNP bifurcations. It is this bistability that is critical for the bursting type behaviour in the model.

The $[Ca^{2+}]_{er}$ null-surface is independent of V, and is relatively linear for $[Ca^{2+}]_{er} < 20$ μM. This null-surface is easily visualised and seems simple, but the way it interacts with the other two null-surfaces leads to interesting behaviour. This interaction is shown in Figure 3.3 A, where the $[Ca^{2+}]_{er}$ nullcline ($\cdot - \cdot$) is superimposed onto the slow manifold. This diagram is useful in understanding of the bursting behaviour previously shown in Figure 3.1 A.

The bursting oscillations result from bistability between two stable periodic solutions, with the silent and active phases of the bursts associated with increasing and decreasing $[Ca^{2+}]_{er}$ respectively (see Figure 3.1). During the spiking train of action potentials $[Ca^{2+}]_{er}$ increases until $[Ca^{2+}]_{er} = 17.76$ μM, the upper SNP bifurcation in Figure 3.3 A. The trajectory is then attracted towards the smaller stable periodic orbit of Figure 3.3 A, and $[Ca^{2+}]_{er}$ decreases because $d[Ca^{2+}]_{er}/dt < 0$ under the $[Ca^{2+}]_{er}$ nullcline ($\cdot - \cdot$). $[Ca^{2+}]_{er}$ decreases until a SNP bifurcation occurs when $[Ca^{2+}]_{er} = 17.46$ μM, and the small periodic orbit disappears. However the trajectory is not immediately attracted onto the upper stable branch. Small voltage oscillations in the membrane potential of increasing amplitude continue until $[Ca^{2+}]_{er}$ decreases to 17.3 μM, as

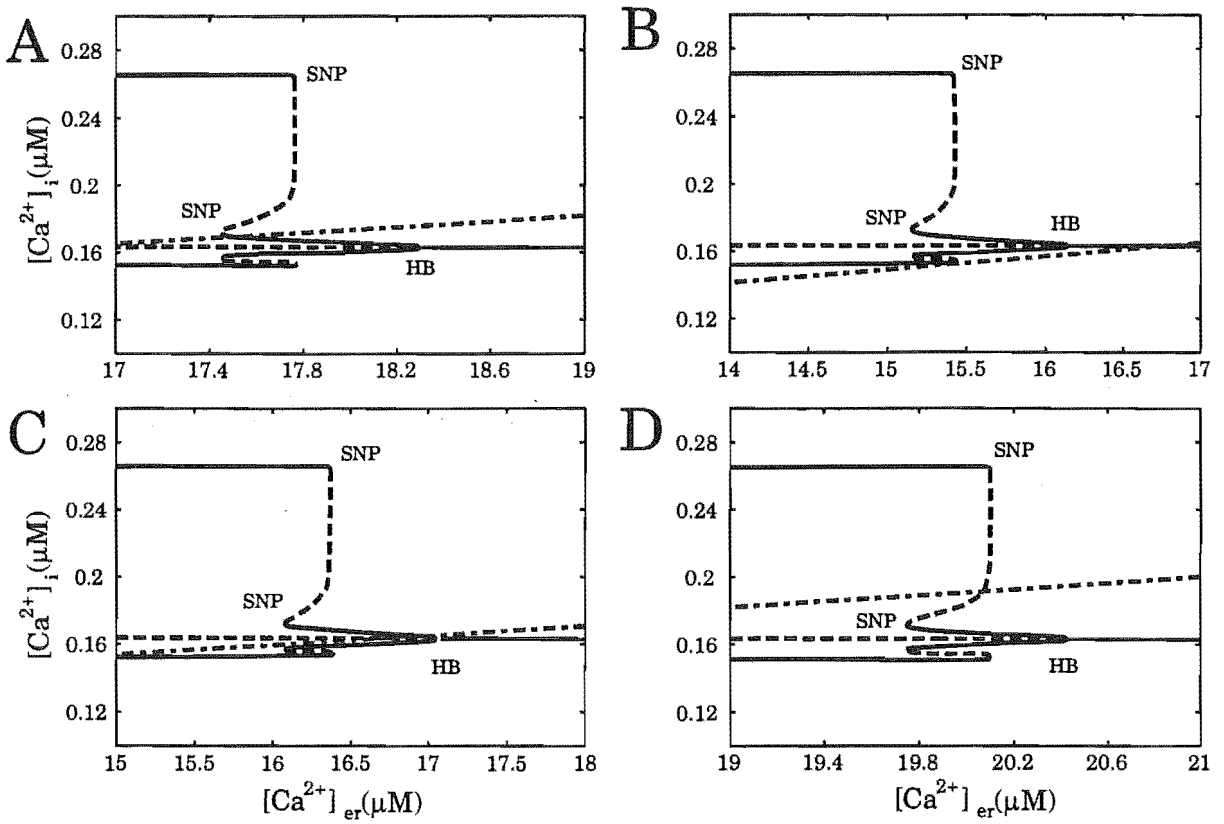

Figure 3.3: Model $[Ca^{2+}]_{er}$ nullcline $(\cdot - \cdot)$ superimposed on the slow manifold for different values of ν_p, the maximum plasma membrane $[Ca^{2+}]_i$ pump rate. Increasing ν_p moves the slow manifold to the right. (A) When $\nu_p = 0.045\ \mu M \cdot \mu m \cdot ms^{-1}$ the model exhibits the "fold cycle/fold cycle" bursting in Figure 3.1. (B) When $\nu_p = 0.04\ \mu M \cdot \mu m \cdot ms^{-1}$ the model reaches a steady state where the $[Ca^{2+}]_{er}$ nullcline intersects the slow manifold . (C) When $\nu_p = 0.042\ \mu M \cdot \mu m \cdot ms^{-1}$ the model exhibits sustained subthreshold oscillations.(D) When $\nu_p = 0.05\ \mu M \cdot \mu m \cdot ms^{-1}$ the model exhibits sustained action potentials and is incapable of bursting.

shown in Figure 3.1 A & C. This slow passage through the SNP bifurcation is similar to the slow passage through a Hopf bifurcation, which is known as the delay or memory effect (Baer et al., 1989; Holden and Erneux, 1993; Arnold et al., 1994). The process of moving between the two stable periodic branches then repeats, and due to the bifurcations involved, this topological type of bursting is named "fold cycle/fold cycle" bursting (Izhikevich, 2000).

One may ask: What happens if the slow manifold is moved relative to the $[Ca^{2+}]_{er}$ *nullcline?* There are two of ways to achieve this, we can either move the $[Ca^{2+}]_{er}$ nullcline or move the slow manifold. The choice is arbitrary, and we choose to decrease the plasma membrane $[Ca^{2+}]_i$ maximum pump rate (ν_p) from 0.045 $\mu M \cdot \mu m \cdot ms^{-1}$ to 0.04 $\mu M \cdot \mu m \cdot ms^{-1}$ to move the slow manifold to the left (see Figure 3.3 B). For a spiking system on the upper branch in Figure 3.3 B it follows that $[Ca^{2+}]_{er}$ will increase since above the $[Ca^{2+}]_{er}$ nullcline $d[Ca^{2+}]_{er}/dt > 0$. $[Ca^{2+}]_{er}$ will continue to increase until $[Ca^{2+}]_{er} = 15.43$ μM, whereupon the action potentials disappear through the upper SNP bifurcation and the system moves onto the smaller stable periodic solution. $[Ca^{2+}]_{er}$ will continue to increase, until the small oscillations die out via a supercritical HB, and a steady state is reached where the $[Ca^{2+}]_{er}$ nullcline intersects the slow manifold at $[Ca^{2+}]_{er} = 16.8$ μM.

If the slow manifold is moved slightly to the right by increasing ν_p to 0.042 $\mu M \cdot \mu m \cdot ms^{-1}$ then the model behaviour changes (Figure 3.3 C). As before $[Ca^{2+}]_{er}$ will increase until the action potentials disappear through a SNP bifurcation, whereupon the system moves onto the smaller stable periodic solution. However the placement of the $[Ca^{2+}]_{er}$ nullcline ensures that the solution remains on the small oscillatory branch with $[Ca^{2+}]_{er}$ increasing to 16.8 μM, which is to the left of the supercritical HB on the lower branch. The model therefore exhibits sustained subthreshold oscillations.

The model behaviour changes again if the slow manifold is moved slightly more to the right by further increasing ν_p to 0.05 $\mu M \cdot \mu m \cdot ms^{-1}$ (Figure 3.3 D). This time $[Ca^{2+}]_{er}$ increases until $[Ca^{2+}]_{er} = 19.5$ μM, which is to the left of the SNP bifurcation on the upper branch. The oscillations therefore remain on the upper branch and the model exhibits sustained action potentials. In Figure 3.3 A,C,D the slow manifold lies both above and below the $[Ca^{2+}]_{er}$ nullcline, and hence $[Ca^{2+}]_{er}$ oscillates in phase with the fast subsystem. These oscillations are very small, but are resolvable in Figure 3.1 C.

A bifurcation diagram summarising the change in the model dynamics with ν_p is shown in Figure 3.4. For $\nu_p = 0.04$ $\mu M \cdot \mu m \cdot ms^{-1}$ the oscillations decay to a steady state (—) as previously illustrated in Figure 3.3 B. As ν_p increases a supercritical HB occurs when $\nu_p = 0.0415$ $\mu M \cdot \mu m \cdot ms^{-1}$ and the model exhibits small stable oscillations (—). This corresponds to the situation in Figure 3.3 C where the placement of the $[Ca^{2+}]_{er}$ nullcline ensures that the solution remains on the small oscillatory branch. A torus bifurcation of limit cycles [2] (TB) occurs when $\nu_p =$

[2] A torus bifurcation or Neimark-Sacker bifurcation of limit cycles occurs when a closed invariant curve bifurcates

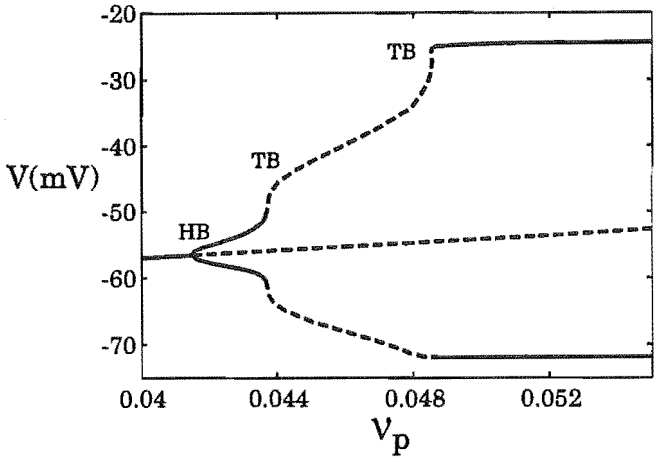

Figure 3.4: A bifurcation analysis of the model with respect to the maximum plasma membrane $[Ca^{2+}]_i$ pump rate, ν_p, summarising the sequence of possibilities in Figure 3.3. For $\nu_p = 0.04$ $\mu M \cdot \mu m \cdot ms^{-1}$ the oscillations decay to a stable steady state (—). As ν_p increases a supercritical HB occurs and the model exhibits small stable oscillations (—). A torus bifurcation (TB) occurs when $\nu_p = 0.0437$ $\mu M \cdot \mu m \cdot ms^{-1}$ and the model exhibits the "fold cycle/fold cycle" bursting behaviour in Figure 3.1 (– – –). This "fold cycle/fold cycle" bursting continues until $\nu_p = 0.0485$ $\mu M \cdot \mu m \cdot ms^{-1}$ where another TB occurs and the model exhibits stable action potentials (—).

0.0437 $\mu M \cdot \mu m \cdot ms^{-1}$, and the model exhibits the "fold cycle/fold cycle" bursting behaviour (– – –) as illustrated in Figure 3.1. This TB corresponds to the moment where left-moving oscillations on the small oscillatory branch in Figure 3.3 A meet the lower SNP bifurcation. This mode of bursting continues until $\nu_p = 0.0485$ $\mu M \cdot \mu m \cdot ms^{-1}$, where another TB occurs and the model exhibits sustained action potentials (—). This corresponds to the situation in Figure 3.3 D where the decrease in $[Ca^{2+}]_{er}$ while the action potential is below the $[Ca^{2+}]_{er}$ nullcline precisely balances the increase in $[Ca^{2+}]_{er}$ while the action potential is above the $[Ca^{2+}]_{er}$ nullcline and sustained action potentials occur.

3.5 "Fold cycle/flip" bursting

The bursting in Figure 3.1 is similar to a mode of cycle–cycle bursting exhibited in the neuron model of Wang (1993), which was termed "mixed-mode bursting". In this Hodgkin–Huxley type model the bursting is generated by injecting a current (I_{app}) and modulated by the slow inactivation kinetics of a K^+ current. The slow inactivation gating variable used in that paper is $\rho h_1 + (1 - \rho)h_2$. To compare the different bursting models, we perform a bifurcation analysis of

from a fixed point of the associated Poincaré map. This closed curve corresponds to a two-dimensional invariant torus.

Wang's neuron model. The model equations and parameters can be found in Wang (1993) .

In Figure 3.5, a bifurcation analysis with respect to the inactivation variable reveals the model bistability. The quiescent state is a small amplitude subthreshold limit cycle attractor and the spiking state a limit cycle attractor. This diagram shares many of the topological features of the bifurcation diagrams in Figure 3.3. Again, the subthreshold limit cycle disappears in a SNP bifur-

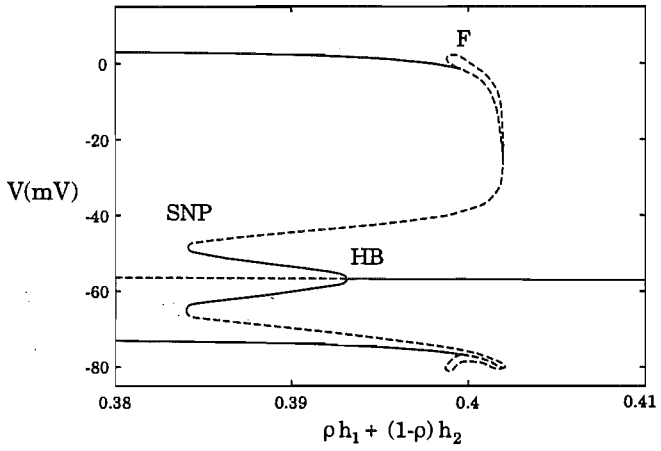

Figure 3.5: Bifurcation analysis of Wang's neuron model with respect to the slow inactivation kinetics of a K^+ current. This slow inactivation gating variable is $\rho h_1 + (1-\rho)h_2$. The bursting is generated by injecting a current ($I_{app} = 3\ \mu A \cdot cm^{-2}$). The model is bistable and exhibits "fold cycle/flip" bursting where the subthreshold limit cycle disappears in a SNP bifurcation and the spiking limit cycle attractor disappears in a subcritical flip (period doubling) bifurcation (F). This burster shares many of the topological features of the "fold cycle/fold cycle" burster in Figure 3.3 A.

cation but now the spiking limit cycle attractor disappears in a subcritical flip (period doubling) bifurcation (F), and thus is a "fold cycle/flip" burster (Izhikevich, 2000). This subcritical flip bifurcation results in three unstable periodic solutions (– – –) for $0.4 \leq \rho h_1 + (1-\rho)h_2 < 0.402$. Although it is difficult to resolve in Figure 3.5, for $0.399 \leq \rho h_1 + (1-\rho)h_2 < 0.4$ the model exhibits four periodic solutions, one of which is stable (—). Unlike the "fold cycle/fold cycle" burster the "fold cycle/flip" burster cannot occur in models where the fast spiking subsystem is two-dimensional. However, the sharp loss in stability of the spiking attractor makes it difficult to distinguish experimentally between the "fold cycle/flip" burster and the "fold cycle/fold cycle" burster.

3.6 Two parameter bifurcation analysis

The "fold cycle/fold cycle" burster is a variant of the "subHopf/fold cycle" (Izhikevich, 2000) burster, also known as the "elliptic" (Rinzel, 1987) or type III (Bertram et al., 1995) burster. This "subHopf/fold cycle" burster for our model is depicted in Figure 3.6, where the quiescent state is a stable equilibrium and the spiking state is a limit cycle attractor. In "subHopf/fold cycle" bursting the rest state disappears in a subcritical Hopf bifurcation and the limit cycle attractor disappears in a fold cycle bifurcation (see Figure 3.7 A). Certain changes in our model parameters generate this "subHopf/fold cycle" burster as we now demonstrate by performing a two-parameter bifurcation analysis of the model with respect to the slow variable $[Ca^{2+}]_{er}$, and the leak conductance g_L.

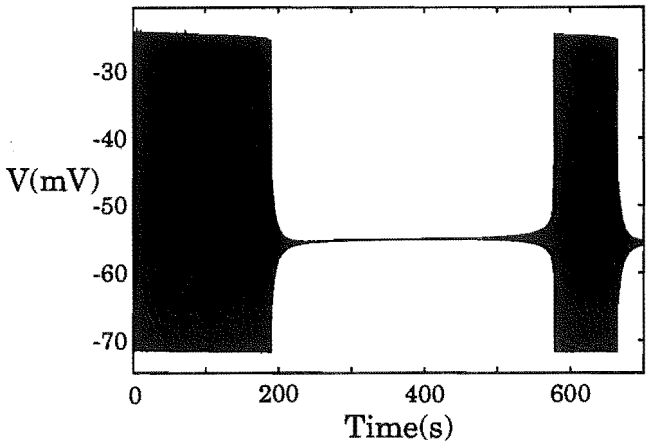

Figure 3.6: "SubHopf/fold cycle" bursting in the model with $g_L = 0.305$ nS, and $\nu_p = 0.0475$ μM $\cdot$ μm $\cdot$ ms^{-1}. The active bursting phase begins in a subcritical HB and terminates in the SNP bifurcation of Figure 3.7 A.

If the leak conductance (g_L) is increased from 0.3 nS to 0.305 nS, then the bifurcation diagram of Figure 3.3 B changes to that shown in Figure 3.7 A. Note that Figure 3.7 is constructed with $\nu_p = 0.04$ μM $\cdot$ μm $\cdot$ ms^{-1}. This parameter change has taken the model through a codimension-2 Bautin bifurcation [3] (BB) (Kuznetsov, 1998), where the supercritical Hopf bifurcation of Figure 3.3 B has coalesced with the SNP bifurcation on the lower branch generating the subcritical HB shown in Figure 3.7 A. By suitable placement of the $[Ca^{2+}]_{er}$ nullcline the model is then capable of exhibiting "subHopf/fold cycle" bursting behaviour by moving between the subcritical HB and the SNP bifurcation. This bursting behaviour is shown in the time domain in Figure 3.6. $[Ca^{2+}]_{er}$ increases and decreases during the active and silent phases respectively in a similar fashion to

[3] A Bautin or generalised Hopf bifurcation occurs when the first Lyapunov exponent changes sign while the complex eigenvalues of the linearization remain simple, converting a supercritical Hopf bifurcation into a subcritical one.

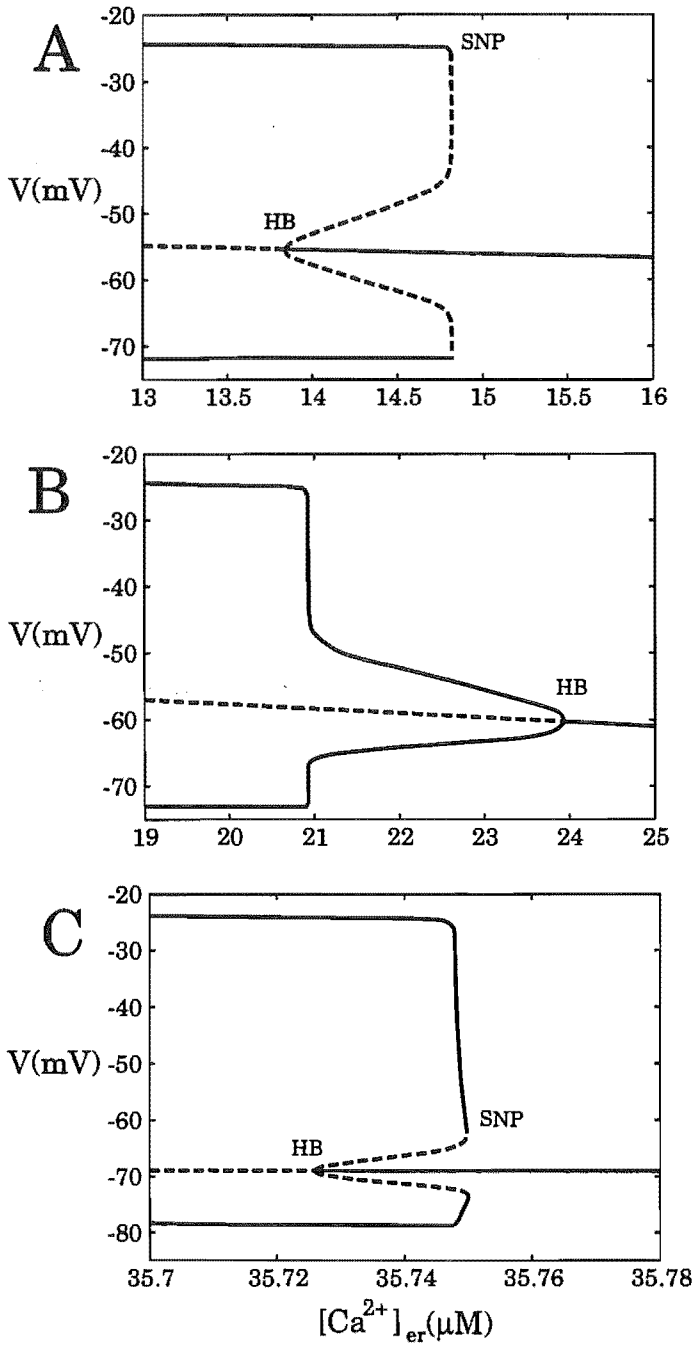

Figure 3.7: Bifurcation analysis of the model with respect to the slow variable $[Ca^{2+}]_{er}$ for different values of the leak conductance g_L. (A) For $g_L = 0.305$ nS a codimension-2 Bautin bifurcation (BB) has occurred where the supercritical HB in Figure 3.3 B has coalesced with the SNP on the lower branch generating a subcritical HB. The model can now exhibit "subHopf/fold cycle" bursting, as shown in Figure 3.6. (B) For $g_L = 0.25$ nS a codimension-2 cusp of periodics bifurcation (CP) has occurred where the two SNP bifurcations in Figure 3.3 B coalesce and disappear. The model is no longer capable of bursting. (C) For $g_L = 0.04$ nS another BB has occurred and the model is again capable of "subHopf/fold cycle" bursting.

that shown in Figure 3.1 B, and the $[Ca^{2+}]_i$ transients mimic the voltage bursting behaviour (not shown).

If g_L is decreased from 0.3 nS to 0.25 nS, then the bifurcation diagram in Figure 3.3 B undergoes a different change and is shown in Figure 3.7 B. This parameter change has taken the model through a codimension-2 cusp of periodics bifurcation [4] (CP), where the two SNP bifurcations of Figure 3.3 B coalesce and disappear. The model does not now exhibit bistability, and hence is incapable of bursting.

If g_L is further decreased to 0.04 nS, then the bifurcation diagram in Figure 3.3 B changes to that in Figure 3.7 C. The model has gone through another codimension-2 Bautin bifurcation, where a subcritical HB and a SNP have emerged from the supercritical HB in Figure 3.7 B. The model is again capable of exhibiting "subHopf/fold cycle"bursting behaviour by moving between the subcritical HB and the SNP bifurcation (not shown but similar to Figure 3.6).

The sequence of bifurcation diagrams in Figure 3.7 is summarised by the two-parameter bifurcation diagram in Figure 3.8. Curves in the diagram display how the subcritical HB (—), supercritical HB (—), and SNP (· · ·) bifurcations move with respect to the bifurcation parameters. The three codimension-2 bifurcations separate the two-parameter bifurcation diagram into four regions. Firstly for $g_L > 0.304$ nS, the model is capable of "subHopf/fold cycle" bursting,

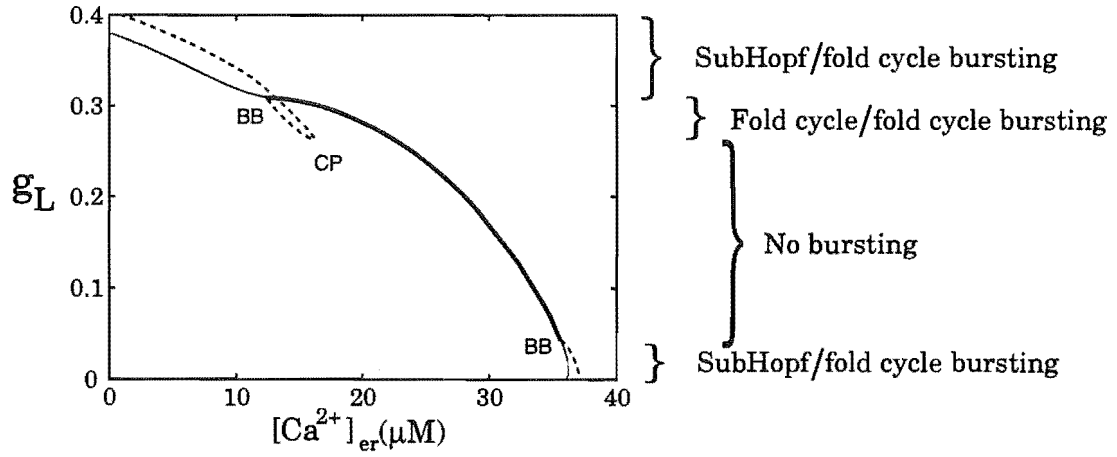

Figure 3.8: Two-parameter bifurcation analysis of the model with respect to the slow variable $[Ca^{2+}]_{er}$, and the leak conductance g_L. Curves in the diagram display how the supercritical HB (— bold), subcritical HB (— thin), and SNP (· · ·) bifurcations move with respect to the bifurcation parameters. For $g_L > 0.304$ nS and $g_L < 0.05$ nS the model is capable of "subHopf/fold cycle" bursting. "Fold cycle/fold cycle" bursting occurs for $0.27 < g_L < 0.304$ nS, and for $0.05 < g_L < 0.27$ nS the model is incapable of bursting.

[4] A cusp of periodics bifurcation occurs when the three equilibria in the associated Poincaré map, two stable and one unstable, merge together at a cusp point.

as shown in Figure 3.6. As g_L is decreased a codimension-2 Bautin bifurcation (BB) occurs and for $0.27 < g_L < 0.304$ nS the model is capable of "fold cycle/fold cycle" bursting, as shown in Figure 3.1. As g_L is further decreased the model undergoes a codimension-2 cusp of periodics bifurcation (CP) when $g_L = 0.27$ nS, and the two SNP bifurcations coalesce and disappear. For $0.05 < g_L < 0.27$ nS the model does not exhibit bistability and hence is incapable of bursting. Another Bautin bifurcation occurs as g_L is further decreased, and for $g_L < 0.05$ nS the model can again generate "subHopf/fold cycle" bursting.

3.7 Summary

Model bursting was investigated in a reduced model of corticotroph electrophysiology. The bursting is indirectly driven by slow modulation of the endoplasmic reticulum Ca^{2+} concentration which gives rise to a slow component in $[Ca^{2+}]_i$ and results in electrical bursting via a Ca^{2+}-activated K^+ current. The bursting frequency is dependent on the endoplasmic reticulum Ca^{2+} storage capacity, the Ca^{2+} transport mechanisms, and the activation of a Ca^{2+}-activated K^+ current. This store operated burst modulation mechanism has also been observed in other Hodgkin–Huxley type models (Chay, 1997; Gall and Susa, 1999). The bursting behaviour can be interpreted as the evolution of a fast oscillatory system through a slow subsystem. Thus, bifurcation theory along with the null-surfaces assist in analysing the bursting mechanism and allow a geometric interpretation of action potential generation.

The model exhibits a novel form of bursting due to bistability between two stable oscillatory solutions. Due to the bifurcations involved, this type of bursting is named "fold cycle/fold cycle" bursting (Izhikevich, 2000), and is topologically equivalent to flow on a two-dimensional torus. The "fold cycle/fold cycle" bursting behaviour can be interpreted as a variant of the "subHopf/fold cycle" burster, and changes in the underlying model topology allow the model to exhibit this mode of bursting. Transitions between these different modes of bursting using bifurcation theory were investigated.

The model bursting is similar to a mode of cycle–cycle bursting exhibited in the neuron model of Wang (1993). However, in this later model the bursting is modulated by the slow inactivation kinetics of a K^+ current. A bifurcation analysis with respect to this inactivation variable reveals that the spiking state disappears in a subcritical flip bifurcation, and thus is a "fold cycle/flip" burster. This mode of bursting shares many of the topological features of the "fold cycle/fold cycle" burster and has also not previously been observed in a Hodgkin–Huxley type model.

This chapter aims to highlight interesting modes of bursting in Hodgkin–Huxley type models and the underlying mechanisms. In particular it illustrates how slight parameter changes can lead to quite complex changes in the model behaviour. Many interesting questions regarding the

physiological significance of the different bursting modes, and their use in distinguishing bursters experimentally remain to be resolved.

3.8 Appendix: Equations and parameter values

The full seven-variable model equations for the excitable corticotroph cell are as follows:

Ionic currents

$$c_{\mathrm{m}}\frac{dV}{dt} = -(I_{\mathrm{Ca-L}} + I_{\mathrm{Ca-T}} + I_{\mathrm{K-DR}} + I_{\mathrm{K-Ca}} + I_{\mathrm{Leak}})$$

$$I_{\mathrm{Ca-L}} = g_{\mathrm{Ca\text{-}L}} m_{\mathrm{L}}^2 J_{\mathrm{Ca}}$$

$$I_{\mathrm{Ca-T}} = g_{\mathrm{Ca\text{-}T}} m_{\mathrm{T}}^2 h_{\mathrm{T}} J_{\mathrm{Ca}}$$

$$I_{\mathrm{K-DR}} = g_{\mathrm{K\text{-}DR}} n J_{\mathrm{K}}$$

$$I_{\mathrm{K-Ca}} = g_{\mathrm{K\text{-}Ca}} \frac{[\mathrm{Ca}^{2+}]_{\mathrm{i}}^4}{[\mathrm{Ca}^{2+}]_{\mathrm{i}}^4 + K_c^4} J_{\mathrm{K}}$$

$$I_{\mathrm{Leak}} = g_{\mathrm{L}}(V - V_{\mathrm{L}})$$

$$J_{\mathrm{j}} = V\frac{[\mathrm{j}]_{\mathrm{i}} - [\mathrm{j}]_{\mathrm{e}}\exp[-z_j FV/(RT)]}{1 - \exp[-z_j FV/(RT)]}, \quad \mathrm{j} \in \{\mathrm{Ca}^{2+}, \mathrm{K}^{+}\},$$

Gating variables

$$\tau_x \frac{dx}{dt} = x_\infty - x, \quad x \in \{m_{\mathrm{L}}, m_{\mathrm{T}}, h_{\mathrm{T}}, n\}$$

$$x_\infty = \frac{1}{1 + \exp\left[(V_x - V)/k_x\right]}, \quad x \in \{m_{\mathrm{L}}, m_{\mathrm{T}}, n\}$$

$$h_{\mathrm{T}\infty} = \frac{1}{1 + \exp\left[(V - V_{\mathrm{h_T}})/k_{\mathrm{h_T}}\right]}$$

$$\tau_x(V) = \frac{\bar{\tau}_x}{\exp\left[(V - V_\tau)/k_\tau\right] + 2\exp\left[2(V_\tau - V)/k_\tau\right]}, x \in \{m_{\mathrm{L}}, m_{\mathrm{T}}\}$$

ER Ca^{2+} equations

$$\frac{d[\mathrm{Ca}^{2+}]_{\mathrm{er}}}{dt} = -\frac{f_{\mathrm{er}}}{V_{\mathrm{er}}}(J_{\mathrm{rel}} - J_{\mathrm{up}})$$

$$J_{\mathrm{rel}} = P([\mathrm{Ca}^{2+}]_{\mathrm{er}} - [\mathrm{Ca}^{2+}]_{\mathrm{i}})$$

$$J_{\mathrm{up}} = \frac{\nu_{\mathrm{er}}[\mathrm{Ca}^{2+}]_{\mathrm{i}}^2}{[\mathrm{Ca}^{2+}]_{\mathrm{i}}^2 + K_{\mathrm{er}}^2}$$

Cytosolic Ca^{2+} equations

$$\frac{d[\mathrm{Ca}^{2+}]_{\mathrm{i}}}{dt} = \frac{f_{\mathrm{cyt}}}{V_{\mathrm{c}}}(J_{\mathrm{rel}} - J_{\mathrm{up}}) + f_{\mathrm{cyt}}\beta(J_{\mathrm{in}} - J_{\mathrm{eff}})$$

$$J_{\mathrm{in}} = -\alpha(I_{\mathrm{Ca-L}} + I_{\mathrm{Ca-T}})$$

$$J_{\mathrm{eff}} = \frac{\nu_{\mathrm{p}}[\mathrm{Ca}^{2+}]_{\mathrm{i}}^2}{[\mathrm{Ca}^{2+}]_{\mathrm{i}}^2 + K_{\mathrm{p}}^2}$$

The parameter values in the model are listed in Table 2.1.

Chapter 4

The inward rectifier in a model of corticotroph electrical activity

4.1 Introduction

Pituitary corticotroph cells generate repetitive action potentials and associated Ca^{2+} transients in response to the agonist corticotropin releasing hormone (CRH). CRH also induces a membrane depolarization (Mollard et al., 1987), which is associated with the generation of action potentials in quiescent corticotrophs, and increases action potential frequency in spontaneously active corticotrophs (Guérineau et al., 1991; Kuryshev et al., 1996). The intracellular mechanisms activated in response to CRH have been only partially characterised. However CRH is known to activate the adenosine 3',5'-cyclic monophosphate (cAMP) dependent protein kinase A (PKA) pathway (Labrie et al., 1982; Aguilera et al., 1983; Reisine et al., 1986; Kuryshev et al., 1995a). The phosphorylation targets for PKA in corticotrophs have not been identified, however PKA is known to phosphorylate L-type voltage dependent Ca^{2+} channels (Mundiña-Weilenmann et al., 1991; Hille, 1992; Sculptoreanu et al., 1993). H-89, an inhibitor of PKA, significantly attenuates CRH-induced action potentials (Kuryshev et al., 1995a), demonstrating a major role for PKA in mediating the changes in electrical excitability and Ca^{2+}-mobilising actions of CRH. There is thus indirect evidence supporting the hypothesis of a CRH-induced PKA-dependent phosphorylation of the L-type Ca^{2+} channels embedded in the plasma membrane (LeBeau et al., 1997), resulting in action potentials, and Ca^{2+} transients.

The model introduced in LeBeau et al. (1997) is central to our discussion; we henceforth denote it by (I). In this model it was found that an increase in the L-type current was sufficient to generate repetitive action potentials from a resting state in the model. The increase in the L-type current could be elicited by either a shift in the voltage dependence of the current to more negative potentials, or by an increase in the conductance. However the model action potential

frequency was much higher than observed experimentally (Guérineau et al., 1991; Kuryshev et al., 1996). In this chapter we address this issue to obtain action potential frequencies more in line with the experimental data.

A CRH-induced inhibition of K^+ currents, that help maintain a negative resting membrane potential, is believed to contribute to the membrane depolarization and an increase in excitability (Mollard et al., 1987; Kuryshev et al., 1995a; Kuryshev et al., 1996; Kuryshev et al., 1997; Lee and Tse, 1997). This depolarization is resistant to H-89 (Kuryshev et al., 1995a), an inhibitor of PKA, demonstrating that the membrane depolarization is mediated by cAMP dependent and independent pathways. In rat corticotrophs a CRH-induced inhibition of an identified Ba^{2+}-sensitive inwardly rectifying K^+ channel is believed to contribute to the membrane depolarization and increase in firing frequency (Kuryshev et al., 1997). In this chapter we investigate a role of the inwardly rectifying K^+ current in the action potential firing frequency and membrane excitability.

Some corticotrophs exhibit complex action potential kinetics where the depolarization spike is followed by small oscillations in the membrane potential (Kuryshev et al., 1996; Kuryshev et al., 1997; Adler et al., 1983). This complex bursting phenomena is also displayed in the model. We investigate this model bursting and the underlying mechanisms.

CRH-induced exocytosis of ACTH allows an increase in the cell surface area by up to 50% (King and Baertschi, 1990; Westlund et al., 1985). Thus it is important to understand how changes in cellular volume affect plasma membrane excitability, action potentials and the associated $[Ca^{2+}]_i$ dynamics. In this chapter we investigate this volume sensitivity in the model.

4.2 The model

4.2.1 The inward rectifier current

It has been identified recently that a significant ionic current not explicitly included in the original model of CRH-induced corticotroph action potentials is a highly selective inwardly rectifying K^+ current (I_{K-IR}) (Kuryshev et al., 1997). This current contributes to the maintenance of the membrane resting potential. The application of CRH is believed to inhibit this inwardly rectifying current contributing to the CRH-induced depolarization and altering the frequency of the action potentials. This inhibition is believed to occur after some delay. The current through this channel is appropriately described by

$$I_{K-IR}(V) = \begin{cases} g_{K-IR}(V - V_{K-IR}), & \text{if } V \leq V_{K-IR} \\ I_{max}(1 - \exp((V_{K-IR} - V)/k_s)), & \text{if } V > V_{K-IR} \end{cases} \tag{4.2.1}$$

where g_{K-IR} is the channel conductance for $V < V_{K-IR}$, I_{max} is the maximal channel current, and k_s determines the rate of inward rectification. As this channel exhibits quick activation kinetics

and minimal inactivation (Kuryshev et al., 1997), an extra differential equation for an activation or inactivation gating variable is not required. The I–V curve for I_{K-IR} is shown in Figure 4.1 (—). This representation is constructed from data in Kuryshev et al. (1997), Lee and Tse (1997),

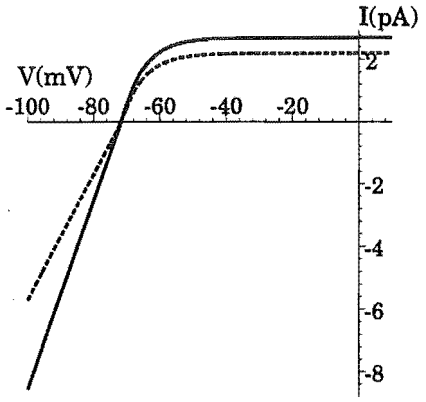

Figure 4.1: Model current-voltage curve for the inwardly rectifying K^+ current (I_{K-IR}) (—). CRH is believed to inhibit I_{K-IR} by about 25% (– – –).

and Hille (1992). It should be noted some of the experimental data was obtained for $[K^+]_o$ up to 50 mM, and hence were adjusted to the model value of $[K^+]_o = 5.6$ mM. The voltage dependence of the channel gating depends on $[K^+]_o$, shifting with the quantity $RT \log [K^+]_o$. CRH is believed to inhibit I_{K-IR} by about 25% (Kuryshev et al., 1997). Hence to mimic the CRH induced inhibition we accordingly decrease I_{max} from 2.7 pA to 2.2 pA and g_{K-IR} from 0.3 nS to 0.2 nS respectively (Figure 4.1 (– – –)). This inhibition is believed to occur 45 s after the application of CRH, a time chosen to correspond with experimental observations (Kuryshev et al., 1997; Ritchie et al., 1996; Lee and Tse, 1997).

In the original model (I), the electrical effects of all ionic currents not explicitly included were lumped together into the leak current I_{Leak}. In place of this leak current we now insert our description of the inward rectifier (equation (4.2.1)). It follows that the plasma membrane potential difference is now given by the differential equation

$$c_m \frac{dV}{dt} = -(I_{Ca-L} + I_{Ca-T} + I_{K-DR} + I_{K-Ca} + I_{K-IR}). \tag{4.2.2}$$

By comparing equations (2.2.1) and (4.2.2) it can be seen that the simple ohmic I_{Leak} current has been replaced by I_{K-IR}. The model descriptions of the I_{Ca-L}, I_{Ca-T}, I_{K-DR}, and I_{K-Ca} ionic currents are presented in Section 2.2.

4.2.2 The model equations

The cell is modeled as a spherical body, bounded by a plasma membrane containing Ca^{2+}-ATPase pumps and various ionic currents as outlined above. A schematic diagram of the various ionic

transport processes is shown in Figure 4.2. Ca^{2+} influx through voltage-sensitive Ca^{2+} channels

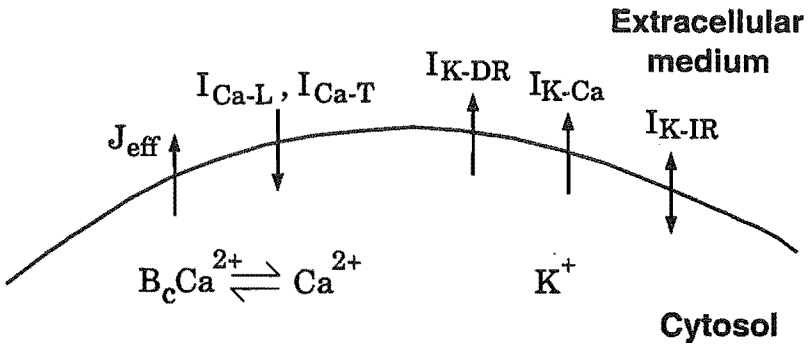

Figure 4.2: Schematic diagram of the ionic pathways included in the model. Bold arrows indicate the various channels and pumps. Within the cytosol significant portions of Ca^{2+} are bound to buffers B_c. Five ionic currents are included in the model: an L-type voltage-sensitive Ca^{2+} current I_{Ca-L}, a fast inactivating T-type voltage-sensitive Ca^{2+} current I_{Ca-T}, a voltage-sensitive K^+ current I_{K-DR}, a non-voltage sensitive Ca^{2+}-activated K^+ current I_{K-Ca}, and an inwardly rectifying K^+ current I_{K-IR}. Also indicated is the plasma membrane Ca^{2+}-ATPase pumps, J_{eff}.

(J_{in}), and efflux via the plasma membrane Ca^{2+}-ATPase pump (J_{eff}) are given by

$$J_{in} = -\alpha(I_{Ca-L} + I_{Ca-T}), \tag{4.2.3}$$

$$J_{eff} = \frac{\nu_p [Ca^{2+}]_i^2}{[Ca^{2+}]_i^2 + K_p^2}, \tag{4.2.4}$$

respectively, where α converts a Ca^{2+} ionic current into a Ca^{2+} flux density, ν_p is the maximum pump rate, and K_p is the $[Ca^{2+}]_i$ for which the pump is half-maximally activated (see Table 4.1). Thus neglecting Ca^{2+} transport between the cytosol and the ER, the differential equation for $[Ca^{2+}]_i$ is then given by

$$\frac{d[Ca^{2+}]_i}{dt} = f_{cyt}\beta(J_{in} - J_{eff}), \tag{4.2.5}$$

where β is the ratio of cell surface area to cytosolic volume, relating ionic fluxes in the plasma membrane to the rate of intracellular concentration accumulation.

Intracellular Ca^{2+} is bound to Ca^{2+} buffers (signified by B_cCa^{2+} in Figure 4.2), each with as yet undetermined binding kinetics, hence our model of Ca^{2+} buffering is simple. In the cytosol, approximately 99% of Ca^{2+} is bound to buffers (Neher and Augustine, 1992; Tse et al., 1994). Cytosolic Ca^{2+} is also transported into the endoplasmic reticulum (ER), an intracellular organelle that sequesters cytosolic Ca^{2+}. The buffering of Ca^{2+} in the ER is believed to be greater than that in the cytosol, with the ER filling approximately 15% of the cell volume (Alberts et al., 1983,

Parameter	Definition	Value	Source
f_{cyt}	Cytosolic Ca^{2+} buffering factor	0.005	This chapter
β	Ratio of cell surface area to cytosolic volume	0.4 μm^{-1}	A_{cell}/V_{cell}
ν_p	Maximum plasma membrane Ca^{2+}-ATPase flux	0.025 $\mu M \cdot \mu m \cdot ms^{-1}$	This chapter
V_{K-IR}	Inward rectifier reversal potential	−71.5 mV	This chapter
I_{max}	Maximum I_{K-IR} current	2.7 pA	This chapter
g_{K-IR}	Inward rectifier conductance	0.3 nS	This chapter
K_c	I_{K-Ca} half maximal $[Ca^{2+}]_i$	0.5 μM	This chapter
k_s	I_{K-IR} rate of inward rectification	6.5 mV	This chapter

Table 4.1: Table of relevant model parameters.

p320). To account for the combined buffering properties of the cytosol and the ER, the fraction of unbuffered intracellular Ca^{2+} is $f_{cyt} = 0.005$. (See Table 4.1)

In Chapter 2 a model incorporating the ER along with more complicated Ca^{2+} dynamics was investigated. It was concluded from this investigation that the I_{K-Ca} efflux current used in the original model (I) was too sensitive to $[Ca^{2+}]_i$, and hence we decrease the channel sensitivity by increasing the half-maximal $[Ca^{2+}]_i$ (K_c) from 0.4 μM to 0.5 μM.

4.2.3 Numerical methods

The system of six ordinary differential equations (equations (4.2.2) and (4.2.5) along with the four gating variable equations (1.1.9)) were solved using a stiff system solver in the numerical package XPPAUT(3.0)[1].

4.3 Results

4.3.1 Model behaviour

CRH has been shown to activate the cAMP secondary messenger system (Aguilera et al., 1983). Experimentally, application of cAMP has been shown to increase the whole-cell Ca^{2+} current in corticotroph tumor cells (Luini et al., 1985). Such an increase in the current can be generated either by an increase in the macroscopic conductance or by a shift in the voltage-sensitivity of the L-type Ca^{2+} current to more hyperpolarised potentials, the latter effect having experimental support from other cell-types (Nargeot et al., 1983; Mundiña-Weilenmann et al., 1991; Sculptoreanu et al., 1993). In the model, both effects lead to the generation of repetitive action potentials. At present, it would seem that neither the currently available experimental data, nor the model, can resolve which of these mechanisms genuinely underlies action potential generation in response to CRH. Previously it was arbitrarily chosen to shift in the voltage-dependence of the L-type Ca^{2+}

[1]Written by Bard Ermentrout, and available at ftp.math.pitt.edu/pub/bardware.

current but an increase in the macroscopic conductance always produced very similar results (I). We continue with the same choice in the following analysis. The model parameter that controls the voltage-sensitivity of the L-type current is V_{m_L} (as described in Section 2.2). Analysis of experimental data suggested a control V_{m_L} value of -12 mV under rest conditions, and a negative shift of 6–8 mV is typically used to generate action potentials (I).

One well documented experimental observation in corticotrophs is a small CRH-induced depolarization, which apparently occurs independently of the firing of action potentials (Mollard et al., 1987; Kuryshev et al., 1995a; Kuryshev et al., 1996). These reports indicate that the depolarization is due to a reduction in a K^+ current. A component of this current is a recently identified inward rectifier (Kuryshev et al., 1997) that is active at rest and inhibited by CRH. This inhibition, which is believed to occur after about a 45 s delay, contributes to the membrane depolarization and increases the firing frequency (Kuryshev et al., 1997). Although no clear role for this effect has been determined, it could result in an increase in membrane excitability. In this paper we investigate the role of this inward rectifier channel in the model dynamics.

4.3.2 Action potential frequency

The model firing frequency in (I) was approximately 1–2 Hz, an order of magnitude larger than typical experimental data (See Figure 4.3). We now investigate this to bring the model firing frequency in line with experimental data.

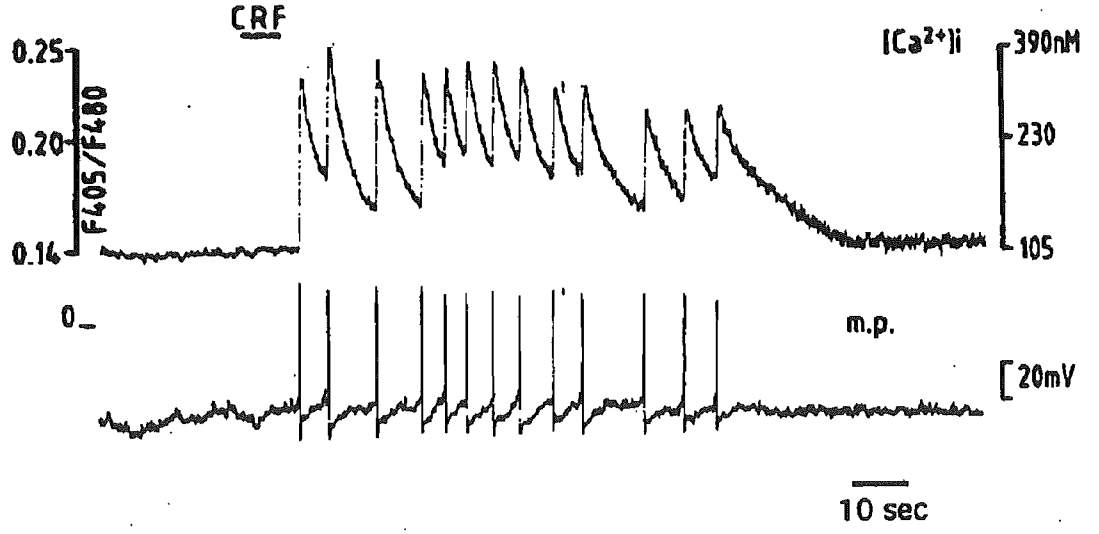

Figure 4.3: Corticotroph experimental data showing a train of action potentials and associated $[Ca^{2+}]_i$ transients in response to a 10 s application of 100 nM CRH (= CRF), as indicated by the horizontal underline. The firing frequency is 0.1–0.2 Hz. Data from Guérineau et al. (1991).

The frequency of oscillations in the model is highly dependent on the rate of clearance of Ca^{2+} from the cytosol (due to the gradual removal of the hyperpolarizing influence of the Ca^{2+}-activated K^+ current). The model $[Ca^{2+}]_i$ decrease in (I) is much faster than that observed experimentally (Guérineau et al., 1991). To reduce the rate that $[Ca^{2+}]_i$ decreases, we can either reduce the rate at which Ca^{2+} is pumped out of the cytosol, or increase the Ca^{2+} storage capacity of the cytosol by altering the buffering coefficient. The buffering is well established and less amenable to change, hence because the rate of Ca^{2+} removal from the cytosol is less well characterised we decrease the maximum Ca^{2+}-ATPase pump rate ν_p from 0.04 $\mu M \cdot \mu m \cdot ms^{-1}$ to 0.025 $\mu M \cdot \mu m \cdot ms^{-1}$. With these new components introduced into the model we now compare its behaviour with the original model (I), and some experimental data.

In Figure 4.4 are the model action potentials and $[Ca^{2+}]_i$ transients associated with the application of CRH. These action potentials are initiated after 10 s by left-shifting the voltage sensitivity of the L-type Ca^{2+} current, V_{m_L}, from -12 mV to -20 mV. The firing frequency is now much slower than in (I) and more consistent with the experimental data in Figure 4.3. After a 45 s delay, the inhibition of the I_{K-IR} current is mimicked by decreasing I_{max} from 2.7 pA to 2.2 pA and g_{K-IR} from 0.3 nS to 0.2 nS. The action potential firing frequency now increases by about

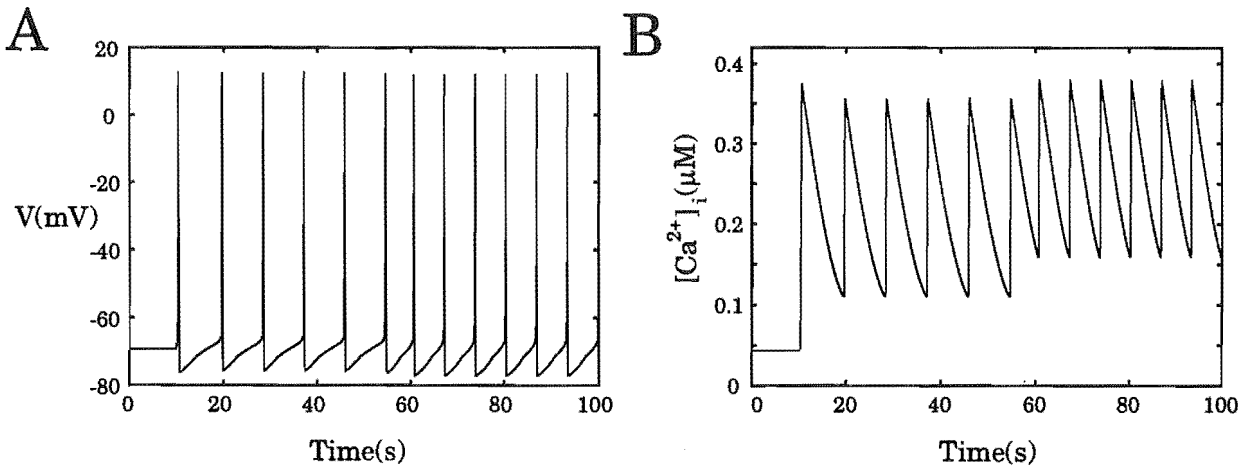

Figure 4.4: Model action potentials and calcium transients associated with the application of CRH. (A) The action potentials are initiated after 10 s by firstly left-shifting the voltage sensitivity of the L-type Ca^{2+} current. Secondly, after a 45 s delay, inhibition of the inwardly rectifying K^+ current (I_{K-IR}) causes the action potential firing frequency to increase by about 50%. This is consistent with the experimental data in Figure 4.5. (B) Each action potential is associated with a single $[Ca^{2+}]_i$ transient. Associated with the increase in firing frequency is an increase in average $[Ca^{2+}]_i$.

50%. This result is similar to the experimental data in Figure 4.5, which undergoes a doubling in

firing frequency about 45 s after the application of CRH. Thus the inhibition of the I_{K-IR} current appears to be a significant component of the CRH-induced increase in firing frequency. Associated with this increase in firing frequency is an increase in average $[Ca^{2+}]_i$, and thus presumably an enhanced secretory response.

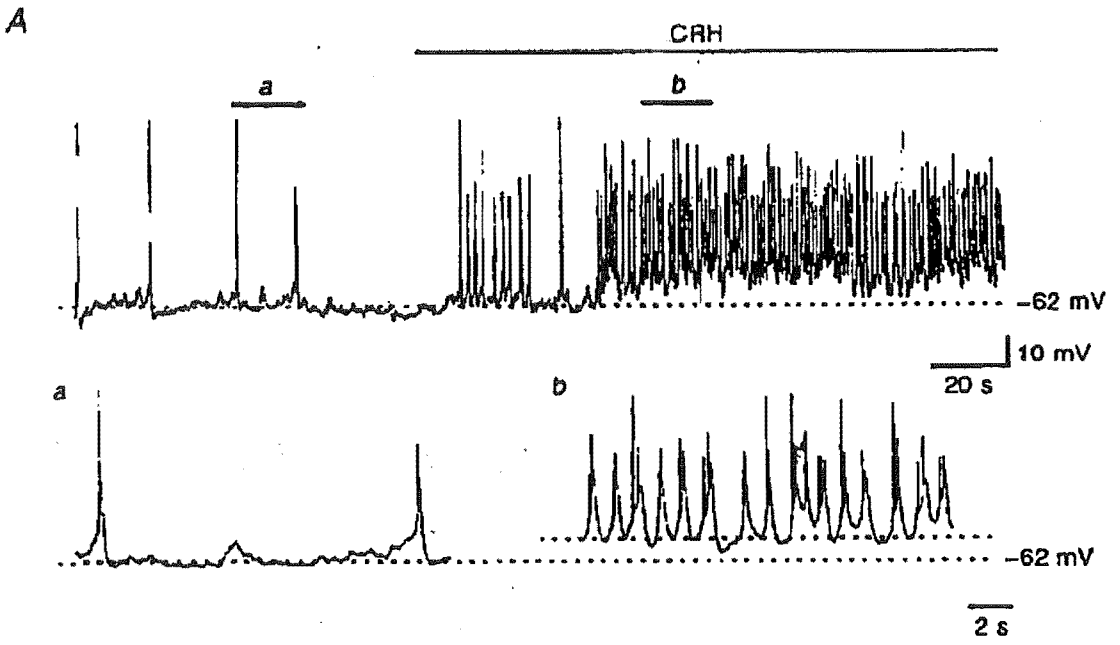

Figure 4.5: Experimental data showing action potentials and $[Ca^{2+}]_i$ transients in response to a 150 s application of 20 nM CRH, as indicated by the horizontal bar. There is a 10 mV depolarization and a doubling in the firing frequency 45 s after the application of CRH. Bursting type behaviour is shown in the expanded trace b. Data from Kuryshev et al. (1997).

As in the original model (I) the action potentials display typical experimentally observed features such as a rapid upstroke, a rapid downstroke which overshoots the resting potential, and a slow ramping hyperpolarization leading to the firing of the next action potential. The model $[Ca^{2+}]_i$ profiles in Figure 4.4 display kinetic features similar to the experimental data of Guérineau et al. (1991) (Figure 4.3), such as a rapid rising phase, and a slower falling phase where $[Ca^{2+}]_i$ falls most of the way back to its basal value before the next action potential.

The change in firing frequency with respect to the voltage sensitivity of the L-type Ca^{2+} current (V_{m_L}) is shown in Figure 4.6. This relationship is shown before (—) and after (- - -) the inhibition of I_{K-IR}. Both curves exhibit threshold behaviour, where a suitable left-shift in V_{m_L} from the rest value of -12 mV is required to generate oscillations. The threshold value of V_{m_L} is -18.9 mV when $g_{K-IR} = 0.3$ and $I_{max} = 2.7$ (—), and is -12.4 mV when $g_{K-IR} = 0.2$ and $I_{max} = 2.2$ (- - -). This change in the threshold value of V_{m_L} implies that a smaller left-shift in the voltage sensitivity of the L-type Ca^{2+} current is required to generate action potentials and thus

the inhibition of I_{K-IR} increases membrane excitability. The other significant feature of Figure 4.6 is the increase in firing frequency due to the inhibition of I_{K-IR}. This increase in firing frequency is shown in Figure 4.4 for $V_{m_L} = -20$ mV. In Figure 4.6 there is also a sudden drop in firing frequency at $V_{m_L} = -16.5$ mV. This transition occurs when an extra spike immediately follows the initial depolarization spike (this is discussed in Section 4.3.3). This extra spike enhances the rise in $[Ca^{2+}]_i$ and results in a decrease in the firing frequency.

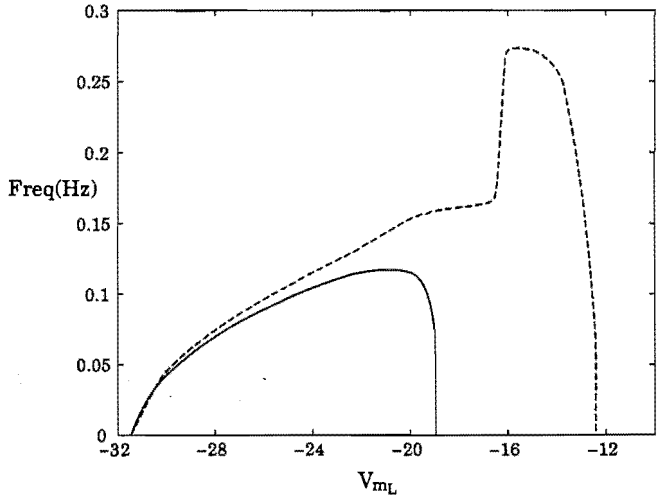

Figure 4.6: The change in firing frequency with respect to the voltage sensitivity of the L-type Ca^{2+} current (V_{m_L}). This relationship is shown before (—) and after (- - -) the inhibition of I_{K-IR}. Both curves exhibit a threshold behaviour, where a suitable left-shift in V_{m_L} from the rest value of -12 mV is required to generate oscillations. The inhibition of I_{K-IR} increases membrane excitability and firing frequency.

The model indicates that inhibition of I_{K-IR} alone is not quite sufficient to generate action potentials. This situation is modeled by setting $V_{m_L} = -12$ mV, $I_{max} = 2.2$ mV and $g_{K-IR} = 0.2$ nS. In this case the inhibition of I_{K-IR} causes a membrane depolarization of 2 mV. This scenario may possibly explain some of the experimental data (Lee and Tse, 1997) where application of CRH causes a membrane depolarization of about 10 mV, but not action potentials. Thus the inhibition of I_{K-IR} is not obligatory for action potential generation.

4.3.3 Bursting

An interesting feature of the model is that of bursting. This behaviour is consistent with experimental observations (Kuryshev et al., 1996; Kuryshev et al., 1997; Adler et al., 1983). A model action potential in Figure 4.4 is shown over a much shorter time scale in Figure 4.7. The initial depolarization spike is followed by two smaller oscillations in the membrane potential in accordance with the experimental trace in Figure 4.5. From the quiescent state, both V and

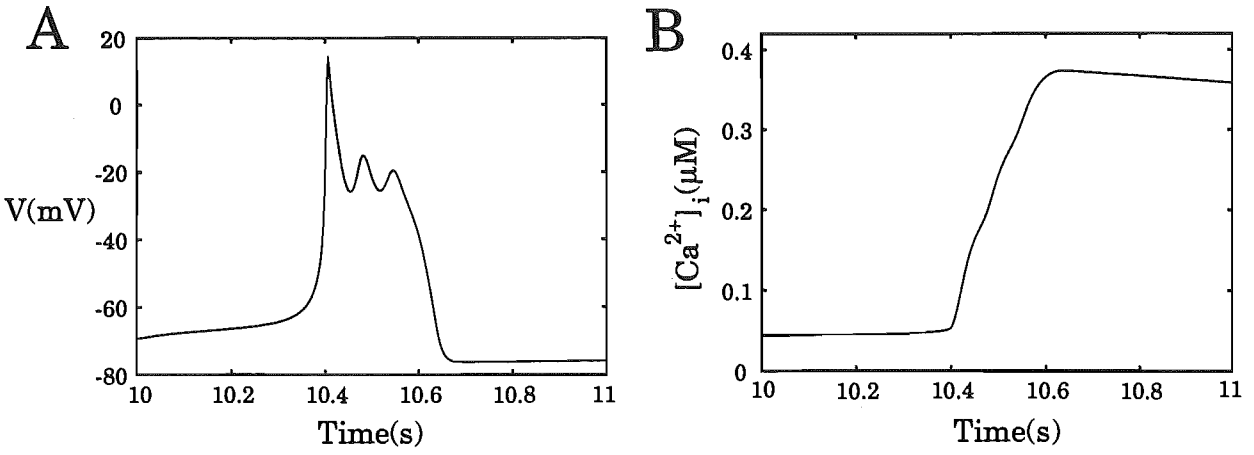

Figure 4.7: (A) CRH induced model action potentials shown over a much shorter time scale with $V_{m_L} = -20$ mV, $I_{max} = 2.7$ mV and $g_{K-IR} = 0.3$ nS. The initial depolarization spike is followed by two smaller oscillations in the membrane potential in accordance with the experimental trace in Figure 4.5. (B) The bursting ends when $[Ca^{2+}]_i$ is sufficiently high to activate the Ca^{2+}-activated K^+ current allowing a repolarization of the membrane potential.

$[Ca^{2+}]_i$ start to increase. V soon peaks just above 10 mV, and then begins to repolarize as $[Ca^{2+}]_i$ increases further. Note that $[Ca^{2+}]_i$ increases considerably during the repolarization phase, because although the L-type Ca^{2+} current is being shut off as V falls, the driving force for Ca^{2+} is increasing. These post-spike oscillations occur while $[Ca^{2+}]_i$ is still increasing, and terminate when $[Ca^{2+}]_i$ is sufficiently high to activate the I_{K-Ca} current allowing a repolarization of the membrane potential. In the model the I_{K-DR} and I_{K-IR} currents together cannot repolarize the membrane potential. The added influence of the I_{K-Ca} current is necessary. However because the rise in $[Ca^{2+}]_i$ is slower than the depolarization in the membrane potential there is a delay in the activation of the I_{K-Ca} current allowing the observed bursting behaviour. When V reaches its minimum value of -76 mV, the rise in $[Ca^{2+}]_i$ is complete, and V slowly ramps up as $[Ca^{2+}]_i$ falls. This represents the interspike interval. When V reaches about -65 mV the next bursting spike in the train of action potentials is initiated. Traditional action potentials with a much faster rehyperpolarization can be obtained from the model by suitably increasing or decreasing the K^+ or Ca^{2+} currents respectively (not shown).

Bursting behaviour in a model of corticotroph electrical activity has previously been analysed from a more mathematical viewpoint (LeBeau et al., 1998). However significant parameter changes were made in that work to generate the different aspects of the bursting phenomena. The current model of the bursting is more physiological with the firing frequency, parameter values, and $[Ca^{2+}]_i$ transient levels more consistent with the experimental data.

The model bursting pattern depends on the delicate balance between inward and outward

currents. It is therefore difficult to isolate the current responsible for the bursting pattern. However model simulations suggest that the duration of the bursting is due to the gradual increase in $[Ca^{2+}]_i$ and the related I_{K-Ca} current. That is $[Ca^{2+}]_i$ changes slowly relative to the other model variables and thus can be treated as a slow variable (LeBeau et al., 1998). Hence we can apply a fast-slow subsystem analysis (Rinzel, 1985; Rinzel, 1987) to the model, treating $[Ca^{2+}]_i$ as a fixed parameter. This approach yields valuable insight into the bursting kinetics and membrane excitability. A bifurcation analysis with respect to $[Ca^{2+}]_i$ is shown in Figure 4.8 for different values of V_{m_L}. Also superimposed in Figure 4.8 are the six variable model limit cycles (— bold).

When $V_{m_L} = -29$ mV the model exhibits the behaviour in Figure 4.8 A. Because the $[Ca^{2+}]_i$ nullcline $(\cdots)$ intersects the Z-shaped steady state curve on the unstable branch, there does not exist a stable steady state solution to the six variable model. Consider a point on the lower stable branch of the Z-shaped curve. Because this point is beneath the $[Ca^{2+}]_i$ nullcline, $[Ca^{2+}]_i$ decreases and the solution moves leftward until the steady state becomes unstable via a saddle-node bifurcation (SN). The trajectory (— bold) is then attracted onto the stable branch above the $[Ca^{2+}]_i$ nullcline and $[Ca^{2+}]_i$ begins to increase. The solution moves rightward until the steady state becomes unstable via a SN and is then attracted onto the lower branch. The process then repeats in a oscillatory manner. This oscillatory behaviour is called a fold/fold hysteresis loop (Izhikevich, 2000).

If V_{m_L} is decreased from -29 mV to -20 mV then the bifurcation diagram in Figure 4.8 A changes to that shown in Figure 4.8 B. This parameter change has taken the model through a codimension-2 Bogdanov-Takens bifurcation (BT) (Kuznetsov, 1998), where a subcritical Hopf bifurcation (HB) and a homoclinic bifurcation (HC) have emerged from the saddle-node bifurcation (SN) on the upper branch. The initial action potential spike is now followed by a small amplitude oscillation in the membrane potential. Because the steady state on the upper branch becomes unstable via a subcritical Hopf bifurcation, this oscillatory behaviour is called a fold/subHopf hysteresis loop (Izhikevich, 2000).

If V_{m_L} is further decreased to -17.8 mV then the model behaviour changes to that shown in Figure 4.8 C. The model has gone through a codimension-2 neutral-saddle-loop bifurcation (NSL) (de Vries, 1998), where a stable periodic branch has emerged from the homoclinic bifurcation via a saddle-node of periodics bifurcation (SNP). The oscillations following the initial spike are now much larger in amplitude than those in Figure 4.8 B. Due to the bifurcations involved this is called a subHopf/homoclinic burster (Izhikevich, 2000). If V_{m_L} is further decreased to -14 mV then the model behaviour changes to that shown in Figure 4.8 D. This time the model has gone through a codimension-2 cusp of periodics bifurcation (CP), where two SNP bifurcations collide and disappear (Kuznetsov, 1998), (p 448), and a cusp of Hopf bifurcations (CHB), where two

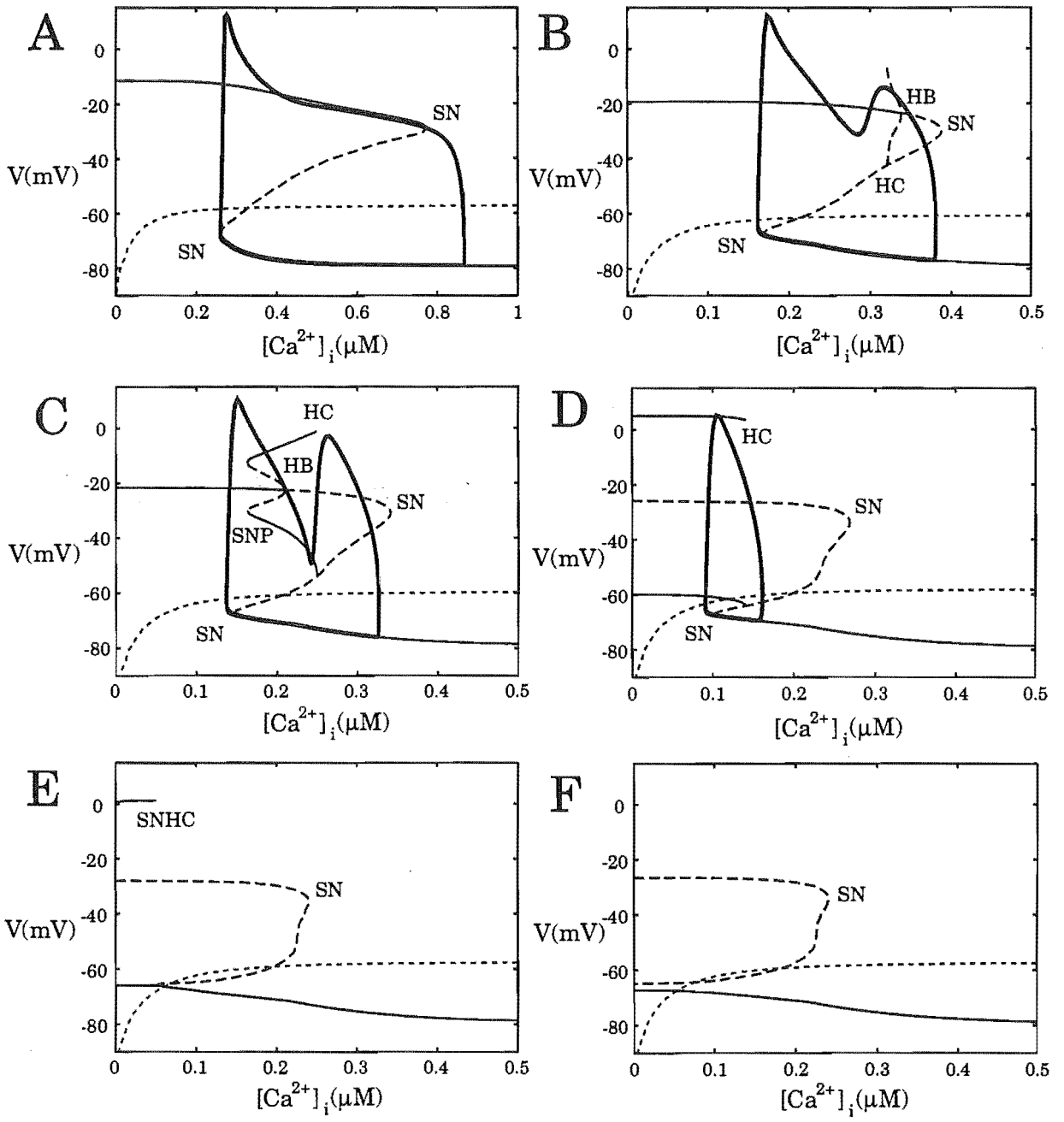

Figure 4.8: Bifurcation analysis with respect to the slow variable $[Ca^{2+}]_i$ for V_{m_L} values of -29 mV (A), -20 mV (B), -17.8 mV (C), -14 mV (D), -12.3 mV (E), and -12 mV (F). Stable and unstable solutions are denoted by (—) and (– – –) respectively. The $[Ca^{2+}]_i$ nullclines are indicated by $(\cdots)$, and limit cycles in the six variable model are denoted by bold lines.

HB bifurcations collide and disappear (Kuznetsov, 1998). Because the homoclinic bifurcation is approaching the saddle-node bifurcation the initial action potential spike is no longer followed by the smaller oscillations in the membrane potential. This transition to a one-spike action potential results in the increase in action potential frequency apparent in Figure 4.6 (– – –). Due to the bifurcations involved this is called a fold/homoclinic burster (Izhikevich, 2000).

If V_{m_L} is further decreased to -12.3 mV then the model behaviour changes to that shown in Figure 4.8 E. The model has gone through a codimension-2 stable saddle-node-loop bifurcation (SSNL) (Schecter, 1987) where the saddle-node and homoclinic bifurcations in Figure 4.8 D have aligned to form a codimension-1 saddle-node-homoclinic bifurcation (SNHC) (Kuznetsov, 1998), (p 250). The $[Ca^{2+}]_i$ nullcline now intersects the stable lower branch and thus oscillations no longer exist in the six variable model. If V_{m_L} is further decreased to -12 mV then the model behaviour changes to that in Figure 4.8 F. This time the model has gone through a codimension-2 cusp of saddle-node-homoclinic bifurcations (CSNHC), where two SNHC bifurcations collide and disappear (Kuznetsov, 1998), thus eliminating the stable periodic solutions and resulting in an isola of unstable steady state solutions. The model does not now exhibit any oscillatory solutions. The sequence of bifurcation diagrams in Figure 4.8 is similar for $I_{max} = 2.7$ mV and $g_{K-IR} = 0.3$ nS although it occurs over a different range in V_{m_L}.

The sequence of model behaviour in the bifurcation diagrams in Figure 4.8 can be summarised by the bifurcation diagram in Figure 4.9. For $V_{m_L} \leq -12.4$ the model exhibits stable periodic solutions, and for $V_{m_L} > -12.4$ there only exists a steady state solution. This bifurcation diagram

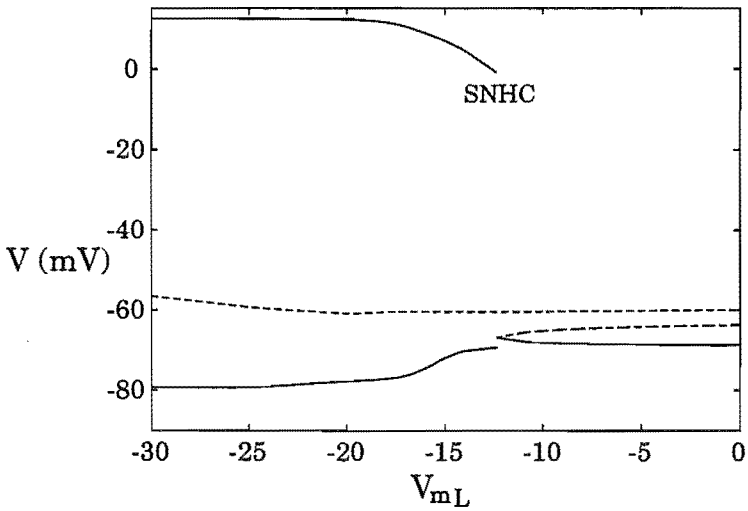

Figure 4.9: Bifurcation diagram of the model behaviour with respect to V_{m_L} for $g_{K-IR} = 0.2$ and $I_{max} = 2.2$. A SNHC bifurcation mediates the sudden change in the model behaviour.

is slightly different than the corresponding bifurcation diagram in Figure 2.6 for the model discussed in Chapter 2. However, the sudden change in the steady state via the SNHC bifurcation

indicates that as observed experimentally, the repetitive model action potentials are generated in an all-or-none manner.

The model resting state is slightly different from that in the original model (I); at equilibrium the $[Ca^{2+}]_i$ is 0.04 μM (compared with 0.1 μM in (I)) and the plasma membrane potential difference V is -69 mV (compared with -55 mV in (I)). These resting model values are slightly lower than what is generally found in corticotrophs. However the model only includes the major ionic currents behind action potential generation, with no formal descriptions of the many other smaller uncharacterised ionic currents (some of which are described in Section 2.2). These smaller currents, although less significant in action potential generation will play a more crucial role in setting the resting membrane potential.

The CRH-induced inhibition of the inward rectifier K^+ current results in enhanced entry of Ca^{2+} and thus, presumably, an enhanced secretory response. Therefore these results suggest that an integrated response to CRH (i.e., activation of the L-type Ca^{2+} current and the inhibition of the inward rectifier) is important in the CRH induced plasma membrane electrophysiology.

4.4 Cellular volume dependent membrane kinetics

Corticotroph cells are regarded to be 10–20 μm in diameter (d_{cell}) from immunocytochemical micrograph experiments (Mollard et al., 1987; Westlund et al., 1985) and cell membrane capacitance measurements (Tse and Tse, 1998; Tse and Lee, 1998). CRH-induced exocytosis of ACTH [2] allows the cell surface area to increase by up to 50% (King and Baertschi, 1990; Westlund et al., 1985). It is therefore important to understand how changes in cellular volume affect plasma membrane excitability, action potentials and the associated $[Ca^{2+}]_i$ dynamics. In this section we investigate this volume sensitivity in the model.

The model variables that are dependent on d_{cell} are A_{cell}, V_{cell}, c_m, α, β, and ν_p (see Table 2.1). The functional dependence on d_{cell} is indicated in the source column of Table 2.1, and because ν_p is a flux density, the dependence of ν_p on d_{cell} is obtained by multiplying ν_p by $15^2/{d_{cell}}^2$. Equations (4.2.2) and (4.2.5) indicate that the rate of change in V and $[Ca^{2+}]_i$ is proportional to $1/{d_{cell}}^2$ and $1/{d_{cell}}^3$ respectively, and thus a change in d_{cell} has a more significant effect on the $[Ca^{2+}]_i$ dynamics. We now consider the model dynamics when d_{cell} is increased from 15 μm to 18.4 μm, which corresponds to a 50% increase in cell area.

A model action potential with d_{cell} = 18.4 μm, I_{max} = 2.7 mV, g_{K-IR} = 0.3 nS, and V_{m_L} = -20 mV is shown in Figure 4.10 A. This increase in the cell diameter results in a doubling in the burst duration (compare with Figure 4.7 A). The nature of this change in burst duration is apparent in Figure 4.10 B (compare with Figure 4.8 B). Increasing d_{cell} makes $[Ca^{2+}]_i$ a slower

[2] individual secretory vesicles are 0.2 μm in diameter (Childs, 1993).

variable, thus the trajectory remains on the upper branch for much longer, allowing further small oscillations in the membrane potential. The Z-shaped steady state curve is independent of d_{cell}, thus the $[Ca^{2+}]_i$ transients operate over a similar range in $[Ca^{2+}]_i$ when d_{cell} changes.

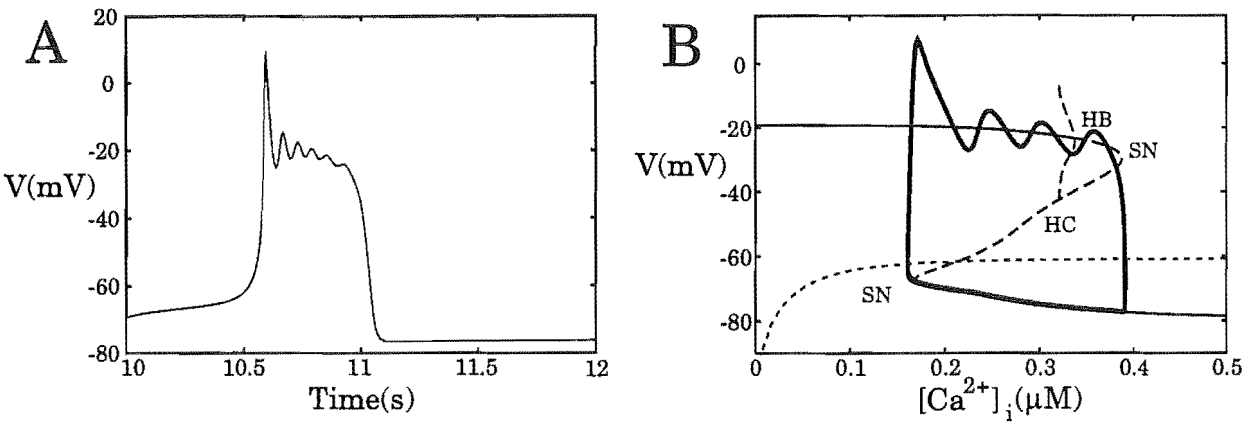

Figure 4.10: (A) The model action potential burst duration increases from 250 ms (Figure 4.7 A) to 500 ms when d_{cell} is increased from 15 μm to 18.4 μm ($V_{m_L} = -20$ mV, $I_{max} = 2.7$ mV and $g_{K-IR} = 0.3$ nS). (B) Increasing d_{cell} from 15 μm to 18.4 μm makes $[Ca^{2+}]_i$ a slower variable, and thus the trajectory remains on the upper branch for a longer period of time than in Figure 4.8 B ($V_{m_L} = -20$ mV, $I_{max} = 2.2$ mV and $g_{K-IR} = 0.2$ nS). $[Ca^{2+}]_i$ transients operate over a similar range in $[Ca^{2+}]_i$.

Because increasing d_{cell} makes $[Ca^{2+}]_i$ a slower variable there is also a corresponding decrease in the spike frequency. When d_{cell} increases from 15 μm to 18.4 μm, the spiking frequency bifurcation diagram in Figure 4.6 changes to that shown in Figure 4.11 (note the change in scale). There is an approximate halving in the spiking frequency. Because c_m is the only variable in equation (4.2.2) that is sensitive to d_{cell}, there is no effect on the cell excitability or steady state with changes in d_{cell}.

Alternatively decreasing d_{cell} results in an increase in firing frequency and a decrease in burst duration. This dependence on d_{cell} is shown in Figure 4.12 for $V_{m_L} = -20$ mV, $I_{max} = 2.2$ mV, and $g_{K-IR} = 0.2$ nS. A crude measure of the burst duration is the spike width at -50 mV. The abrupt changes in the firing frequency (—) and burst duration (- - -) occur when an extra small oscillation is added to the oscillations that follow the initial spike. This functional dependence of the spike duration and firing frequency with d_{cell} is also exhibited in the ER model described in Chapter 2 (not shown).

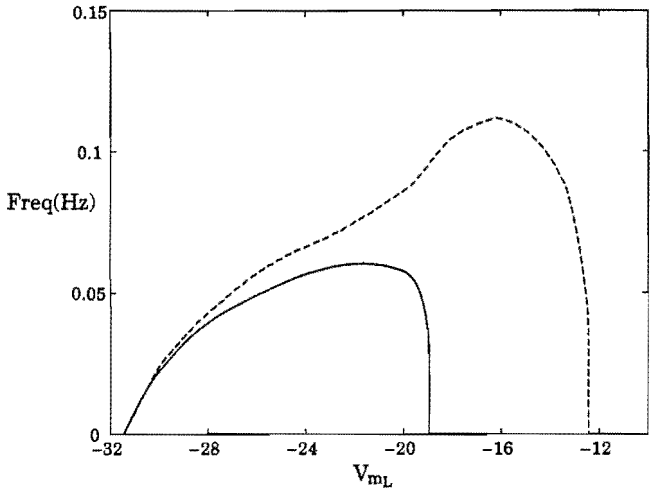

Figure 4.11: The change in firing frequency with respect to the voltage sensitivity of the L-type Ca^{2+} current (V_{m_L}) when d_{cell} is increased from 15 μm to 18.4 μm. This relationship is shown before (—) and after (- - -) the inhibition of I_{K-IR}. This increase in d_{cell} makes $[Ca^{2+}]_i$ a slower variable resulting in a decrease in spiking frequency (compare with Figure 4.6). Because d_{cell} does not effect the threshold behaviour, where a suitable left-shift in V_{m_L} from the rest value of -12 mV is required to generate oscillations, there is no change in membrane excitability.

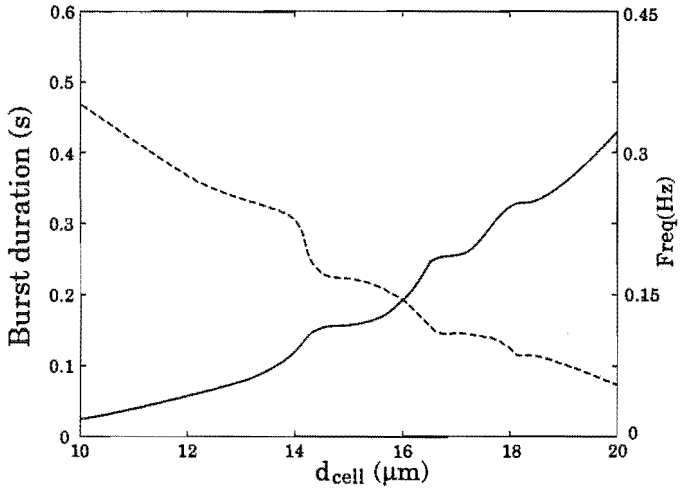

Figure 4.12: Dependence of the firing frequency (- - -) and burst duration (—) on d_{cell} (V_{m_L} = -20 mV, $I_{max} = 2.2$ mV, and $g_{K-IR} = 0.2$ nS) .

4.5 Summary

To investigate mechanisms by which CRH induces membrane electrical activity, an extension of a model of corticotroph electrical activity (I) was made by including a representation of a recently identified inwardly rectifying K^+ current. The potential role of a CRH-induced reduction of an inward rectifier K^+ current, an effect observed experimentally by Kuryshev et al., 1997, was tested. This reduction increased the action potential firing frequency, membrane excitability, and $[Ca^{2+}]_i$ transient levels, but was not obligatory for action potential generation. These results support the hypothesis that a delayed inhibition of an inwardly rectifying K^+ current is a significant component in an observed delayed increase in action potential firing frequency after the application of CRH. However the inhibition of the inwardly rectifying K^+ current did not produce an experimentally observed 10 mV depolarization. Possibly the CRH-induced depolarization may involve the modulation of other channels, or the absence of smaller uncharacterised ionic currents from the model, which are less significant in action potential generation, may eliminate the possibility of this depolarization.

The previous model action potential firing frequency was an order of magnitude larger than typical experimental data. The modified model has a firing frequency more consistent with experimental observations.

Some corticotrophs exhibit bursting action potential kinetics where the depolarization spike is followed by small oscillations in the membrane potential (Kuryshev et al., 1996; Kuryshev et al., 1997; Adler et al., 1983). The model also exhibits this bursting behaviour and the underlying mechanisms were investigated using a fast-slow subsystem analysis. The model burst duration was due to a gradual increase in $[Ca^{2+}]_i$ and the related Ca^{2+}-activated K^+ current. The model produced results similar to those observed experimentally.

CRH-induced exocytosis of ACTH allows an increase in the cell surface area by up to 50% (King and Baertschi, 1990; Westlund et al., 1985). Therefore it is important to understand how changes in cellular volume affect plasma membrane excitability, action potentials and the associated $[Ca^{2+}]_i$ dynamics. Increasing the cell diameter (d_{cell}) makes $[Ca^{2+}]_i$ a slower variable, resulting in an increase in the burst duration and a corresponding decrease in the spike frequency. However there is no effect on the cell excitability or steady state with changes in d_{cell}.

Using this electrophysiological model we have found that an increase in the L-type Ca^{2+} current is sufficient to initiate repetitive action potentials in an all-or-none manner from a previous quiescent model state as observed experimentally. It must be emphasized that our hypothesis of action potential generation via a PKA-induced enhancement of the L-type Ca^{2+} current remains valid.

CRH may also affect other ion channels through PKA or some other CRH-receptor-coupled G-

protein activated kinase. Possibilities identified include the acceleration in the activation kinetics of a hyperpolarization-activated K^+/Na^+ current (Ritchie et al., 1996) (which may increase the spike frequency), the inhibition of a K^+ current active at depolarized potentials (which could create a longer action potential allowing greater Ca^{2+} entry) and the inhibition of a BK-type Ca^{2+}-activated K^+ current (Shipston et al., 1996). It is therefore possible that the observed bursting behaviour or membrane depolarization depend on ionic currents or CRH-induced effects not explicitly included in the model.

Chapter 5

The AVP model

5.1 Introduction

Other major agonists influencing corticotroph ACTH secretion are arginine vasopressin (AVP), noradrenaline (NA), angiotensin-II (AII), and oxytocin (OXT). In this chapter we include a description of cellular responses to the agonist AVP[1]. However there appears to be at least two different sub-populations of secretory corticotrophs in response to AVP (Corcuff et al., 1993; Corcuff et al., 1995), and only one such sub-population is modeled in this chapter. Future work would be aimed at understanding the fundamental secretory mechanisms underlying the other sub-population response to AVP.

AVP is believed to activate the intracellular inositol 1,4,5-triphosphate (IP_3) phospholipase C (PLC) signaling pathway (Raymond et al., 1985; Todd and Lightman, 1987; Abou-Samra et al., 1987a; Bilezikjian et al., 1987; Won et al., 1990; Won and Orth, 1995; Tse and Lee, 1998). The ACTH releasing activities of OXT, NA, and AII are also thought to be mediated by the activation of PLC (Won et al., 1990; Mollard et al., 1987; Tse and Tse, 1998). The two AVP-induced secondary messengers in the PLC signaling pathway are IP_3 and diacylglycerol (DAG), each having separate domains of influence. The small water soluble IP_3 diffuses rapidly from the cell membrane into the the cell cytosol to its receptor located on the endoplasmic reticulum (ER). The IP_3 receptor is coupled to the opening of a Ca^{2+} channel. When IP_3 occupies the receptor, the Ca^{2+}-permeable channel opens releasing free Ca^{2+} from the ER, thereby increasing $[Ca^{2+}]_i$ (Corcuff et al., 1993; Corcuff et al., 1995). A number of cytosolic factors have been suggested to modulate the IP_3 receptor (IP_3R), including PKA, protein kinase C (PKC), Ca^{2+}-calmodulin kinase II, adenine and guanine nucleotides. These modulatory factors may permit the wide range of IP_3-induced Ca^{2+} responses. The IP_3R is also modulated by Ca^{2+}, with the open probability of the IP_3R displaying a bell-shaped dependence on $[Ca^{2+}]_i$, with low and high $[Ca^{2+}]_i$ inhibiting

[1] AVP is also known as antidiuretic hormone (ADH) due to its water conservation role in the kidney.

Ca^{2+} release (Bezprozvanny et al., 1991; Parys et al., 1992). This biphasic regulation of the IP_3R by $[Ca^{2+}]_i$ may represent the mechanism by which $[Ca^{2+}]_i$ oscillations arise.

The other secondary messenger DAG, which remains in the plasma membrane, activates PKC in the presence of phosphatidylserine and Ca^{2+} (King and Baertschi, 1990; Putney and Bird, 1993). Protein kinase C (PKC) is believed to phosphorylate channels in the plasma membrane, causing a depolarization, resulting in Ca^{2+} influx through voltage sensitive Ca^{2+} channels (VSCC) (Won et al., 1990; Corcuff et al., 1993; Corcuff et al., 1995; Won and Orth, 1995). The specific channel targets for PKC have not been identified in corticotrophs, although PKC activation of Ca^{2+} channels has been demonstrated in other cells such as gonadotrophs (Shangold et al., 1988) and cardiomyocytes (Lacerda et al., 1988). However, experimental evidence in *Xenopus* oocytes, and nucleus basalis neurons also suggests that PKC inhibits an inwardly rectifying K^+ channel (Henry et al., 1996; DiMagno et al., 1996; Takano et al., 1995), which has been identified in pituitary corticotrophs (Kuryshev et al., 1997). A schematic diagram summarising the possible AVP signaling pathway is shown in Figure 5.1.

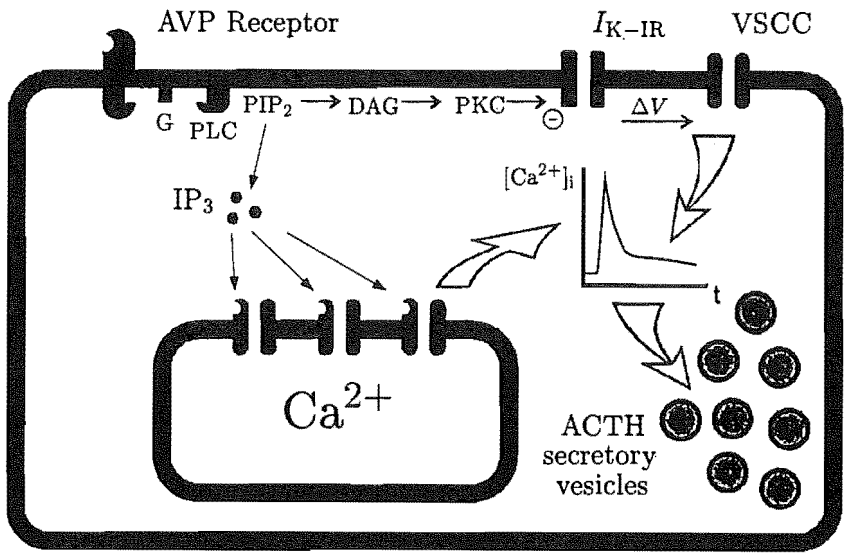

Figure 5.1: Schematic diagram of the hypothesised signaling pathway. AVP is believed to activate the intracellular inositol 1,4,5-triphosphate (IP_3), phospholipase C (PLC) signaling pathway. The first secondary messenger is IP_3, which diffuses rapidly to IP_3 receptors located on the ER, releasing free Ca^{2+} from the ER into the cytosol. The second secondary messenger is protein kinase C (PKC), which is believed to phosphorylate channels in the plasma membrane, causing a depolarization resulting in Ca^{2+} influx through voltage sensitive Ca^{2+} channels (VSCC).

There appears to be two different corticotroph responses to AVP (Corcuff et al., 1993; Corcuff et al., 1995). AVP can generate either a $[Ca^{2+}]_i$ transient response (Figure 5.2 A) or a $[Ca^{2+}]_i$

spike/plateau response (Figure 5.2 B,C) from the respective sub-population. In this chapter we investigate the later response, where the application of AVP results in an initial $[Ca^{2+}]_i$ spike, followed by a sustained elevated plateau response (Figure 5.2 B) (Tse and Tse, 1998). As $[Ca^{2+}]_i$ is closely linked to ACTH secretion, the ACTH response is similar (Won et al., 1990; Won and Orth, 1995). The initial spike is mediated through IP_3-induced Ca^{2+} release from the ER, and the sustained plateau is due to extracellular Ca^{2+} influx through voltage sensitive Ca^{2+} channels (Figure 5.3) (Won et al., 1990; Corcuff et al., 1993; Corcuff et al., 1995; Won and Orth, 1995).

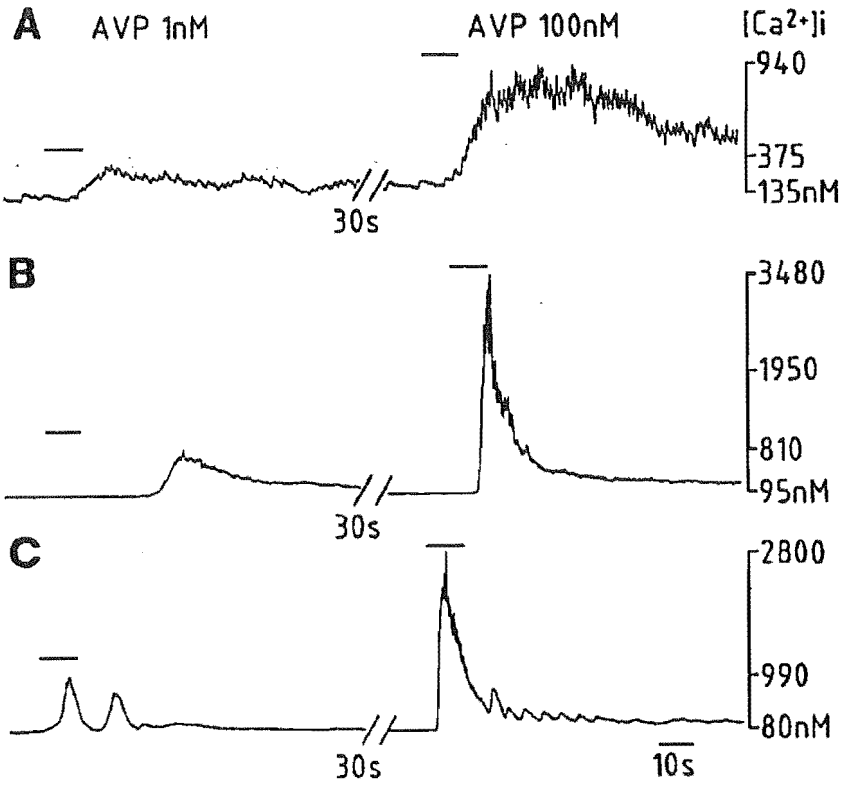

Figure 5.2: Concentration dependence of the AVP-induced $[Ca^{2+}]_i$ response. Each trace represents separate corticotrophs that were sequentially challenged by AVP at 1 and 100 nM respectively. (A) AVP produced $[Ca^{2+}]_i$ transients that show an increase in frequency upon raising peptide concentration. (B) 1 nM AVP produced a slow rising phase, low amplitude $[Ca^{2+}]_i$ step, and 100 nM AVP produced a rapid high amplitude spike followed by a plateau. (C) 1 nM AVP produced sinusoidal $[Ca^{2+}]_i$ oscillations, and 100 nM AVP caused a rapid high amplitude spike followed by an oscillating plateau. Data from Corcuff et al. (1993).

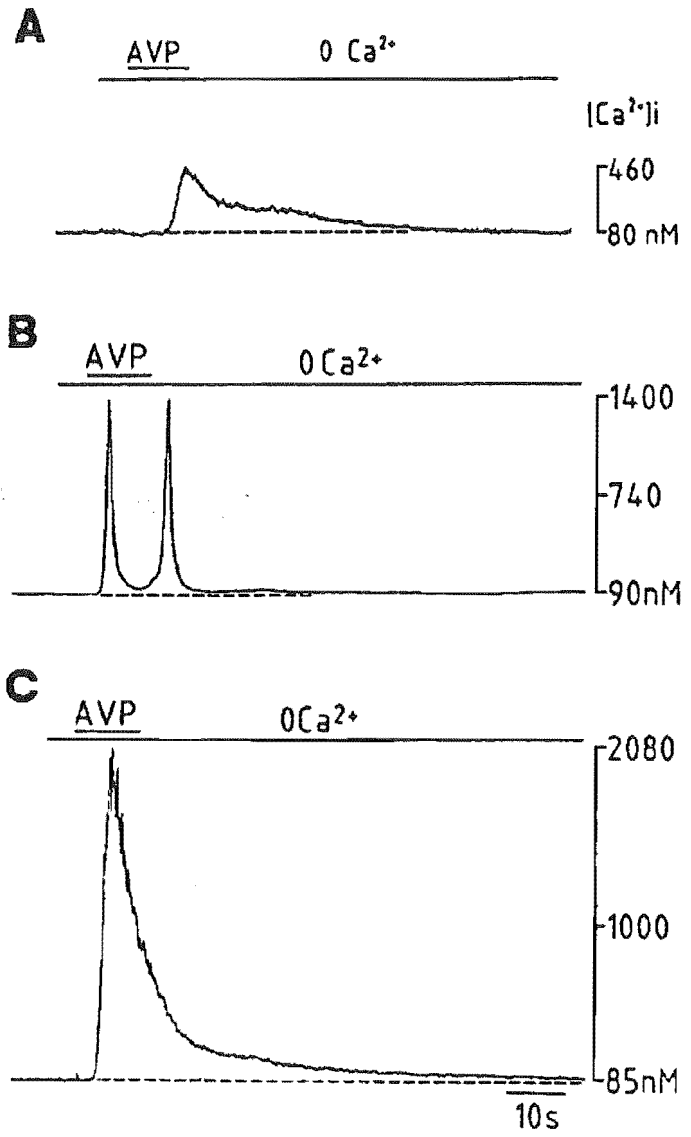

Figure 5.3: Effects of extracellular Ca^{2+} removal on $[Ca^{2+}]_i$ step, oscillation, and spike/plateau patterns induced by AVP in separate cells. Ca^{2+}-free medium was applied to cells prior to AVP challenge as indicated by the horizontal bar. (A) $[Ca^{2+}]_i$ step produced in response to 1 nM AVP. (B) $[Ca^{2+}]_i$ oscillations produced in response to 10 nM AVP. (C) $[Ca^{2+}]_i$ spike produced in response to 100 nM AVP. Data from Corcuff et al. (1993).

5.2 The IP_3 receptor model

A number of models of the IP_3 receptor have been constructed (De Young and Keizer, 1992; Atri et al., 1993; Sneyd et al., 1995; Li et al., 1994; Li et al., 1997; LeBeau et al., 1999). $[Ca^{2+}]_i$ oscillations in these models essentially require fast activation and slow inhibition by $[Ca^{2+}]_i$ of the IP_3R. In this chapter we incorporate the IP_3R model of LeBeau et al. (1999) into the corticotroph model. The model behaviour is similar if the IP_3R models of Atri et al. (1993) and Li et al. (1994, 1997) are incorporated into the corticotroph model (not shown).

The IP_3R is assumed to be composed of four functionally identical independent subunits (LeBeau et al., 1999). The state transition scheme for each subunit is shown in Figure 5.4. S denotes the fraction of units in the shut state, where IP_3 is not bound to the receptor and the channel is closed. Binding of IP_3 allows the IP_3R subunit to convert to the open state (O). IP_3 must be bound to all four subunits for the receptor to be in the conducting state, and thus the receptor conducting probability is O^4. However because the open state is assumed to be relatively unstable, the subunit will progress to the more stable inactivated state (I), where IP_3 is still bound but the channel is closed. The IP_3R can recover from the inactivated state to the shut state when IP_3 dissociates from its binding site. The receptor can then rebind IP_3 and repeat the cycle.

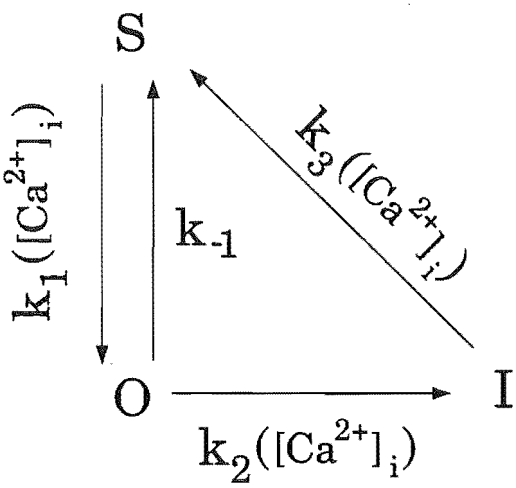

Figure 5.4: Schematic diagram of the receptor states in the model IP_3 receptor. The receptor contains four identical subunits which can be shut (S), open (O), or inactivated (I).

The receptor states are governed by the law of mass action kinetics, where the probability of the receptor subunit being in the open state (O) satisfies

$$\frac{dO}{dt} = k_1([Ca^{2+}]_i)[IP_3](1 - O - I) - (k_{-1} + k_2([Ca^{2+}]_i))O, \tag{5.2.1}$$

where

$$k_1([Ca^{2+}]_i) = \frac{\alpha_1[Ca^{2+}]_i}{\beta_1 + [Ca^{2+}]_i}, \tag{5.2.2}$$

and

$$k_2([Ca^{2+}]_i) = \gamma_2 + \frac{\alpha_2[Ca^{2+}]_i}{\beta_2 + [Ca^{2+}]_i}. \tag{5.2.3}$$

The values of the rate constants are shown in Table 5.1, and the probability that the receptor subunit is shut (S) is $S = 1 - O - I$. The probability that the receptor subunit is in the inactivated state (I) satisfies

$$\frac{dI}{dt} = k_2([Ca^{2+}]_i)O - k_3([Ca^{2+}]_i)I, \tag{5.2.4}$$

where

$$k_3([Ca^{2+}]_i) = \alpha_3\left(1 - \frac{[Ca^{2+}]_i}{\beta_3 + [Ca^{2+}]_i}\right). \tag{5.2.5}$$

Experimental observations suggest that $[Ca^{2+}]_i$ enhances the binding of IP_3 to the IP_3R receptors (Dufour et al., 1997; Marshall and Taylor, 1993), and thus $k_1([Ca^{2+}]_i)$, and $k_3([Ca^{2+}]_i)$ are increasing and decreasing functions of $[Ca^{2+}]_i$ respectively. Thus $[Ca^{2+}]_i$ enhances the rate of channel activation ($S \rightarrow O$) and acts in an inhibitory manner at high concentrations by holding receptor subunits in the inhibited state (I) for as long as $[Ca^{2+}]_i$ remains elevated. Experimental evidence also suggests that $k_2([Ca^{2+}]_i)$ is an increasing function of $[Ca^{2+}]_i$ (Finch et al., 1991; Dufour et al., 1997). Thus, as observed experimentally the steady state open probability (O^4) of the model IP_3R has a bell-shaped dependence on $[Ca^{2+}]_i$ (Figure 5.5) (Bezprozvanny et al., 1991; Parys et al., 1992).

5.3 Results

In this section we investigate the ER corticotroph model discussed in Section 2.3 with the IP_3R model discussed in Section 5.2 included. A model based on the spatio-temporal model presented in Section 2.4 exhibits similar behaviour. Although the spatial distribution of $[Ca^{2+}]_i$ is significant in some IP_3R models (Jafri and Keizer, 1995; Sneyd et al., 1995; Sneyd and Sherratt, 1997; McKenzie and Sneyd, 1998), the distribution of $[Ca^{2+}]_i$ in the corticotroph spatio-temporal IP_3R model was very nearly uniform. The only change to the ER model discussed in Section 2.3 is an addition to the ER Ca^{2+} release term in equation (2.3.1). The Ca^{2+} release from the ER is now

$$J_{rel} = (P + k_{flux}O^4)([Ca^{2+}]_{er} - [Ca^{2+}]_i), \tag{5.3.1}$$

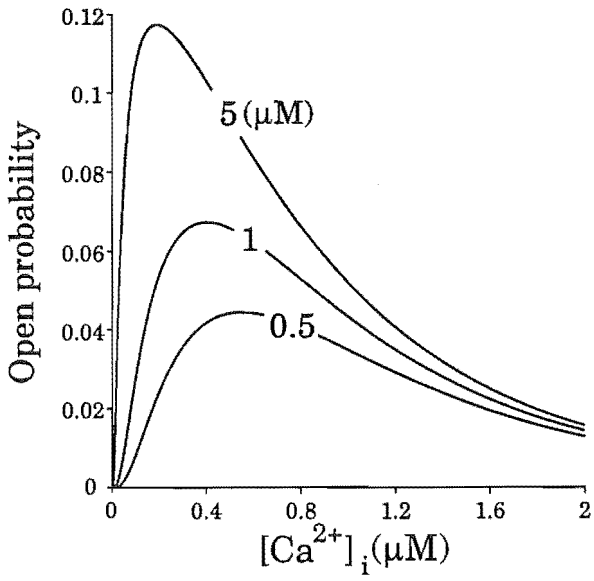

Figure 5.5: Biphasic steady state channel opening probability of the model IP_3R with $[Ca^{2+}]_i$. As IP_3 is increased the peak of the bell-shaped curve increases.

Parameter	Definition	Value	Source
f_{er}	ER Ca^{2+} buffering factor	0.001	This chapter
P	ER permeability	0.003 pL $\cdot$ ms^{-1}	This chapter
ν_{er}	Maximum ER Ca^{2+}-ATPase current	0.2 μM $\cdot$ pL $\cdot$ ms^{-1}	This chapter
ν_p	Maximum plasma membrane Ca^{2+}-ATPase flux	0.075 μM $\cdot$ μm $\cdot$ ms^{-1}	This chapter
k_{flux}	maximum IP_3R permeability	0.75 pL $\cdot$ ms^{-1}	(Li et al., 1997)
k_{-1}	rate of channel closing	0.00088 ms^{-1}	(LeBeau et al., 1999)
α_1	maximum rate of k_1	0.1 μM $\cdot$ ms^{-1}	(LeBeau et al., 1999)
β_1	$[Ca^{2+}]_i$ for half-maximal k_1	6 μM	(LeBeau et al., 1999)
α_2	maximum rate of k_2	0.002 ms^{-1}	(LeBeau et al., 1999)
β_2	$[Ca^{2+}]_i$ for half-maximal k_2	5 μM	(LeBeau et al., 1999)
γ_2	offset for k_2	0.00053 ms^{-1}	(LeBeau et al., 1999)
α_3	maximum rate of k_3	0.001 ms^{-1}	(LeBeau et al., 1999)
β_3	$[Ca^{2+}]_i$ for half-maximal k_3	1.6 μM	(LeBeau et al., 1999)
$[IP_3]$	IP_3 concentration	1 μM	This chapter

Table 5.1: Table of relevant model parameters.

where k_{flux} is the IP_3R permeability, and O is the probability that a receptor subunit is in the open state. The model parameters are shown in Table 5.1, which include an increase in the ER Ca^{2+} storage capacity, f_{er}, and an increase in the Ca^{2+} pumping parameters.

The model $[Ca^{2+}]_i$ response is shown in Figure 5.6 for different IP_3 concentrations. When $[IP_3] = 5$ μM the model exhibits a high amplitude spike followed by a slowly decreasing elevated $[Ca^{2+}]_i$ plateau. This is similar to the 100 nM AVP-induced response in Figure 5.2 B. When $[IP_3] = 1$ μM the model displays a high amplitude spike followed by an oscillating plateau, which is similar to the 100 nM AVP-induced response in Figure 5.2 C. When $[IP_3] = 0.6$ μM the model produces two smaller oscillations that are similar to the 1 nM AVP-induced response in Figure 5.2 C. When $[IP_3] = 0.5$ μM the model displays a low amplitude $[Ca^{2+}]_i$ step that is similar to the 1 nM AVP-induced response in Figure 5.2 B. Thus the concentration dependent sequence of behaviour in Figures 5.2 and 5.3 is also exhibited in the model.

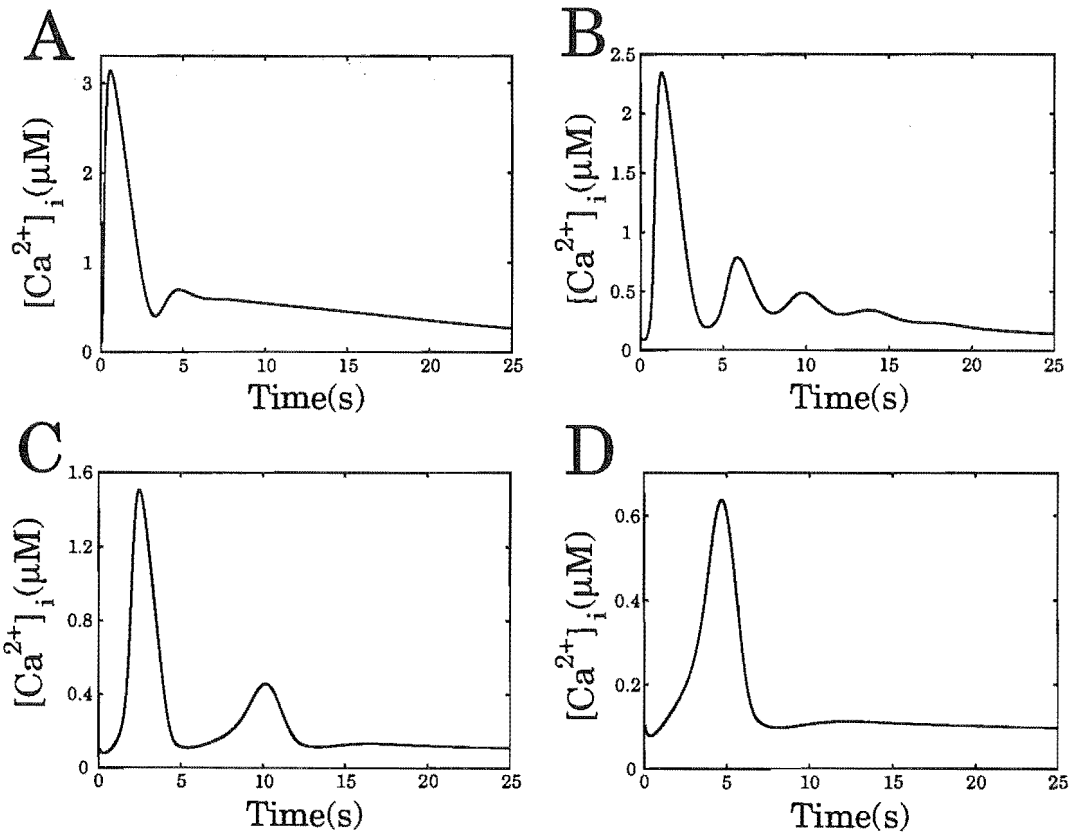

Figure 5.6: Model IP_3-induced $[Ca^{2+}]_i$ response. (A) When $[IP_3] = 5$ μM the model exhibits a high amplitude spike (compare with Figure 5.2 B). (B) When $[IP_3] = 1$ μM the model displays a high amplitude spike followed by an oscillating plateau (compare with Figure 5.2 C). (C) When $[IP_3] = 0.6$ μM the model produces two oscillations (compare with Figure 5.2 C). (D) When $[IP_3] = 0.5$ μM the model displays a low amplitude $[Ca^{2+}]_i$ step (compare with Figure 5.2 B). Note the different vertical scales in these diagrams.

Associated with the AVP-stimulated $[Ca^{2+}]_i$ response is a change in the membrane potential (see Figure 5.7). The increase in $[Ca^{2+}]_i$ activates an apamin-sensitive Ca^{2+}-activated K^+ current (Tse and Lee, 1998; Corcuff et al., 1993), which causes a membrane hyperpolarization. Low concentrations of AVP generate $[Ca^{2+}]_i$ oscillations and an associated oscillating hyperpolarization (see Figure 5.7 A). The model also produces this $[Ca^{2+}]_i$-induced, Ca^{2+}-activated K^+ current

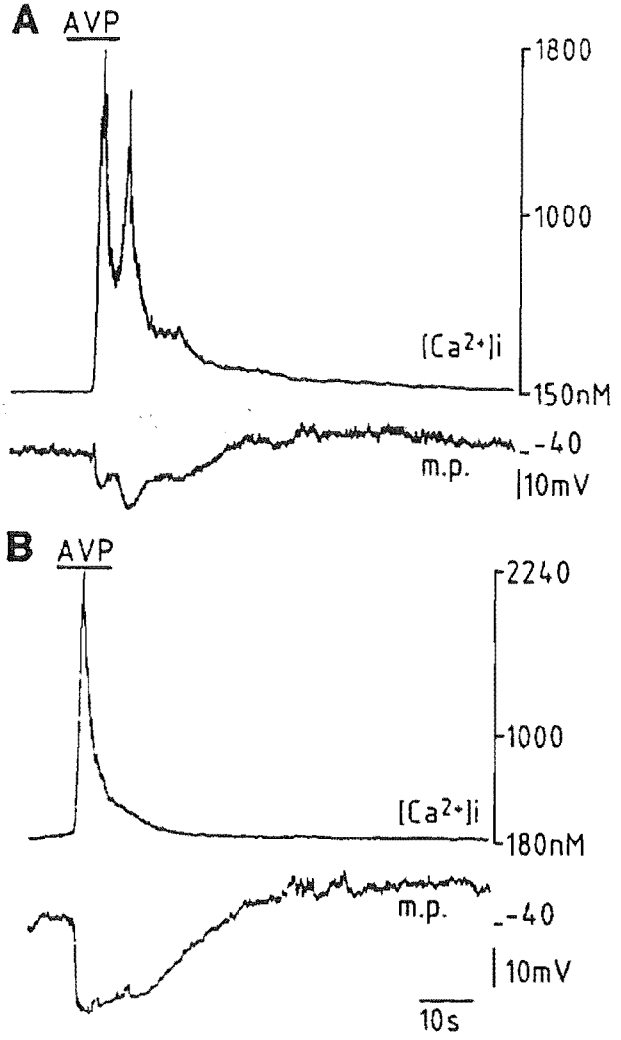

Figure 5.7: Membrane potential responses in AVP-stimulated cells presenting Ca^{2+}-mobilising responses. (A) 10 nM AVP produced $[Ca^{2+}]_i$ oscillations associated with an oscillating hyperpolarization (B) 100 nM AVP produced a $[Ca^{2+}]_i$ spike associated with a transient hyperpolarization followed by a sustained 10 mV depolarization. Data from Corcuff et al. (1993).

mediated, membrane hyperpolarization (see Figure 5.8). When $[IP_3] = 5$ μM the model displays a transient hyperpolarization (– – –), and when $[IP_3] = 1$ μM the model exhibits an oscillating

hyperpolarization which repolarizes at a faster rate (—). When $[IP_3] = 0.5$ μM the oscillating hyperpolarization is larger, with a faster rate of repolarization (not shown).

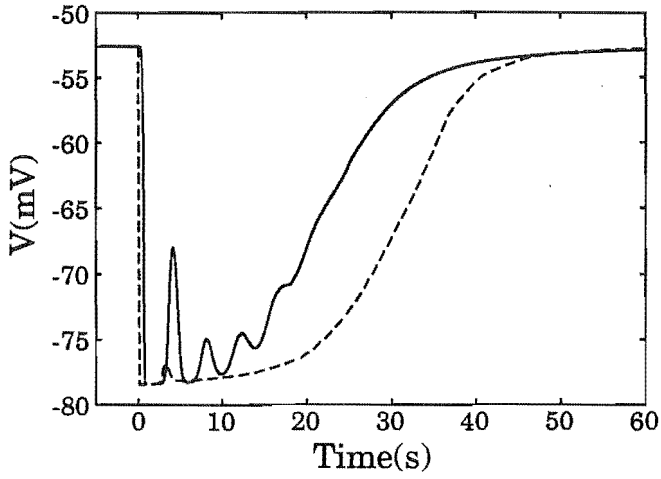

Figure 5.8: Model IP_3-induced membrane potential responses. When $[IP_3] = 5$ μM the model displays a transient hyperpolarization (- - -) (compare with Figure 5.7 B). When $[IP_3] = 1$ μM the model exhibits an oscillating hyperpolarization which repolarizes at a faster rate (—) (compare with Figure 5.7 A).

The IP_3-induced model $[Ca^{2+}]_{er}$ response is shown in Figure 5.9. When $[IP_3] = 5$ μM the ER Ca^{2+} store is initially rapidly depleted, generating the $[Ca^{2+}]_i$ spike response in Figure 5.6 A. While $[Ca^{2+}]_i$ is high the IP_3R is inactivated and there is an increase in the ER Ca^{2+}-ATPase pumping. This results in a brief increase in $[Ca^{2+}]_{er}$, which is followed by a steady decrease. The ER Ca^{2+} release allows $[Ca^{2+}]_i$ to remain elevated for approximately 30 s (see Figure 5.6 A). After about 50 s, the ER Ca^{2+} store is depleted, and $[Ca^{2+}]_i$ returns to basal as excess Ca^{2+} is pumped out of the cell. When $[IP_3] = 1$ μM the ER Ca^{2+} store is similarly depleted, although at a lower rate, which allows small oscillations in $[Ca^{2+}]_{er}$ as it decreases (Figure 5.9 B). Note that when $[IP_3]$ returns to basal, the ER Ca^{2+} stores are refilled with Ca^{2+} from the cytosol, which is simultaneously replenished by extracellular Ca^{2+} (not shown).

The oscillations in $[Ca^{2+}]_{er}$ are associated with oscillations in the fraction of open (O) IP_3 receptors (Figure 5.10 A (—)). A high receptor subunit open probability corresponds with a rapid increase in $[Ca^{2+}]_i$. However high $[Ca^{2+}]_i$ inactivates the IP_3R, and thus the fraction of inactivated channels (I) increases, generating a decrease in $[Ca^{2+}]_i$ (Figure 5.10 A (- - -)). The subsequent decrease in the fraction of inactivated subunits is followed by an increase in the fraction of shut subunits (S) (Figure 5.10 A (- — -)). The shut receptor can then rebind IP_3 and repeat the cycle. The oscillations in the receptor subunit states are shown in Figure 5.10 B.

The second secondary messenger is protein kinase C (PKC), which is believed to phosphorylate

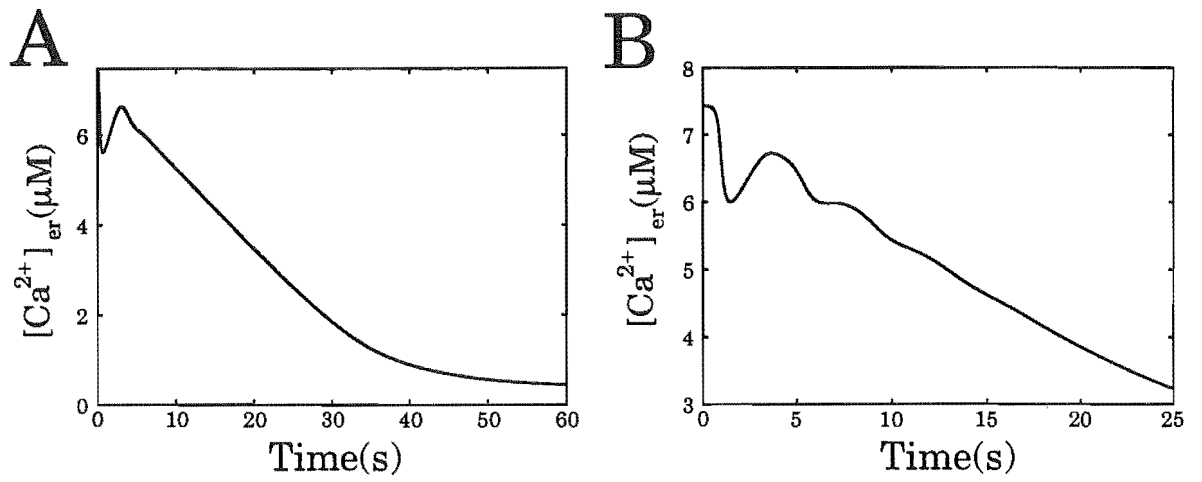

Figure 5.9: The model $[Ca^{2+}]_{er}$ response to IP_3. (A) When $[IP_3] = 5\ \mu M$ the ER Ca^{2+} store is initially rapidly depleted, followed by a brief increase and then a steady decrease.(B) When $[IP_3] = 1\ \mu M$ the ER Ca^{2+} store is depleted at a lower rate, which allows small oscillations in $[Ca^{2+}]_{er}$.

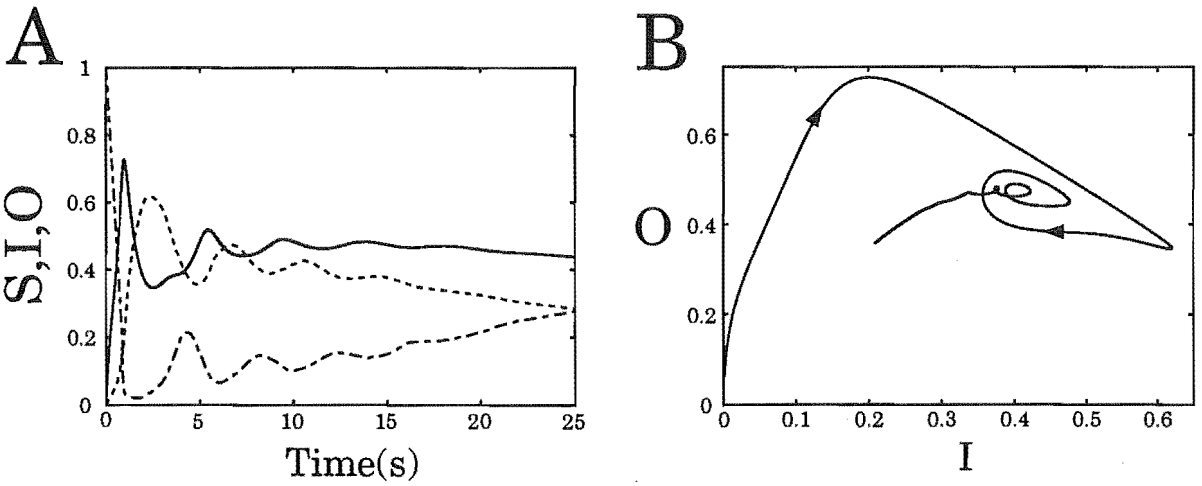

Figure 5.10: (A) IP_3-induced oscillations in the receptor subunit states. Oscillations in the fraction of open states (—) are followed by oscillations in the fraction of inactivated states (– – –) and shut states (– — –). (B) The $[Ca^{2+}]_i$-induced oscillations in the receptor subunit states S and I are out of phase.

ion channels in the plasma membrane, causing a depolarization, resulting in Ca^{2+} influx through voltage sensitive Ca^{2+} channels (VSCC). However the specific channel targets for PKC have not been identified in corticotrophs. Experimental evidence indirectly suggests two likely phosphorylation targets; L-type Ca^{2+} channels (Won et al., 1990; Corcuff et al., 1993; Corcuff et al., 1995; Won and Orth, 1995) or an inwardly rectifying K^+ channel (Henry et al., 1996; DiMagno et al., 1996; Takano et al., 1995). We now briefly investigate these two possible PKC-induced responses in the model.

To mimic the possible PKC-induced inactivation of the inwardly rectifying K^+ channel we consider a reduction in the leak channel conductance, g_L from 0.3 nS to 0.2 nS. The model transient hyperpolarization when $[IP_3] = 5$ μM and $g_L = 0.3$ nS is shown in Figure 5.11 A (—). When g_L is reduced from 0.3 nS to 0.2 nS the transient hyperpolarization is followed by a sustained 11 mV depolarization (see Figure 5.11 A (- - -)). This agrees with the experimental data in Figure 5.7, where 100 nM AVP induced a 10 mV depolarization. Associated with this membrane depolarization is Ca^{2+} influx through voltage sensitive Ca^{2+} channels, which results in an increase in the plateau level from 0.07 μM to 0.13 μM (see Figure 5.11 B). This agrees with the experimental data in Figure 5.3 C and Figure 5.7 B, which indicate that the Ca^{2+} influx through voltage sensitive Ca^{2+} channels causes a rise in the plateau level from 0.08 μM to 0.18 μM. To mimic the possible

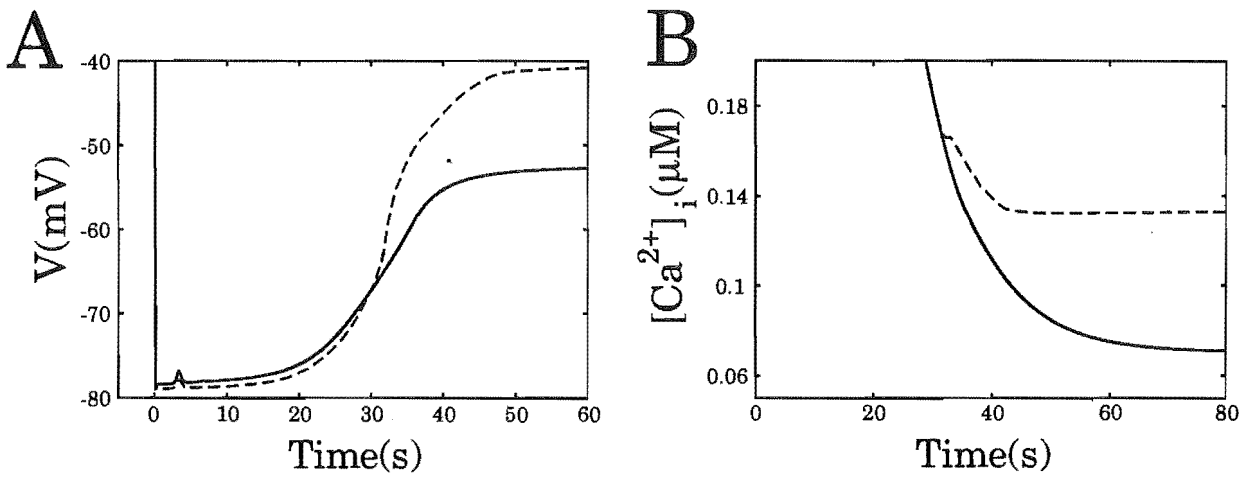

Figure 5.11: The PKC-induced model response. (A) When $[IP_3] = 5$ μM, the PKC-induced inhibition of the inwardly rectifying K^+ channel results in a similar transient hyperpolarization which is now followed by a sustained 11 mV depolarization from -52 mV (—) to -41 mV (- - -) (compare with Figure 5.7 B). (B) Associated with this PKC-induced membrane depolarization is Ca^{2+} influx through voltage sensitive Ca^{2+} channels, which results in an increase in the plateau level from 0.07 μM (—) to 0.13 μM (- - -).

PKC-induced activation of the L-type Ca^{2+} channel, a left-shift in V_{m_L} from -12 mV to -15 mV

produces a 6 mV depolarization and a rise in the plateau level from 0.07 μM to 0.12 μM (not shown).

5.4 Discussion

The corticotroph AVP model developed in this chapter exhibits the experimentally observed concentration dependent step, spike/plateau, oscillating plateau, and sinusoidal $[Ca^{2+}]_i$ responses. The oscillations are due to $[Ca^{2+}]_i$ regulation of the binding of IP_3 to the IP_3R. The ER Ca^{2+}, in addition to providing Ca^{2+} for IP_3-stimulated release, also appears to be required for the sustained activity of PLC (Won and Orth, 1995). This feedback mechanism could possibly eliminate excessive ER Ca^{2+} depletion, and may even generate $[Ca^{2+}]_i$ oscillations. The model also displays the experimentally observed transient and oscillating hyperpolarization. The hyperpolarization is mediated by an apamin-sensitive $[Ca^{2+}]_i$-activated K^+ current. Interestingly the transition from oscillations to spike upon raising AVP concentration in some corticotroph cells resembles the concentration dependent shift in gonadotropin-releasing hormone (GnRH)-stimulated gonadotrophs (Shangold et al., 1988; Leong and Thorner, 1991). However, although AVP elicits fewer oscillations in corticotrophs than GnRH in gonadotrophs, it seems likely that corticotrophs can encode AVP concentration by shifting between $[Ca^{2+}]_i$ oscillations and spike responses.

The PKC-dependent membrane depolarization and $[Ca^{2+}]_i$ plateau are also exhibited in the model. Both effects are due to Ca^{2+} influx through voltage sensitive Ca^{2+} channels, although the model does not indicate whether PKC activates Ca^{2+} channels, or inactivates K^+ channels. Some experimental data indicates that the plateau-phase of the AVP-induced $[Ca^{2+}]_i$ elevation was still present when corticotroph cells were voltage clamped at -90 mV, to prevent voltage gated Ca^{2+} entry, or when extracellular Ca^{2+} was omitted (Tse and Lee, 1998). It is possible that actual cytosolic Ca^{2+} removal into the extracellular medium is much lower than that in the model, allowing $[Ca^{2+}]_i$ to remain elevated for a much longer period of time. Alternatively the plateau pattern may involve complex Ca^{2+} removal kinetics. PKC also inhibits I_{K-Ca} in pituitary corticotroph AtT20 cells (Tian et al., 1999), although PKC enhances I_{K-Ca} in pituitary gonadotrophs (Tse et al., 1995). However these PKC-induced responses had little effect on the model depolarization and $[Ca^{2+}]_i$ plateau.

The release of ACTH is synergistic with respect to AVP and CRH, that is together they produce a greater effect than the sum of their effects acting alone (Evans et al., 1988; Gillies et al., 1982; Rivier and Vale, 1983a). It has been observed that AVP potentiates the CRH-induced increase in cAMP (Labrie et al., 1984; Abou-Samra et al., 1987b). This synergism is believed to be due to interaction between the CRH and AVP activated intracellular messenger systems. A number of possible interactions exist between these two pathways. PKC appears to be

responsible for the potentiation (Carvallo and Aguilera, 1988), possibly by phosphorylating the CRH receptor, adenylate cyclase, or cAMP-dependent phosphodiesterase (PDE). The later is the most likely candidate since it has been observed that AVP decreases PDE activity (Abou-Samra et al., 1987b), which is responsible for the degradation of cAMP to AMP. It is also possible that PKA, PKC, and Ca^{2+}-calmodulin kinases interact by phosphorylating substrates involved in the ACTH exocytosis (King and Baertschi, 1990).

Noradrenaline also activates the PLC signalling pathway in corticotrophs, generating large amplitude, short frequency $[Ca^{2+}]_i$ oscillations (Tse and Tse, 1998). Whether a maintained or oscillatory level of IP_3 is essential for $[Ca^{2+}]_i$ oscillation generation is not clear, although in pituitary gonadotrophs $[Ca^{2+}]_i$ oscillations are generated when IP_3 is maintained at constant elevated levels (Tse et al., 1995). Similar behaviour occurs in pancreatic acinar cells, where acetylcholine (ACh) and cholecystokinin (CCK) elicit high and low frequency IP_3R-induced $[Ca^{2+}]_i$ oscillations respectively (LeBeau et al., 1999). Therefore it is possible that noradrenaline similarly modulates the IP_3R via an intracellular messenger that is not significantly activated by AVP.

Future work would be aimed at understanding the AVP-induced $[Ca^{2+}]_i$ transient response and associated action potentials (Corcuff et al., 1993), which may be mediated by the phosphorylation of L-type Ca^{2+} channels by PKC (Won et al., 1990).

Chapter 6

Introduction to the perifusion apparatus

Information transfer in a number of endocrine systems occurs through rapid modulation of hormone levels in concentration pulses. The temporal architecture of the endocrine glandular signaling process is believed to convey important biochemical information to the target tissue, and also represents a signature of the responsive endocrine cells. Hence to understand the endocrine glandular physiology, the time domain structure of hormone synthesis and release is required.

The perifusion apparatus is an *in vitro* experimental tool used to model the dynamics of information transfer in a number of endocrine systems (McIntosh and McIntosh, 1983; McIntosh et al., 1984; Evans et al., 1985) (see Figure 6.1). This transfer is mediated by rapid modulation of hormone concentration levels. The perifusion apparatus allows the hormonally stimulated release of hormones to be investigated. In this system, a liquid saline medium flowing at a constant rate, is pumped through the pipe over cells, which secrete a hormone in response to a hormone in the flowing medium. The temporal concentration profile of this released substance is then measured at some downstream location. This downstream temporal measurement is a hormone concentration measurement averaged over the cross-section of the pipe. The pipe is typically 1 mm in diameter, and has a total length ($\ell_1 + \ell_3$) of about 0.75 m. A schematic diagram of the perifusion apparatus is shown in Figure 6.2. The perifusion chamber is 4 mm in diameter and 25 mm in length, and typically contains about five million cells, predominantly in the top layer of a porous packing material (see Figure 6.3). This packing material is typically a combination of substances in the from of beads. The chamber is sealed with rubber plugs, pierced with a length of syringe needle over which is stretched a length of nylon cloth (10 μm pore size) to retain the contents of the column. The chamber is sealed within a thermojacket, allowing a constant cellular temperature of 37 °C.

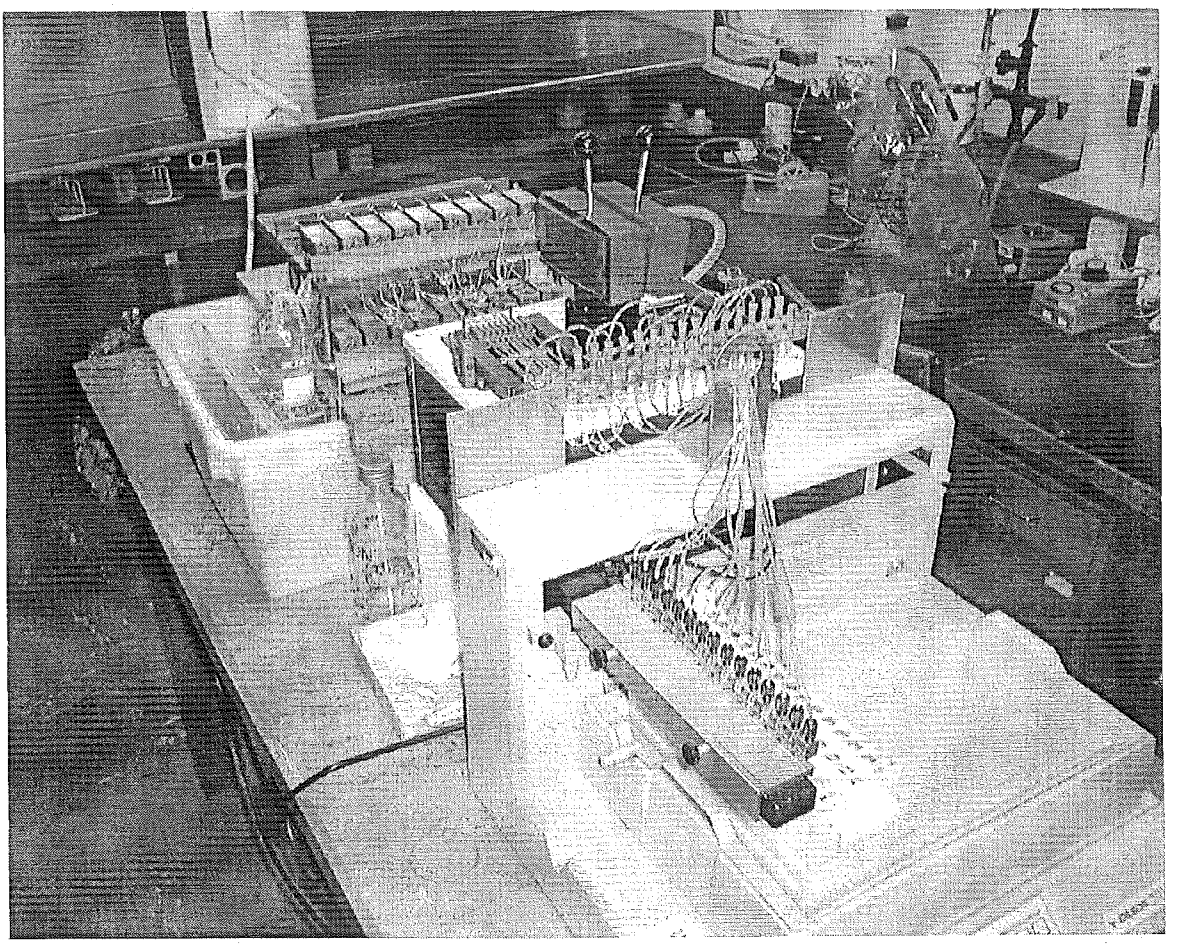

Figure 6.1: The perifusion apparatus. Photo courtesy of M. Hickman©.

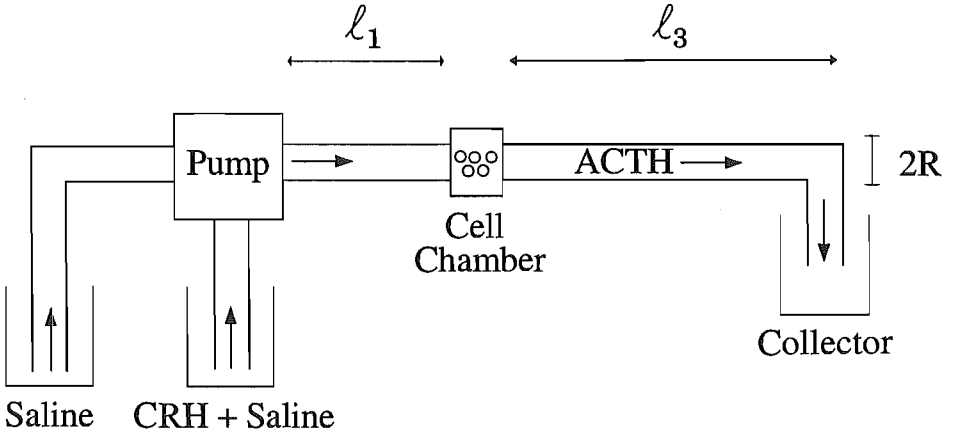

Figure 6.2: Schematic diagram of the perifusion apparatus. A saline solution carrying CRH is pumped via a peristaltic pump down a pipe of length ℓ_1 to the cell chamber. A solenoid system allows the flowing medium to be switched between the saline and the CRH solutions. Corticotroph cells in the perifusion chamber then secrete ACTH, which travels down a pipe of length ℓ_3 to the collector.

One may ask: What features does the engineering of the perifusion apparatus confer on the measured secretory profile? The major drawback of the perifusion system derives from the dispersion, diffusion and mixing of the released hormone in the tubing of the perifusion apparatus. This generates a distortion in the experimentally observed hormone concentration profile. Although the direct problem of the prediction of elution concentration has been considered in connection with the perifusion apparatus, very little has addressed associated inverse problems. These inverse problems, or deconvolution strategies, take account of the introduced experimental errors, enabling the unmasking of the underlying secretory events. However, due to the ill-posedness of the inverse problem, one cannot expect to completely remove the distortion in the measurement.

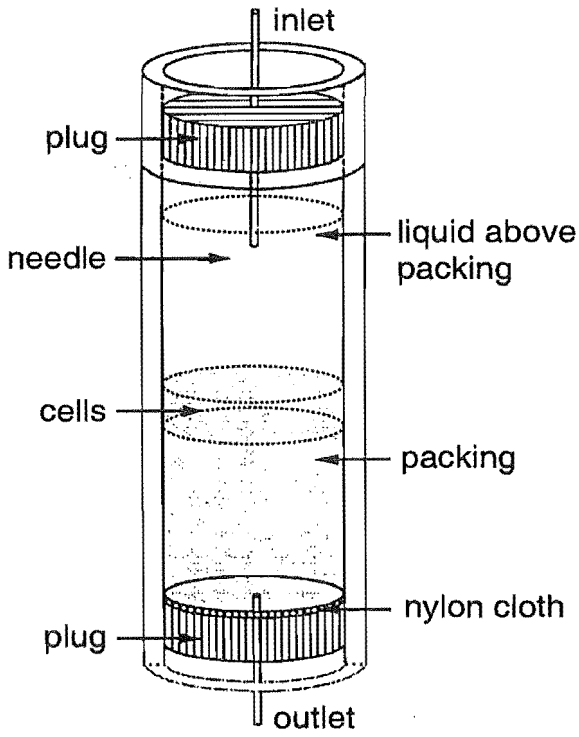

Figure 6.3: Schematic diagram of the perifusion chamber. Pituitary corticotroph cells lie in the top layer of the bead slurry packing. The bead packing material is a combination of Sephadex G25 and Bio-Gel P2, which absorb water and small molecules by diffusion, but do not allow the passage of larger molecules such as ACTH. Based on figure from Smith et al. (1991).

The model of the perifusion apparatus yields a number of interesting mathematical problems in order to deconvolve, or take account of the introduced experimental errors. In Chapter 7 we consider an inverse problem associated with the mass transport of a material concentration down a tube, when the flowing medium has a two-dimensional velocity profile. The fluid flow transports a concentration of suspended material down the tube, and its concentration is measured

downstream. From this measured concentration the temporal variation of the concentration at an upstream location is to be estimated. In Chapter 8 we consider the inverse problem of determining the two-dimensional fluid velocity profile from temporally varying cross-sectional average concentration measurements at upstream and downstream locations. This is shown to be a well-posed problem.

In experiments associated with stress-levels in horses, a cannula tube is inserted *in vivo* to sample blood downstream from the pituitary, allowing the cells to be monitored in their natural environment. However blood displays a marked shear-dependent viscosity, and a finite yield stress may be necessary before flow can commence. Thus for the pipe diameters used in these experiments blood does not behave in a Newtonian manner. Deconvolution problems for non-Newtonian fluids are examined in Chapter 9.

Although diffusion effects in the direction of fluid flow are negligible, the contribution of molecular diffusion transverse to the direction of fluid flow is an important contributing factor in the observed distortion in perifusion experiments. More general inverse problems including diffusive effects are investigated in Chapter 9. A number of researchers have incorporated this molecular diffusion into models of the perifusion chamber via an advection-diffusion equation. In Chapter 10, a general theory indicating under what conditions this approximation is valid, and how the parameters in the advection-diffusion model relate to measurable quantities in the perifusion system is investigated.

In Chapter 10 the tools and techniques developed in Chapters 7, 8, and 9 are used to understand the distortion in the experimentally observed hormone concentration profile. We use the developed deconvolution strategies to enhance data measurements in the perifusion system, allowing the unmasking of the underlying secretory events. The mathematical model of the two dimensional flow in the perifusion pipe accounts for a number of observable features in the measured secretory profile.

In Chapter 11 we investigate the interesting mathematical problem of signal reconstruction after transmission through an advective and diffusive medium. The transformation of the associated parabolic partial differential equation, by way of singular perturbation, to a hyperbolic one, enables the construction of a stable numerical algorithm for signal reconstruction. Wave splitting and invariant imbedding techniques have been successfully applied to inverse problems for hyperbolic equations, however they have not been effective for parabolic equations. By considering more generalised mass transport processes, these wave splitting and invariant imbedding techniques can also be applied to phenomena that are generally considered parabolic in nature. This approach yields valuable theoretical insight into this and other related problems.

Chapter 7

Signal restoration for a mass transport problem involving shear dispersion

7.1 Introduction

In this chapter we consider an inverse problem associated with mass transport of a material concentration down a pipe, when the flowing medium has a two-dimensional velocity profile. The fluid flow transports a concentration of suspended material down the pipe, and its concentration is measured at some fixed downstream location. From this cross-sectional average concentration measurement, the temporal variation of the concentration at an upstream location is to be estimated. The model problem considered in this chapter has practical application to the perifusion system, an experimental apparatus used in endocrinology experiments.

In viscous flow problems, involving a solute concentration in a pipe, the variation of the velocity over the cross-section of the pipe is an important factor in the dispersion of the solute; it is called shear dispersion. The dispersion of a pulse of concentration flowing down the pipe is in general due to the combined action of shear dispersion, parallel to the axis of the pipe, and molecular diffusion, predominantly in the radial direction. When the molecular diffusion coefficient within the flow is very small then fluid shear dispersion is the dominant dispersive effect. It is this regime that is examined in this chapter.

The first paper providing an approximate analysis of the direct problem related to these effects is due to Taylor (Taylor, 1953), and a considerable literature has built up about this direct problem (for recent application of modern theory to this direct problem see Watt and Roberts (1995)). Of interest for inverse problem practitioners is Taylor's paper (Taylor, 1954a), in which he estimates

the molecular diffusion coefficient from measured concentration profiles, after dispersion. This inverse problem solution is one of the earliest inverse problem investigations in this area.

Information transfer in a number of endocrine systems occurs through rapid modulation of hormone levels in concentration pulses. Experimental methods of investigating how the dynamics of signal transmission in endocrine systems relates to the mechanisms involved is often carried out *in vitro* by use of a perifusion apparatus (McIntosh and McIntosh, 1983; McIntosh et al., 1984). In this apparatus, measurement of an averaged hormone concentration is made downstream, along a pipe (up to a few metres in length) from pituitary cells which are attached to micro-beads in the perifusion chamber (see Figure 6.2). The flow rate of the carrying medium, a saline preparation, in the pipe is low and the internal diameter of the pipe is small. For this problem, longitudinal molecular diffusion effects of the hormone concentration suspended in the saline solution are small with respect to the dispersion due to the two-dimensional velocity distribution. In fact for the molecular particles and temperatures used in these *in vitro* experiments, longitudinal molecular diffusion is several orders of magnitude less dominant. A model of the perifusion apparatus as a one-dimensional advective-diffusive flow problem has been provided by Smith et. al. (1991). The analysis of the inverse problem associated with this simplified one-dimensional model was done in Smith and Wake (1990). However this model neglects shear dispersion and radial-diffusion effects, both of which are significant in the observed dispersion in perifusion experiments.

Inverse mass transport problems involving one-dimension flow, but without diffusion, have also been analysed in Wall and Lundstedt (1998), where inverse source problems associated with linear transport equations were solved. Various inverse problems associated with nonlinear transport equations have also been described in Connolly and Wall (1997).

This chapter concentrates on the inverse problem when the dispersion of the concentration of contaminant is due solely to the velocity profile. In Section 7.2.1 the equations modeling the flow of hormone concentration down the pipe are given, and the mathematical operator mapping the temporally varying input concentration to the experimentally measured output concentration is examined. In Section 7.2.2 it is shown that the inverse of this operator is unbounded on the Hilbert space of square integrable functions, L^2, and it is shown that the deconvolution problem, described by this operator, is an ill-posed problem. In Section 7.3 the mollification method is used to regularise the inverse problem, and the stability of the regularised solution is analysed. Numerical results are presented in Section 7.4, where it is shown that the regularised deconvolution problem can be effectively solved, even in the presence of a moderate amount of measurement noise.

7.2 Problem description

The two-dimensional laminar flow model is first analysed, and then the inverse problem is described.

7.2.1 The basic mass transport equations

The velocity profile of a viscous, incompressible fluid flowing through a rigid pipe of circular cross-section with a no-slip boundary condition, is described by the well known Poiseuille distribution (Landau and Lifshitz, 1959), (p 57 *et seq.*)

$$v(r) = v_m\left(1 - \left(\frac{r}{R}\right)^2\right), \tag{7.2.1}$$

where r is the circular polar radial coordinate associated with a cylindrical coordinate system oriented so that the z-axis is aligned with the axis of the pipe, and the wall of the pipe is located at $r = R$ (see Figure 7.1). The maximum velocity of the parabolic velocity profile, v_m, depends upon the pressure differential applied down the pipe. The fluid flowing in the pipe is assumed to be Newtonian, and have a suitably low Reynolds number[1] so that the fluid flow is laminar.

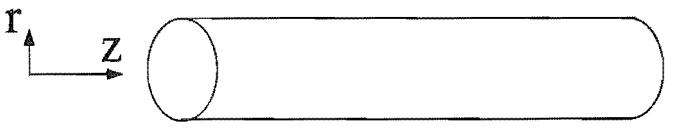

Figure 7.1: Model geometry.

The mass transport, of a volume concentration of a hormone $c(z, r, t)$ down the pipe, is described by the transport equation (one-way wave equation),

$$\frac{\partial c}{\partial t} + v(r)\frac{\partial c}{\partial z} = 0, \quad z \in [0, \infty), \quad r \in [0, R], \quad t > 0, \tag{7.2.2}$$

where the advection velocity distribution is prescribed by (7.2.1). This equation is a Cauchy initial value problem with the specification of the boundary value $c(0, r, t)$, which is assumed to be independent of r, i.e., it is assumed that the concentration is uniformly distributed across the cross-section of the pipe at $z = 0$. Because of this assumed radial independence we write $c(0, r, t) \equiv c_0(t)$. This assumption is essential for the development of the method presented in this chapter.

When the concentration level in the pipe is initially zero, $c(z, r, t)|_{t=0} = 0$, then elementary integration of equation (7.2.2) shows that

$$c(z, r, t) = c_0\left(t - \frac{z}{v(r)}\right)\mathrm{H}\left(t - \frac{z}{v(r)}\right), \quad z \in [0, \infty), \quad r \in [0, R], \quad t > 0, \tag{7.2.3}$$

[1]For a saline solution typically used in perifusion experiments the Reynolds number is of order 1.

where H denotes the Heaviside step function. If it is possible to measure this concentration, $c(\ell, r_1, t)$, at a fixed station, say $z = \ell$ and $0 \leq r_1 < R$, downstream of the injection point, then estimation of the injection temporal profile, $c_0(t)$, is a straightforward well-posed problem; see Wall and Lundstedt (1998) for discussion of such hyperbolic inverse problems. However, generally the concentration, at the station $z = \ell$, must be assayed over the whole pipe. The simplest inverse problem will then require the measurement of an average concentration, $Q(t)$, across the cross-section of the pipe. Simple analysis of the geometry and (7.2.3) then shows that

$$Q(t) = \frac{2}{R^2} \int_0^R c_0\left(t - \frac{\ell}{v(r)}\right) H\left(t - \frac{\ell}{v(r)}\right) r \, dr. \tag{7.2.4}$$

This is the case studied in Section 2 of Taylor (1953). It is readily appreciated that the operator defined in this equation is a smoothing operator. The exact nature of which is easily seen on application of the transformation $s = t - \frac{\ell}{v(r)}$ to the integral in (7.2.4), so yielding

$$Q(t) = \frac{\ell}{v_m} \int_0^{t - \frac{\ell}{v_m}} \frac{c_0(s)}{(t-s)^2} \, ds.$$

This equation can be further reduced to the more standard form

$$Q(t + a) = \int_0^t k(t - s) c_0(s) \, ds, \tag{7.2.5}$$

where the kernel has the functional form

$$k(t) = \frac{a}{(t + a)^2}, \quad \text{with} \quad a = \frac{\ell}{v_m} > 0.$$

The parameter a represents the time that the fluid travelling with the maximum speed v_m takes to reach the station at $z = \ell$.

7.2.2 Inverse problem

It is now straightforward to examine the stability of the inverse problem of estimation of the function c_0, from knowledge of Q. It should firstly be observed that (7.2.5) is a Volterra equation of the first kind, with a regular kernel, which is a well known ill-posed problem (Linz, 1985), (p 161 *et seq.*). To understand the degree of ill-posedness it is convenient to perform a Fourier analysis of (7.2.5). To this end, we extend the data function $Q(t)$, and the kernel function $k(t)$, by zero for $t < 0$, and consider their Fourier transforms. The Fourier transform of the kernel is pivotal in our argument; it is

$$\widehat{k}(\xi) = \frac{a}{\sqrt{2\pi}} \int_{-\infty}^{\infty} \frac{\mathrm{H}(t) \exp(-i\xi t)}{(t + a)^2} \, dt,$$

and on integrating by parts, this transform is converted to

$$\widehat{k}(\xi) = \frac{a}{\sqrt{2\pi}} \left[\frac{1}{i\xi a^2} - \frac{2}{i\xi} \int_{-\infty}^{\infty} \frac{\mathrm{H}(t) \exp(-i\xi t)}{(t + a)^3} \, dt \right].$$

By continuing this procedure, an asymptotic series in reciprocal powers of ξ is obtained, as

$$\widehat{k}(\xi) = \frac{1}{\sqrt{2\pi}}\left(\frac{1}{(i\xi a)} - \frac{2}{(i\xi a)^2}\right) + \mathcal{O}\big((i\xi a)^{-3}\big).$$

It should be noted that the dominant term in the asymptotic expansion of $\widehat{k}(\xi)$, as $|\xi| \to \infty$, is $1/(ia\sqrt{2\pi}\xi)$. Therefore from (7.2.5), using the convolution theorem, it follows that Q is not just a function in $L^2(\mathbb{R})$, but its high frequency behaviour is such that $\|\widehat{Q}\|_2$ decreases faster than $|\xi^{-1}|$, as $|\xi| \to \infty$, because by Parseval's theorem $c_0 \in L^2 \iff \widehat{c_0} \in L^2$. It is readily observed that for a general noise function, $n(t) \in L^2(\mathbb{R})$, assumed to be additive to $Q(t)$, there is no reason to believe that the high-frequency components of $\widehat{n}(\xi)$ will be subject to such rapidly decreasing behaviour, and it therefore follows that there is no guarantee that the product $\xi\widehat{n}(\xi)$ will be in $L^2(\mathbb{R})$. This illustrates that the deconvolution problem associated with the solution of the inverse signal reconstruction is ill-posed. It also follows from the above asymptotic analysis that the inverse problem is *equivalent* to differentiation, and it is therefore necessary to restore continuity with respect to the data in order to successfully solve the problem.

An alternative approach to directly solving (7.2.5) is to differentiate this equation, so leading to

$$Q'(t+a) = \frac{1}{a}c_0(t) + \int_0^t \widetilde{k}(t-s)c_0(s)\,ds, \tag{7.2.6}$$

where the kernel of this Volterra equation of the second kind is, $\widetilde{k}(t-s) \equiv k'(t-s) = -2a/(t-s+a)^3$, and the prime denotes differentiation with respect to the function argument. This equation re-enforces the idea that the inversion of the integral equation (7.2.5) has numerical conditioning equivalent to differentiation. If we denote the function space of n-th order continuously differentiable functions by C^n, and note that as the kernel $\widetilde{k}$ is in $C[0,T]$, the integral operator in equation (7.2.6) is of compact Volterra type, mapping $C[0,T]$ into itself, and similarly for the operator in (7.2.5). Given that Q, on the left-hand-side of equation (7.2.6), is assumed to be in C^1, then there exists a unique solution $c_0 \in C[0,T]$ of the integral equation (7.2.6) (Linz, 1985), (p 30 *et seq.*). Equation (7.2.6) is the basis of the deconvolution method to solve the inverse problem of estimation of c_0 from the measurement of Q.

Equation (7.2.6) defines the operator mapping the concentration signal $c_0(t)$ to the measured average flow $Q(t)$, i.e., $\mathbb{T} : c_0(t) \mapsto Q(t)$. It is the inverse of this map that defines the mathematical properties of the inverse problem, i.e., $\mathbb{T}^{-1}Q \mapsto c_0$. As the differentiation operator is unbounded on the function space C, and as further explained in Section 7.3 that is the space we must work, it follows that this operator is unbounded. Similar reasoning shows that this operator is unbounded on L^2. The regularisation of the inverse operator $\mathbb{T}^{-1}$ is the subject of the next section.

7.3 Regularisation of the deconvolution problem

The inverse problem of source concentration reconstruction presented in Section 7.2.2 is considered here. This inverse problem is always ill-posed for realistic measurement data. This is because data that is measured, can generally only be placed in the function space L^2, or at most C, and in these function spaces differentiation operators are unbounded. As shown in Section 7.2.2, the inverse operator mapping the measurement to the solution involves differentiation. It is therefore central to our treatment to show that numerical differentiation can be made a well-posed problem. That this can be done is well known, and there are a number of regularisation techniques available. We shall choose the method of mollification in this chapter, and we follow the treatment of Murio (Murio, 1993). Other regularisation techniques such as Tikhonov regularisation (Tikhonov, 1963) yield similar results (not shown).

The problem is to get a regularised approximation to the derivative of f when given a modified function f_m; where due to measurement difficulties the true function f, has been corrupted by a noise function n, so that $f_m(x) = f(x) + n(x), \quad x \in I$. The functions f, and n, are defined on the interval $I = [0, T]$, for a given value of $T > 0$.

Consider the mollification, or Gaussian function

$$\rho_\delta = \frac{1}{\delta\sqrt{\pi}} e^{-x^2/\delta^2}, \quad x \in \mathbb{R}$$

The important properties of this function are:

1. $\rho_\delta \in C^\infty$ and is *nearly* compact, as it is *almost* zero outside $|x| < 3\delta$.
2. $\int_{\mathbb{R}} \rho_\delta(x)\, dx = 1$, whereas $\int_{-3\delta}^{3\delta} \rho_\delta(x)\, dx \cong 0.997$.

To proceed, extend the data f_m to the interval $I_\delta = [-3\delta, 3\delta + T]$ by

$$f_m(x) = f_m(0) \exp\left[x^2/[x^2 - (3\delta)^2]\right], \quad -3\delta \le x < 0,$$
$$f_m(x) = f_m(T) \exp\left[(x-T)^2/[(x-T)^2 - (3\delta)^2]\right], \quad T < x \le T + 3\delta,$$

and then define the mollifier of f by

$$\begin{aligned} J_\delta f(x) = (\rho_\delta * f)(x) &= \int_{-\infty}^{\infty} \rho_\delta(x - s) f(s)\, ds, \\ &\cong \int_{x-3\delta}^{x+3\delta} \rho_\delta(x - s) f(s)\, ds, \end{aligned} \tag{7.3.1}$$

where $\delta > 0$ is the radius of mollification. We define the norm $\|f(t)\|_\infty = \sup_{t \in I} |f(t)|$, then the following results are central to the stability proof.

Lemma: Murio's Consistency . If $\|f''\|_\infty \le M_2$ then

$$\|(J_\delta f)' - f'\|_\infty \le 3\delta M_2.$$

This consistency result shows that as $\delta \to 0$, then $\left(J_\delta f\right)' \to f'$.

Lemma: Murio's Stability. With $f_m \in C(I_\delta)$

$$\|\left(J_\delta f\right)' - \left(J_\delta f_m\right)'\|_\infty \leq \frac{2}{\delta\sqrt{\pi}}\|f_m - f\|_\infty.$$

Therefore the mollification method provides the differentiation operator with a Lipschitz continuity result, when the data $f_m \in C$, provided $\delta > 0$ is fixed. Furthermore as $\|f_m - f\| \to 0$, δ can be reduced, and the consistency error is then decreased, provided $f \in C^2$.

We now define the regularised inverse source problem. First mollify the measurement data that is specified in Section 7.2.2, by forming $J_\delta Q(t)$, and then solve the inverse source problem with this regularised measurement data, through (7.2.6).

Theorem 7.3.1. *The signal reconstruction problem, as stated in Section 7.2.2, with mollified measurement data $J_\delta Q$ has a well posed solution, provided that $Q_m \in C[0,T]$.*

Proof. We denote the measured function value that has not been corrupted by noise, by Q, and the modified value due to the noise by Q_m; the actual measurement.

We first must bound the appropriate Volterra operators, before using the stability results from the beginning of this section for the differentiation operator. Consider firstly the equation

$$(\lambda\mathbb{I} - \mathbb{K})v = f, \tag{7.3.2}$$

where $\mathbb{K}$ is a linear compact Volterra integral operator in the function space of continuous functions defined on the interval $[0,T]$, and secondly the perturbed mapping equation

$$(\lambda\mathbb{I} - \mathbb{K})w = f + \Delta f.$$

In these equations f and Δf are continuous functions defined on the interval $[0,T]$, and it is assumed that the operator $\mathbb{K}$ has a continuous kernel $\widetilde{k}$, as given in (7.2.6). Then standard theory (see for example (Linz, 1985), (p 45 *et seq.*)), shows that if there exists two constants $K$and Δ, such that $|\widetilde{k}| < K$, $|\Delta f| < \Delta$, and if λ is a constant, then

$$|v(t) - w(t)| \leq \frac{\Delta}{\lambda}\exp(Kt/\lambda), \qquad t \in [0,T]$$

where for (7.2.6), $K = 2/a^2$, and $\lambda = 1/a$. It follows, with $\mathbb{T}^{-1}$ defined as $\mathbb{T}^{-1}f = (\lambda\mathbb{I} - \mathbb{K})^{-1}f$, together with mollification of the measurement function, Q_m, and by Murio's stability lemma, we have the Lipschitz continuity result

$$\|\mathbb{T}^{-1}\left(J_\delta Q\right)' - \mathbb{T}^{-1}\left(J_\delta Q_m\right)'\|_\infty \leq \frac{2\exp(KT/\lambda)}{\lambda\delta\sqrt{\pi}}\|Q_m - Q\|_\infty.$$

□

Consistency of the mollified problem solution to the exact c_0 can be shown from Murio's consistency lemma, provided that $Q(t) \in C^2[0,T]$. Examination of (7.2.5) shows, with the assumption that $c_0 \in C^1[0,T]$ and because of the smooth kernel, k, that $Q \in C^2[0,T]$.

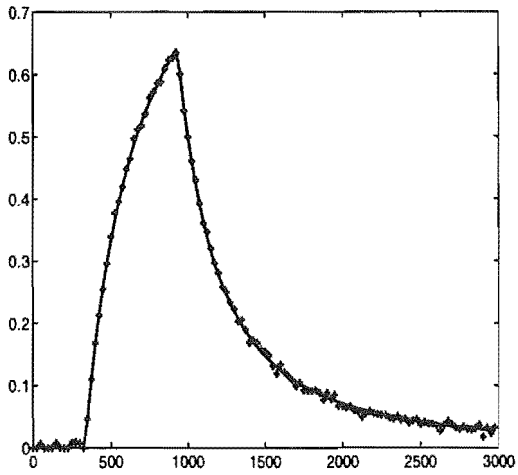

(a) The simulated measured time signal, Q, with no noise present (—), and with 2.5% noise present, $Q_m = Q + n$, as indicated by + +.

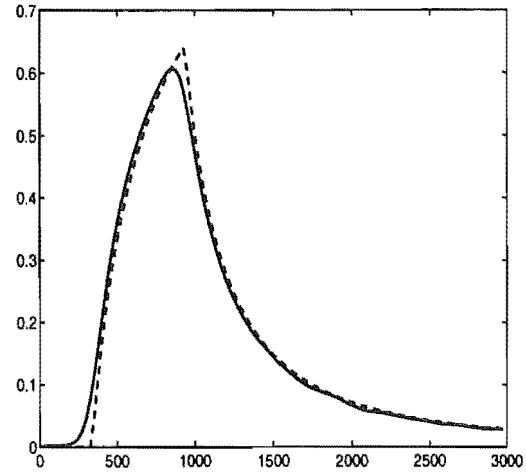

(b) The simulated measured time signal, Q, with no noise present (– – –), and the mollified time signal, $J(Q_m)$ (—) with 2.5% mollification when 2.5% noise is present on Q_m.

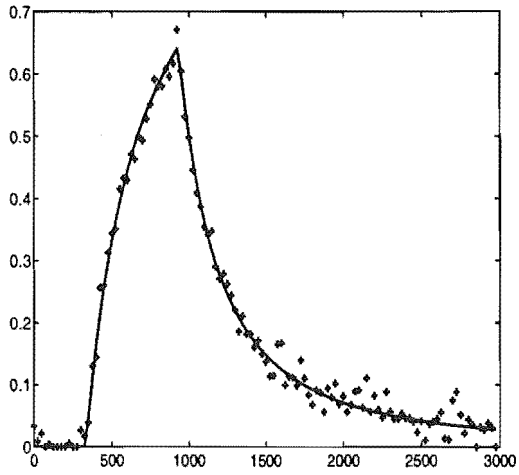

(c) The simulated measured time signal, Q, with no noise present (—), and with 5% noise present, $Q_m = Q + n$, as indicated by + +.

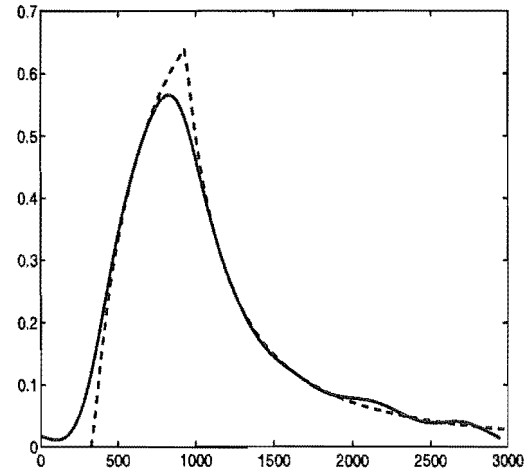

(d) The simulated measured time signal, Q, with no noise present (– – –), and the mollified time signal, $J(Q_m)$ (—) with 5% mollification when 5% noise is present on Q_m.

Figure 7.2: The measured temporal signal $Q(t)$, the noisy signal $Q_m(t)$, and the mollified signal $J(Q_m)(t)$.

7.4 Numerical method and results

In the results presented in this section the various parameters are taken from the perifusion experimental setup associated with ACTH [2] measurements (Evans et al., 1993b; Evans et al.,

[2] *Adrenocorticotropic hormone* (ACTH) is the major hormone released from the corticotroph cells in the pituitary gland in response to stimulation, and is often the hormone concentration measured in perifusion experiments.

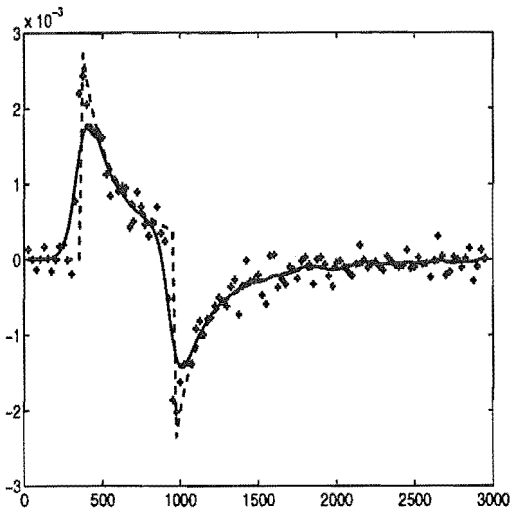

(a) The derivative of the measured time signal, $Q'(t)$, with no noise present (– – –), the mollified derivative $(J(Q_m))'(t)$ with 2.5% mollification (—), and the direct derivative $Q'_m(t)$, indicated by + +. The noise level in Q_m is 2.5%.

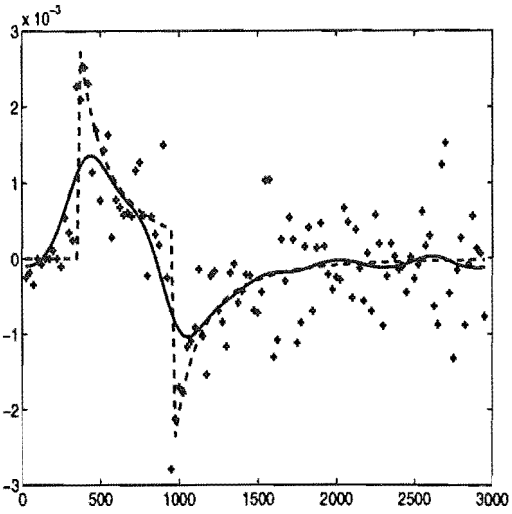

(b) The derivative of the measured time signal, $Q'(t)$, with no noise present (– – –), the mollified derivative $(J(Q_m))'(t)$ with 5% mollification (—), and the direct derivative $Q'_m(t)$, indicated by + +. The noise level in Q_m is 5%.

Figure 7.3: Estimation of the derivative $Q'(t)$ for noise levels of 2.5% and 5%.

1993a), and they are: $v_m = 6 \times 10^{-3}$ ms^{-1}, $\ell = 2$ m, $R = 0.5 \times 10^{-3}$ m, so that $a = 1/3 \times 10^3$ s. The measured time signal $Q(t)$ for $0 \leq t \leq T$, with $T = 3000$ s, is assumed to be the known function in the inverse problem. An important property of the problem is the finite speed of mass transport, so that $Q'(t) = 0$, when $t < a$. It is therefore assumed that $Q(t) = 0$ for $t < a$, implying that $c_0(t) = 0$ for $t < 0$.

We now describe the numerical algorithm used to solve the inverse problem. Define the natural numbers $i, j, M, N \in \mathbb{N}$, and then a mesh $\{t_i\}_{i=0}^N$, with uniform mesh interval $h = T/N$, and $t_0 = 0$, $t_i = t_{i-1} + h$, $1 \leq i \leq N$, is established on the time axis. The signal function $c_0(t)$ is now approximated by a B-spline of degree n, denoted by $\mathcal{S}_n$, such that

$$c_0(t) = \sum_{i=0}^{M} \alpha_i b_i(t), \tag{7.4.1}$$

where $M + 1$ is the cardinality of the B-spline basis, $\{b_i(t)\}_{i=0}^M \in \mathcal{S}_n[0, T]$. Collocation of the equation (7.2.6) then provides the finite dimensional equation

$$\frac{\alpha_j}{a} + \sum_{i=0}^{M} \alpha_i \int_0^{t_j} \widetilde{k}(t_j - s) b_i(s)\, ds = Q'(t_j + a), \quad j \in [0, N] \tag{7.4.2}$$

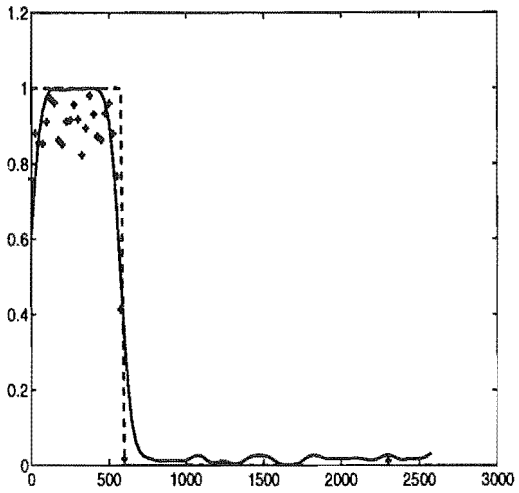

(a) The reconstructed time signal, $c_0(t)$. The mollified reconstructed c_0 (—), with 2.5% mollification, the directly reconstructed c_0 (++), and the exact c_0 (− − −). Both the former two reconstructions are from Q_m with 2.5% noise present.

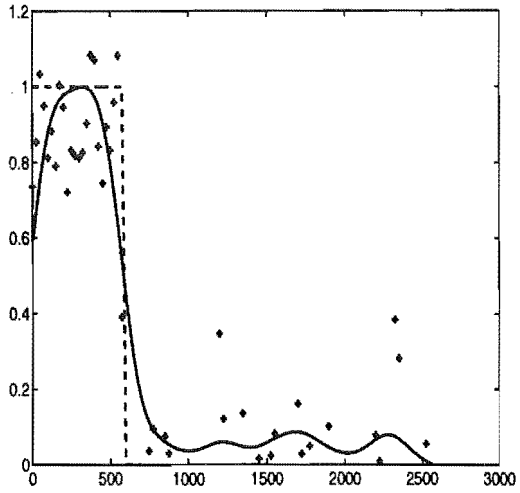

(b) The reconstructed time signal, $c_0(t)$. The mollified reconstructed c_0 (—), with 5% mollification, the directly reconstructed c_0 (++), and the exact c_0 (− − −). Both the former two reconstructions are from Q_m with 5% noise present.

Figure 7.4: Reconstruction of the temporal boundary concentration c_0.

The properties of the B-splines and their support implies that the matrix defined by this equation will be lower triangular. For a concrete implementation of the algorithm, the integral is approximated by the trapezoidal rule, and n is chosen to be one; so that the B-spline basis functions are the piecewise linear, or *roof* functions.

Now denote $Q'(t_i + a)$, $\widetilde{k}(t_i)$ and $(J(Q))'(t_i)$ by Q'_i, $\widetilde{k}_i$, and $(J(Q))'_i$ respectively. Note for notational simplicity the subscript δ has been suppressed from the mollification operator J. Then (7.4.2) can be solved for the unknown coefficients $\{\alpha_i\}_{i=0}^N$, so yielding

$$\begin{aligned} \alpha_0 &= aQ'_0, \\ \alpha_j &= \left(Q'_j - h{\sum_{i=1}^{j}}' \widetilde{k}_i \alpha_{j-i}\right) \Big/ \left(\frac{1}{a} + \frac{h}{2}\widetilde{k}_0\right), \quad 1 \le j \le N, \end{aligned} \tag{7.4.3}$$

where the prime on the summation sign is to signify that the last value in the summation is to be halved.

All that remains to ensure that the algorithm is well-posed, is to evaluate the coefficients $\{Q'_i\}_{i=0}^N$ as the mollified derivative values, $\{(J_\delta Q)'_i\}_{i=0}^N$, as described in Section 7.3, but with the standard numerical central differences formula used to estimate the numerical derivative.

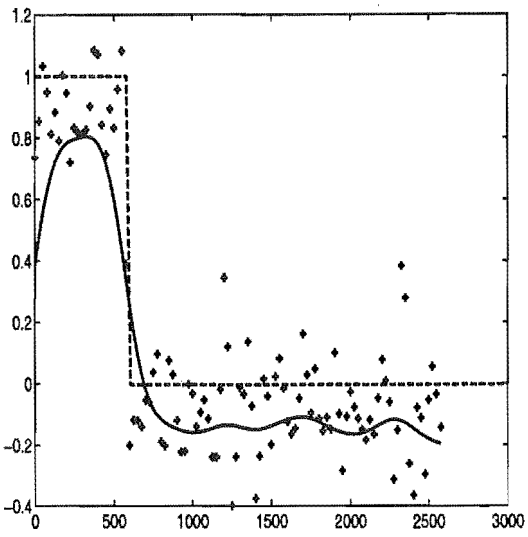

(a) The reconstructed time signal, $c_0(t)$. The mollified reconstructed c_0 (—), with 5% mollification but without the positivity adjustment, the directly reconstructed c_0 (++), and the exact c_0 (− − −). Both the former two reconstructions are from Q_m with 5% noise present.

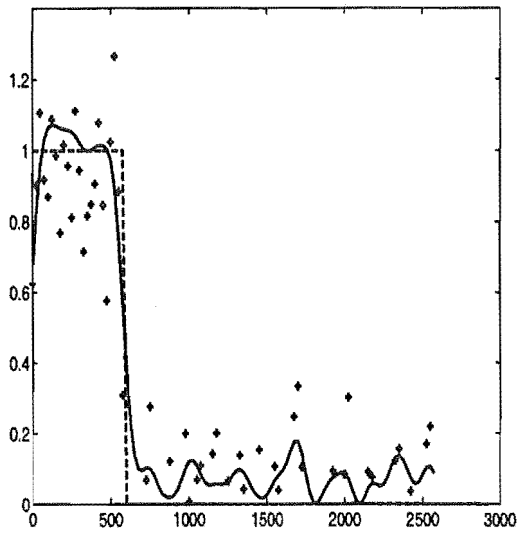

(b) The reconstructed time signal, $c_0(t)$. The mollified reconstructed c_0 (—), with 2.5% mollification, the directly reconstructed c_0 (++), and the exact c_0 (− − −). Both the former two reconstructions are from Q_m with 5% noise present.

Figure 7.5: Reconstruction of the temporal boundary concentration c_0.

7.4.1 Numerical results

The measurement data utilised in this section was simulated through the use of equation (7.2.5). The calculated data Q, were corrupted with white noise having a normal distribution and zero mean, so that the averaged concentration, $Q_m = Q + n$, was used in the measured simulation. The quoted value of the noise level, in the results, is a relative measure of the standard deviation of the noise to $\|Q\|_2$, where $\|\cdot\|_2$ denotes the ℓ_2 sequence space norm. In a practical experiment it is not possible to measure a negative concentration, so when Q_m was found to be negative in the simulation, it was replaced by a zero value.

In Figure 7.2 the computer simulation of averaged concentrations at $z = \ell$ is illustrated for various noise levels. The boundary value, of the concentration at $z = 0$, was chosen as representative of the initial hormone input into the pipe, namely the pulse function

$$c_0(t) = \mathrm{H}(t) - \mathrm{H}(t - L), \quad 0 \leq t \leq T, \tag{7.4.4}$$

where $L = 600$ s, and this is the boundary value used throughout this chapter. This figure shows how the mollification of the noisy signal provides an acceptable smoothing on the noisy data, and

provides a good approximation to the main features of the clean signal. The time signal $Q(t)$ can be found analytically from (7.2.5), when the concentration at $z = 0$ is given by (7.4.4). In all simulated results presented in this chapter $T = 3000$ s and $N = 120$, so that $h = 25$.

The amount of mollification utilised in the numerical reconstructions is stated as a relative percentage of δ/T, with T denoting the maximum time for which the data is collected. Another way of quoting this is to express the δ size in seconds. The value of the mollification parameter δ, was generally chosen to be approximately the same relative percentage of T as the relative percentage noise level. More sophisticated methods of optimising δ can be found in Murio (1993). However experience indicates that the choice of δ is not *too* critical provided $\delta > h$. Relative percentage values of mollification of 2.5% and 5%, correspond to δ values of 75 and 150, respectively, in this chapter.

Figure 7.3 shows the directly estimated, the mollified, and accurate derivatives of the function $Q'(t)$; these are used in equation (7.2.6) of the algorithm. It is seen from these figures, that for low noise levels direct differentiation of the data $Q'_m(t)$ provides an acceptable estimate of the true derivative. This is not true for the higher noise level illustrated, and in this case the mollification technique described in Section 7.3 is essential. The mollified derivative is utilised in the deconvolution algorithm (7.4.3). It is to be observed, by comparison of this figure with Figure 7.2, the noise amplification introduced by the differentiation operator.

In Figure 7.4 the concentration signals $c_0(t)$ which have been reconstructed from two Q_m signals, with respective noise levels of 2.5% and 5%, are illustrated. It is again observed, for low noise levels, the direct reconstruction (without mollification) provides an acceptable estimate. However, for the higher noise level this is no longer true, and the mollification algorithm is essential. In these results the *best* values for δ have been taken, as previously explained; smaller values for δ produce more oscillations as can be seen from comparison of Figures 7.4(b) and 7.5(b), which have δ values of 150 and 75, respectively. The larger values of δ resulting in more smoothing.

It is possible to extend the results in Section 7.3, and find optimum values for δ, given the noise level $\|Q_m - Q\|_\infty \leq \epsilon$. However, for the problem this chapter addresses, the measurement actually made is $\int_{t_1}^{t_2} Q(t)\,dt$ for a sequence of values of t_1 and t_2, but with uniform spacing, i.e., $t_2 - t_1 = \Delta t$. It follows that there is little point in choosing $\delta < \Delta t$. The problem where $Q(t)$ is averaged over a sequence of uniformly spaced time periods, say Δt, is not discussed here.

In Figures 7.4 and 7.5(b), for the mollified reconstruction presented, it is seen that the reconstructed c_0 is positive; this is an obvious physical requirement, and this requirement has been added to the algorithm. Observe Figure 7.5(a) which shows the same result as Figure 7.4(b), but without this constraint; the concentration becomes negative. It is difficult to add such constraints as positivity to the mollification algorithm without resulting in a nonlinear problem.

In order to include positivity in the algorithm therefore, we employ a simple artifice. From the solution of (7.4.3) we find $l_b = \min_i \alpha_i$, and use as a solution to the deconvolution problem, the modified $\overline{\alpha_i}$ values

$$\overline{\alpha_i} = \begin{cases} \alpha_i, & l_b > 0, \\ \alpha_i - l_b, & l_b < 0, \end{cases} \quad i \in \{0, N\}.$$

These $\{\overline{\alpha_i}\}_{i=0}^{N}$ are used in the mollified results shown in Figures 7.4 and 7.5(b). In Figures 7.4 and 7.5(b) no negative concentrations are shown. However, for the un-mollified noisy data, negative values are obtained as shown in Figure 7.5(a), but they have been suppressed in the other figures.

7.5 Conclusions

It has been shown that mollification leads to acceptable solutions to the concentration deconvolution problem. The method proposed is sequential, and computationally efficient, involving only the solution of a triangular system of linear algebraic equations. The deconvolution procedure advocated leads to improved interpretation of experimental data in perifusion experiments, and we discuss this data enhancement in Chapter 10.

The Newtonian fluid model used in this chapter is appropriate for the *in vitro* experiment described in this chapter. However, for *in vivo* experiments (Alexander et al., 1988) blood is the transporting medium, and for the pipe diameters utilised in these experiments blood does not behave in a Newtonian manner. More appropriate fluid velocity profiles for this case will be discussed in Chapter 9.

As discussed in Section 7.1, the Taylor theory would enable an apparent diffusion coefficient to be used to model both the shear and cross-diffusion dispersion effects as a one-dimensional advection-diffusion problem. For the appropriate inverse problem, invariant imbedding techniques similar to those used in (Wall, 1997) can be used to solve this *side-ways heat* problem (see Chapter 11). However, it should be pointed out that the experimental setup, for some of the perifusion apparatus used, seems to be on the borderline of applicability of pure shear dispersion theory, as presented in this chapter, and the Taylor theory. These ideas will be examined in Chapters 9 and 10.

Chapter 8

Fluid velocity profile reconstruction for non-Newtonian shear dispersive flow

8.1 Introduction

In this chapter we consider an inverse problem associated with the mass transport of a material concentration down a pipe, where the flowing non-Newtonian medium has a two-dimensional velocity profile. An inverse problem associated with shear dispersive flow in Newtonian media was investigated in Chapter 7, and in this chapter more general inverse problems for certain non-Newtonian fluids are considered. For viscous flow problems, the variation in fluid velocity over the cross section of the pipe leads to shear dispersion of the solute concentration. Molecular diffusion of the solute may also significantly contribute to the dispersive transport of the solute, however in this chapter shear dispersion is assumed to be the dominant dispersive effect.

The approach examined in this chapter is to use the shear dispersive properties of the concentration of a material tracer down a pipe to deduce the underlying velocity profile of the medium. An early problem of this nature involved estimating the average flow velocity in water mains by injecting salt into the main and measuring the electrical conductivity of the water at some fixed location downstream of the injection point (Allen and Taylor, 1923).

The problem considered is that of determining the fluid velocity profile over the cross section of the pipe from temporally varying cross-sectional average concentration measurements at upstream and downstream locations. The determination of the two-dimensional fluid velocity profile is in general a difficult nonlinear ill-posed inverse problem. However assuming a strictly decreasing velocity profile and a specified continuous upstream concentration with a time zero step, then the

problem becomes well-posed. It is assumed that no tracer is input before the time zero step which is required in the input concentration or one of its derivatives.

The problems considered in this chapter are applicable to the perifusion apparatus, an *in vitro* experimental apparatus used in endocrinology investigations (McIntosh and McIntosh, 1983; McIntosh et al., 1984), and pituitary effluent sampling experiments associated with blood flow in pipes (Alexander et al., 1988). In these experimental systems the observed temporal architecture of the cellular responses to various stimuli is significantly altered by the measurement process. The inverse problem considered in this chapter allows the underlying cellular responses to be unmasked.

In Section 8.2 the type of non-Newtonian fluid is specified. In Section 8.3 the equations modeling the flow of a tracer concentration down a tube are given, and the mathematical operator mapping the temporally varying cross-sectional average concentration measurements at upstream and downstream locations is specified. In Section 8.4 it is shown that the inverse of this operator is unbounded on the Hilbert space of square integrable functions, L^2, and that the inverse problem is ill-posed. The special case of known input concentration with a time zero step and a decreasing velocity profile is also examined and is shown to be a well-posed problem. A related problem of finding the relationship between the rate of shear and the shear stress is shown to be ill-posed. In Section 8.5 the mollification method is used to regularise the ill-posed inverse problem and the stability of the regularisation is analysed. In Section 8.6 a simple numerical algorithm is constructed, and it is verified by numerical experiment that stable approximations to the velocity profile can be obtained in the presence of moderate amounts of data noise. In Section 8.7 this numerical algorithm is tested on data including small amounts of molecular diffusion.

8.2 Consideration of non-Newtonian Flow

In Chapter 7, the fluid was assumed to be Newtonian, and therefore the fluid velocity profile in the pipe was governed by Poiseuille's equation (Landau and Lifshitz, 1959), (p 57 *et seq.*). It is natural to consider associated problems for non-Newtonian fluid flow. The motivation for this generalisation arose from investigating blood flow in endocrinology experiments (Alexander et al., 1988), which is known to behave in a non-Newtonian manner (McDonald, 1974).

Suppose that the velocity profile of a viscous, incompressible fluid flowing through a rigid pipe of circular cross section, with a no-slip boundary condition is given by $v(r)$, where r is the circular polar radial coordinate associated with the cylindrical coordinate system so that the z-axis is aligned with the axis of the tube. The radius of the pipe is R, and the maximum flow velocity is v_m. The fluid is assumed to have a suitably low Reynolds number [1], so that the flow

[1] For the saline solution used in perifusion experiments the Reynolds number less than 10.

is laminar. The dispersion of matter with high Reynolds number can be analysed by considering a virtual coefficient of diffusion (Taylor, 1954b). The pipe cross-sectional geometry is assumed to be circular. The theory is applicable to more general pipe geometries (Berker, 1963), however this aspect is not pursued here.

Many fluids display a marked shear-dependent viscosity. Solutions such as blood have a reduced viscosity when the shear rate is large and are termed pseudoplastic. Conversely some fluids such as concentrated solutions of sugar in water exhibit an increase in viscosity with the rate of shear and are termed dilatant. Materials requiring a finite yield stress before flow can commence are called plastic and are not considered here. For steady fully developed flow in a circular pipe, the rate of shear is assumed to be a function of the shear stress (τ) only, that is

$$\frac{dv}{dr} = f(\tau) \tag{8.2.1}$$

where r is the distance from the centre of the pipe. Equation (8.2.1) is termed the velocity gradient or the rate of shear. This assumption excludes rheopectic, thixotropic and viscoelastic materials. For developed flow, the relation between the shear stress in the fluid (τ) and the radial position (r) is

$$\tau = \tau_0 \frac{r}{R} \tag{8.2.2}$$

where τ_0 is the mean stress on the fluid at the pipe boundary (Massey, 1991), (p 150 *et seq.*). The functional form of $f(\tau)$ and $v(r)$ for the different types of non-Newtonian fluids is indicated schematically in Figure 8.1. It follows that there is less shear dispersion for pseudoplastic fluids than for dilatant fluids.

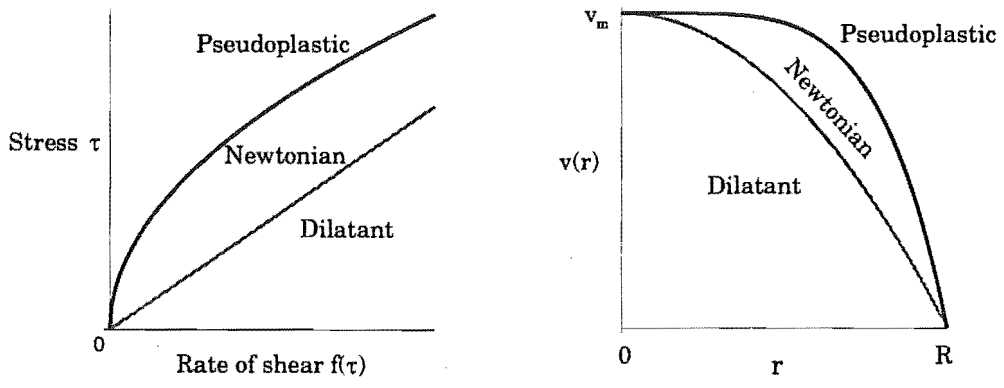

Figure 8.1: The functional form of the rate of shear, $f(\tau)$, and the fluid velocity profile, $v(r)$, for the different types of non-Newtonian fluids.

8.3 The mass transport equations

The mass transport of the concentration of a tracer, $c(z,r,t)$, down the pipe is described by the simple transport equation

$$\frac{\partial c}{\partial t} + v(r)\frac{\partial c}{\partial z} = 0 \quad z \in [0,\infty) \quad r \in [0,R] \quad t > 0, \tag{8.3.1}$$

where $v(r)$ is the fluid velocity profile. Because the injection of the tracer into the pipe at $z = 0$ is assumed to be independent of r, the boundary condition takes the simple form $c(0,r,t) = c_0(t)$. Assuming the initial concentration in the pipe is zero, i.e., $c(z,r,0) = 0$, then the solution of (8.3.1) is given by (7.2.3). If radial dependence in the downstream concentration is available, then reconstruction of the velocity profile is a simple well-posed problem (Wall and Lundstedt, 1999). However in applications radial concentration measurements are unavailable, and the concentration measurement at the station $z = \ell$ is assayed over the whole pipe. Simple analysis then shows that the cross-sectional average concentration at a fixed station $z = \ell$ is given by (7.2.4). The nature of the smoothing operator defined in (7.2.4) is dependent on the functional form of $v(r)$. A reasonable physical assumption is to assume that the velocity profile is a strictly decreasing function of the radial distance from the centre of the pipe, i.e., $v'(r) < 0$. With this assumption the maximum fluid velocity is at the centre of the pipe and is denoted by v_m. The nature of the smoothing operator can then be seen after the transformation $s = t - \frac{\ell}{v(r)}$ to the integral in equation (7.2.4), so yielding

$$Q(t+a) = \int_0^t k(t-s)c_0(s)\,ds \quad t > 0 \tag{8.3.2}$$

where the kernel has the functional form

$$k(t) = \frac{-2\ell}{R^2} \cdot \frac{v^{-1}\left(\frac{\ell}{t+a}\right)\left(v^{-1}\left(\frac{\ell}{t+a}\right)\right)'}{(t+a)^2} \quad \text{with} \quad a = \frac{\ell}{v_m} > 0. \tag{8.3.3}$$

The parameter a represents the time for fluid travelling at speed v_m to reach the station at $z = \ell$, and use has been made of the identity $r = v^{-1}\left(\ell/(t+a)\right)$. It is important to note that the strict monotonicity of the flow is used in rewriting (7.2.4) in the form (8.3.2).

The lower limit of integration in equation (8.3.2) would be $-\infty$ if the assumption that the tracer is injected into the pipe at $t = 0$ is relaxed. This change makes equation (8.3.2) a singular integral equation, altering the character of the problem. If the upstream and downstream concentrations are measured over finite intervals, then since the concentration in the pipe may be nonzero, the downstream measurement may be contaminated with an unknown concentration. Thus the determination of the velocity profile becomes more difficult.

8.4 Velocity profile determination

The problem of determining fluid velocity profiles has generated a large number of different experimental procedures (Streeter, 1968), (chapter 8). Methods used to measure the flow properties can be characterised as invasive or non-invasive, depending on whether the flow properties are disturbed by the measurement process. The techniques employed utilise the electrical, optical, chemical, thermal and kinetic properties of the medium. The approach considered in this chapter is to use the shear dispersive properties of the concentration of a material tracer down a pipe to deduce the underlying velocity profile of the medium.

Consider the problem of determining the fluid velocity profile over the cross section of the pipe from temporally varying cross-sectional average concentration measurements at upstream and downstream locations. In terms of equation (7.2.4) if we measure c_0 and Q, can we determine v. This inverse problem is a nonlinear Fredholm integral equation of the first kind, and is in general highly ill-posed. The ill-posedness of the problem is strongly dependent on the functional form of c_0. However, if we make the assumption that the velocity profile is a strictly decreasing function of the radial distance from the centre of the pipe, then we can use equation (8.3.2) to determine $v(r)$. Observe that equation (8.3.2) is a linear Volterra integral equation of the first kind, which are well known ill-posed problems (Linz, 1985). However, we are really more interested in finding the velocity profile, $v(r)$, than the function $k(t)$. Therefore on integrating equation (8.3.2) by parts we obtain the Volterra integral equation of the second kind

$$Q(t+a) = K(t)c_0(0) + \int_0^t c_0'(t-s)K(s)\,ds \tag{8.4.1}$$

where $K(t) = \int k(t)\,dt$ satisfies

$$K(t) = \frac{1}{R^2} \cdot \left(v^{-1}\left(\frac{\ell}{t+a}\right)\right)^2 \tag{8.4.2}$$

with $K(0) = 0$. Because the variable of interest is $K(t)$, the derivative of the downstream cross-sectional average concentration does not appear in equation (8.4.1). It follows from equation (8.4.2) and the assumption $v'(r) < 0$, that $K(t)$ is a strictly increasing function such that $\lim_{t\to\infty} K(t) = 1$.

Volterra equations of the second kind are known to be well-posed problems (Linz, 1985), (p 45 *et seq.*). To avoid the degenerate case of equation (8.4.1) reducing to a Volterra equation of the first kind we shall assume that $c_0(0) \neq 0$. With $c_0(0)$ vanishing the conditioning of the Volterra equation of the first kind will be directly related to the smoothness properties of the input function c_0. However the experimentalist can adjust the input concentration to improve the conditioning of the velocity profile reconstruction. It is obvious from equation (8.4.1) that the best conditioning is achieved with a c_0 having discontinuities, generating wavefronts of concentration travelling down the pipe. This enables a "layer stripping" type solution to the velocity reconstruction problem.

A unique continuous solution $K(t)$ to equation (8.4.1) exists if Q and c_0' lie in the space of continuous functions, $C[0,\infty]$ (Linz, 1985), (p 30 *et seq.*). The velocity profile can then be determined from

$$v^{-1}\left(\frac{\ell}{t+a}\right) = R\sqrt{K(t)} \tag{8.4.3}$$

by a simple inverse functional relationship (see Connolly and Wall (1997) for another inverse problem in nonlinear optics leading to a similar relation). Thus the following theorem follows.

Theorem 8.4.1. *The inverse problem of determination of the strictly decreasing velocity profile has a well-posed solution provided that* $c_0(0) \neq 0$ *and* $c_0', Q \in C[0,\infty]$.

Thus for example if $c_0(t) = {c_0}^2$ is constant, then equation (8.4.1) reduces to

$$v^{-1}\left(\frac{\ell}{t+a}\right) = \frac{R}{c_0}\sqrt{Q(t+a)} \quad t > 0. \tag{8.4.4}$$

Another useful special case is when the upstream input concentration is the pulse function, $c_0(t) = c_0(H(t) - H(t-L))$, $L > 0$. Equation (8.4.1) then reduces to the simple recursive relationship

$$Q(t+a) = c_0 K(t) - c_0 K(t-L)H(t-L) \quad t > 0$$

and v can be determined from equation (8.4.3).

However in a practical application, the computation of the derivative of the upstream concentration profile, c_0', renders equation (8.4.1) ill-posed. This is because realistic measurement data can generally only be placed in the function spaces L^2, or C, and in these function spaces differentiation operators are unbounded. It follows that the operator mapping the measured data to the velocity profile is unbounded. The regularisation of this operator mapping is examined in Section 8.5.

A related inverse problem is determining the functional relationship between the rate of shear and the shear stress specified in equation (8.2.1), which provides a fuller understanding of the constitutive laws underlying the flow mechanism. It follows from equations (8.2.1) and (8.2.2) that the functional form of f can be determined by differentiating the constructed velocity profile. Thus the determination of f is an ill-posed problem. The ill-posed nature of the problem is immediately apparent upon differentiating equation (8.3.2). The operator mapping the measured data to the velocity profile is now associated with the derivative of both data inputs, and again is unbounded.

The determination of the velocity profile assumes that $v(r)$ is a strictly decreasing function. A similar theory applies to plastic materials which display a finite yield stress. However because plastic materials can be suitably approximated by pseudoplastic materials the theory offers little extra insight.

8.5 Problem regularisation

As observed in Section 8.4, the ill-posed nature of reconstructing the strictly decreasing velocity profile from noisy input concentration measurements is equivalent to differentiation. Because the measured data lie in function spaces where differentiation operators are unbounded it is therefore necessary to restore continuity with respect to the data to solve the problem. The regularisation procedure for solution of equation (8.4.1) is simply to compute c_0' in a stable manner. It is well known that numerical differentiation can be made a well-posed problem, and there are a number of regularisation methods available. Any of these regularisation methods can be used to yield stable solutions to equation (8.4.1). In this chapter we use the method of mollification (Vasin, 1973) based on the treatment of Murio (Murio, 1993), in a similar manner to the use in Chapter 7. Suppose that due to measurement difficulties an ideal data function g has been corrupted by noise n and is measured as g_m. That is

$$g_m(t) = g(t) + n(t) \quad t \in I$$

where the functions are defined on some interval $I = [0, T]$, for some $T > 0$. Let the extension of the data function g_m to the interval $I_\delta = [-3\delta, T + 3\delta]$ be defined by

$$g_m(t) = \begin{cases} g_m(0)\exp\left[t^2/[t^2 - (3\delta)^2]\right] & -3\delta \le t < 0 \\ g_m(T)\exp\left[(t-T)^2/[(t-T)^2 - (3\delta)^2]\right] & T < t \le T + 3\delta \end{cases} \tag{8.5.1}$$

and define the Gaussian convolution, or mollification of g by

$$\begin{aligned} J_\delta g(t) = \left(\rho_\delta * g\right)(t) &= \int_{-\infty}^{\infty} \rho_\delta(t-s)g(s)\,ds \\ &\cong \int_{t-3\delta}^{t+3\delta} \rho_\delta(t-s)g(s)\,ds \end{aligned} \tag{8.5.2}$$

where δ is the radius of mollification. Then if we define the function norm $\|g(t)\|_\infty = \sup_{t\in I}|g(t)|$, the following results can be obtained (Murio, 1993), (p 6 *et seq.*).

Lemma: Murio's Consistency . If $\|g''\|_\infty \le M_2$ then

$$\|\left(J_\delta g\right)' - g'\|_\infty \le 3\delta M_2$$

This consistency result shows that $\left(J_\delta g\right)' \to g'$ as $\delta \to 0$.

Lemma: Murio's Stability. With the extended noisy measurement function $g_m \in C(I_\delta)$

$$\|\left(J_\delta g\right)' - \left(J_\delta g_m\right)'\|_\infty \le \frac{2}{\delta\sqrt{\pi}}\|g_m - g\|_\infty.$$

The mollification method provides the differentiation operator with a Lipschitz continuity result provided that the data $g_m \in C$, and $\delta > 0$ is fixed. Furthermore as $\|g_m - g\|_\infty \to 0$, δ can be reduced, and the consistency error then decreases provided that $g \in C^2$.

The regularised solution to the inverse problem consists of first mollifying the measured upstream concentration data, which is denoted $\overline{c_0}$, by forming $J_\delta \overline{c_0}(t)$, and then solving the well-posed inverse problem (8.4.1) with this regularised data. The measured downstream cross-sectional average concentration is denoted by Q_m.

Theorem 8.5.1. *The strictly decreasing velocity profile reconstruction problem, as stated in Section 8.4, with mollified measurement data $J_\delta \overline{c_0}$, has a well-posed solution provided that $\overline{c_0}(0) \neq 0$ and $\overline{c_0}, Q_m \in C[0,T]$.*

Proof. Before we use the stability result for the differentiation operator we must first bound the Volterra operator in equation (8.4.1). Consider the equation

$$(\lambda \mathbb{I} - \mathbb{K})h = g \tag{8.5.3}$$

where $\mathbb{I}$ is the identity operator, $\mathbb{K}$ is a compact linear Volterra integral operator in a space of continuous functions defined on an appropriate interval, and $\lambda > 0$ is constant. The associated perturbed mapping equation is

$$((\lambda + \Delta\lambda)\mathbb{I} - (\mathbb{K} + \Delta\mathbb{K}))(h + \Delta h) = g + \Delta g$$

where g and Δg are continuous functions, the operators $\mathbb{K}$ and $\mathbb{K} + \Delta\mathbb{K}$ have continuous kernels $\widetilde{k}$ and $\widetilde{k} + \Delta\widetilde{k}$, and $(\lambda + \Delta\lambda) > 0$ is constant. The continuity of g and $\widetilde{k}$ will guarantee the existence of a unique continuous solution h to equation (8.5.3) (Linz, 1985), (p 30 *et seq.*). It also follows from the theory of Volterra operators (Linz, 1985), (p 45 *et seq.*) that if $|\widetilde{k}| \leq K$, $|\Delta\widetilde{k}| \leq \Delta K$, $|g| \leq G$, $|\Delta g| \leq \Delta G$, and $\widetilde{\lambda} = (\lambda + \Delta\lambda)$ then

$$|\Delta h(t)| \leq \frac{1}{\widetilde{\lambda}}\left[\Delta G + \frac{\Delta K t}{\widetilde{\lambda}}(G + \Delta G)\exp\left((K + \Delta K)\frac{t}{\widetilde{\lambda}}\right) + \frac{|\Delta\lambda| G}{\lambda}\exp\left(\frac{Kt}{\lambda}\right)\right]\exp\left(\frac{Kt}{\widetilde{\lambda}}\right). \tag{8.5.4}$$

The $|\Delta\lambda|$ term in equation (8.5.4) is obtained by considering a perturbed mapping equation with $\Delta\mathbb{K} = \Delta g = 0$ (Linz, 1985), (p 41 *et seq.*). Hence the solution h has continuous dependence on the data inputs $\widetilde{k}$, g and λ, and it follows that equation (8.5.3) is well-posed. The bound in equation (8.5.4) indicates that the modulus of continuity of the solution on the measurement depends *strongly* on the magnitude of $\widetilde{\lambda}$, which is $c_0(0)$ in our problem. This implies that unless $c_0(0)$ is much larger than any measurement noise then well-posedness will be lost. It follows that if we define the family of operators $\mathbb{T}^{-1}$ by $\mathbb{T}^{-1}(\widetilde{k}, g) = (\lambda\mathbb{I} - \mathbb{K})^{-1}g$, then the mollification of the upstream data function, $J_\delta \overline{c_0}$, and Murio's stability lemma imply the continuity result

$$\|\mathbb{T}^{-1}((J_\delta c_0)', Q) - \mathbb{T}^{-1}((J_\delta \overline{c_0})', Q_m)\|_\infty \leq \mathcal{O}(\|Q_m - Q\|_\infty) + \mathcal{O}(\|\overline{c_0} - c_0\|_\infty).$$

It then follows that the solution of equation (8.4.1), and the computation of the velocity profile $v(r)$ through equation (8.4.4) can be performed in a stable manner. □

Consistency of the mollified problem solution to the exact K can be shown from Murio's consistency lemma provided that $c_0 \in C^2[0,T]$.

8.6 Numerical method and results

In practice the upstream and downstream cross-sectional average concentration measurements, $c_0(t)$ and $Q(t+a)$, can only be measured over some finite interval $0 \leq t \leq T$. This means $v(r)$ cannot be reconstructed completely, the minimum resolvable velocity is ℓ/T. The parameters in this section are taken from the perifusion apparatus (Evans et al., 1993b; Evans et al., 1993a), they are $v_m = 6 \times 10^{-3}$ m/s, $\ell = 2$ m, $R = 5 \times 10^{-4}$ m, $T = 3000$ s, so that $a = 1/3 \times 10^3$ s.

We now describe a simple numerical algorithm to solve the inverse problem of velocity reconstruction. Consider a uniform time mesh $\{t_i\}_{i=0}^N$ with $t_0 = 0$, $t_i = t_{i-1} + h$, $1 \leq i \leq N$, where $h = T/N$. Then the kernel $K(t)$ can be approximated by a B-spline of degree n

$$K(t) = \sum_{i=0}^{M} \alpha_i b_i(t)$$

where $M+1$ is the cardinality of the B-spline basis $\{b_i\}_{i=0}^M$. If $n = 1$ so that the B-spline basis functions are *roof* functions, and the spline knot points are chosen to coincide with the time mesh points, then collocation of equation (8.4.1) provides the finite dimensional equation

$$Q(t_j + a) = \alpha_j c_0(0) + \sum_{i=0}^{M} \alpha_i \int_0^{t_j} c_0'(t_j - s) b_i(s)\, ds \quad j \in [0, N].$$

The properties of B-splines and their support imply that this matrix system is lower triangular. If the integral is approximated by the trapezoidal rule then the solution for the coefficients $\{\alpha_i\}_{i=0}^N$ is

$$\begin{aligned} c_0(0)\alpha_0 &= Q(t_0 + a) \\ \alpha_j \left(c_0(0) + \frac{h}{2} c_0'(t_0) \right) &= Q(t_j + a) - h \sum_{i=1}^{j}{}' \alpha_{j-i} c_0'(t_i) \quad j \in [1, N] \end{aligned} \tag{8.6.1}$$

where the prime on the summation signifies that the last value in the summation is to be halved. To ensure the algorithm is well-posed the coefficients $\{c_0'(t_i)\}_{i=0}^N$ must be replaced by their mollified derivatives. This is achieved by constructing $\{J_\delta c_0(t_i)\}_{i=0}^N$ and then using central differencing to estimate the numerical derivatives. The extension and mollification of the data functions utilises equations (8.5.1) and (8.5.2).

One can reason that due to noise, $J_\delta c_0(0)$, and $J_\delta Q(t+a)$ are better approximations to the true data functions $c_0(0)$ and $Q(t+a)$ respectively. Due to the nature of the smoothing operator in equation (8.3.2), $Q(t+a)$ is expected to contain less high frequency information than c_0. Therefore

the mollified functions $J_\delta c(0)$, and $J_\delta Q(t+a)$ are used in equation (8.6.1) for improved accuracy. The numerical approximation to $K(t)$ then allows the reconstruction of the velocity profile $v(r)$ through use of equation (8.4.3).

The measurement data is simulated through computation with equation (8.3.2), the results of which are corrupted with noise n having a normal distribution with zero mean and a standard deviation of 0.05. Because concentrations must be positive, simulated negative concentrations are set to zero. For the numerical results presented in this chapter $N = 100$, so that the sampling time interval is $h = 30$ s.

The amount of mollification to be used in the numerical reconstruction is dependent on the perceived amount of noise. There are methods for determining the optimum mollification radius (Murio, 1993), however in this chapter a moderate amount of smoothing with $\delta = 75$ is employed. In general the noise levels in the measured data functions c_0 and Q will be different, and hence their appropriate optimal mollification radiuses will also differ.

The simulated non-Newtonian fluid is pseudoplastic and the velocity profile obeys the power law relation (Ostwald and Auerbach, 1926)

$$v(r) = v_m\left(1 - \left(\frac{r}{R}\right)^{\frac{5}{2}}\right) \tag{8.6.2}$$

The upstream concentration input is chosen to be the pulse-like Gaussian function

$$c_0(t) = \exp\left(-\left(\frac{t}{300} - \frac{5}{6}\right)^2\right) \qquad t \in [0, T]. \tag{8.6.3}$$

The downstream cross-sectional average concentration profile, $Q(t+a)$, is calculated by equation (8.3.2). These true data functions, the noise corrupted measurements $\overline{c_0}$ and Q_m, and the mollified signals are shown in Figure 8.2. The directly estimated, the mollified, and the true derivatives of the upstream input concentration c_0' are shown in Figure 8.3. Note the noise amplification of the directly estimated derivative.

The true velocity profile (– – –) and the reconstructed velocity profile (—) are shown in Figure 8.4. Given the data noise levels, the reconstruction is reasonably accurate. At lower velocities the noise is more significant and the reconstruction is more difficult. The reconstructed velocity is observed to be not uniformly spaced and the resolution of the higher velocity components is much lower. This velocity spacing is given by equation (8.4.2) and is $\ell/(t+a)$. If the input data functions are measured according to this spacing, then the reconstructed velocity spacing is uniform (not shown).

Also shown in Figure 8.4 is the reconstructed velocity profile (—) for a dilatant power law fluid (···). This power law fluid is simulated through equation (8.6.2) with the flow index 5/2 replaced by 5/4. The upstream concentration input, simulated noise, and mollification radius remain

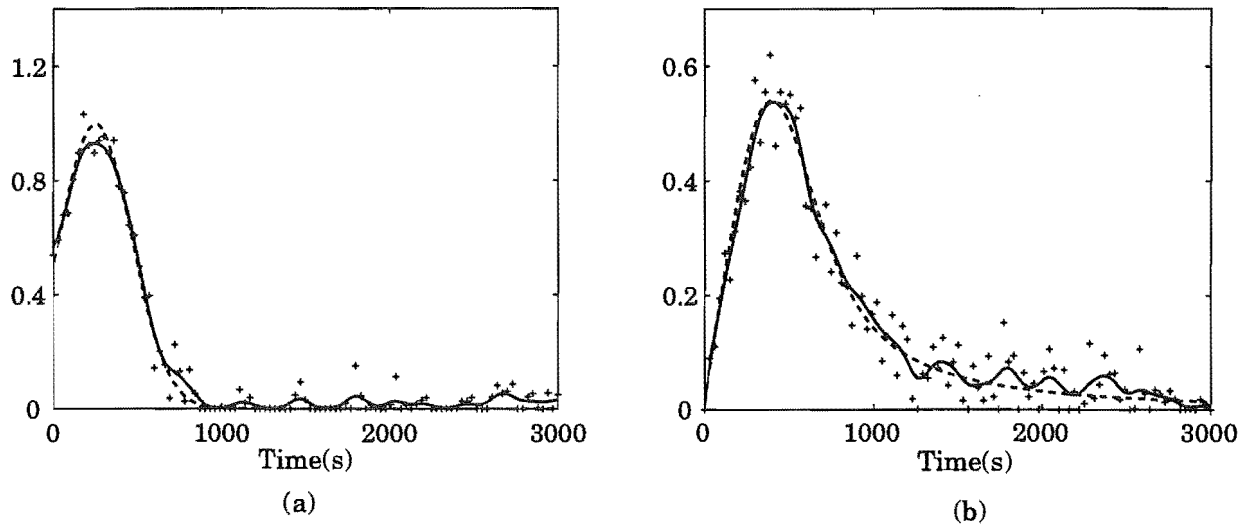

Figure 8.2: The true data functions, the noise corrupted measurements, and the mollified signals. (a) The true upstream input concentration profile c_0 (– – –), the noise corrupted measurement $\overline{c_0}$ (+), and the mollified signal $J_\delta \overline{c_0}$ (—). (b) The true downstream cross-sectional average concentration profile Q (– – –), the noise corrupted measurement Q_m (+), and the mollified signal $J_\delta Q_m$.

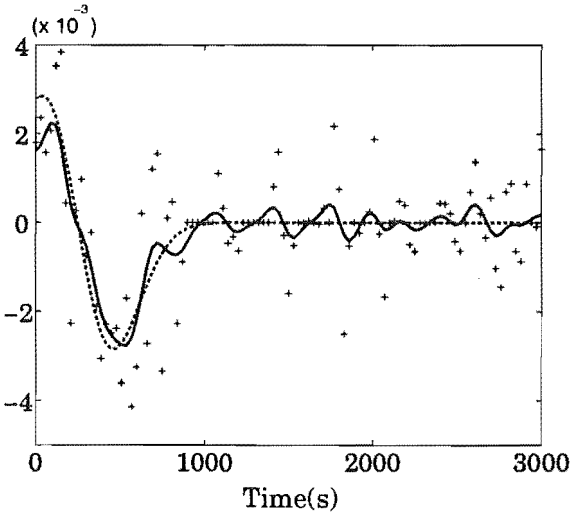

Figure 8.3: The directly estimated (+), the mollified (—), and the true (– – –) derivatives of the upstream input concentration c_0'.

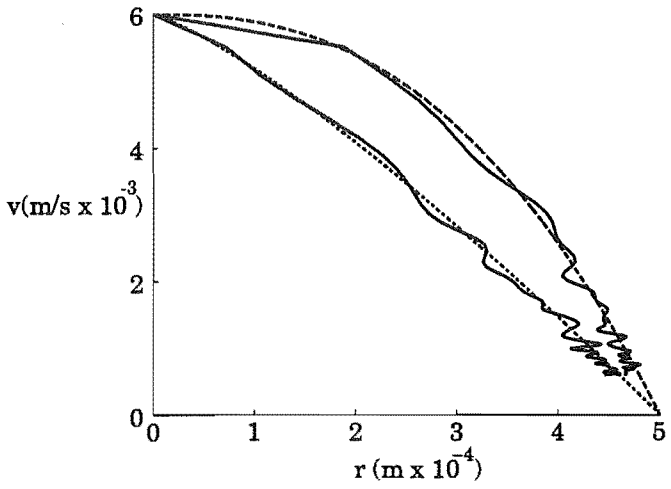

Figure 8.4: The true velocity profile (– – –) and the reconstructed velocity profile with a linear spline fit through the reconstructed points (—). The minimum resolvable velocity is 1/1500 m/s. This reconstructed velocity profile is distinguishable from the reconstructed velocity profile (—) for a dilatant power law fluid (· · ·).

unchanged. Thus, even with moderate data noise levels, the reconstructed velocity profiles allow the different non-Newtonian fluids to be distinguished.

The relationship between the rate of shear and the shear stress as specified by equations (8.2.1) and (8.2.2), can now be found by differentiating the reconstructed velocity profile. This can be found in a stable manner by computing the mollified derivative of the reconstructed velocity profile. Provided the mollification radius is suitably large, this method yields satisfactory results, but reconstruction algorithms that require a strictly decreasing velocity profile yield better results. However this added constraint will result in a more difficult nonlinear inverse problem.

8.7 Consideration of molecular diffusion

In this section the numerical method presented in Section 8.6 is tested on simulated data including small amounts of molecular diffusion. The molecular diffusion of the solute may significantly contribute to the dispersive transport of the solute. A simple finite difference scheme that incorporated shear dispersion and molecular diffusion was used in the data simulation. This simulated data is not corrupted with noise, and the sampling time interval is $h = 30$ s. The upstream input concentration is the pulse-like Gaussian function in equation (8.6.3), and the pseudoplastic fluid is specified by the power law relationship in equation (8.6.2).

The simulated downstream cross-sectional average concentration is shown in Figure 8.5 for different molecular diffusion coefficients (D). As diffusion increases the concentration peak increases and shifts to the right. There is also a more rapid concentration decrease after the concentration

peak. These effects are predominantly due to the diffusive transport of the tracer transverse to the fluid flow.

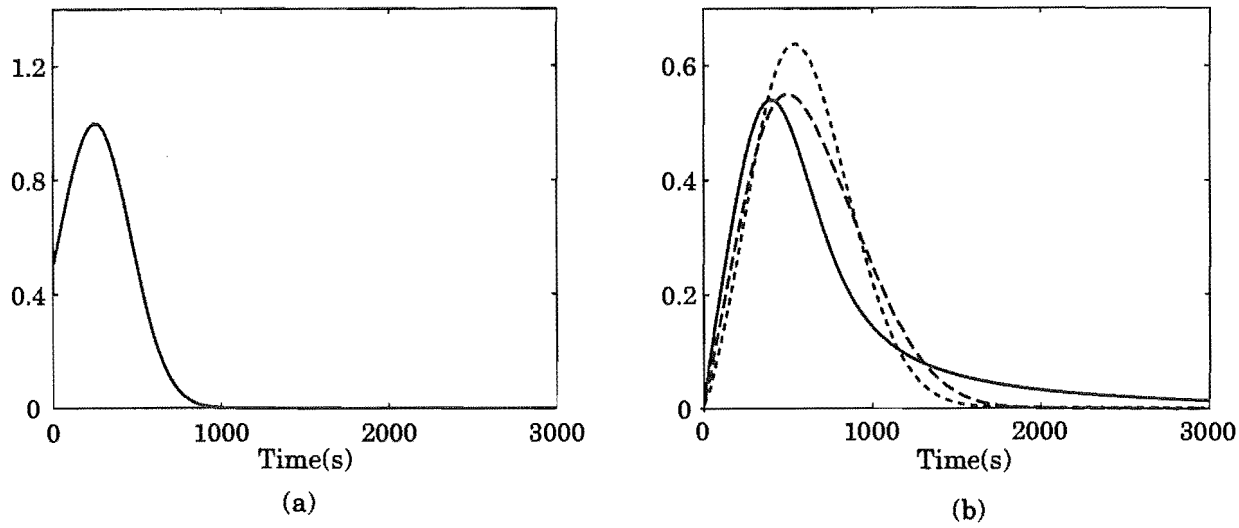

Figure 8.5: The true data functions and the diffusion adjusted measurements. (a) The true upstream input concentration profile (—). (b) The downstream cross-sectional average concentration profile with no diffusion (—), and the diffusion adjusted measurements with D = 5×10^{-11} $m^2 \cdot s^{-1}$ (– – –), and D = 10^{-10} $m^2 \cdot s^{-1}$ ($\cdots$).

The reconstructed velocity profiles are shown in Figure 8.6 with a linear spline fit through the reconstructed points. The jump in the velocity profiles at v_m reflect the fact that molecular diffusion allows some of the tracer to travel at velocities higher than in pure shear dispersive flow. The velocity reconstruction for the diffusion adjusted data underestimates the high velocities down the centre of the pipe. This is due to the high initial concentration gradient across the pipe and the resulting diffusive transport of the tracer towards the pipe boundary. Similarly, after the bulk of the tracer has travelled down the centre of the pipe the tracer is transported towards the centre of the pipe. This results in the overestimation of the small velocities near the pipe boundary. Hence as the amount of diffusion increases, the downstream cross-sectional average concentration measurement contains less information about the fluid velocity profile, and the velocity profile determination becomes more ill-posed.

8.8 Discussion

We have considered the problem of determining the two-dimensional fluid velocity profile from temporally varying cross-sectional average concentration measurements at upstream and downstream locations. Assuming a strictly decreasing velocity profile and a specified continuous upstream

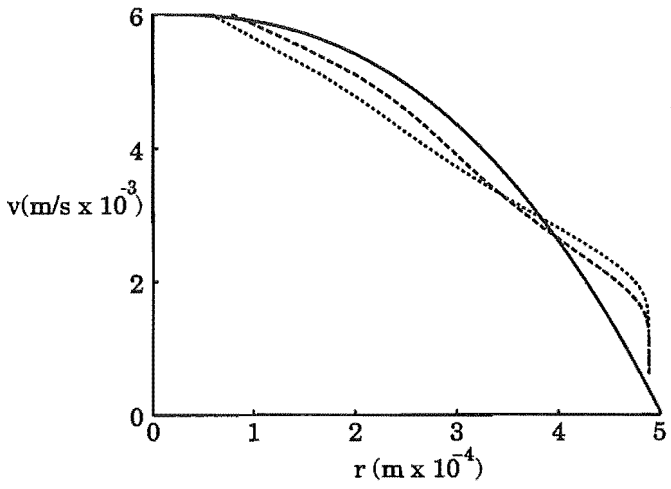

Figure 8.6: The true velocity profile (—) and the reconstructed velocity profile for diffusion adjusted measurements with D = 5×10^{-11} $m^2 \cdot s^{-1}$ (– – –), and D = 10^{-10} $m^2 \cdot s^{-1}$ ($\cdots$). The minimum resolvable velocity is 1/1500 m/s.

concentration with a time zero step, then the problem becomes well-posed. It is assumed that no tracer is input before the time zero step which is required in the input concentration or one of its derivatives. Failure to use this time zero step protocol produces an ill-posed problem.

In contrast if the upstream concentration also has to be measured, then the problem of determining the velocity profile is an ill-posed deconvolution problem with ill-conditioning equivalent to the problem of numerical differentiation. A simple sequential deconvolution procedure is constructed and it is verified by numerical experiment that stable approximations to the velocity profile can be obtained in the presence of moderate amounts of data noise, and small amounts of molecular diffusion.

The contribution of molecular diffusion is an important factor in perifusion experiments. We will include this aspect into more general inverse problems in Chapter 9. Interestingly for problems in which diffusion transverse to fluid flow is significant the determination of the upstream concentration profile becomes better posed and the determination of the velocity profile becomes more ill-posed.

The velocity profile in the pipe was determined for a tracer in solution system. A related problem is to deduce the velocity profile for the solution with no tracer injected. One might also wish to consider problems in which the velocity profile to be determined had some time dependency. Problems of this nature are highly ill-posed.

Some interesting inverse problems arise if one considers developing fluid flow. In this case a component of the fluid velocity is into the centre of the pipe, and there is also an acceleration of the fluid down the pipe. Problems include the reconstruction of an upstream tracer concentration

and the determination of the flow development characteristics. These are interesting problems for future work.

Chapter 9

Inverse problems associated with diffusive non-Newtonian shear dispersive flow

9.1 Introduction

The ill-posed inverse problem of estimation of a temporally varying upstream concentration from measurement of a cross sectional average material concentration at some downstream location for shear dispersion in Newtonian media was investigated in Chapter 7. For viscous flow problems, the variation in fluid velocity over the cross section of a pipe leads to the shear dispersion of the solute concentration. In this chapter we consider more general inverse problems incorporating two additional features. Firstly the flow of a more general non-Newtonian fluid is considered. This consideration arises in endocrinology experiments associated with blood flow in pipes. Secondly, molecular diffusion of the solute may significantly contribute to the dispersive transport of the solute, and we consider this effect on the associated inverse problem. This effect is believed to be an important contributing factor in perifusion experiments, which is analysed in more detail in Chapter 10. Inverse problems associated with fluid flow in pipes in series with well-mixed chambers are also considered. These types of problems are applied to the perifusion apparatus in Chapter 10.

9.2 Pure shear dispersive flow

9.2.1 Consideration of non-Newtonian Flow

As in Chapter 7, the problem of estimation of a temporally varying upstream concentration from measurement of a cross sectional average concentration at some downstream location is considered. This inverse problem, which is associated with shear dispersion, is an ill-posed deconvolution problem. The nature of the shear dispersion is dependent on the variation in the fluid velocity over the cross section of the pipe. This variation in velocity is dependent on the functional relationship between the viscosity and the rate of shear for the particular non-Newtonian fluid.

Suppose the velocity profile of a viscous, incompressible fluid flowing through a rigid pipe of circular cross section, with a no-slip boundary condition is given by $v(r)$, where r is the circular polar radial coordinate associated with the cylindrical coordinate system so that the z-axis is aligned with the axis of the tube. The radius of the pipe is R, and the maximum flow velocity is v_m. The fluid is assumed to have a suitably low Reynolds number N_R [1], so that the flow is laminar.

Many fluids display a marked shear-dependent viscosity. Solutions such as blood have a reduced viscosity when the shear rate is large and are termed pseudoplastic. Conversely dilatant fluids exhibit an increase in viscosity with the rate of shear. Materials requiring a finite yield stress before flow can commence are called plastic. For steady fully developed flow in a circular pipe suppose that the rate of shear is a function of the shear stress (τ) only, that is

$$\frac{dv}{dr} = f(\tau), \tag{9.2.1}$$

where r is the distance from the centre of the pipe. This assumption excludes rheopectic, thixotropic and viscoelastic materials. The relationship between $f(\tau)$ and $v(r)$ for the different types of non-Newtonian fluids is indicated schematically in Figure 9.1. Naturally there is less shear dispersion for pseudoplastic fluids than for dilatant fluids.

The mass transport of a volume concentration of a tracer, $c(z, r, t)$, down the pipe, is described by the simple transport equation

$$\frac{\partial c}{\partial t} + v(r)\frac{\partial c}{\partial z} = 0, \quad z \in [0, \infty), \quad r \in [0, R], \quad t > 0, \tag{9.2.2}$$

where $v(r)$ is the fluid velocity profile. Because the injection of material into the pipe at $z = 0$ is assumed to be independent of r, the boundary condition takes the simple form $c(0, r, t) = c_0(t)H(t)$, where H denotes the Heaviside function. It is also assumed that the initial concentration in the pipe is zero, i.e., $c(z, r, 0) = 0$. As outlined in Section 8.3, if one assumes that $v'(r) < 0$,

[1] $N_R = \frac{2\rho\overline{v}R}{\mu} = 5$ for the saline solution used in perifusion experiments, and is of similar order for blood flow in the equine experiment.

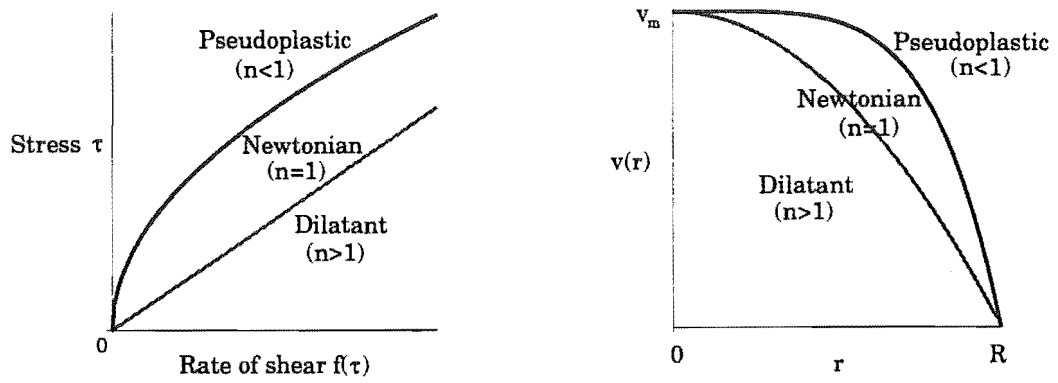

Figure 9.1: The functional relationship between $f(\tau)$ and the fluid velocity profile, $v(r)$, for different non-Newtonian power law fluids.

then the measurement of an average concentration, $Q(t)$, across the cross-section of the pipe at a fixed station $x = \ell$ is given by

$$Q(t+a) = \int_0^t k(t-s)c_0(s)\,ds, \quad t > 0, \tag{9.2.3}$$

where the kernel has the functional form

$$k(t) = \frac{-2\ell}{R^2} \cdot \frac{v^{-1}\left(\frac{\ell}{t+a}\right)\left(v^{-1}\left(\frac{\ell}{t+a}\right)\right)'}{(t+a)^2}, \quad \text{with} \quad a = \frac{\ell}{v_m} > 0. \tag{9.2.4}$$

The parameter a represents the time for fluid travelling at speed v_m to reach the station at $z = \ell$. Note that the lower limit of integration in equation (9.2.3) can be set to minus infinity if the assumption that $t > 0$ is relaxed. This change makes equation (9.2.3) a singular integral equation, significantly altering the character of the problem.

The inverse problem is to estimate the function c_0, from knowledge of Q. Observe that equation (9.2.3) is a Volterra integral equation of the first kind, which is a well known ill-posed problem (Linz, 1985). To understand the degree of ill-posedness it is convenient to perform a Fourier transform of (9.2.3). Extending the data function Q(t), and the kernel function k(t), by zero for $t < 0$, we obtain the Fourier transform of the kernel

$$\widehat{k}(\xi) = \frac{1}{\sqrt{2\pi}} \int_{-\infty}^{\infty} H(t)k(t) \exp(-i\xi t)\,dt, \tag{9.2.5}$$

However it is not apparent from (9.2.5), how the functional form of $v(r)$ affects the degree of ill-posedness of the inverse problem of estimating the function c_0 from Q. To understand this dependence we now consider the power law family of fluids.

Power law fluids are non-Newtonian fluids without yield stress. They satisfy the following power-law constitutive relation (Ostwald and Auerbach, 1926) (*c.f.* (9.2.1))

$$\tau = -\mu\left(\frac{dv}{dr}\right)^n, \tag{9.2.6}$$

where μ is the consistency, and $n > 0$ is the flow index. The flow of blood in tubes of small diameter, and low shear rate, can be represented as a power law fluid (Charm and Kurland, 1965; Huckaba and Hahn, 1968). If n is greater than or less than one the fluid is dilatant, or pseudoplastic respectively, with the fluid being Newtonian when $n = 1$ (see Figure 9.1). Using (8.2.2), it follows that the velocity profile of a viscous, incompressible fluid flowing through a rigid pipe of circular cross section, with a no-slip boundary condition is given by

$$v(r) = v_m\left(1 - \left(\frac{r}{R}\right)^{\frac{n+1}{n}}\right) \tag{9.2.7}$$

For a power law fluid

$$v^{-1}(u)\left(v^{-1}(u)\right)' = \frac{-nR^2}{v_m(n+1)}\left(1 - \frac{u}{v_m}\right)^{\frac{n-1}{n+1}}, \tag{9.2.8}$$

and thus the kernel in (9.2.4) now has the functional form

$$k(t) = \frac{2an}{(n+1)} \cdot t^{\frac{n-1}{n+1}} \cdot \left(\frac{1}{t+a}\right)^{\frac{3n+1}{n+1}}, \quad \text{with} \quad a = \frac{\ell}{v_m} > 0. \tag{9.2.9}$$

The inverse problem is to estimate the function c_0, from knowledge of Q. Observe that (9.2.3) is a Volterra integral equation of the first kind, which is a well known ill-posed problem (Linz, 1985). For $n \geq 1$ the kernel k is bounded, however for $n \in (0,1)$, the kernel is unbounded, with a singularity at $s = 0$. We now investigate these two different regimes.

The pseudoplastic power law fluid regime

Although the kernel is not regular when $n \in (0,1)$, it is integrable. The theory of singular Volterra equations of the first kind is less developed than that for bounded kernels (Linz, 1985). However for $n \in (0,1)$, the kernel singularity is of the form $t^{(1-n)/(n+1)}$, with $(1-n)/(n+1) \in (0,1)$, and hence equation (9.2.3) is a generalised Abel equation (Linz, 1985), (p 71 *et seq.*) (Atkinson, 1974). The generalised Abel equation can be converted to the Volterra equation of the first kind (Linz, 1985), (p 75, 166 *et seq.*)

$$\int_0^t \frac{Q(u+a)}{(t-u)^{\frac{2n}{n+1}}}\,du = \int_0^t h(t-s)c_0(s)\,ds, \tag{9.2.10}$$

with kernel

$$h(t) = \frac{2an}{(n+1)}\int_0^1 u^{\frac{n-1}{n+1}}(1-u)^{\frac{-2n}{n+1}}(tu+a)^{\frac{-3n-1}{n+1}}\,du. \tag{9.2.11}$$

It follows that because the non-singular term in the kernel (9.2.9), $(t+a)^{(-3n-1)/(n+1)} \in C^\infty$, is bounded and sufficiently differentiable, that $h(t) \in C^\infty$ is also bounded and suitably differentiable

(Linz, 1985), (p 75). Differentiating (9.2.10) with respect to t we obtain by integration by parts, Leibniz's rule, and elementary convolution properties

$$\int_0^t \frac{Q'(u+a)}{(t-u)^{\frac{2n}{n+1}}}\,du = h(0)c_0(t) + \int_0^t h'(t-s)c_0(s)\,ds, \tag{9.2.12}$$

where $Q(a) = 0$,

$$h(0) = \frac{2n}{n+1}a^{\frac{-2n}{n+1}}\int_0^1 u^{\frac{n-1}{n+1}}(1-u)^{\frac{-2n}{n+1}}\,du, \tag{9.2.13}$$

$$= \frac{2n}{n+1}a^{\frac{-2n}{n+1}}\mathcal{B}\left(\frac{1-n}{n+1}, \frac{2n}{n+1}\right), \tag{9.2.14}$$

and $\mathcal{B}$ is the Beta function (Abramowitz and Stegun, 1964), (p 258).

The ill-posed nature of the problem is apparent by taking the Fourier transform of (9.2.10). Therefore, extending the left-hand side of (9.2.10) and h to be zero for $t < 0$ it follows by a change in the order of integration that

$$\frac{\Gamma\left(\frac{1-n}{n+1}\right)}{i\xi^{\left(\frac{1-n}{n+1}\right)}}\widehat{Q}(\xi) = \widehat{h}(\xi)\widehat{c_0}(\xi), \tag{9.2.15}$$

where Γ is the Gamma function. Through an integration by parts argument similar to that in Section 7.2.2, the asymptotic expansion for $\widehat{h}(\xi)$ as $|\xi| \to \infty$ is

$$\widehat{h}(\xi) = \frac{1}{i\xi}a^{\frac{-3n-1}{n+1}}\mathcal{B}\left(\frac{1-n}{n+1}, \frac{2n}{n+1}\right) + \mathcal{O}\left(\frac{1}{\xi^2}\right) \tag{9.2.16}$$

It follows from (9.2.15) and (9.2.16) that the ill-posed nature of (9.2.10) is equivalent to computing a derivative of order $1 - (1-n)/(n+1) = 2n/(n+1)$. This degree ill-posedness is also apparent from (9.2.12), which is a Volterra integral equation of the second kind, with a regular kernel. The inversion of this second kind Volterra integral equation is a well known well-posed problem. The degree ill-posedness appears on the left-hand side of (9.2.12), which is the fractional derivative of Q of order $2n/(n+1)$ (Oldham and Spanier, 1974), (p 59).

Mollification combined with a suitable quadrature formula allows the left-hand side of (9.2.12), or the derivative of the left-hand side of (9.2.10), to be computed in a stable manner (Murio, 1993), (p 27, 38). It can be shown from (9.2.11) that

$$h'(t) = \frac{-2an(3n+1)}{(n+1)^2}\int_0^1 \left(\frac{u}{1-u}\right)^{\frac{2n}{n+1}}(tu+a)^{\frac{-4n-2}{n+1}}\,du, \tag{9.2.17}$$

and it follows that the numerical techniques in Section 7.4 can be used to solve the more general problem when $n \in (0,1)$.

The dilatant power law fluid regime

When $n \in (1,\infty)$ it follows that $(n-1)/(n+1) \in (0,1)$. Therefore differentiating (9.2.3) with respect to t, we obtain

$$Q'(t+a) = \int_0^t k'(t-s)c_0(s)\,ds. \tag{9.2.18}$$

where

$$k'(t) = \frac{2an}{(n+1)^2} t^{\frac{-2}{n+1}} \left(\frac{1}{t+a}\right)^{\frac{3n+1}{n+1}} \left[(n-1) - \frac{t}{t+a}(3n+1)\right], \tag{9.2.19}$$

and $k(0) = 0$. Thus $k'(t)$ has a singularity at $t = 0$ of the form $t^{-2/(n+1)}$, and (9.2.18) is a generalised Abel equation. As before, this generalised Abel equation can be converted to the Volterra equation of the first kind (Linz, 1985), (p 75, 166 *et seq.*)

$$\int_0^t \frac{Q'(u+a)}{(t-u)^{\frac{n-1}{n+1}}}\, du = \int_0^t h(t-s)c_0(s)\, ds, \tag{9.2.20}$$

with kernel

$$h(t) = \frac{2an}{(n+1)^2} \int_0^1 u^{\frac{1-n}{n+1}} (1-u)^{\frac{-2}{n+1}} (tu+a)^{\frac{-3n-1}{n+1}} \left[(n-1) - \frac{tu}{tu+a}(3n+1)\right] du. \tag{9.2.21}$$

Again, since the nonsingular term in (9.2.19) is bounded and sufficiently differentiable, then $h(t) \in C^\infty$, is also bounded and suitably differentiable (Linz, 1985), (p 75). Differentiating (9.2.20) with respect to t we obtain

$$\frac{d^2}{dt^2} \int_0^t \frac{Q(u+a)}{(t-u)^{\frac{n-1}{n+1}}}\, du = h(0)c_0(t) + \int_0^t h'(t-s)c_0(s)\, ds, \tag{9.2.22}$$

where

$$h(0) = \frac{2n}{(n+1)^2(n-1)} a^{\frac{-2n}{n+1}} \mathcal{B}\left(\frac{n-1}{n+1}, \frac{2}{n+1}\right). \tag{9.2.23}$$

Equation (9.2.22) is a Volterra integral equation of the second kind with a regular kernel, and therefore the inversion is a well-posed problem. Observe that the left-hand side of (9.2.22) is the fractional derivative of Q of order $1 + (n-1)/(n+1) = 2n/(n+1)$ (Oldham and Spanier, 1974), (p 59), agreeing with the degree of ill-posedness discussed earlier. Therefore when $n \in (1, \infty)$ the problem has numerical conditioning equivalent to that of computing a fractional derivative between one and two. Mollification combined with a suitable quadrature formula allows the left-hand side (9.2.22) to be computed in a stable manner (Murio, 1993), (p 27, 38), and the numerical techniques in Section 7.4 can also be used to solve the problem when $n \in (1, \infty)$.

We have seen that as n decreases, and thus the velocity gradient decreases, that the inverse problem of finding c_0 from Q becomes less ill-posed. Naturally this is reflected in the Fourier transform of the kernel k(t), which after extending by zero for $t < 0$ can be shown to be $\widehat{k}(\xi) = \mathcal{O}(\xi^{-2n/(n+1)})$. Thus the operator $\mathbb{T}$ defined by (9.2.3) maps H^0 to $H^{2n/(n+1)}$, and the inverse problem is numerically *equivalent* to computing a fractional derivative of order $2n/(n+1)$. It is therefore necessary to restore continuity with respect to the data in order to successfully solve the problem. Since $n \geq 0$ for real fluids it follows that $2n/(n+1) \in [0, 2]$, and thus the problem conditioning is at worst *equivalent* to computing a second derivative. Hence the inverse problems

for $n < 1$ and $n > 1$ have conditioning better and worse than that of differentiation respectively. If one considers more general fluids, rather than a power law fluid, where the index $(n+1)/n$ in (9.2.7) can also take values between 0 and 1, then $2n/(n+1) \in [0, \infty)$, and the problem conditioning can be *equivalent* to computing a derivative of any order.

Radially dependent input concentration

It is natural to consider the source reconstruction problem where the input concentration is also radially dependent. If the injection of material into the pipe at $z = 0$ is radially dependent, then the boundary condition takes the form $c(0, r, t) = c_0(t, r)H(t)$, where H denotes the Heaviside function. It follows that the average concentration, $Q(t)$, across the cross-section of the pipe at a fixed station $x = \ell$, is now given by

$$Q(t+a) = \int_0^t k(t-s)c_0\big(s, v^{-1}\Big(\frac{\ell}{t-s+a}\Big)\big)\,ds, \quad t > 0, \tag{9.2.24}$$

where $k(t)$ is given by (9.2.4). Furthermore, if c_0 is a separable function of t and r, so that $c_0(t, r) = c_0(t)c_r(r)$, then

$$Q(t+a) = \int_0^t k_r(t-s)c_0(s)\,ds, \quad t > 0, \tag{9.2.25}$$

where

$$k_r(t) = k(t)c_r\big(v^{-1}\Big(\frac{\ell}{t+a}\Big)\big). \tag{9.2.26}$$

For each function c_r, there exists a unique solution c_0 to the Volterra integral equation (9.2.25) (Linz, 1985). It follows that the source reconstruction problem of determining both c_0 and c_r from a single measurement $Q(t)$ in (9.2.25) is not unique. Therefore, unless some extra system information is available, this inverse problem is highly ill-posed.

Shear dispersion in elliptical pipes

It is natural to to consider how different pipe geometries effect the shear dispersion. For example, the velocity profile of a Newtonian fluid in a straight elliptical pipe is

$$v(x, y) = v_m\Big(1 - \frac{x^2}{b^2} - \frac{y^2}{c^2}\Big), \tag{9.2.27}$$

where x and y are the minor and major axis of the elliptical pipe, and b and c are the semi-axes of the ellipse (Landau and Lifshitz, 1959), (p 58). It follows that the cross-sectional average concentration is

$$Q(t) = \frac{4}{\pi bc}\int_0^c \int_0^{b\sqrt{1-\frac{y^2}{c^2}}} c_0\Big(t - \frac{\ell}{v(x,y)}\Big)H\Big(t - \frac{\ell}{v(x,y)}\Big)\,dx\,dy, \tag{9.2.28}$$

where c_0 is the upstream input concentration. The change in coordinates defined by the transformation $x = b\cos\theta, y = c\sin\theta$, reduces equation (9.2.28) to equation (7.2.4). Therefore shear dispersion in elliptical pipes is identical in nature to that in circular pipes. However, although deformities in the pipe have no effect on the amount of shear dispersion, they are more significant if diffusive effects are also considered (Aris, 1953). We note that curvature in the piping also effects the amount of shear dispersion, with the emergence of a secondary flow directed from the centre of the pipe towards the boundary (Dean, 1927). This is because particles near the flow axis are acted upon by larger centrifugal forces than particles near the pipe boundary.

9.2.2 The perifusion chamber

A schematic diagram of the perifusion model was shown in Figure 6.2 of Chapter 6. An extended schematic diagram of the system geometry is shown in Figure 9.2. The length of pipe from the

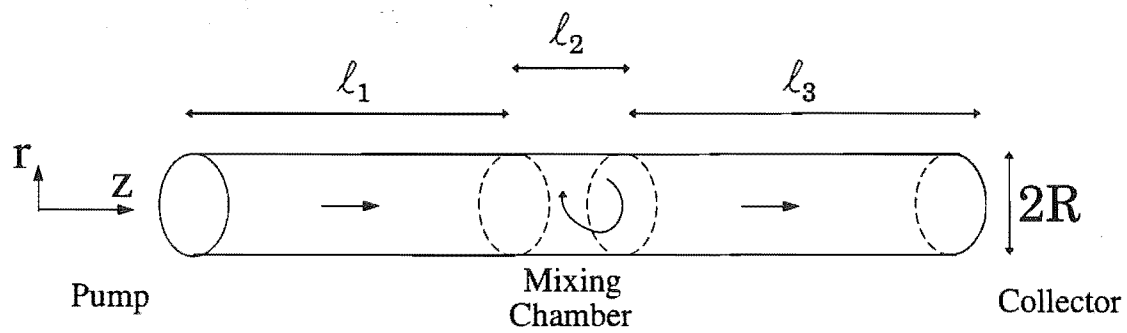

Figure 9.2: A schematic diagram of the perifusion model geometry.

pump to the cell chamber is ℓ_1, the length of pipe from the cell chamber to the collector is ℓ_3, and the pipe diameter is $2R$. The cell chamber is assumed to be the same radius as the pipe, with an effective length[2] of ℓ_2. Thus the volume of the chamber is $\pi R^2\ell_2$. Let c_0, Q_1, Q_2, Q_3 be the cross-sectional average material concentration at the pump, chamber entrance, chamber exit, and collector respectively. Hence Q_2 is the concentration in the chamber. In perifusion experiments it has been observed that mixing occurs within the cell chamber (Mason, 2000). The effect of the mixing chamber on the concentration profiles is now investigated. The net rate of change in the chamber concentration is the net amount of material entering the chamber per second divided by the chamber volume. That is

$$\frac{dQ_2}{dt} = \frac{2}{R^2\ell_2}\int_0^R v(r)(Q_1(r,t) - Q_2(t))r\,dr, \tag{9.2.29}$$

[2] A mixing chamber of arbitrary radius is considered in Section 10.2.

where $v(r)$ is the fluid velocity profile. Integrating this equation we obtain the chamber output concentration

$$Q_2(t) = \frac{2}{R^2\ell_2}\int_0^t e^{(s-t)/a_2}\int_0^R v(r)Q_1(r,s)r\,dr\,ds, \tag{9.2.30}$$

where

$$\frac{1}{a_2} = \frac{2}{R^2\ell_2}\int_0^R v(r)r\,dr = \frac{\overline{v}}{\ell_2}, \tag{9.2.31}$$

and $\overline{v}$ is the average flow velocity. An interesting inverse problem is to reconstruct Q_1 from measurement of Q_2. In general this is severely ill-posed. However in the radial-independent case with $Q_1(r,t) = Q_1(t)$, or equivalently $v(r) = \overline{v}$, (9.2.30) reduces to

$$Q_2(t) = \int_0^t k(t-s)Q_1(s)\,ds, \tag{9.2.32}$$

where

$$k(t) = \frac{\exp(-t/a_2)}{a_2}. \tag{9.2.33}$$

Extending the data function $Q_2(t)$, and the kernel function k(t), by zero for $t < 0$, we obtain the Fourier transform of the kernel

$$\widehat{k}(\xi) = \frac{1}{i\xi a_2 + 1}. \tag{9.2.34}$$

It should be noted that the dominant term in the asymptotic expansion of $\widehat{k}(\xi)$, as $|\xi| \to \infty$, is $1/(i\xi a_2)$. Thus, as is apparent from (9.2.29), the ill-posedness in computing $Q_1(t)$ from $Q_2(t)$ is *equivalent* to a differentiation. A simple procedure for numerically computing Q_1 is to compute the derivative in (9.2.29) in a stable manner using the mollification method outlined in Section 7.3.

In Chapter 7, and Section 9.2.1 the problem of reconstructing c_0 from measurement of Q_1 in shear dispersive flow was investigated. The problem of reconstructing c_0 from measurement of Q_2 after mixing has occurred in the chamber is now considered. For simplicity it is assumed that $c_0(z,r,t) = c_0(t)H(t)$. In pure shear dispersive flow

$$Q_1(r,t) = c_0\left(t - \frac{\ell_1}{v(r)}\right)H\left(t - \frac{\ell_1}{v(r)}\right). \tag{9.2.35}$$

Therefore we can express Q_2 in terms of c_0,

$$Q_2(t) = \frac{2}{R^2\ell_2}\int_0^t e^{(s-t)/a_2}\int_0^R v(r)c_0\left(s - \frac{\ell_1}{v(r)}\right)H\left(s - \frac{\ell_1}{v(r)}\right)r\,dr\,ds. \tag{9.2.36}$$

The nature of this operator is apparent after the transformation $u = s - \ell_1/v(r)$, followed by a change in the order of integration, and the transformation $u' = s - u$, to yield

$$Q_2(t + a_1) = \int_0^t k(t-s)c_0(s)\,ds, \quad t > 0 \tag{9.2.37}$$

where

$$k(t) = \frac{-2\ell_1^2}{R^2\ell_2} e^{-(t+a_1)/a_2} \int_{a_1}^{t+a_1} \frac{e^{u'/a_2}}{u'^3} v^{-1}\left(\frac{\ell_1}{u'}\right)\left(v^{-1}\left(\frac{\ell_1}{u'}\right)\right)' du', \tag{9.2.38}$$

and $a_1 = \ell_1/v_m$. In a Newtonian fluid, it follows from (9.2.8) with $n = 1$ that $v^{-1}(u)(v^{-1}(u))' = -R^2/2v_m$, so that $k(t)$ reduces to

$$k(t) = \frac{\ell_1^2}{v_m\ell_2} e^{-(t+a_1)/a_2} \int_{a_1}^{t+a_1} \frac{e^{u'/a_2}}{u'^3}\, du'. \tag{9.2.39}$$

Extending the kernel function k(t), by zero for $t < 0$, we obtain the Fourier transform of the kernel

$$\widehat{k}(\xi) = \frac{\ell_1^2}{\sqrt{2\pi}v_m\ell_2} \int_0^\infty e^{-i\xi t} e^{-(t+a_1)/a_2} \int_{a_1}^{t+a_1} \frac{e^{u/a_2}}{u^3}\, du\, dt. \tag{9.2.40}$$

Because $k \in L^1$, it follows from a change in the order of integration that

$$\widehat{k}(\xi) = \frac{\sqrt{2}a_1^2}{\sqrt{\pi}(i\xi a_2 + 1)} \int_0^\infty \frac{e^{-i\xi u}}{(u + a_1)^3}\, du. \tag{9.2.41}$$

The dominant term in the asymptotic expansion of $\widehat{k}(\xi)$, as $|\xi| \to \infty$, is $-\sqrt{2}/(\sqrt{\pi}\xi^2 a_1)$. It follows from the discussion in Section 7.2.2 that the inverse problem of reconstructing c_0 from Q_2 is *equivalent* to computing a second derivative. Thus the problem of reconstructing c_0 from Q_2 is more ill-posed than the problem of reconstructing c_0 from Q_1.

A related problem is to reconstruct Q_1 from Q_3. The first kind Volterra operator mapping can be obtained by substituting (9.2.32) into equation (8.3.2). The ill-posedness of this problem is apparent from the following lemma, which is a simple application of composition of bounded operators.

Lemma 9.2.1. *If* $\mathbb{T}_1 : \mathrm{H}^p \to \mathrm{H}^{p+a}$, $p \geq 0$, $a \geq 0$, *and* $\mathbb{T}_2 : \mathrm{H}^s \to \mathrm{H}^{s+b}$, $s \geq 0$, $b \geq 0$, *then* $(\mathbb{T}_1 \circ \mathbb{T}_2) : \mathrm{H}^s \to \mathrm{H}^{s+a+b}$, *and the inverse operator equation* $(\mathbb{T}_1 \circ \mathbb{T}_2)f = g$ *has the numerical conditioning of computing an* $(a+b)^{th}$ *derivative.*

Proof. The result follows by choosing p=s+b. □

Applying this lemma to the operators in (9.2.32) and (8.3.2), it follows that the ill-posedness of reconstructing Q_1 from Q_3 is *equivalent* to computing second derivative.

Another interesting inverse problem is to reconstruct c_0 from measurement of Q_3. The first kind Volterra operator mapping can be obtained by substituting (9.2.37) into equation (8.3.2). Lemma 9.2.1, using the operators defined in (9.2.37) and (8.3.2), then indicates that the ill-posedness of this problem is *equivalent* to computing third derivative. It should be noted that Lemma 9.2.1 does not apply to the problem of reconstructing c_0 from Q_2, because the problem cannot be decoupled into two smaller inverse problems. However the lemma applied to the operators defined in (9.2.32) and (9.2.3) provides an upper bound on the degree of ill-posedness.

9.3 Flow with diffusion and shear dispersion

The contribution of molecular diffusion on the associated inverse problem is now considered. The basic phenomenon of dispersion in shear flow has been understood since Taylor (1953) considered the direct problem of the transport of a diffusing tracer injected into a Poiseuille flow. Many researchers have analysed the direct problem in more detail for a range of applications (Aris, 1953; Watt and Roberts, 1995; Phillips and Kaye, 1996). An inverse problem associated with the estimation of the molecular diffusion coefficient, from measured concentration profiles after dispersion, was also considered by Taylor (1954a). This inverse problem is one of the earliest inverse problem investigations in this area. We wish to consider more general inverse problems associated with dispersive flow in pipes.

9.3.1 The transport equations

The mass transport of the tracer volume concentration, $c(z,r,t)$, accounting for molecular diffusion is

$$\frac{\partial c}{\partial t} + v(r)\frac{\partial c}{\partial z} = D\nabla^2 c, \quad z \in [0,\infty), \quad r \in [0,R], \quad t > 0, \tag{9.3.1}$$

where D is the coefficient of molecular diffusion, assumed to be independent of c, and $\nabla^2 = \partial_z^2 + \partial_r^2 + \frac{1}{r}\partial_r$ is the Laplacian operator in circularly symmetric cylindrical coordinates. The wall of the pipe is assumed to be impermeable, hence

$$\left.\frac{\partial c}{\partial r}\right|_{r=R} = 0. \tag{9.3.2}$$

Secondly, we assume that the injection of the material into the pipe is independent of r, i.e., $c(0,r,t) = c_0(t)$, and that the initial concentration in the pipe is zero, i.e., $c(z,r,0) = 0$.

Simple analytic solutions to the direct problem (equation (9.3.1), along with boundary and initial conditions) are not readily available, and thus a numerical procedure must be employed to solve the problem. This problem is very well known, and there exists a multitude of approaches. The solution scheme considered here is an explicit finite difference scheme where the operators ∂_t, ∂_z, ∂_z^2, ∂_r^2, and ∂_r in (9.3.1) are approximated by the finite difference operators δ_{t+}, δ_{z-}, δ_z^2, δ_r^2, and δ_{r0} respectively, where δ_-, δ_+, δ_0, and δ^2 are the backward, forward, central, and second central finite difference operators respectively (Strikwerda, 1989; Mitchell and Griffiths, 1980). This is an explicit time stepping method, and if the time step is sufficiently small then the scheme is stable. This scheme provides adequate resolution if the time step is suitably small, and the spatial mesh sizes are smaller than their associated mesh Reynolds numbers. Specific numerical solutions to (9.3.1) for the perifusion apparatus are considered in Section 10.3. Similar numerical results could be obtained with the alternating direction implicit (A.D.I.) and locally one-dimensional (L.O.D.)

methods, which are unconditionally stable. We now proceed by constructing approximate solutions to the direct problem, and consider the resulting inverse problems.

9.3.2 The Taylor approximation

Taylor (1953) observed that under certain conditions, the dispersion of concentration could be approximated by a more simple model, a one-dimensional advection-diffusion equation. That is, because of diffusive migration between different streamlines, the tracer not only experiences a translatory motion with mean flow velocity, but an apparent diffusive spreading in the axial direction. We now consider a similar analysis, but for non-Newtonian fluids. This analysis is straightforward, but does not appear to be readily accessible in the literature and will be useful in the deconvolution of data from the perifusion system in Chapter 10.

Assuming that the time necessary for appreciable changes in concentration to appear, owing to advective transport, is large when compared with the time during which radial variations in concentration are reduced via molecular diffusion, we can construct approximate solutions to (9.3.1). To find conditions under which this approximation will be valid, it is necessary to calculate how rapidly a concentration which varies with r degenerates into a uniform concentration (Taylor, 1953). The solutions of (9.3.1) for which $v(r) = 0$, and the variables r and t are separated, are of the form

$$c(r,t) = \exp(-mt) J_0(r\sqrt{m/D}), \tag{9.3.3}$$

where J_n denotes the Bessel function of order n. The boundary condition (9.3.2) ensures that

$$J_1(R\sqrt{m/D}) = 0. \tag{9.3.4}$$

The root of this equation corresponding to the lowest value of m is $R\sqrt{m/D} = 3.8$, so that the time necessary for the radial variation in the concentration represented by (9.3.3) to degenerate to $1/e$ of its initial value is

$$t_1 = \frac{R^2}{(3.8)^2 D}. \tag{9.3.5}$$

If the length of pipe the material is spread over is of order ℓ, then the time necessary for advection to make appreciable changes in concentration is ℓ/v_m, so that the Taylor approximation is valid when

$$\frac{\ell}{v_m} \gg \frac{R^2}{(3.8)^2 D}. \tag{9.3.6}$$

Taylor heuristically suggested that ratios of $10:1$ are permitted in the inequality (9.3.6) (Taylor, 1954a).

Proceeding with the approximate solutions, if diffusion in the direction of fluid flow is assumed to be negligible, then writing $y = r/R$ we obtain

$$\frac{\partial^2 c}{\partial y^2} + \frac{1}{y}\frac{\partial c}{\partial y} = \frac{R^2}{D}\frac{\partial c}{\partial t} + \frac{R^2}{D} v_m (1 - y^{\frac{n+1}{n}}) \frac{\partial c}{\partial z}. \tag{9.3.7}$$

From (9.2.7), the mean flow velocity is given by

$$\overline{v} = v_m \left(\frac{n+1}{3n+1} \right). \tag{9.3.8}$$

Considering advection across a plane which moves at velocity $\overline{v}$, and writing $z_1 = z - \overline{v}t$ in (9.3.1), then implies that the radial variation in c satisfies

$$\frac{\partial^2 c}{\partial y^2} + \frac{1}{y}\frac{\partial c}{\partial y} = \frac{R^2}{D} v_m \left(\frac{2n}{1+3n} - y^{\frac{n+1}{n}} \right) \frac{\partial c}{\partial z_1}, \tag{9.3.9}$$

where the transfer of material across planes for which z_1 is constant depends only on the radial material diffusion. Because we have assumed that the radial variation in c is small relative to that in the axial direction, we can assume that $\frac{\partial c}{\partial z_1}$ is independent of y. A solution to (9.3.9) satisfying the boundary condition $\frac{\partial c}{\partial y} = 0$ when $y = 1$ is

$$c = \bar{c} + \frac{bn}{2(1+3n)} y^2 - \frac{bn^2}{(1+3n)^2} y^{\frac{1+3n}{n}}, \tag{9.3.10}$$

where $\bar{c}$ is the value of c at $y = 0$, and the constant b is

$$b = \frac{R^2 v_m}{D} \frac{\partial c}{\partial z_1}. \tag{9.3.11}$$

The rate of transfer of the material c across the plane at z_1 is

$$q_c = 2\pi R^2 \int_0^1 v_m \left(\frac{2n}{1+3n} - y^{\frac{n+1}{n}} \right) c \cdot y \, dy \tag{9.3.12}$$

Since we are assuming the radial variations in c are small compared with those in the axial direction, then $\frac{\partial c}{\partial z_1} \approx \frac{\partial Q}{\partial z_1}$ (Taylor, 1954a), where Q is the mean cross-sectional concentration, we then obtain

$$q_c = -\frac{\pi R^4 {v_m}^2}{D} \left(\frac{n^2 (n+1)^2}{2(1+5n)(1+3n)^3} \right) \frac{\partial Q}{\partial z_1}. \tag{9.3.13}$$

Hence Q, relative to a plane z_1, obeys a diffusive process with effective diffusion coefficient

$$\eta = \frac{R^2 {v_m}^2}{D} \left(\frac{n^2 (n+1)^2}{2(1+5n)(1+3n)^3} \right) = \frac{\kappa(n) R^2 \overline{v}^2}{D}, \tag{9.3.14}$$

where

$$\kappa(n) = \frac{n^2}{2(1+5n)(1+3n)} \tag{9.3.15}$$

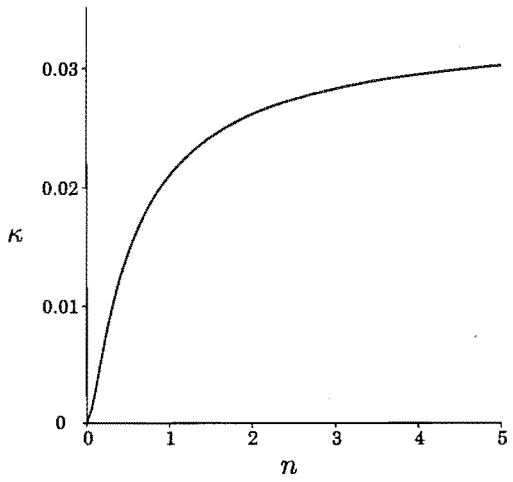

Figure 9.3: Functional form of $\kappa(n)$.

is Taylor's constant (Aris, 1953), which is 1/48 in Newtonian flow. The functional behaviour of $\kappa(n)$ is shown in Figure 9.3. Notice that as $n \to 0$, $\kappa \to 0$, and the effective diffusion coefficient, $\eta \to 0$. In the other limit, as $n \to \infty$, $\kappa \to 1/30$. Furthermore, if one considers a more general fluid with $(n+1)/n \in (0,1)$ in (9.2.7), rather than a power law fluid, then κ becomes arbitrarily large.

The conservation of material within the pipe is expressed by the continuity equation for Q, namely

$$\frac{\partial q_c}{\partial z_1} = -\pi R^2 \frac{\partial Q}{\partial t}, \tag{9.3.16}$$

where ∂_t denotes differentiation with respect to time at a point where z_1 is constant. Therefore by substituting (9.3.13) into (9.3.16), we obtain

$$\frac{\partial Q}{\partial t} + \overline{v}\frac{\partial Q}{\partial z} = \eta \frac{\partial^2 Q}{\partial z^2}, \tag{9.3.17}$$

the advection-diffusion equation approximation to the concentration dispersion. This result can also be derived from the more general theory in Aris (1956) for shear dispersion in a pipe of arbitrary cross-section, with an arbitrary velocity profile and spatially varying diffusion coefficient (not shown here). This more general analysis considers the movement of the centre of gravity of the distribution of solute, and the associated higher moments. This theory indicates that the solute distribution tends to normality with an effective diffusion coefficient of $(D + \eta)$.

Bounded solutions to equation (9.3.17) are of the form

$$Q(z,t) = \int_0^t K(z, t-s) c_0(s)\, ds, \tag{9.3.18}$$

where the kernel for this equation is

$$K(z,t) = e^{\left(\frac{\overline{v}z}{2\eta}\right)} \cdot \frac{z}{2\sqrt{\eta\pi t^3}} \cdot e^{\left(\frac{-\overline{v}^2 t}{4\eta} - \frac{z^2}{4\eta t}\right)}. \tag{9.3.19}$$

The kernel associated with the ill-posed problem of finding c_0 given Q, defined by the first kind Volterra operator equation in (9.3.18), is bounded. However $\partial_t^m K(z,0) = 0 \ \forall m \in \mathbb{Z}$, so as expected the problem cannot be transformed, via differentiation of (9.3.18), into a Volterra equation of the second kind.

9.3.3 Boundary conditions

In this section we consider how the model boundary conditions affect the inverse problem of source reconstruction. In certain situations, the model boundary conditions are important (Smith et al., 1991), and we discuss this further in Section 10.2 for the perifusion system.

The boundary condition $c(0,t) = c_0(t)$ is in fact an approximation to the true boundary condition

$$\overline{v}c_0(t) = \overline{v}c(0,r,t) - D\frac{\partial c}{\partial z}(0,r,t), \tag{9.3.20}$$

where c_0 is the concentration time profile of the released hormone at the injection point, and $\overline{v}$ is the average cross-sectional flow velocity. This equation is simply obtained by balancing the concentration flux across the inlet, which includes an advective and a diffusive component. It should be noted that D in (9.3.20) is the material molecular diffusion coefficient not the effective diffusion coefficient, η, from Taylor theory. This is because the Taylor theory does not apply to very short lengths of pipe where the flow is yet to develop. We discuss this boundary condition, in connection with the perifusion apparatus further in Section 10.2.

The solution to (9.3.17) with the boundary condition (9.3.20) can be found using Laplace transforms, and is of the form (9.3.18), where the kernel is now

$$K(z,t) = \frac{\overline{v}\sqrt{\eta}}{D}\exp\left(\frac{\overline{v}z}{2\eta} - \frac{\overline{v}^2 t}{4\eta}\right)\left[\frac{\exp\left(\frac{-z^2}{4\eta t}\right)}{\sqrt{\pi t}} - \varphi\mathrm{erfc}\left(\frac{z}{2\sqrt{\eta t}} + \varphi\sqrt{t}\right)\cdot\exp\left(\frac{\varphi z}{\sqrt{\eta}} + \varphi^2 t\right)\right], \tag{9.3.21}$$

where erfc is the complementary error function, and

$$\varphi = \frac{(2\eta - D)\overline{v}}{2D\sqrt{\eta}}. \tag{9.3.22}$$

It is assumed that the solutions are bounded. However, this solution is for a semi-infinite pipe, and for the more realistic finite length pipe the appropriate boundary condition at the pipe exit is Danckwerts' boundary condition (Smith, 1988), which expresses the fact that there is purely advective flow out the end of the pipe (i.e., $\frac{\partial c}{\partial z}(\ell,t) = 0$). The solution to this more complicated problem can be found by separation of variables, and is of the form (9.3.18), where now the kernel is

$$K(z,t) = \sum_{n=-\infty}^{\infty} a_n(-\beta^2 - \lambda_n^2\eta)\exp\left(\beta\left(z - \frac{\overline{v}t}{2}\right) - \lambda_n^2\eta t\right)\left[\frac{\alpha\sin\lambda_n z}{\lambda_n} + \cos\lambda_n z\right], \tag{9.3.23}$$

where a_n satisfies

$$\int_0^\ell -e^{-\beta z}\left[\frac{\alpha \sin \lambda_n z}{\lambda_n} + \cos \lambda_n z\right] dz = a_n \int_0^\ell \left[\frac{\alpha \sin \lambda_n z}{\lambda_n} + \cos \lambda_n z\right]^2 dz, \tag{9.3.24}$$

and λ_n are solutions to

$$\lambda^2 \tan \lambda \ell - (\alpha + \beta)\lambda - \alpha\beta = 0, \tag{9.3.25}$$

where

$$\alpha = \left(\frac{1}{D} - \frac{1}{\eta}\right)\overline{v} \quad \text{and} \quad \beta = \frac{\overline{v}}{2\eta}. \tag{9.3.26}$$

This solution simplifies significantly if $\eta = D$, and this specific case was considered in Smith et al. (1991) as a model of the perifusion chamber. However, this assumption is not valid since η is typically at least four orders of magnitude larger than D in the perifusion system. In fact, because the advective effects are assumed to be more significant than the diffusive effects in the perifusion system, the diffusive term in (9.3.20) can be omitted. Therefore, as was concluded in Smith et al. (1991), the specification of the boundary conditions is particularly important, particularly so for the perifusion system, and this is discussed further in Chapter 10.

9.3.4 The inverse advection-diffusion equation

Under certain conditions (equation (9.3.6)), the dispersive flow of concentration in a pipe can be approximated by an advection diffusion equation (equation (9.3.17)). We now consider the degree of ill-posedness of the associated inverse problem, the problem regularisation, and the construction of numerical schemes for the stabilised problem. This inverse problem has also been analysed by Smith and Wake (1990) and Hào (1996, 1997). Smith and Wake (1990) found an analytical solution to the inverse problem, involving an infinite series of time derivatives of the downstream concentration measurement. Hào (1996) considered numerical methods based on a mollification method with Dirichlet and de la Vallée Poussin kernels. The solution scheme presented here is based on the method of mollification with a Gaussian kernel. Similar problems excluding advection have been examined in (Weber, 1981; Eldén, 1987; Eldén, 1988; Murio and Roth, 1988; Murio, 1989; Guo et al., 1990; Seidman and Eldén, 1990; Murio, 1993; Regińska and Eldén, 1997; Berntsson, 1999).

Problem regularisation

The inverse problem of reconstruction of the source concentration $c_0(t)$ from $Q(\ell, t)$, via equation (9.3.18), is considered here. As we shall see, this inverse problem is always ill-posed for realistic measurement data. This is because measured data can generally only be placed in the

function space L^2, or at most C, and in these function spaces the inverse problem mapping operators are unbounded. It is therefore central to show that the inverse problem can be made a well-posed problem. That this can be done is well known, and there are a number of regularisation techniques available. We shall choose the method of mollification, based on the treatment of Murio (Murio, 1993). An alternative regularisation technique based on the hyperbolisation of the parabolic problem (9.3.17) is considered in Chapter 11.

We now examine the stability of the inverse problem of estimation of c_0, from knowledge of $Q = Q(\ell, t)$. To understand the degree of ill-posedness it is convenient to perform a Fourier analysis of (9.3.17). Taking the Fourier transform of (9.3.17) with respect to time, we obtain the differential equation

$$i\xi\widehat{Q}(z,\xi) + \overline{v}\widehat{Q}_z(z,\xi) = \eta\widehat{Q}_{zz}(z,\xi), \quad z \in (0,\infty), \quad \xi \in (-\infty,\infty). \tag{9.3.27}$$

Requiring bounded solutions as $z \to \infty$, then implies that the operator mapping $Q \to c_0$ in the Fourier transform domain is

$$\widehat{c_0}(\xi) = \widehat{Q}(\ell,\xi)\exp\left(\frac{-\overline{v}}{2\eta}\ell\right)\exp\left(\sqrt{\frac{|\xi|}{2\eta}}I(\xi,a)\ell\right), \tag{9.3.28}$$

where

$$I(\xi,a) = \left(\sqrt{1+a^2}+|a|\right)^{1/2} + i\sigma\left(\sqrt{1+a^2}-|a|\right)^{1/2}, \quad \text{with} \quad a = \frac{\overline{v}^2}{4\xi\eta}, \tag{9.3.29}$$

where $\sigma = \text{sign}(a)$, and we have used the principal square root. Because $\mathcal{R}e(I(\xi,a)) \to 1$ as $|\xi| \to \infty$, it follows that that Q is not just a function in $L^2(\mathbb{R})$, but its high frequency behaviour is such that $\|\widehat{Q}\|_2$ decreases at exponential order, as $|\xi| \to \infty$, because by Parseval's theorem $c_0 \in L^2 \iff \widehat{c_0} \in L^2$. It is readily observed that for a general noise function, $n(t) \in L^2(\mathbb{R})$, assumed to be additive to $Q(t)$, there is no reason to believe that the high-frequency components of $\widehat{n}(\xi)$ will be subject to such rapidly decreasing behaviour, and it therefore follows that there is no guarantee that the resultant $\widehat{c_0}(\xi)$ will be in $L^2(\mathbb{R})$. This illustrates that the inverse signal reconstruction problem is ill-posed.

The degree of ill-posedness is apparent if we consider the family of Hilbert spaces E^s furnished with the norm

$$\|u\|_s = \int_{\mathbb{R}} e^{\sqrt{s|\xi|}}|\widehat{u}(\xi)|^2 d\xi. \tag{9.3.30}$$

It then follows that $E^0 = L^2$, $E^{s_1} \subseteq E^{s_2}$ if $s_1 \geq s_2$, and $E^s = C^\infty$ for $s > 0$. One can also show that if $s_1 \geq s_2$, then E^{s_1} is dense in E^{s_2}, and E^{s_1} is compactly embedded in E^{s_2} with the compact isometry operator $\mathbb{J}$. The proof is similar to that for Sobolev spaces (Kress, 1989), (p 111). It follows that if L is a bounded operator then the inverse of the compact operator $(L \circ \mathbb{J}) : E^0 \to E^0$

is an unbounded operator. Rewriting (9.3.28) allows the operator $\mathbb{T}$ defined by (9.3.18) to be expressed in the Fourier domain by

$$\widehat{Q}(\ell,\xi) = \widehat{c_0}(\xi)\exp\left(\frac{\overline{v}}{2\eta}\ell\right)\exp\left(-\sqrt{\frac{\ell^2|\xi|}{2\eta}}I(\xi,a)\right). \tag{9.3.31}$$

Therefore $\mathbb{T} : E^0 \to E^{\ell^2/2\eta}$, and as we deduced previously $(\mathbb{T}\circ\mathbb{J})^{-1}$ is an unbounded operator. Therefore increasing ℓ generates a more ill-posed problem, and increasing η generates a more well-posed problem.

We have observed that $\|\widehat{Q}\|_2$ decreases at exponential order as $|\xi| \to \infty$. We can therefore interpret the exponential terms in (9.3.31) as a low-pass filter. A simple measure of the degree smoothing is the frequency for which the filter attains half-maximum. For our problem this is

$$\xi_{\frac{1}{2}}(\eta,\overline{v}) = \frac{\sqrt{\eta\ln(2)(\ln(2)\eta+\overline{v})}(\overline{v}+2\ln(2)\eta)}{\eta}. \tag{9.3.32}$$

Because $\xi_{\frac{1}{2}}$ is a strictly increasing function of $\overline{v}$, it follows that the inverse problem is in some sense more well-posed as $\overline{v}$ increases. However for $\overline{v} > 0$, $\lim_{\eta\to\infty}\xi_{\frac{1}{2}} = \lim_{\eta\to 0}\xi_{\frac{1}{2}} = \infty$, and $\xi_{\frac{1}{2}}$ is not a strictly increasing function of ξ. For fixed $\overline{v}$, $\xi_{\frac{1}{2}}$ is a convex function, and thus attains a minimum when $\partial_\eta\xi_{\frac{1}{2}} = 0$. The maximum amount of smoothing occurs at this minimum, which is when

$$\eta = \frac{(\sqrt{5}-1)}{4\ln(2)}\overline{v}, \tag{9.3.33}$$

which interestingly contains a golden mean type number. This critical diffusive value separates the inverse problem into two domains, where the diffusive processes respectively increase and decrease the amount of data smoothing respectively.

The advection-diffusion equation approximation to the dispersion in the pipe has generated a more ill-posed inverse problem than that for pure shear dispersive flow. We now investigate the regularisation of this more ill-posed inverse problem. The problem is to get a regularised approximation to the function c_0 when given a modified function Q_m; where due to measurement difficulties the true function Q, has been corrupted by a noise function n, so that

$$Q_m(x) = Q(x) + n(x), \quad x \in I.$$

The functions Q, and n, are defined on the interval $I = [0,T]$, for a given value of $T > 0$. To proceed, we extend the data Q_m to the interval $I_\delta = [-3\delta, 3\delta + T]$, and define the mollifier of Q, $J_\delta Q$, with mollification radius δ as discussed in Section 7.3. The following result is central to our stability proof.

Lemma: Murio's Consistency . With $f \in C^1$ and if $\|f'\|_2 \le M$ then

$$\|(J_\delta f) - f\|_2 \le \frac{\delta M}{2}.$$

This consistency result shows that as $\delta \to 0$, then $(J_\delta f) \to f$.

To convert this problem into a well-posed problem consider the effect of mollification of the measured function Q, that is look at the solution to the problem when Q is replaced by $J_\delta Q$. Observe that due to the linearity of the direct problem that c_0 is then replaced by $J_\delta c_0$, and it can also be shown that (9.3.28) becomes

$$\widehat{J_\delta c_0}(\xi) = \frac{1}{\sqrt{2\pi}} \exp\left(\frac{-\overline{v}}{2\eta}\ell\right) \exp\left(\sqrt{\frac{|\xi|}{2\eta}} I(\xi, a)\ell - \frac{\xi^2\delta^2}{4}\right) \widehat{Q}(\xi). \tag{9.3.34}$$

It is now seen that the effect of the mollification is to bound the growth of the exponential function for large values of $|\xi|$. In fact

$$\left|\exp\left(\frac{-\overline{v}}{2\eta}\ell\right) \exp\left(\sqrt{\frac{|\xi|}{2\eta}} I(\xi, a)\ell - \frac{\xi^2\delta^2}{4}\right)\right| < e^{f(\delta)} = \exp\left(\frac{\overline{v}}{2} + \frac{3}{4\eta^{\frac{2}{3}}\delta^{\frac{2}{3}}}\right), \tag{9.3.35}$$

with $f > 0$ and bounded above. It follows that

$$\|(\widehat{J_\delta c_0}) - (\widehat{J_\delta \overline{c_0}})\|_2^2 \leq \frac{1}{\sqrt{2\pi}} e^{f(\delta)} \|\widehat{Q_m} - \widehat{Q}\|_2^2, \tag{9.3.36}$$

where $\overline{c_0}$ corresponds to c_0 when Q is replaced by Q_m. The stability result then follows from Parseval's theorem.

Lemma 9.3.1. *If $Q, Q_m \in L^2$ then*

$$\|(J_\delta c_0) - (J_\delta \overline{c_0})\|_2^2 \leq \frac{1}{\sqrt{2\pi}} e^{f(\delta)} \|Q_m - Q\|_2^2. \tag{9.3.37}$$

We see the mollification method provides the inverse mapping operator with a Lipschitz continuity result, when the data $Q_m \in C$, provided $\delta > 0$ is fixed. Furthermore as $\|Q_m - Q\| \to 0$, δ can be reduced, and the consistency error is then decreased, provided $Q \in C^1$.

Then well-posedness of the inverse problem is provided by use of Lemma 9.3.1 and Murio's consistency lemma.

Theorem 9.3.2. *The mollified inverse problem is stable with respect to perturbations in the data Q. If the exact boundary function $Q \in C^1$ with $\|Q'\|_2 < M$ then the solution $J_\delta \overline{c_0}$ to the mollified inverse problem satisfies*

$$\|(J_\delta \overline{c_0}) - c_0\|_2^2 \leq \frac{1}{\sqrt{2\pi}} e^{f(\delta)} \|Q_m - Q\|_2^2 + \frac{\delta M}{2}. \tag{9.3.38}$$

Numerical methods

We now investigate stable marching schemes to solve the regularised inverse problem. The stabilised problem is to find $J_\delta Q(0,t)$ for times t of interest, and some $\delta > 0$, given that $J_\delta Q(z,t)$ satisfies

$$\begin{aligned} \frac{\partial(J_\delta Q)}{\partial t} + \overline{v}\frac{\partial(J_\delta Q)}{\partial z} &= \eta \frac{\partial^2(J_\delta Q)}{\partial z^2}, \quad t > 0 \\ (J_\delta Q)(z,0) &= 0, \quad z > 0 \\ (J_\delta Q)(\ell,t) &= J_\delta Q_m(t), \quad t \geq 0, \end{aligned} \tag{9.3.39}$$

where Q_m is the noise corrupted data measurement. We now consider approximate solutions to (9.3.39) by means of finite difference equations. Consider the uniform discretisation of the z-t plane: $\{(z_n = nh, t_j = jm), n = 0,1,...,N; Nh = \ell; j = 0,1,...,M; Mm = L > \ell\}$, where L depends on h and m in a way to be specified later. If we define the grid function $V_j^n = J_\delta Q(z_n, t_j)$, then the partial differential equation in (9.3.39) can be approximated by the consistent finite-difference scheme

$$\frac{1}{2m}(V_{j+1}^n - V_{j-1}^n) + \frac{\overline{v}}{h}(V_j^n - V_j^{n-1}) = \frac{\eta}{h^2}(V_j^{n+1} - 2V_j^n + V_j^{n-1}), \tag{9.3.40}$$

for $j = 1,2,...,M$, $n = 1,2,...,N$, where $V_j^N = J_\delta Q_m(t_j)$, $j = 0,1,...,M$ and $V_0^n = 0$, $n = 0,1,...,N$. This space marching scheme has local truncation error $\mathcal{O}(h + m^2)$ as $h, m \to 0$, and requires two initial conditions, V_j^N and V_j^{N+1}. The second data function, $J_\delta G_m = J_\delta Q(\ell + h, t)$, can easily be obtained by solving the well-posed direct problem (9.3.18) in the quarter plane $z > \ell$, $t > 0$, with initial condition $Q(x,0) = 0$, and boundary condition $Q(\ell,t) = J_\delta Q_m$. Note that as we march back in space, at each step we must drop the estimation of the concentration profile by one temporal discretisation step. Therefore if we want to determine the solution V_j^0 on the interval $[0,T]$, then $L = T + \ell m/h$.

In order to analyse the stability of the marching scheme we consider the following equivalent scheme:

$$\begin{aligned} \frac{1}{h}(V_j^n - V_j^{n-1}) &= U_j^{n-1} \\ \frac{1}{2m}(V_{j+1}^n - V_{j-1}^n) + \overline{v}U_j^{n-1} &= \frac{\eta}{h}(U_j^n - U_j^{n-1}), \end{aligned} \tag{9.3.41}$$

where U can be interpreted as an intermediate flux variable. The discrete Fourier transform, $\widetilde{f}$, of $f_j = f(jm)$, for j an integer, is defined by

$$\widetilde{f} = \sum_j f_j \exp(ijmw), \quad 0 \leq |w| \leq \pi/m. \tag{9.3.42}$$

Taking the discrete Fourier transform of (9.3.41) we have

$$\begin{bmatrix} \widetilde{U}^{n-1} \\ \widetilde{V}^{n-1} \end{bmatrix} = \begin{bmatrix} \dfrac{\eta}{\overline{v}h+\eta} & \dfrac{-ih\sin(wm)}{m(\overline{v}h+\eta)} \\ \dfrac{-\eta h}{\overline{v}h+\eta} & 1-\dfrac{ih^2\sin(wm)}{m(\overline{v}h+\eta)} \end{bmatrix} \begin{bmatrix} \widetilde{U}^{n} \\ \widetilde{V}^{n} \end{bmatrix},$$

where for h sufficiently small

$$\max(|\widetilde{V}^{n-1}|, |\widetilde{U}^{n-1}|) \leq \left(1+h+\frac{h|w|}{\eta}\right) \max(|\widetilde{V}^{n}|, |\widetilde{U}^{n}|), \tag{9.3.43}$$

where $|\sin(wm)| \leq m|w|$. The following stability argument is based on a similar argument in Murio, 1993 (p 80) . It follows that

$$\max(|\widetilde{V}^{0}|, |\widetilde{U}^{0}|) \leq \left(1+h+\frac{h|w|}{\eta}\right)^{N} \max(|\widetilde{\rho}_\delta \widetilde{Q}_m|, |\widetilde{\rho}_\delta \widetilde{F}_m|), \tag{9.3.44}$$

where F_m is the flux at $z=\ell$, which can be estimated through the second kind operator

$$F_m(t) = \frac{1}{h_1}\left(\int_0^t K(h_1, t-s) Q_m(s)\, ds - Q_m(t)\right), \quad t \in [0, L], \tag{9.3.45}$$

where K is given by (9.3.19), and $h_1 > 0$ is fixed. It follows from standard theory that $\|F_m\|_2$ is bounded by $c_1\|Q_m\|_2$, for some fixed positive constant c_1 (Linz, 1985), (p 40). Therefore

$$|\widetilde{V}^{0}|^2, |\widetilde{U}^{0}|^2 \leq \left(1+h+\frac{h|w|}{\eta}\right)^{2N} |\widetilde{\rho}_\delta|\, (|\widetilde{Q}_m|^2 + |\widetilde{F}_m|^2). \tag{9.3.46}$$

From Poisson's summation formula

$$\widetilde{\rho}_\delta(w) = \sum_{j=-\infty}^{\infty} \widehat{\rho}_\delta\left(w+\frac{2\pi j}{m}\right), \quad 0 \leq |w| \leq \frac{\pi}{m}, \tag{9.3.47}$$

we can show that

$$|\widetilde{\rho}_\delta(w)| \leq 4\exp\left(\frac{-w^2\delta^2}{4}\right), \tag{9.3.48}$$

for $\delta \geq m$. Therefore integrating (9.3.46) with respect to w, and taking square roots we have

$$\max(\|\widetilde{V}^{0}\|_2, \|\widetilde{U}^{0}\|_2) \leq 4 \sup_{0\leq|w|\leq\frac{\pi}{m}} \left[\exp\left(\ell + \frac{\ell|w|}{\eta} - \frac{w^2\delta^2}{4}\right)\right] (\|\widetilde{Q}_m\|_2 + \|\widetilde{F}_m\|_2), \tag{9.3.49}$$

where $Nh = \ell$, and $(1+x)^N \leq \exp(Nx)$. It follows that if $\delta \geq \sqrt{2m/\pi}$ then

$$\max(\|\widetilde{V}^{0}\|_2, \|\widetilde{U}^{0}\|_2) \leq 4\exp\left(\ell + \frac{\ell^2}{\eta^2\delta^2}\right) (\|\widetilde{Q}_m\|_2 + \|\widetilde{F}_m\|_2), \tag{9.3.50}$$

and the stability result for fixed $\delta > 0$ follows from Parseval's equality. We summarise this stability result in the following theorem

Theorem 9.3.3. *For h sufficiently small, the space marching scheme in* (9.3.40), *with initial conditions $V^N(t) = J_\delta Q_m(t)$ and*

$$V^{N+1}(t) = \int_0^t K(h, t-s) J_\delta Q_m(s)\, ds, \tag{9.3.51}$$

where K is given by (9.3.19), *is consistent with the stabilised problem* (9.3.39), *and is stable.*

9.4 Discussion

In this chapter we have considered a number of inverse problems associated with advective dispersive flow. The initial tracer distribution in the pipe was always assumed to be initially zero, i.e., $c(z, r, 0) = 0$. The theory is also applicable if the initial tracer distribution is nonzero and known. An interesting inverse problem is that of reconstructing the initial solute distribution in the pipe. This inverse problem can be formulated as a Fredholm integral equation of the first kind. If in addition one wishes to reconstruct $c(0, r, t)$ as well as the initial solute distribution in the pipe, then some extra measurement information is required for the solution to the inverse problem to be unique. This extra measurement may be an average concentration at a different fixed downstream location, or a flux measurement at the same fixed location.

Another interesting inverse problem is the reconstruction of $c(0, r, t)$ and the velocity profile $v(r)$ from two cross-sectional average concentration measurements at different fixed downstream locations. This inverse problem is inherently nonlinear and an iterative solution scheme such as Newton's method is required to solve the problem.

The regularisation procedure used to solve the ill-posed advective dispersive problem in this chapter is the mollification method. A multitude of other regularisation procedures exist, including Tikhonov regularisation (Tikhonov, 1963), the maximum entropy method (Wu, 1997), truncated singular value decomposition (TSVD) (Vogel, 1986), the algebraic reconstruction technique (ART) (Censor and Herman, 1987), the Backus-Gilbert method (Backus and Gilbert, 1968), optimisation techniques (Vogel, 1987), and bounded variation (Acar and Vogel, 1994; Rudin et al., 1992). The suitability of these various methods for regularising parabolic equations warrants further study.

Chapter 10

Dispersion in perifusion systems and data enhancement

10.1 Introduction

The temporal architecture of the endocrine glandular signaling process is believed to convey important biochemical information to the target tissue, and also represents a signature of the responsive endocrine cells. Hence to understand the endocrine glandular physiology, the time domain structure of hormone synthesis and release is required.

The perifusion apparatus (McIntosh and McIntosh, 1983), has been used to investigate the hormonally stimulated release of other hormones. In this system, a liquid medium flowing at a constant rate, flows through a pipe over cells, releasing a substance in response to a stimulus in the flowing medium, and the temporal concentration profile of this released substance is then measured at some downstream location. However dispersion, mixing, and diffusion of the released hormone in the tubing of the perifusion apparatus generates a distortion in the experimentally observed hormone concentration profile. In this chapter we construct a model of the perifusion apparatus to understand this observed distortion in the hormone concentration profile. The mathematical model of the fluid flow in the perifusion system accounts for a number of observable features in the measured secretory profile.

Although the direct problem of prediction of elution concentration has been considered in connection with the perifusion apparatus (Smith et al., 1991), very little research has addressed associated inverse problems. In this chapter we consider inverse problems associated with the perifusion apparatus, and their relevance to the improvement of data interpretation. These deconvolution strategies allow the underlying secretory events to be unmasked.

A number of researchers have modeled the perifusion chamber via an advection-diffusion equation (Kao, 1989; Smith et al., 1991). We consider a general theory indicating under what conditions

this approximation is valid, and how the parameters in the advection-diffusion model relate to measurable quantities in the perifusion apparatus.

10.2 The perifusion model

The model of the perifusion apparatus is simple, including the geometry of the system, and the shear dispersion, mixing and molecular diffusion of the tracer. A schematic diagram of the perifusion model geometry is shown in Figure 10.1. The pipe from the pump to the perifusion

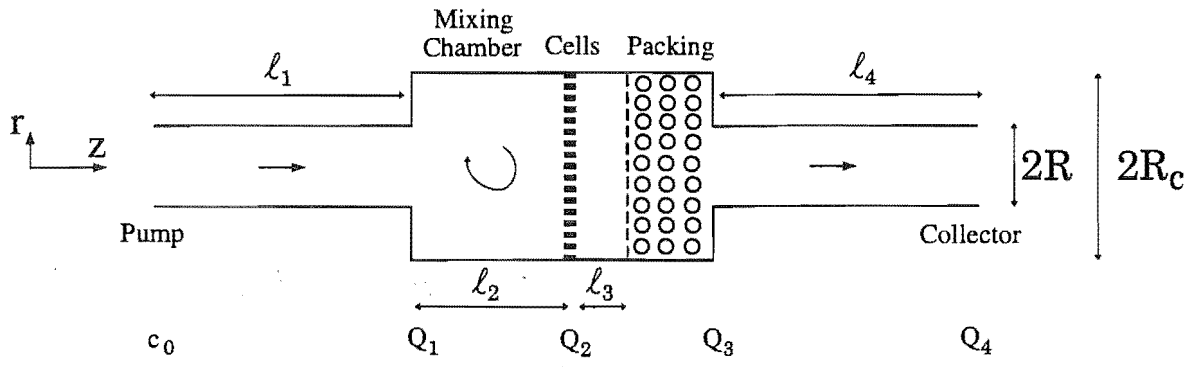

Figure 10.1: Schematic diagram of the perifusion apparatus.

chamber is 10^{-3} m in diameter ($2R$), and on average is 0.35 m in length (ℓ_1). The perifusion chamber is 2.5×10^{-2} m in length and 4×10^{-3} m in diameter ($2R_c$). The pipe from the chamber to the collector is 10^{-3} m in diameter, and on average is 0.4 m in length (ℓ_4). Therefore the perifusion chamber volume is 0.31 mℓ. However, 20% of the chamber volume is filled by the plugs, (see Figure 6.3), and the fluid before the cells comprises about 0.125 mℓ of the chamber volume. The cells are located in the centre of the chamber above the packing material. The packing material fills about 60 % of the volume in the region between the pituitary cells and the chamber outlet. The packing material is largely settled in the lower part of the chamber. Therefore the volume of fluid in the chamber between the pituitary cells and the chamber outlet is 0.05 mℓ.

There are four different regions of fluid flow in the model of the perifusion system. The fluid is assumed to be Newtonian, and thus the fluid velocity profile of the viscous, incompressible fluid is described by the well known Poiseuille distribution (equation (7.2.1)). The tracer in the pipes undergoes shear dispersion, and diffusion across and along the pipe. For the Reynolds number in the perifusion system, the fluid flow in the pipes develops after 6 pipe diameters (Knudsen and Katz, 1958), (p 228 *et seq.*). Therefore the region of developing flow is negligible in the pipes. However the flow within the chamber is slightly different. The fluid before the cells undergoes mixing (Mason, 2000), and we shall assume that the tracer in this region is perfectly mixed. As the secreted ACTH does not enter the region before the cells and the length of pipe in the

Parameter	Definition	Value
R	pipe radius	5×10^{-4} m
R_c	chamber radius	2×10^{-3} m
ℓ_1	input pipe length	0.35 m
ℓ_2	chamber mixing region length	0.01 m
ℓ_3	length of fluid below cells	3.75×10^{-3} m
ℓ_4	output pipe length	0.4 m
v_m	maximum pipe fluid velocity	6.8×10^{-3} ms^{-1}
$\overline{v}$	average pipe fluid velocity	3.4×10^{-3} ms^{-1}
$\overline{v_c}$	average chamber fluid velocity	2.125×10^{-4} ms^{-1}
D_{CRH}	CRH diffusion coefficient	1.7×10^{-10} m$^2 \cdot$ s^{-1}
D_{AVP}	AVP diffusion coefficient	3.5×10^{-10} m$^2 \cdot$ s^{-1}
D_{ACTH}	ACTH diffusion coefficient	1.5×10^{-10} m$^2 \cdot$ s^{-1}
η_{CRH}	effective CRH diffusion coefficient	3.5×10^{-4} m$^2 \cdot$ s^{-1}
η_{AVP}	effective AVP diffusion coefficient	1.7×10^{-4} m$^2 \cdot$ s^{-1}
η_{ACTH}	effective ACTH diffusion coefficient	4.0×10^{-4} m$^2 \cdot$ s^{-1}

Table 10.1: Table of relevant perifusion model parameters.

chamber between the pituitary cells and the chamber outlet is small, the flow is assumed to be laminar and not developed within this region. Because the flow is not developed in the chamber between the pituitary cells and the chamber outlet, only axial diffusion need be considered. The packing material distribution has an effect on the amount of diffusion that can occur. If the packing is evenly distributed, then the amount of signal distortion is less than if the packing settles in the lower part of the chamber. This is because the fluid travels faster through an evenly distributed packing material and the diffusion coefficient remains unchanged. The flow rate through the perifusion system is 0.16 mℓ/min, and the travel time from the pump to the collector is about 150 s (Evans et al., 1988). It follows that v_m, the maximum flow rate in the pipes, is 6.8×10^{-3} ms^{-1}, and $\overline{v_c}$, the average chamber fluid velocity, is 2.125×10^{-4} ms^{-1}. Note that the fluid velocity through the packing material is much greater than $\overline{v_c}$.

CRH, AVP, and ACTH have molecular weights of 1084, 4872, and 5500 Da respectively (Watanabe and Orth, 1987). These molecular weights allow the diffusion coefficients for these hormones in the saline solution to be estimated (Weast, 1999; Washburn, 1926), and are shown in Table 10.1 along with the model parameters. The cross-sectional average material concentration at the pump, chamber entrance, pituitary cells, chamber exit, and collector are denoted c_0, Q_1, Q_2, Q_3, and Q_4 respectively (see Figure 10.1). We now discuss the model equations.

The mass transport of the tracer volume concentration, $c_1(z, r, t)$, in the pipe from the pump

to the perifusion chamber is given by

$$\frac{\partial c_1}{\partial t} + v(r)\frac{\partial c_1}{\partial z} = D\nabla^2 c_1, \quad z \in [0, \ell_1], \quad r \in [0, R], \quad t > 0, \tag{10.2.1}$$

where D is the coefficient of molecular diffusion, $v(r)$ is the Poiseuille distribution with maximum velocity v_m, and ∇^2 is the Laplacian operator in cylindrical coordinates. Because the injection of material into the pipe is independent of r, $c_1(0, r, t) = c_0(t)$. Due to the mixing in the chamber before the pituitary cells,

$$Q_2(t) = \frac{2}{{R_c}^2 \ell_2} \int_0^t e^{(s-t)/a_2} \int_0^R v(r) c_1(\ell_1, r, s) r \, dr \, ds, \tag{10.2.2}$$

where

$$\frac{1}{a_2} = \frac{2}{{R_c}^2 \ell_2} \int_0^R v(r) r \, dr = \frac{\overline{v_c}}{\ell_2}. \tag{10.2.3}$$

The mass transport of the tracer volume concentration, $c_3(z, t)$, in the chamber from the pituitary cells to the chamber outlet is given by

$$\frac{\partial c_3}{\partial t} + \overline{v_c}\frac{\partial c_3}{\partial z} = D\frac{\partial^2 c_3}{\partial z^2}, \quad z \in [0, \ell_3], \qquad t > 0, \tag{10.2.4}$$

where $\overline{v_c}$ is the chamber fluid velocity, ℓ_3 is the length of fluid below the pituitary cells, and $c_3(0, t) = Q_2(t)$. The mass transport of the tracer volume concentration, $c_4(z, r, t)$, in the pipe from the chamber to the collector is given by

$$\frac{\partial c_4}{\partial t} + v(r)\frac{\partial c_4}{\partial z} = D\nabla^2 c_4, \quad z \in [0, \ell_4], \quad r \in [0, R], \quad t > 0. \tag{10.2.5}$$

Because the injection of material into the pipe is independent of r, $c_4(0, r, t) = c_3(\ell_3, t)$. The initial concentration in the pipe is assumed to be zero, i.e., $c_1(z, r, 0) = Q_2(0) = c_3(z, 0) = c_4(z, r, 0) = 0$, and the walls of the pipes are assumed to be impermeable, so that

$$\left.\frac{\partial c_1}{\partial r}\right|_{r=R} = \left.\frac{\partial c_4}{\partial r}\right|_{r=R} = 0. \tag{10.2.6}$$

Because fluid flow into and out of the perifusion chamber is through needles of small diameter (see Figure 6.3), we assume that there is purely advective flow at these points, that is $\frac{\partial c_1}{\partial z}(\ell_1, t) = \frac{\partial c_3}{\partial z}(\ell_3, t) = 0$. Similarly at the collector there is purely advective flow with $\frac{\partial c_4}{\partial z}(\ell_4, t) = 0$. Therefore Danckwerts' boundary condition (Smith, 1988), which was discussed in Section 9.3.3, implies that the tracer cannot travel by diffusive means from the chamber to the inlet pipe, from the outlet pipe into the chamber, or from the collector into the outlet pipe. For simplicity, we shall also assume that there is no diffusive transport between the mixing chamber and the region between the pituitary cells and the chamber outlet. Given that the region before the pituitary cells is assumed to be perfectly mixed, this assumption does not significantly affect the problem solution.

10.3 Perifusion AVP pulse experiments

In this section we compare numerical solutions of the perifusion model with pulse validation experiments. In these experiments pulses of radioactive AVP are injected into the apparatus, and AVP concentrations are measured at the collector. The numerical simulations and experimental results are shown in Figure 10.2. The numerical technique outlined in Section 9.3.1 to solve (10.2.1) and (10.2.5) is used to predict the downstream cross-sectional average concentration profile generated by a 2 min upstream injection pulse of AVP with concentration 5900 cpm/50$\mu\ell$. The input pulse, c_0, is shown in Figure 10.2 A, Q_1 is shown in Figure 10.2 B, Q_2 is shown in

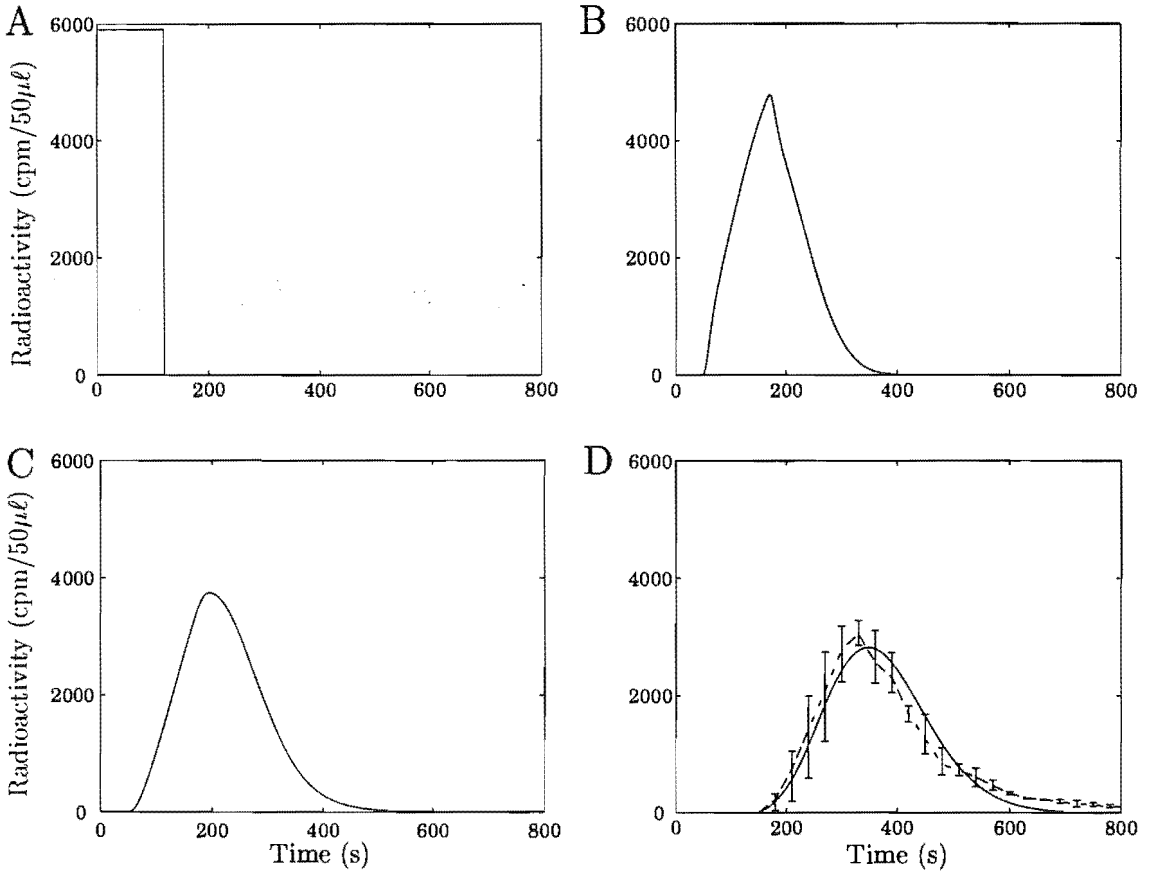

Figure 10.2: Comparison of the perifusion model and the 2 min pulse experimental data. (A) The input pulse c_0. (B) The concentration at the chamber entrance Q_1. (C) The concentration at the cells Q_2. (D) The concentration at the collector, Q_4 (—), and the average of three experimental data sets (- - -). The error bars indicate the maximum and minimum values in the data sets.

Figure 10.2 C, and Q_4 is shown in Figure 10.2 D along with the experimental measurement (Evans, 2000). A linear spline (- - -) has been fit through the average of three experimental data sets, and the error bars indicate the maximum and minimum values in the data sets. The pipes allow

a moderate amount of dispersion of the pulse, and the mixing operator in (10.2.2) slightly delays the peak in concentration and smoothes the incoming pulse. Because the diffusion coefficient in (10.2.4) is a molecular diffusion coefficient, there is little dispersion in the region in the perifusion chamber from the cells to the chamber outlet, and therefore the functional form of Q_3 is very similar to Q_2 and is not shown.

The model prediction for 1, and 5 min upstream injection pulses is shown in Figure 10.3 B and D. There is significant attenuation of the 1 min pulse, whereas the 5 min pulse retains much of its original shape. These results show that the model, based on the fluid flow and the geometry

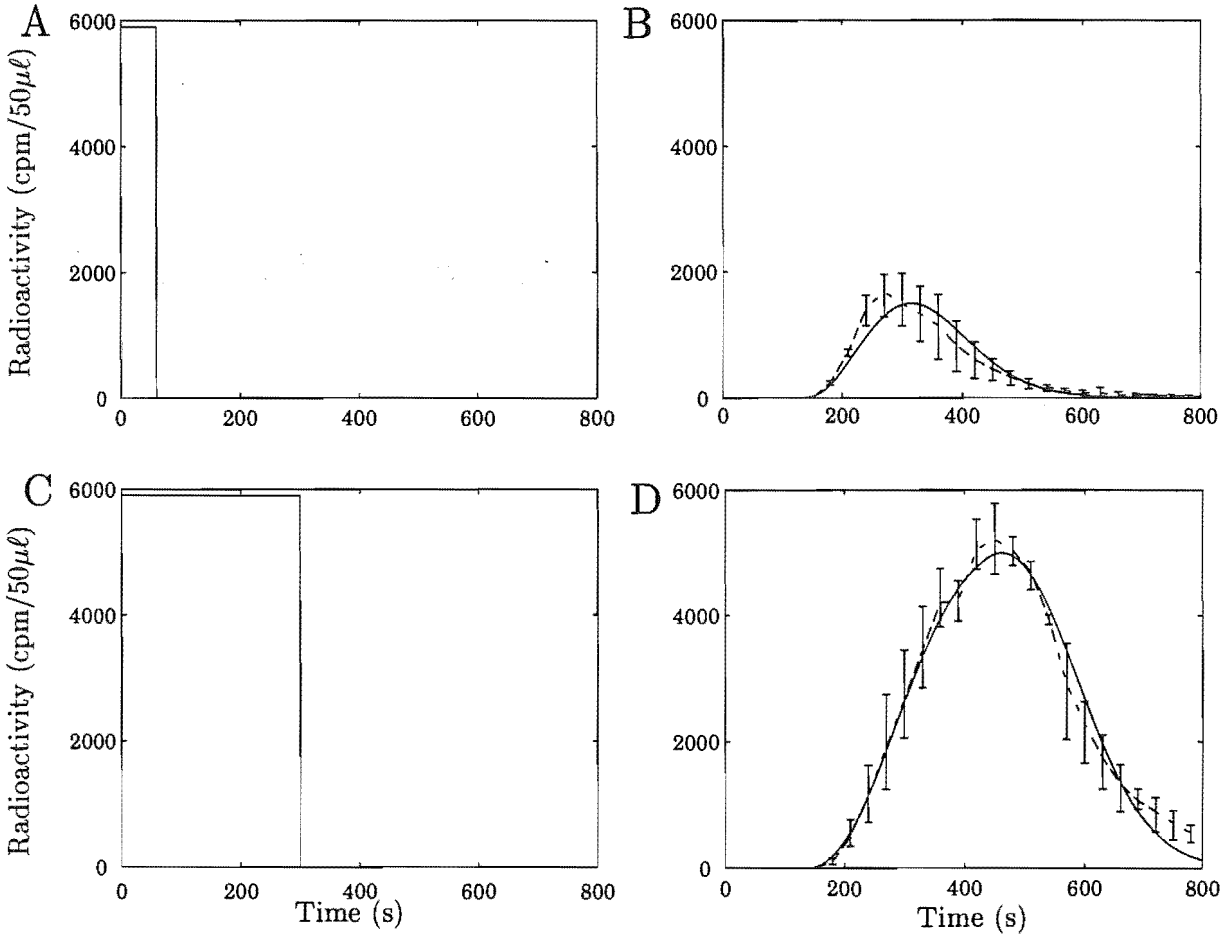

Figure 10.3: Comparison of the perifusion model (—) for the 1 and 5 min pulse experimental data (- - -). The 1 min pulse is significantly attenuated, whereas the 5 min pulse retains much of its original shape.

of the system, agrees favourably with the experimental data, particularly for the longer pulses, where the relative amount of noise is lower.

The major discrepancy with the experimental data is that the predicted model concentration profiles decrease to zero at a faster rate. It is possible that the bead matrix in the chamber slightly

impedes the flow of the tracer, thus delaying the decrease in the measured concentration profile. However it would be speculative to include such an effect in the model. The model also predicts slightly lower peak concentration levels. Possible causes of this are that the fluid is partially pseudoplastic, there is only partial mixing within the cell chamber, or we have slightly underestimated D_{AVP} for the saline solution. These three aspects all enable less dispersion. However, the current system data is not sufficiently accurate to elucidate the finer details of the dispersion.

The Taylor theory of Section 9.3.2 allows the partial differential equations (10.2.1) and (10.2.5) to be suitably approximated by the equation

$$\frac{\partial c_i}{\partial t} + \bar{v}\frac{\partial c_i}{\partial z} = \eta \frac{\partial^2 c_i}{\partial z^2}, \quad z \in [0, \ell_i], \quad t > 0, \quad i \in \{1, 4\} \tag{10.3.1}$$

where $\bar{v}$ is the average flow velocity, and η is the Taylor's effective coefficient of diffusion given by (9.3.14). Observe that η is significantly larger than the molecular diffusion coefficient D (see Table 10.1). This approximation is valid if (9.3.6) exhibits a ratio of at least 10 : 1. However for the geometry and molecules under consideration in the perifusion system, a ratio of at most 3 : 1 can be obtained. Therefore the Taylor approximation (10.3.1) is on the borderline of reasonable approximations to (10.2.1). This approximation is shown in Figure 10.4. A notable feature of this

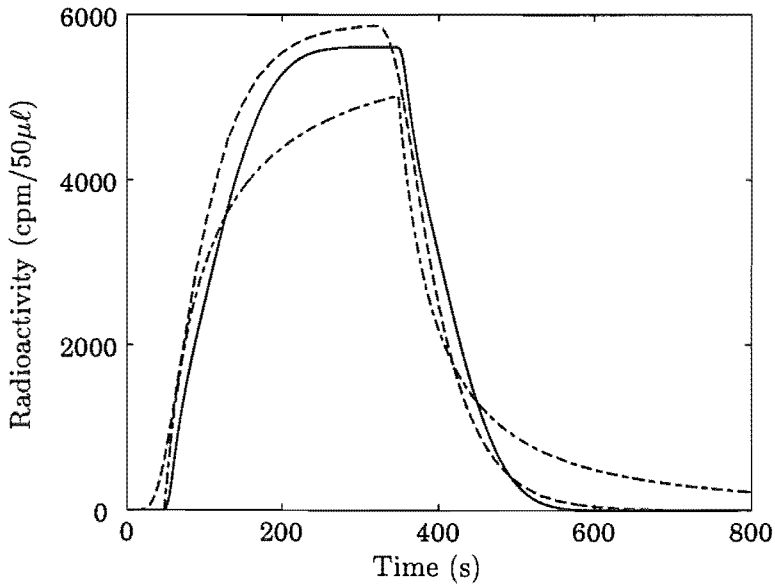

Figure 10.4: Comparison of Q_1 for the full perifusion model (—), the pure shear dispersion model (– — –), and the Taylor approximation (– – –) for a 5 min injection pulse (c_0) of AVP.

diagram is that the concentration peak for the Taylor and full perifusion model is higher than that for the pure dispersion model. This is because the tracer is able to diffuse from the centre of the pipe into the slower fluid near the pipe boundary, thus counteracting the pure dispersive effect of the velocity gradient. Although the minimum travel time down the pipe is shorter in the

Taylor model, the Taylor approximation to the full perifusion model is quite good, given that the approximation is near the suggested borderline of reasonable approximation.

As discussed in Section 9.3.3 the true injection boundary condition is of the form (9.3.20). The extra diffusive term in (9.3.20) was deemed to be particularly important in a model of the perifusion column (Smith et al., 1991). However, the diffusion coefficient in this diffusive term is the molecular diffusion coefficient, and so this diffusive term in the boundary condition can be omitted. This assumption can also be verified numerically, where inclusion of this extra term has no effect on the model solutions.

We now consider the inverse problem of predicting the input concentration c_0 from knowledge of the output concentration measurement Q_4. Associated inverse problems have been previously analysed in Chapters 7, 8, and 9, and we now wish to apply them to the perifusion apparatus. The inverse problem can be divided into four smaller inverse problems; three inverse advection-diffusion equations and one inverse mixing problem. The deconvolution procedures for these problems have been discussed in Sections 9.3.4 and 9.2.2. Unless specified otherwise, the results in this section were obtained with a mollification radius of $\delta = 62.5$ s, and mesh intervals of $N = 50$, and $M = 250$ respectively (see Section 9.3.4). Results based on the hyperbolic regularisation procedures in Chapter 11 yield similar results to the mollification method.

The deconvolution process is shown in Figure 10.5, where a 2 min experimental curve from Figure 10.2 D is used as the concentration measurement Q_4. The predicted concentration at the cells, chamber entrance, and pump are shown in Figure 10.2 B, C, and D respectively. The input pulse is unable to be completely reconstructed for two reasons. Firstly the model is an approximation to the actual system, and we have used the Taylor approximation to this model. The second and more important reason is that because the inverse problem is ill-posed, we cannot expect to reconstruct the high frequency components of the input concentration. What we have reconstructed is a reasonable approximation to the mollified input. The reconstructions for the 1 and 5 min pulses in Figure 10.3 B, D are similar (not shown).

10.4 CRH-induced ACTH data enhancement

We have observed that there is a certain amount of dispersion in the signal travelling down the perifusion system, particularly for pulses of short duration. The methods of the previous section are now used to account for this in CRH-induced ACTH measurements from equine corticotrophs (Evans et al., 1993b), (p 396).

Firstly, using (10.2.1) and (10.2.2), we can predict the CRH concentration profile that the cells are exposed to (see Figure 10.6 B (– – –)). Secondly, given the collected ACTH concentration profile measurement, the ACTH concentration profile secreted by the pituitary cells can be

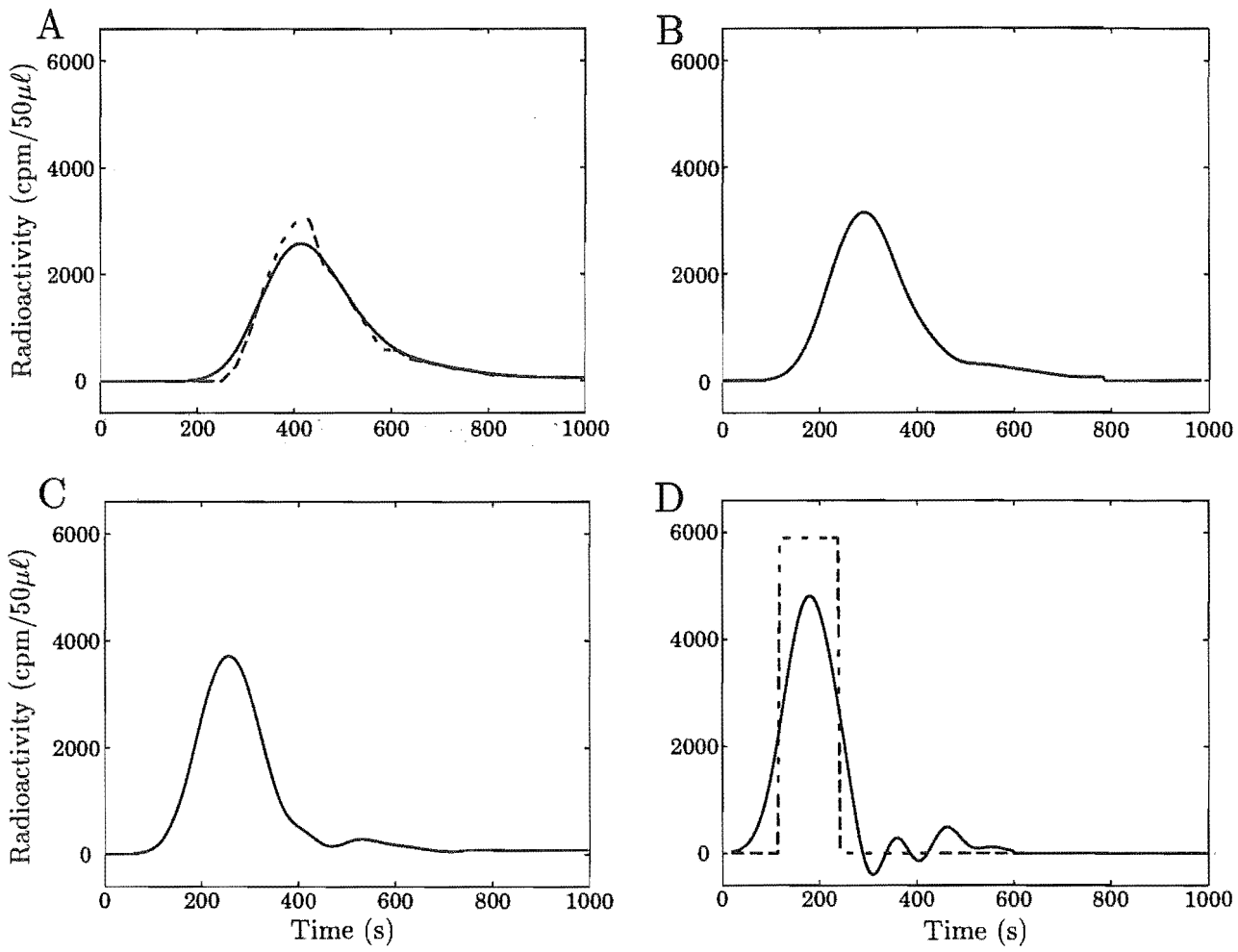

Figure 10.5: Prediction of the input concentration from an output concentration measurement in a 2 min pulse validation experiment. (A) The output concentration measurement Q_4 (– – –), and its mollification (—). (B) The predicted concentration at the cells (Q_2). (C) The predicted chamber entrance concentration (Q_1). (D) The predicted input concentration (c_0) (—), and the actual input concentration (– – –).

estimated. This reconstruction is shown in Figure 10.6 B(—). This deconvolution supports the

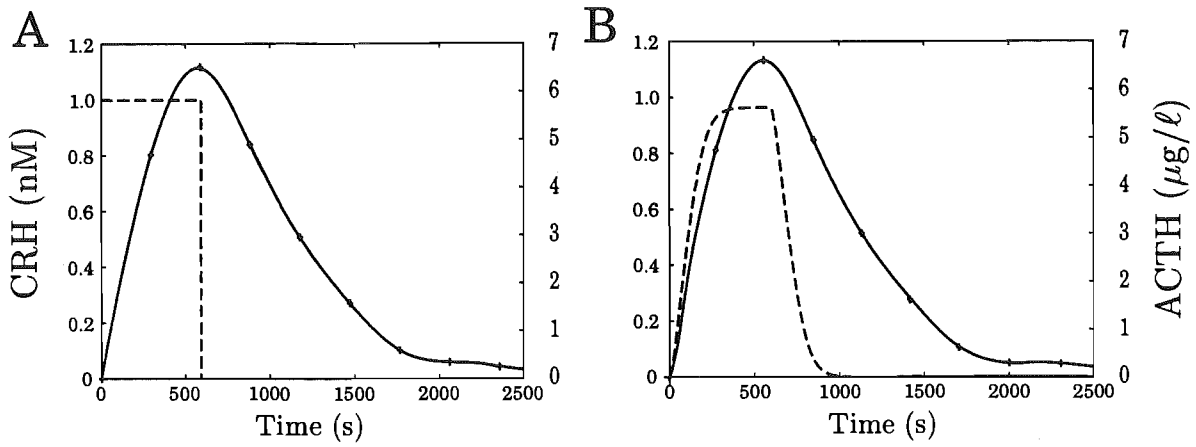

Figure 10.6: CRH-induced ACTH secretion data. (A) The 10 min CRH input pulse (c_0) of 0.1 nM (- - -), and the ACTH measurement (Q_4) (—) collected in 5 min fractions (+). (B) Predicted CRH concentration profile at the pituitary cells (Q_2) (- - -), and the predicted ACTH concentration profile secreted by the pituitary cells (—).

concentration dependent, rapid activation of CRH-induced ACTH secretion, and a delayed return to basal ACTH secretion following the termination of the CRH pulse. This contrasts with the raw data, which suggests a significant delay in activation of the CRH-induced ACTH secretion. This interpretation agrees with data from the microperifusion system, which allows the delivery of square wave pulses to the cells, and an ACTH measurement very near the cells. The ACTH response for a 3 min CRH pulse from the microperifusion system (Watanabe and Orth, 1987) is shown in Figure 10.7. The onset of ACTH secretion is rapid compared with the delay in the return to basal ACTH secretion levels following the termination in the CRH pulse.

The decay in ACTH secretion following the termination of the CRH pulse can be suitably approximated by an exponentially decaying function. The rate of decay in this function is then a simple measure of the time for ACTH secretion to return to basal levels. This rate of decay can be more accurately determined from the deconvolved data, particularly for data obtained from short CRH pulses. Interestingly this rate of decay appears to depend on [CRH] (see Figure 10.7).

For the raw data in Figure 10.6, one can associate 1 nM CRH with an ACTH secretion rate of about 6.5 mg/ℓ. Because the cells are nearly exposed to 1 nM CRH, there is little error in this statement. However due to dispersion, similar associations between the injected CRH concentration and the measured ACTH concentration for shorter CRH pulses will not be valid.

The cell does not see a square wave CRH profile, and it is difficult to predict what the cell would secrete given a square wave CRH profile. To do so would require knowledge of the cellular functional relationship between CRH and ACTH secretion. However this relationship is not

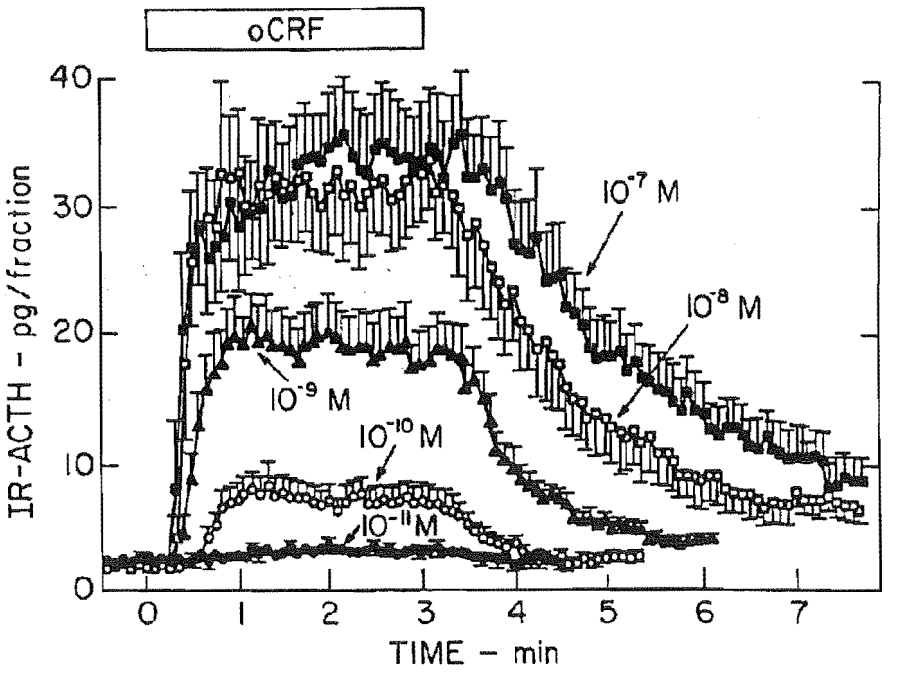

Figure 10.7: Experimental ACTH output from ovine pituitary corticotroph cells for a 3 min CRH pulse (indicated by the horizontal oCRF bar). Higher concentrations of CRH induce a greater ACTH response. The onset of ACTH secretion is rapid compared to the delay in ACTH secretion returning to basal following the termination in the CRH pulse. Data from Watanabe and Orth (1987), p1139.

known, and in fact the experiments are designed to infer this relationship. One can also argue that cells *in vivo* are never exposed to square wave hormone pulses. This is because the hormone must travel in the bloodstream, and therefore a certain amount of signal dispersion must occur. However the microperifusion system is superior to the perifusion system, as it enables the delivery of a wider range of CRH inputs, with higher resolution in the ACTH secretion rate. Justifiably this superior system is more expensive to setup.

10.5 Discussion

The major drawback of the perifusion system derives from the dispersion and mixing of the tracer in the pipe. This is particularly significant for input pulses of short duration. We have constructed a mathematical model of the fluid flow in the perifusion system, and observed that it explains a number of observable features in the measured concentration profile. We have also constructed a useful approximation to the model, the advection-diffusion equation, and outlined under what conditions the approximation is valid and how the associated parameters relate to measurable quantities.

We have also introduced a class of inverse problems in order to deconvolve, or take account of the introduced experimental errors in the perifusion apparatus. Due to the ill-posedness of the inverse problem, there is a limit to the degree of data improvement. However, in contrast with the raw data, this deconvolution supports a concentration dependent, rapid activation of CRH-induced ACTH secretion, and a delayed return to basal ACTH secretion following the termination of the CRH pulse. This interpretation agrees with data obtained from the microperifusion system.

The major drawbacks of the perifusion system have been highlighted, and a number of improvements can be based on these drawbacks. In order to circumvent the dispersion in the perifusion system a number of improved systems have been devised, notably the microperifusion apparatus designed by Watanabe and Orth (1987), which eliminates the pipes altogether. One can also decrease the dispersion in the pipes by using a pseudoplastic fluid, or by increasing the fluid flow rate. However the pituitary cells do not behave normally if the fluid flow rate is too large, so this is not a viable option. Decreasing the cell chamber volume will also reduce the amount of dispersion in the input concentration profile.

Chapter 11

Signal Restoration after transmission through an advective and diffusive medium

11.1 Introduction

This chapter considers an inverse problem associated with mass transport in a pipe. It illustrates how wave splitting techniques can be utilised for an inverse problem associated with one-dimensional mass transport processes. This is done by using a generalisation of Fick's law which introduces a relaxation parameter into the problem, so converting the parabolic partial differential equation by a singular perturbation into a hyperbolic one. This generalised law by ensuring finite mass flux propagation speeds, enables a stable equation to be utilised to reconstruct the interior boundary condition; so providing a regularised solution to the inverse problem.

When a mass concentration of a material is transported within a fluid of a different material, the estimation of the final temporal profile, downstream of the injection point, from the knowledge of the initial injection temporal profile, is a relatively straight-forward problem; it is required to solve a well-posed parabolic partial differential equation. This is termed a *direct* problem. However, when a mass concentration of a material flowing and diffusing within an advecting fluid is measured downstream of the injection point, the estimation of the initial injection profile is a difficult problem. This is termed an *inverse* problem; in particular an inverse source problem. As discussed in Section 9.3.4, this problem is difficult because it is *ill-posed*, and besides the difficulty of problem formulation, it must also be made well-posed.

It is assumed throughout this chapter that the advective medium also allows diffusion. If this is not the case the problem is considerably simpler, and can be solved by the techniques

illustrated in (Wall and Lundstedt, 1998; Connolly and Wall, 1997). In many other applications it is required to estimate an input signal given a signal that has been modified by transmission through a distorting system (Lundstedt and He, 1994; Lundstedt and He, 1997; Weber, 1981; Eldén, 1988; Murio and Roth, 1988; Connolly and Wall, 1997; Wall, 1997).

We now discuss a source reconstruction problem, for the advection equation, in a well known transport situation. If a pollutant, with concentration $c(x,t)$, is emitted upstream, at a station $x = 0$, in a medium flowing with speed $\overline{v}$, and the pollutant concentration is measured down stream, the methods given in this chapter can be utilised to estimate the magnitude and temporal distribution of the emission, expressed by $c(0,t)$. The model is simplistic, and the problem is considered one-dimensional; in this case the model equation, one is first lead to would be

$$\partial_t c + \overline{v}\partial_x c - \kappa^2 \partial_x^2 c = 0,$$

where κ^2 is the fluid diffusivity. As explained above, as this partial differential equation is parabolic, the problem of estimation of $c(0,t)$, from a down-stream measurement of $c(\ell,t)$, where $\ell > 0$, is ill-posed. In this chapter, this problem is converted to a well-posed one by studying a related hyperbolic equation.

Weber (Weber, 1981) has converted a parabolic equation into a hyperbolic one in order to produce a well-posed inverse problem, and this idea has been further developed by a number of authors (Eldén, 1988; Murio and Roth, 1988; Murio, 1993; Wall, 1997). Similarly, in this chapter, which considers the solution of inverse problems associated with parabolic direct problems, the wave speed of an associated hyperbolic problem is to be considered as a regularisation parameter.

Wave splitting and invariant imbedding techniques have been very successful in their application to many inverse problems for hyperbolic equations. They have also been successful when applied to elliptic problems (Powell, 1995), but they have not been effective for parabolic equations. Indeed it has been shown by Vogel (Vogel, 1992) that layer stripping techniques are not suitable for parabolic equations.

The paper Wall and Olsson (1997), which is henceforth denoted as (I), is the outcome of research towards the application of wave splitting and invariant imbedding techniques to phenomena that are generally considered parabolic in nature. We concentrate, in the sequel, our ideas towards the evaluation of mass transport processes in fluids, through wave splitting techniques when a generalised form of Fick's law is utilised. This generalised law provides physical motivation for the extension of the direct parabolic problem to a hyperbolic one. The wave splitting method enables us to extend the integral equation method of (Murio and Roth, 1988), as has been done for purely diffusive processes in (Wall, 1997), to advective problems in which the material parameters are functions of the spatial variable.

The problem considered here has direct application to a problem involving the estimation

of secretion of adrenocorticotropic hormone (ACTH) from the pituitary gland. In this problem, assays of the blood flow are taken downstream from the pituitary in a horse, which is secreting ACTH, and it is then required to estimate the concentration of ACTH at the pituitary, (Alexander et al., 1988).

In viscous flow problems, involving a solute concentration in a pipe, the variation of the velocity over the cross-section of the pipe is an important factor in the dispersion of the solute; it is called shear dispersion. The dispersion of a pulse of concentration flowing down the pipe is in general due to the combined action of shear dispersion, parallel to the axis of the pipe, and molecular diffusion, predominantly in the radial direction. When the molecular diffusion coefficient within the flow is very small, then shear dispersion is the dominant dispersive effect; this regime is examined in Chapter 7 for an inverse problem similar to the one considered in this chapter. Taylor (Taylor, 1953) has developed a theory which in a certain parameter regime enables the combined effects of shear dispersion and radial molecular diffusion to be replaced by an equivalent one-dimensional advection-diffusion equation. A considerable literature has built up about this direct problem (for recent application of modern theory to this direct problem see Watt and Roberts (1995)). The Taylor theory therefore enables an apparent diffusion coefficient to be used to model both the shear and cross-diffusion dispersion effects as a one-dimensional advection-diffusion problem. The theory presented here is therefore again applicable with the molecular diffusion parameter replaced by an appropriate effective value.

When $\overline{v}$ tends to zero, the reconstruction problem reverts to the one for a pure diffusion problem, as considered in (I). For non-zero $\overline{v}$ and small κ, the problem may be solved without regularisation by techniques similar to those in Wall and Lundstedt (1997)[1]. However, for moderate values of κ, techniques which restore the continuity of the solution on the data like those discussed in this chapter, must be utilised.

Wave splitting techniques, as used in other problems, proceed by finding an analytic representation of the square root of an operator. This operator is often a differential operator, and the square root is a pseudo-differential operator. In this chapter, because of the complex phenomena under consideration, a new feature is that the pseudo-differential operator is related to the factorisation of a quadratic operator equation (see Karlsson and Rikte (1998) for another interesting operator factorisation).

In Section 11.2 the prerequisite equations are developed for *one-dimensional* mass transport, through hyperbolisation. The homogeneous parameter model and its reduction to various problems is discussed in Section 11.3. It is proven in this section, that the hyperbolic case is well conditioned and provides a regularised solution to the parabolic problem. The parabolic problem

[1]Similar techniques can be applied to problems with non-zero κ and large $\overline{v}$.

can be considered as the limiting case of the hyperbolic problem by a singular perturbation. Then in Section 11.4, the wave splitting concept is used to transform these equations into two coupled one-way wave equations, with only the second-order differential form covered. In Section 11.5, the equations for the wave propagators are derived, and these are specialised to the forward and transmission Green propagators in Section 11.5.1 and Section 11.5.2, respectively. These propagators are used in the signal reconstruction problem discussed in Section 11.6.

As many multivariate derivative operators are involved in this chapter, it is convenient to use a number of commonly used derivative notations for clarity of exposition; these are represented by:

$$\partial_t f(x,t,s) \equiv D_t f(x,t,s) \equiv \mathbf{D}_2 f(x,t,s).$$

11.2 Preliminaries

It has been shown that when heat waves are important, the equation connecting the heat flux to the temperature must at least have an extra thermal inertia term added, when compared to Fourier's conduction law. The Cattaneo equation (Cattaneo, 1948) for heat flow in a heat conducting solid has such a term[2]. This leads to the idea of generalising the Fickean law connecting mass flux J, directed in the x-coordinate direction, to the mass concentration per unit volume, and this can be written as

$$\tau \frac{\partial J}{\partial t} + J = -\kappa^2 \frac{\partial c}{\partial x}, \tag{11.2.1}$$

where τ is a relaxation time, and κ^2 is the mass diffusivity of the media[3]. The relaxation time depends on the mechanism of mass transport, and represents the time lag needed to establish steady-state mass transfer in an element of volume when a concentration gradient is suddenly applied to that element.

When Fick's law is utilised as the constitutive equation connecting mass flux and the gradient of mass concentration, the resultant equation governing the dynamics of the mass flow is a parabolic equation, and consequently has the non-physical property that information propagates at an infinite speed; this results in the zero propagation time paradox. When such an equation is used in applications such as those modeling spatio-temporal population density distributions it can lead to erroneous densities. It also means that the partial differential equation describing the phenomenon is unilateral with respect to time flow. However parabolic equations do propagate some properties at a finite velocity (Day, 1997b; Day, 1997a; Herrera and Falcón, 1995). The theory considered in this chapter is linear, and can therefore only be considered as appropriate for

[2]See (I) and the references quoted therein.

[3]For convenience it is expedient for us to define diffusivity, κ^2, as the square of the usual terminology.

a small perturbation theory, or alternatively as a linearization of a more general nonlinear theory (Barletta and Zanchini, 1997).

The other equation necessary to link concentration density to the transport mass flux, the velocity field of the embedding medium $\overline{v}$,[4] and the internal rate of production of mass concentration, r, is the conservation of mass equation

$$\frac{\partial c}{\partial t} + \frac{\partial (J + c\overline{v})}{\partial x} = r.$$

These two linear equations can be written as the system

$$\begin{bmatrix} 1 & 0 \\ \overline{v} & 1 \end{bmatrix} \partial_x \begin{bmatrix} c \\ J \end{bmatrix} = \begin{bmatrix} 0 & -\kappa^{-2}(\tau\partial_t + 1) \\ -\partial_t - \partial_x(\overline{v}) & 0 \end{bmatrix} \begin{bmatrix} c \\ J \end{bmatrix} + \begin{bmatrix} 0 \\ r \end{bmatrix}, \tag{11.2.2}$$

where in what follows, unless stated to the contrary, all coefficients in the partial differential equation will be assumed to be independent of the dependent variables, but functions of the spatial variable x. The coefficients will further be assumed to be time independent; such an assumption holds for many materials (see for example Åberg et al. (1996), and Wall and Lundstedt (1997), for problems for which this is not the case). Throughout this chapter it is assumed that the material parameters κ^2, $\overline{v}$, and τ are continuously differentiable in the region of interest. All parameters are assumed to be positive. The parameters which are essential to the discussion in this chapter are the diffusivity κ^2, the relaxation time τ, and the mass flux wave slowness ν, with $\nu^2 = \kappa^{-2}\tau$.

As the leading matrix of the system (11.2.2) is non-singular, these equations can be rewritten as the system

$$\partial_x \begin{bmatrix} c \\ J \end{bmatrix} = \begin{bmatrix} 0 & -\kappa^{-2}(\tau\partial_t + 1) \\ -\partial_t - \partial_x(\overline{v}) & \overline{v}\kappa^{-2}(\tau\partial_t + 1) \end{bmatrix} \begin{bmatrix} c \\ J \end{bmatrix} + \begin{bmatrix} 0 \\ r \end{bmatrix}, \tag{11.2.3}$$

and this modified system is what is considered in the sequel. This system can also be written as a second order partial differential equation, but only when τ is a constant (*c.f.* (I) where $\overline{v} \equiv 0$).

$$\nu^2\partial_t^2 c + \kappa^{-2}\partial_t c - \partial_x^2 c + \kappa^{-2}\overline{v}\partial_x c - 2\partial_x(\ln(\kappa))\partial_x c + \kappa^{-2}\partial_x(\overline{v})c + \nu^2\partial_x(\overline{v})\partial_t c + \nu^2\overline{v}\partial_t\partial_x c = \kappa^{-2}(\tau\partial_t r + r). \tag{11.2.4}$$

It is considered in the remainder of the chapter that τ will *not* be x-dependent if the second-order equation (11.2.4) is under consideration; this is because this equation is only valid in this case. For the system (11.2.3), it is *not* necessary to make this assumption. However when the hyperbolic equations are considered as a singular perturbation of the parabolic equations, τ is generally thought of as constant.

[4]The velocity field of the embedding medium advects the mass concentration.

11.3 Homogeneous Material Parameters

Hyperbolic layer stripping procedures are well-conditioned problems. This is because a point in space-time, for one of the coupled one-way wave equations has only one line of dependency. Therefore there is a simple travel time map enabling layer stripping type algorithms to proceed. This is *not* true for parabolic problems. These problems have solutions of non-compact support even when the initial condition has compact support. This is a manifestation of the *infinite speed of propagation* synonymous with these equations.

We start by examining the solution properties for the inverse problem associated with parabolic and hyperbolic versions of the problem when the medium parameters are constant.

11.3.1 Parabolic Advection equation with constant coefficients

Consider the equation (11.2.4) with $\nu \equiv 0$, $r \equiv 0$ on the semi-infinite x-axis and with all material parameters homogeneous

$$\kappa^{-2}\overline{v}\partial_x c + \kappa^{-2}\partial_t c = \partial_x^2 c, \quad 0 < x < \infty, \quad t > 0, \tag{11.3.1}$$

with prescribed initial–boundary values

$$\begin{aligned} c(0,t) &= h(t), \quad t > 0, \\ c(x,0) &= 0, \quad 0 < x < \infty. \end{aligned} \tag{11.3.2}$$

Equation (11.3.1) is parabolic and therefore requires two boundary conditions for well-posedness; boundedness of the solution as $x \to \infty$ is also imposed as well as the boundary value at $x = 0$.

The inverse problem we pose is one of measuring the concentration at a station $x = \ell$, i.e.,

$$c(\ell, t) = f(t), \tag{11.3.3}$$

and from this it is required to estimate the boundary function $h(t) = c(0,t)$. The direct map is described through (11.3.1).

It can be shown that the solution to this initial–boundary value problem is

$$c(x,t) = \int_0^t k(x,s)h(t-s)\,ds, \tag{11.3.4}$$

where the kernel $k(x,t)$ is

$$k(x,t) = \frac{x}{2\kappa\sqrt{\pi}t^{3/2}} \exp\left(\frac{-(x-\overline{v}t)^2}{4\kappa^2 t}\right). \tag{11.3.5}$$

Since (11.3.5) defines a delta family (Stakgold, 1979), (p 110), it follows that $\lim_{x\to 0} k(x,t) = \delta(t)$, where δ is the Dirac delta distribution, and $k(x,t)$ is the kernel in (11.3.5). When $\kappa \to \infty$, which

corresponds to perfect mixing where the fluids are instantaneously mixed, $\lim_{\kappa\to\infty} k(x,t) = \delta(t)$, and the solution to (11.3.4) is

$$\lim_{\kappa\to\infty} c(x,t) = h(t). \tag{11.3.6}$$

When $\kappa \to 0$, the flow corresponds to perfect displacement and diffusion disappears. It follows that $\lim_{\kappa\to 0} k(x,t) = \delta(x - \overline{v}t)$, and the solution to equation (11.3.4) then reduces to

$$\lim_{\kappa\to 0} c(x,t) = h(t - \overline{v}^{-1}x)\mathrm{H}(t - \overline{v}^{-1}x). \tag{11.3.7}$$

This is intuitively correct, as in the limit $\kappa \to 0$, the equation (11.3.1) becomes the advective equation. The final limit to consider is when $\overline{v} \to \infty$, where the advective effects dominate the diffusive effects. In this case $\lim_{\overline{v}\to\infty} k(x,t) = \delta(t)$, and the solution to (11.3.4) is given by

$$\lim_{\overline{v}\to\infty} c(x,t) = h(t). \tag{11.3.8}$$

For non-zero κ the kernel provides a non-localised propagation mechanism in contra-distinction to the case when $\kappa = 0$, where the equation (11.3.1) is hyperbolic. In this limit case the initial condition will propagate along the characteristics $t = \overline{v}^{-1}x$. In order to perform layer stripping it is necessary that the physical phenomenon which is used to probe the medium propagates at finite speed and has a wave-like behaviour. The solution for (11.3.1) has such behaviour when κ is very small. If κ is moderately large, it is not possible to solve the problem by layer stripping, see (I) and (Vogel, 1992). One feature of the solution to (11.3.1), is that a wave will propagate at a velocity near $\overline{v}$, but only in the direction of increasing x. This means the equation (11.3.1) can be considered as a one-way wave equation; as such no reflection experiments are possible. Transmission measurements are the only possible method of solving the inverse problem; see (Wall and Lundstedt, 1998) for further information on inverse problems for a one-way wave equation.

The regularisation of the inverse problem of source concentration reconstruction by mollification has been examined in Section 9.3.4. We now consider regularisation of the problem by hyperbolisation of the parabolic problem.

11.3.2 Hyperbolic Advection Equation

The use of a hyperbolic problem to regularise parabolic problems seems a sensible physical extension, given the development of Section 11.2. We show here that the equivalent hyperbolic inverse problem to that discussed in Section 11.3.1 is well conditioned.

When the material parameters are homogeneous equation (11.2.4) becomes

$$\nu^2\partial_t^2 c + \nu^2\overline{v}\partial_t\partial_x c + \kappa^{-2}\overline{v}\partial_x c + \kappa^{-2}\partial_t c = \partial_x^2 c, \quad 0 < x < \infty, \quad t > 0, \tag{11.3.9}$$

with prescribed initial–boundary values

$$c(0,t) = h(t) \quad t > 0, \tag{11.3.10}$$
$$c(x,0) = 0, \quad 0 < x < \infty.$$

Equation (11.3.9) is hyperbolic and therefore requires two boundary conditions for well-posedness; boundedness of the solution as $x \to \infty$ is also imposed as well as the boundary value at $x = 0$. It is seen that as $\nu \to 0$, (11.3.1) can be considered a singular perturbation of (11.3.9).

To examine the well-posedness of the problem we extend the function $c(x,t)$, and the partial differential equation (11.3.9), by zero for $t < 0$, and consider its Fourier transform. The Fourier transform of the dependent variable is pivotal in our argument; it is

$$\widehat{c}(x,\xi) = \widehat{h}(\xi) \exp\left(\frac{\kappa^{-2}\overline{v}}{2}x\right) \exp\left(i\xi\frac{\nu^2\overline{v}}{2}x - \sqrt{\frac{\beta|\xi|}{2\kappa^2}}I(\xi,a)x\right), \tag{11.3.11}$$

with

$$a = \frac{1}{\beta}\left(\frac{\overline{v}^2}{4\xi\kappa^2} - \xi\nu^2\kappa^2\widetilde{\beta}\right), \quad \beta = 1 + \frac{\nu^2\overline{v}^2}{2}, \quad \widetilde{\beta} = 1 + \frac{\nu^2\overline{v}^2}{4}, \tag{11.3.12}$$

and where

$$I(\xi,a) = \left(\sqrt{1+a^2} + \sigma a\right)^{1/2} + i\sigma\left(\sqrt{1+a^2} - \sigma a\right)^{1/2}, \tag{11.3.13}$$

with $\sigma = \text{sign}(\xi)$. It should be noted that there is a difference in definition between the I used here and that in equation (9.3.29)[5], but they are identical when $\nu = 0$. When use is made of the boundary condition (11.3.10) it can be seen that for the inverse signal reconstruction problem, the operator mapping $f \to h$ in the Fourier transform domain can be written as

$$\widehat{h}(\xi) = \widehat{f}(\xi) \exp\left(-\frac{\kappa^{-2}\overline{v}}{2}\ell\right) \exp\left(-i\xi\frac{\nu^2\overline{v}}{2}\ell + \sqrt{\frac{\beta|\xi|}{2\kappa^2}}I(\xi,a)\ell\right). \tag{11.3.14}$$

It should be noted, forgetting any ill-posedness, that the function h, denoted here by h^H reconstructed from (11.3.14), will not be equal to the solution reconstructed from (11.3.1), denoted here by h^P, as the later is associated with the parabolic problem, while the former is associated with the hyperbolic problem. This is just a statement that the inverse mapping operators for these two problems are not identical, although as $\nu \to 0$, $\|h^H - h^P\| \to 0$ with a rate of convergence given by the following consistency estimate.

Lemma 11.3.1. *If* $h^P \in \mathrm{H}^1$ *and* $M = \max(\|h^P\|, \|h^{P'}\|)$, *then* $\|h^H - h^P\| = M\mathcal{O}(\nu^2)$.

[5]Both references (Murio, 1993) and (Murio and Roth, 1988) have typographical errors in the definition of a function similar to our I function.

Proof. Using (11.3.14), and (11.3.11) when $\nu = 0$, it follows that

$$\|h^P - h^H\|_2 = \|(1-\chi)\widehat{h^P}(\xi)\|_2. \tag{11.3.15}$$

where

$$\chi = \exp\left(\frac{-i\xi\nu^2\overline{v}\ell}{2} + \sqrt{\frac{|\xi|}{2\kappa^2}}\left(\sqrt{\beta}I(\xi,a) - I\left(\xi, \frac{\overline{v}^2}{4\xi\kappa^2}\right)\right)\ell\right), \tag{11.3.16}$$

with $0 \leq |\chi| \leq 1$, and $\lim_{\nu\to 0}|\chi| = 1$. Since $h^P \in \mathrm{H}^1$, then $\xi\widehat{h^P}(\xi) \in \mathrm{L}^2$, and it follows that $\exists N > 0$ such that

$$\|h^P - h^H\|_2 = \sqrt{4\int_0^N |1-\chi|^2|\widehat{h^P}|^2\, d\xi} \tag{11.3.17}$$

$$\leq 2M\sqrt{N}\max_{\xi\in[0,N]}|1-\chi| \tag{11.3.18}$$

$$\leq 2M\sqrt{N}, \quad \forall\nu \tag{11.3.19}$$

This bounds the error for large ν. For small ν, a series expansion of (11.3.18) about $\nu = 0$ yields

$$\|h^P - h^H\|_2 = M\mathcal{O}(\nu^2), \quad \forall\nu. \tag{11.3.20}$$

A weaker form of this lemma when $\overline{v} = 0$ appears in Murio (1993), Murio and Roth (1988), and Roth (1989) . □

The important behaviour of (11.3.14) is as $|\xi| \to \infty$ and we observe that

$$\max_{|\xi|\in[0,\infty]}\left|\sqrt{\frac{\beta|\xi|}{2\kappa^2}}\mathcal{R}e(I(\xi,a))\ell\right| \leq \max\left\{\frac{\overline{v}\ell}{2\kappa^2}, \frac{\beta\ell}{2\kappa^2\nu\widetilde{\beta}^{\frac{1}{2}}}\right\} = \overline{k}. \tag{11.3.21}$$

It is now seen that the effect of hyperbolicity is to bound the growth of the exponential function for large values of $|\xi|$, with

$$\left|\exp\left(\sqrt{\frac{\beta|\xi|}{2\kappa^2}}\mathcal{R}e(I(\xi,a))\ell\right)\right| < e^{\overline{k}}. \tag{11.3.22}$$

It therefore follows that

$$\|\widehat{h^H} - \widehat{h_m^H}\|_2^2 \leq e^{\overline{k}}\|\widehat{f_m} - \widehat{f}\|_2^2, \tag{11.3.23}$$

where h_m corresponds to $u(0,t)$ when f is replaced by f_m. The stability result then follows from Parseval's theorem.

Lemma 11.3.2. *If $f, f_m \in L^2$ then*

$$\|h^H - h_m^H\|_2^2 \leq e^{\overline{k}}\|f_m - f\|_2^2 \tag{11.3.24}$$

We see the hyperbolic problem ensures that the inverse mapping operator has a Lipschitz continuity result, when the data $f_m \in C$, and $\nu > 0$ is fixed. Furthermore, considering the hyperbolic problem (11.3.9) as a regularisation of (11.3.1), as $\|f_m - f\| \to 0$, ν can be reduced. Well-posedness of the inverse problem then follows from the two lemmata.

Theorem 11.3.3. *The inverse problem is stable with respect to perturbations in the data f. If the exact boundary function $h^P \in C^1$ with $\max(|h^P|, |h^{P\prime}|) < M$ then the solution h^P to the inverse problem satisfies*

$$\|h^P - h_m^H\|_2^2 \leq e^{\bar{k}} \|f - f_m\|_2^2 + \mathcal{O}(\nu^2) \tag{11.3.25}$$

The well-posedness of the problem is also apparent from the solution to (11.3.9) which is

$$c(x,t) = \exp\left(\frac{\overline{v}x}{2\kappa^2}\left(1 - \frac{\beta}{2\widetilde{\beta}}\right)\right)\left[\exp\left(\frac{-\beta x}{2\kappa\sqrt{\tau}\sqrt{\widetilde{\beta}}\gamma_+}\right) h\left(t - \frac{x\nu}{\gamma_+}\right) + \int_{\frac{x\nu}{\gamma_+}}^{t} k(x,s)h(t-s)\,ds\right], \tag{11.3.26}$$

where the kernel is

$$k(x,s) = \exp\left(\frac{-\beta s}{2\tau\sqrt{\widetilde{\beta}}}\right)\left(\frac{x\nu\sqrt{\widetilde{\beta}}\alpha I_1\left(\alpha\sqrt{\left(s - \frac{x\nu}{\gamma_+}\right)^2 + 2x\nu\sqrt{\widetilde{\beta}}\left(s - \frac{x\nu}{\gamma_+}\right)}\right)}{\sqrt{\left(s - \frac{x\nu}{\gamma_+}\right)^2 + 2x\nu\sqrt{\widetilde{\beta}}\left(s - \frac{x\nu}{\gamma_+}\right)}}\right), \tag{11.3.27}$$

with boundary condition $h(t) \equiv 0$, $t < 0$, where I_n denotes the modified Bessel function of order n, and

$$\alpha = \frac{1}{2\tau\widetilde{\beta}}\sqrt{\beta^2 - \widetilde{\beta}\overline{v}^2\nu^2}, \quad \text{and} \quad \gamma_+ = \sqrt{\widetilde{\beta}} + \sqrt{\widetilde{\beta} - 1}. \tag{11.3.28}$$

Therefore the inverse problem with homogeneous material parameters can be formulated as a Volterra integral equation of the second kind, and the inversion of this equation provides the solution to the signal restoration problem. The theory of second kind Volterra operators implies that the problem is well-posed (Linz, 1985).

The first part of the solution on the right-hand-side of (11.3.26) represents the hyperbolic wave that travels into the medium undistorted but with attenuation. From this part of the solution it can be seen, that the distance into the medium, in which the leading edge of the wave traveling twice this distance is attenuated by e^{-1}, the so-called e-fold distance (Weston, 1988), is

$$x_e = \kappa\sqrt{\tau}\beta^{-1}\sqrt{\widetilde{\beta}}\gamma_+. \tag{11.3.29}$$

The maximum e-fold distance occurs when $\nu\overline{v} = \sqrt{2(\sqrt{2}-1)}$, and $\kappa\sqrt{\tau} \leq x_e < 1.21\kappa\sqrt{\tau}$. The second part of the solution, represented by the convolution integral, directly represents the dissipative or diffusive nature of the problem. Further discussion on the interpretation of this equation can be found in (I).

If the term $\nu^2\overline{v}\partial_t\partial_x c$ is omitted from (11.3.9), then the hyperbolic partial differential equation

$$\nu^2\partial_t^2 c + \kappa^{-2}\overline{v}\partial_x c + \kappa^{-2}\partial_t c = \partial_x^2 c, \quad 0 < x < \infty, \quad t > 0, \tag{11.3.30}$$

can still be considered a valid singular perturbation of the parabolic problem (11.3.1). The solution for the concentration field c within a semi-infinite region with zero initial condition can be found by Laplace transform techniques to be

$$c(x,t) = \exp\left(\frac{\overline{v}x}{2\kappa^2}\right)\left[\exp\left(\frac{-x}{2\kappa\sqrt{\tau}}\right)h(t-\nu x) + \int_{\nu x}^{t} k(x,s)h(t-s)\,ds\right], \tag{11.3.31}$$

where the kernel of the integral is

$$k(x,t) = \exp\left(-\frac{t}{2\tau}\right)\frac{\alpha\nu x \mathrm{I}_1\left(\alpha\sqrt{t^2-\nu^2x^2}\,\right)}{\sqrt{t^2-\nu^2x^2}},$$

with boundary condition $h(t) \equiv 0$, $t < 0$, and

$$\alpha = \frac{1}{2\tau}\sqrt{1-\overline{v}^2\nu^2}.$$

Note that when $\overline{v} = 0$, the solutions in (11.3.26) and (11.3.31) are identical to the solution found in (I). Again the first part of the solution on the right-hand-side of (11.3.31) represents the hyperbolic wave that travels into the medium undistorted but with attenuation, and the second part of the solution is associated with the problem dispersion. In this case the e-fold distance is $x_e = \kappa\sqrt{\tau}$.

For the inverse problem under consideration the measurement is $c(\ell,t)$, so that equation (11.3.31) can be written as

$$c(\ell,t) = \exp\left(\frac{\overline{v}\ell}{2\kappa^2}\right)\left[\exp\left(\frac{-\ell}{2\kappa\sqrt{\tau}}\right)h(t-\nu\ell) + \int_{\nu\ell}^{t} k(\ell,s)h(t-s)\,ds\right], \tag{11.3.32}$$

and again the inverse problem with homogeneous material parameters can be formulated as a Volterra integral equation of the second kind, with the inversion of this equation providing the well-posed solution to the signal restoration problem. This integral equation approach has been examined in Murio and Roth (1988) for the parabolic heat equation.

11.4 Wave Splitting and System Dynamics

We now return to obtaining numerically useful techniques based on wave splitting ideas to find algorithms for the inverse problem when the material parameters are spatially varying.

The equations (11.2.3) and (11.2.4), with $r \equiv 0$, can now both be written in the system form

$$\partial_x \mathbf{u} = \mathbf{C}\mathbf{u} + \mathbf{B}\mathbf{u}, \tag{11.4.1}$$

where for the conversion of the second order partial differential equations $\mathbf{u} = \begin{bmatrix} c & \partial_x c \end{bmatrix}^T$, with component matrices

$$\mathbf{C} = \begin{bmatrix} 0 & \mathbb{I} \\ (\nu^2\partial_t^2 + \kappa^{-2}\partial_t) & \nu^2\overline{v}\partial_t \end{bmatrix}, \qquad (11.4.2)$$

$$\mathbf{B} = \begin{bmatrix} 0 & 0 \\ \partial_x(\overline{v})(\kappa^{-2} + \nu^2\partial_t) & \kappa^{-2}\overline{v} - 2\partial_x(\ln(\kappa)) \end{bmatrix},$$

where $\mathbb{I}$ is the identity operator. In the system case, given by (11.2.3), $\mathbf{u} = \begin{bmatrix} c & J \end{bmatrix}^T$ and the component matrices are

$$\mathbf{C} = \begin{bmatrix} 0 & -\kappa^{-2}(\tau\partial_t + \mathbb{I}) \\ -\partial_t & \overline{v}\kappa^{-2}\tau\partial_t \end{bmatrix}, \qquad \mathbf{B} = \begin{bmatrix} 0 & 0 \\ -\partial_x(\overline{v}) & \overline{v}\kappa^{-2} \end{bmatrix}. \qquad (11.4.3)$$

It should be noted that the preliminary partitions[6], of the matrices $\mathbf{C}$ and $\mathbf{B}$, used in the previous equations are not unique and other partitions may be profitable. The particular choice we have made includes the advection velocity and this seems to be essential in order to provide the methods developed in the next sections. In the next section we diagonalise the operator matrix $\mathbf{C}$; the $\mathbf{B}$ matrix contains only terms irrelevant to this. A consistent partition has been chosen for $\mathbf{C}$ in equations (11.4.2) and (11.4.3) to ensure that they are *similar*, namely they have the same eigenvalue operator-valued matrices (see (11.4.18)).

We note that the $\mathbf{C}$ matrix has an extra advection derivative term, the term $\nu^2\overline{v}\partial_t$ for (11.4.2), and the term $\overline{v}\kappa^{-2}\tau\partial_t$ for (11.4.3), when compared to the wave splitting for one dimensional hyperbolic diffusion wave equations of (I). We have included this term in $\mathbf{C}$ because any physically realistic media involving mass transport must involve advection. To not include this term in the $\mathbf{C}$ matrix will result in non-physical split fields, which will mean that we will be unable to measure the appropriate field to solve the inverse problem specified in Section 11.3.1. One central feature of this inverse problem investigation is that we assume that the measurements are carried out in an advective diffusive medium — not an ideal non-diffusive medium. Inverse problems similar to this but not including advection have been examined in (I).

We shall make use of diagonalising transformations to convert the equations (11.4.1) into the appropriate split form. The pseudo-differential operators found in this section are most easily found by using Laplace transformation techniques on the $\mathbf{C}$ matrices given in equations (11.4.2), (11.4.3), and then finding the algebraic eigen-systems. The pseudo-differential operators are then found by inverse Laplace transformation. Examples of this technique are found in (I).

[6]We use the term preliminary, as a splitting based on this partition will be used later to diagonalise the operator matrix $\mathbf{C}$.

11.4.1 Second Order equation

Using Laplace transform techniques similar to those in (I), it is found that the appropriate diagonalising transformation for the **C** matrix (11.4.2), is given by

$$\mathbf{u} = \mathbf{P}\boldsymbol{v}^{\pm}. \tag{11.4.4}$$

The $\boldsymbol{v}^{\pm}$ have the properties of right and left moving waves and this is discussed further latter in this section. Note that as in (I), it is assumed that

$$c(x,0) = \partial_t c(x,t)|_{t=0} = 0. \tag{11.4.5}$$

The operator-valued matrix in the equation (11.4.4) is defined by

$$\mathbf{P} = \begin{bmatrix} \mathbb{I} & \mathbb{I} \\ \\ \kappa^{-1}\mathbb{K}_-^{-1} & \kappa^{-1}\mathbb{K}_+^{-1} \end{bmatrix}.$$

The inverse operator $\mathbb{K}_{\pm}^{-1}$ is the operator representation of the temporal pseudo-differential operator defined through

$$\mathbb{K}_{\pm}^{-1} = \left(\gamma\sqrt{\tau}\partial_t \pm \sqrt{\partial_t(\chi\partial_t + 1)}\right),$$

where the ratio of the advection velocity to the hyperbolic wavespeed is

$$\gamma = \frac{\overline{v}\nu}{2} = \frac{\overline{v}\kappa^{-1}\sqrt{\tau}}{2},$$

and

$$\chi = \tau(1+\gamma^2).$$

With the definition

$$\gamma_{\pm} = \left(\gamma \pm \sqrt{1+\gamma^2}\right),$$

the operator $\mathbb{K}_{\pm}^{-1}$ has the representation

$$\mathbb{K}_{\pm}^{-1} f = \left(\gamma_{\pm}\sqrt{\tau}\partial_t \pm \frac{1}{2\sqrt{\chi}}(\mathbb{I} - \mathbb{L})\right) f(t), \tag{11.4.6}$$

where $\mathbb{L}$ is the convolution operator

$$\left(\mathbb{L}f\right)(t) = \int_0^t L(x, t-t')f(t')\,dt',$$

with kernel

$$L(x,t) = \exp\left(\frac{-t}{2\chi}\right)\frac{\mathrm{I}_1(t/2\chi)}{t}. \tag{11.4.7}$$

In this equation I_n denotes the modified Bessel function of order n. The operator $\mathbb{K}_\pm$ is the pseudo-differential operator defined through

$$\mathbb{K}_\pm = \left(\gamma\sqrt{\tau}\partial_t \pm \sqrt{\partial_t(\chi\partial_t + 1)}\right)^{-1},$$

and this operator can be represented by the convolution operator

$$\big(\mathbb{K}_\pm f\big)(t) = \int_0^t \widetilde{K}_\pm(x, t-t')f(t')\,dt'.$$

A closed form representation for $\widetilde{K}_\pm$ can be obtained, although the kernel involves a convolution term. In this chapter it suffices to find a convergent series representation for $\widetilde{K}_\pm$, which for $\gamma < 1$ is

$$\widetilde{K}_\pm(x,t) = \pm K_\tau(x,t) - \frac{\gamma}{\sqrt{\tau}}e^{-t/\tau} \pm \frac{\gamma^2}{2\sqrt{\tau}}\left(F\left(\frac{3}{2},1,-\frac{t}{\tau}\right) - \frac{\gamma^2}{4}F\left(\frac{5}{2},1,-\frac{t}{\tau}\right) + \frac{\gamma^4}{8}F\left(\frac{7}{2},1,-\frac{t}{\tau}\right) + \mathcal{O}(\gamma^6)\right), \tag{11.4.8}$$

where the kernel K_τ is the same kernel found for the corresponding operator for thermal processes in (I), namely

$$K_\tau(x,t) = \frac{1}{\sqrt{\tau}}e^{-t/2\tau}\mathrm{I}_0(t/2\tau). \tag{11.4.9}$$

The convolution operator corresponding to this kernel is

$$\big(\mathbb{K}_\tau f\big)(t) = \int_0^t K_\tau(x, t-t')f(t')\,dt'. \tag{11.4.10}$$

The term $F(n,d,z)$, appearing in (11.4.8), is the generalised hypergeometric function. This function is also known as the KummerM function (Abramowitz and Stegun, 1964), (p 504), and is represented by the absolutely convergent series

$$F(n,d,z) = \sum_{k=0}^{\infty}\frac{\Gamma(n+k)\Gamma(d)z^k}{\Gamma(n)\Gamma(d+k)k!},$$

where Γ is the gamma function.

The inverse of the operator-valued matrix $\mathbf{P}$ is then found to be

$$\mathbf{P}^{-1} = \frac{1}{2}\begin{bmatrix} \mathbb{I} + \frac{\gamma}{\sqrt{1+\gamma^2}}(\mathbb{M}+\mathbb{I}) & -\kappa\mathbb{K}_\chi \\ \mathbb{I} - \frac{\gamma}{\sqrt{1+\gamma^2}}(\mathbb{M}+\mathbb{I}) & \kappa\mathbb{K}_\chi \end{bmatrix}, \tag{11.4.11}$$

with the operator $\mathbb{M}$ having the representation

$$\mathbb{M}f = \int_0^t M(x, t-t')f(t')\,dt',$$

with kernel M given by

$$M(x,t) = \frac{e^{-t/2\chi}}{2\chi}\Big(\mathrm{I}_1(t/2\chi) - \mathrm{I}_0(t/2\chi)\Big).$$

The operator $\mathbb{K}_\chi$ is defined by the same representation as $\mathbb{K}_\tau$, namely (11.4.10), but the variable τ in the kernel of this operator, given by equation (11.4.9), is replaced by χ. It is to be noted that $\partial_t K_\chi = \sqrt{\chi}M$.

11.4.2 Operator Properties

We proceed formally and list some of the algebraic properties of the operators developed in the last section. These relationships may be proved via direct manipulation of the operator representations, or through the Laplace transform. As the operators $\mathbb{K}_\pm^{-1}$ are roots of a quadratic characteristic equation they satisfy certain composition, commutation, and trace properties. These are:

$$\mathbb{K}_-^{-1}\mathbb{K}_+^{-1} = \mathbb{K}_+^{-1}\mathbb{K}_-^{-1} = \mathcal{L}_t \equiv -\partial_t(\tau\partial_t + 1) \tag{11.4.12}$$

$$\mathbb{K}_\pm^{-1} = \mathcal{L}_t\mathbb{K}_\mp = \mathbb{K}_\mp\mathcal{L}_t = \partial_t\mathbb{K}_\mp(\tau\partial_t + 1) \tag{11.4.13}$$

$$\mathbb{K}_\pm^{-1}\mathbb{K}_\pm = \mathbb{K}_\pm\mathbb{K}_\pm^{-1} = \mathbb{I}$$

$$\mathbb{K}_+^{-1} + \mathbb{K}_-^{-1} = 2\gamma\sqrt{\tau}\partial_t \tag{11.4.14}$$

$$\mathbb{K}_+^{-1} - \mathbb{K}_-^{-1} = 2\sqrt{\partial_t(\chi\partial_t + 1)}$$

Relations (11.4.12) and (11.4.14) define the operators $\mathbb{K}_\pm^{-1}$, and if the right-hand-side of (11.4.14) is zero these relations provide the definition of the square root of $-\mathcal{L}_t$ (*c.f.* Section 3 of (I)). The relationship (11.4.13) is often called the commutation relation, it appears in many wave splitting problems, albeit with operators different to those considered here. These equations are background to many of the results of this chapter.

The operators $\mathbb{K}_\pm$ are smoothing, compact on the Hilbert space L_2, and as such the inverse operators $\mathbb{K}_\pm^{-1}$ are unbounded and ill-posed on L_2, even though existence of the operators has been proven by construction. We only consider the mapping properties of the operators when $\overline{v} \neq 0$, as the case for $\overline{v} \equiv 0$ has been covered in (I).

Theorem 11.4.1. *For $\tau \neq 0$, the operators are injective and into on the appropriate Sobolev spaces*

$$\mathbb{K}_\pm : H^s \mapsto H^{s+1},$$
$$\mathbb{K}_\pm^{-1} : H^s \mapsto H^{s-1},$$

where the Sobolev space of order m is denoted by H^m.

Proof. To prove the operators are injective it is only necessary to look at the image of the zero function because the operators are linear; it follows trivially from their explicit form they are injective. The mapping properties of the operators follows directly from their Laplace transforms and the symbol mapping theorem (Taylor, 1981), (p 49 et seq.). □

In the limiting case of pure diffusion $\overline{v} \to 0$, $\gamma \to 0$ and $\chi \to \tau$, so it follows that the operators reduce to those of (I):

$$\mathbb{K}_{\pm}^{-1} \to \pm\mathbb{K}_{\tau}^{-1}, \quad \mathbb{K}_{\pm} \to \pm\mathbb{K}_{\tau}.$$

Of major concern also, is the limiting forms of the operators $\mathbb{K}_{\pm}$ as $\tau \to 0$; when $\tau = 0$, the model equations are parabolic. Define

$$\mathbb{H}f = \int_0^t H(t-s)f(s)\,ds,$$

with kernel $H(t) = 1/\sqrt{\pi t}$, then $\mathbb{H}f$ is related to the half derivative of f, that is $\mathbb{H}f = \partial_t^{-1/2} f$. The half derivative has the obvious composition properties (Oldham and Spanier, 1974)

$$\partial_t^{1/2} f = \partial_t \mathbb{H} f = \partial_t \partial_t^{-1/2} f.$$

It is then possible to show

$$\lim_{\tau \to 0} \mathbb{K}_{\pm} = \pm\mathbb{H},$$

and when representation (11.4.6) is used for $\mathbb{K}_{\pm}^{-1}$

$$\lim_{\tau \to 0} \mathbb{K}_{\pm}^{-1} = \pm\partial_t\mathbb{H}.$$

Finally the limit as the equation becomes non-diffusive can be achieved by considering the limit as $\kappa^{-1} \to 0$ while keeping ν fixed, or equivalently allowing $\tau \to \infty$, again while keeping ν fixed. It can be shown that

$$\lim_{\tau \to \infty} \kappa\mathbb{K}_{\pm} = \frac{1}{\nu\gamma_{\pm}}\partial_t^{-1}, \quad \lim_{\tau \to \infty} \kappa^{-1}\mathbb{K}_{\pm}^{-1} = \nu\gamma_{\pm}\partial_t, \tag{11.4.15}$$

which is the corresponding splitting for the hyperbolic partial differential equation

$$\nu^2\partial_t^2 c + \nu^2\overline{v}^2\partial_t\partial_x c = \partial_x^2 c. \tag{11.4.16}$$

In the limit as $\overline{v} \to 0$, $\gamma \to 0$, and $\gamma_{\pm} \to \pm 1$, with (11.4.15) reducing to the standard splitting for the wave equation. Observe that $\gamma_- < 0$ for $\gamma > 0$[7], and as $\gamma \to \infty$, $\gamma_- \to 0$ and $\gamma_+ \to 2\gamma$. Figure 11.1 shows how the wave phase velocity varies with the advection velocity. The relationship between the phase velocity γ_+, and the advection velocity is only approximately linear for $\frac{\overline{v}\nu}{2} > 1$. This nonlinear behaviour is expected, as the velocity of the propagation of the mass wave through the advecting medium is not associated with a Galilean transformation.

[7]Note also that $\gamma_+\gamma_- = -1$.

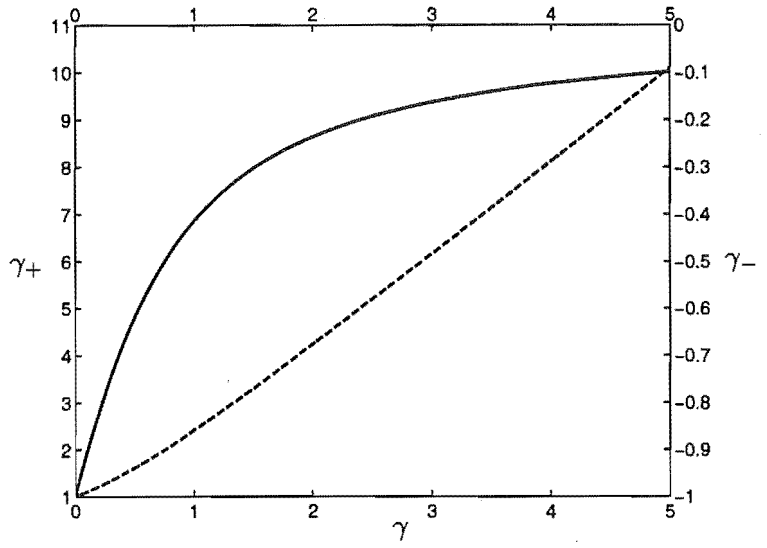

Figure 11.1: The variation of the wavespeed parameters, γ_+ (- - -) and γ_- (—) with γ.

11.4.3 System Dynamics

The transformation (11.4.4) can now be utilised to diagonalise $\mathbf{C}$, and to convert equation (11.4.1) into two coupled one-way wave equations

$$\partial_x \boldsymbol{v}^{\pm} = \boldsymbol{\Lambda} \boldsymbol{v}^{\pm} + \mathbf{D} \boldsymbol{v}^{\pm}, \tag{11.4.17}$$

with the new basis $\boldsymbol{v}^{\pm} = \begin{bmatrix} v^+ & v^- \end{bmatrix}^T$, where $\{v^+, v^-\}$ have the properties of right and left moving mass concentration waves; this is discussed further latter in this section. The matrix $\boldsymbol{\Lambda}$ is the diagonal operator matrix

$$\boldsymbol{\Lambda} = \begin{bmatrix} \kappa^{-1}\mathbb{K}_-^{-1} & 0 \\ 0 & \kappa^{-1}\mathbb{K}_+^{-1} \end{bmatrix}, \tag{11.4.18}$$

and the dynamics matrix $\mathbf{D}$ is

$$\mathbf{D} = -\mathbf{P}^{-1}(\partial_x \mathbf{P}) + \mathbf{P}^{-1}\mathbf{B}\mathbf{P}. \tag{11.4.19}$$

It is important to note that the diagonal matrix $\boldsymbol{\Lambda}$ given by (11.4.18) will be the same for system (11.2.3) and the second order equation (11.2.4), so that the principal part of the dynamics equation will be the same for both these equations. In the sequel we only quote results for the second order equation as analysed in Section 11.4.1. Results for the system equations in (11.4.3) are of a similar nature, but have different functional forms from those listed in Tables 11.1 and 11.2, and will *not* be listed here.

Coefficient	Second order equations (11.2.4)
$d(x)$	$\frac{1}{4}\partial_x \ln[\nu^2(1+\gamma^2)]$
$e(x)$	$-\frac{1}{\tau(1+\gamma^2)} + \frac{\partial_x[\kappa^{-2}]}{\partial_x[\nu^2(1+\gamma^2)]}$
$f(x)$	$\frac{\gamma}{2}\big(\kappa^{-2}\overline{v} - 2\partial_x(\ln\kappa)\big) + \big(\partial_x\overline{v}\big)\kappa^{-1}\sqrt{\tau}$
$g(x)$	$\frac{1}{2}(\kappa^{-2}\overline{v} - 2\partial_x \ln\kappa)$
$h(x)$	$\frac{1}{2\kappa}\partial_x\overline{v}$
$j(x)$	$\frac{1}{2\nu}\partial_x(\nu\gamma)$

Table 11.1: Identification of parameters $d - j$ for hyperbolic mass transport in the second order equation case.

In terms of the material parameters the first part of the system dynamics is

$$\mathbf{P}^{-1}(\partial_x\mathbf{P}) = \begin{bmatrix} -1 & -1 \\ 1 & 1 \end{bmatrix} \frac{j(x)}{\sqrt{1+\gamma^2}}\big(\mathbb{M}+\mathbb{I}\big) + \begin{bmatrix} 1 & -1 \\ -1 & 1 \end{bmatrix} d(x)(\mathbb{I} + e(x)\mathbb{J}), \tag{11.4.20}$$

with $\mathbb{J}$ represented by the convolution operator

$$\big(\mathbb{J}f\big)(t) = \int_0^t J(t-t')f(t')\,dt',$$

with kernel $J(t) = \exp(-t/\chi)$. The spatial functions in equation (11.4.20) are shown in Table 11.1, and the remaining part of the dynamics, after transformation, is

$$\mathbf{P}^{-1}\mathbf{B}\mathbf{P} = \begin{bmatrix} -1 & -1 \\ 1 & 1 \end{bmatrix} \left(h(x)\mathbb{K}_\chi + \frac{f(x)}{\sqrt{1+\gamma^2}}\big(\mathbb{M}+\mathbb{I}\big)\right) + \begin{bmatrix} 1 & -1 \\ -1 & 1 \end{bmatrix} g(x)\mathbb{I}, \tag{11.4.21}$$

with the coefficients d, e, f, g, h, and j given in Table 11.1.

For explicitness we express the system (11.4.17) in terms of the dynamics matrix as

$$\partial_x \boldsymbol{v}^{\pm}(x,t) = \boldsymbol{\Lambda}\boldsymbol{v}^{\pm}(x,t) + \begin{bmatrix} \alpha & \beta \\ \widetilde{\gamma} & \delta \end{bmatrix} \boldsymbol{v}^{\pm}(x,t) + \int_0^t \begin{bmatrix} A(x,t-t') & B(x,t-t') \\ C(x,t-t') & D(x,t-t') \end{bmatrix} \boldsymbol{v}^{\pm}(x,t')\,dt', \tag{11.4.22}$$

(*c.f.* (Åberg et al., 1995) for a similar case where the dynamics include operators[8]). The first part of the dynamics represented by the terms $\{\alpha, \beta, \tilde{\gamma}, \delta\}$ are listed in Table 11.2, and these terms are purely multiplicative functions. The part of the dynamics corresponding to integral operators has been split into the convolutional term; the kernels of these operators are also listed in Table 11.2. The convolutional operators corresponding to the kernels $\{A, B, C, D\}$ will be denoted by $\{\mathbb{A}, \mathbb{B}, \mathbb{C}, \mathbb{D}\}$, respectively. It is to be observed that it is necessary to split the dynamics into functions and operators in order to derive the Green operator equations of the next section.

If $\mathbf{D} \equiv \mathbf{0}$ then the right-hand-side of equation (11.4.22) is just $\mathbf{\Lambda}$, and the system is decoupled into two one-way wave equations, corresponding to right and left moving mass waves which are respectively denoted by v^+ and v^-. We now discuss the interpretation of the $v^\pm$ from these decoupled equations. For concreteness we just consider v^+, and it follows that the right going wave must satisfy

$$\big(\partial_x - \kappa^{-1}\mathbb{K}_-^{-1}\big)v^+ = 0. \tag{11.4.23}$$

In the special case of the non-diffusive limit $\tau \to \infty$, with ν fixed, the equation (11.4.23), with use of (11.4.15), becomes

$$\big(\partial_x - \nu\gamma_-\partial_t\big)v^+ = 0,$$

which is satisfied by solutions of the form $v^+(t + x\nu\gamma_-)$. Now observe that $\gamma_\pm = \pm 1$, for $\gamma = 0$, and that $\gamma_- < 0$ for $\gamma > 0$. It then follows that this solution is the well known right going wave having Galilean translational invariance. In this case the right moving wave front travels with speed γ_+/ν and the left moving wave front travels at speed γ_-/ν [9]. When considering the more general operator found in (11.4.23), we cannot expect the solution of this equation to exhibit such solution symmetry because the wave will be *attenuated* as it moves to the right. However we still call solutions that satisfy (11.4.23) the right moving waves.

When the material properties are such that $\mathbf{D} \neq \mathbf{0}$ we cannot make this physical interpretation for $\boldsymbol{v}^\pm$, however we shall still call such solutions left and right moving waves for convenience. It should be apparent the mathematics still makes sense in that $\boldsymbol{v}^\pm$ satisfy (11.4.17).

We can now examine under what conditions the dynamics matrix provides an exact splitting. If the velocity field, $\overline{v}$, is independent of x, and the limit $\kappa^{-1} \to 0$ while $\kappa^{-1}\sqrt{\tau} \to \nu$ remains fixed is examined, it is found that the splitting is exact and $\mathbf{D} = \mathbf{0}$. This means that the two one-way wave equations are decoupled and can be integrated exactly. Another possibility is that x moves

[8] We note that the equations for the reflection kernel, and the Green operators derived in (I) are derived under the assumption that the lateral loss term, there denoted by χ, was $\chi \equiv 0$, and the relaxation time $\tau \neq \tau(x)$; this was *not* specified in the cited paper.

[9] See Footnote 7 on page 166.

into a region in which the parameters are homogeneous with $\overline{v} \equiv 0$ and $\mathbf{D} = \mathbf{0}$ again. Similar interpretations can be made for left-going waves.

11.5 Wave Propagators

For simplicity, in the rest of the chapter we consider the domain of the problem to be the quarter plane $\Omega = \{(x,t) \in \boldsymbol{R}^2 | 0 \leq x \leq \infty, 0 \leq t \leq \infty\}$. The mass transport processes within the medium in the half space $0 \leq x \leq \infty$ are described by equations (11.4.1). Within the semi-infinite region the material parameters $\kappa, \tau, \overline{v} \in C^1(\mathbb{R})$, and with little loss of generality we assume the initial condition $\boldsymbol{v}^{\pm}(x,0) = 0$, $x \in [0,\infty)$.

Karlsson (Karlsson, 1996) has derived wave propagators for a dispersive electromagnetic problem. We derive the equations for the wave propagators for the advection problem under consideration in this chapter. The wave propagators are linear operators that map a mass concentration, $v^+(x,t)$, at one spatial position $x > 0$, to another position $x' > 0$. The propagators are operators defined by

$$v^+(x', t + \zeta(x,x')) = \mathbb{P}^+(x',x)v^+(x,t), \tag{11.5.1}$$

$$v^-(x', t + \zeta(x,x')) = \mathbb{P}^-(x',x)v^+(x,t), \tag{11.5.2}$$

where ζ is the wave front propagation time of a mass wave moving from the point x to x'; expressions for this function are given in (11.5.15). There is no restriction on the relative magnitudes of x and x' in the definition of the wave propagators. When $x' > x$ the propagators map the field v^+ forward in the positive x-direction, along with the advection, and when $x' < x$ the propagation is backwards, against the advection and in the negative x-direction.

The propagators satisfy the properties of a group (see Karlsson (1996)), and the groups inverse operator is defined through, for example

$$\mathbb{P}^+(x',x)\mathbb{P}^+(x,x') = \mathbb{I} \tag{11.5.3}$$

or

$$\big(\mathbb{P}^+(x',x)\big)^{-1} = \mathbb{P}^+(x,x'). \tag{11.5.4}$$

The properties of linearity, causality and time-translational invariance imply the representation for the propagators is of the form

$$\mathbb{P}^+(x',x)v^+(x,t) = a(x,x')v^+(x,t) + \big(P^+(x',x;\cdot) * v^+(x,\cdot)\big)(t), \tag{11.5.5}$$

$$\mathbb{P}^-(x',x)v^+(x,t) = \big(P^-(x',x;\cdot) * v^+(x,\cdot)\big)(t), \tag{11.5.6}$$

where $P^{\pm}$ is a kernel function, and the $*$ operator denotes the temporal convolution

$$\big(P^{\pm}(x',x;\cdot) * v^{+}(x,\cdot)\big)(t) = \int_0^t P^{\pm}(x',x;s)v^{+}(x,t-s)\,ds.$$

The factor a modifies the wave front, and provides attenuation when $x' > x$, and amplification when $x' < x$, and its functional form is given in equation (11.5.17).

Causality requires that $v^{\pm}(x,t) \equiv 0$ for $t \leq \zeta(0,x)$. In equation (11.5.5) the positive moving field at some point $x' > 0$ has been written in two parts. The first part is due to the direct forward/backward propagation of the incident field, $v^{+}(x,t)$, with attenuation/amplification and time retardation/advancement, depending on whether $x' > x$ or $x' < x$ respectively, and the second part is due to scattering effects in the region — this is provided by $P^{+} * v^{+}$. The other propagation operator in (11.5.2) provides the mapping between the incident right going wave $v^{+}(x,t)$, and a left going wave at $x' > 0$.

From (11.5.5) and (11.5.4) it is seen that the kernel $P^{+}(x,x';t)$ for the inverse propagator in (11.5.4), is related to the propagator kernel $P^{+}(x',x;t)$ through the equation

$$a(x,x')P^{+}(x,x';t) + a(x',x)P^{+}(x',x;t) + \big(P^{+}(x',x;\cdot) * P^{+}(x,x';\cdot)\big)(t) = 0.$$

This equation is a Volterra integral equation of the second kind, so that for appropriately smooth functions the existence of the inverse kernel, given the other kernel, is assured.

Now we shall derive the functional equations that the propagator kernels satisfy. The initial step in the derivation is to differentiate the representations of the propagators with respect to either x or x'. Differentiation with respect to x', the station where the wave is propagating to, leads to a form of the operators that will be required in the sequel. Differentiation with respect to x, the point where the wave has propagated from, leads to an equation suitable for invariant imbedding — these will not be discussed further here (see Karlsson (1996) for information on this case).

Differentiation of equation (11.5.5), with respect to x', yields

$$\big(\mathbf{D}_1 + (\partial_{x'}\zeta(x,x'))\mathbf{D}_2\big)v^{+}(x',t+\zeta(x,x')) = (\partial_{x'}a(x,x'))v^{+}(x,t) + \big(\partial_{x'}P^{+}(x',x;\cdot) * v^{+}(x,\cdot)\big)(t). \tag{11.5.7}$$

Then use of the dynamics, (11.4.22), to rewrite terms on the left-hand-side of (11.5.7), and on interchanging the left-hand-side with the right-hand-side, leads to

$$\begin{aligned}(\partial_{x'}a(x,x'))v^{+}(x,t) + \big(\partial_{x'}P^{+}(x',x;\cdot) * v^{+}(x,\cdot)\big)(t) &= \big(\alpha + \kappa^{-1}\mathbb{K}_{-}^{-1} + \mathbb{A}\big)v^{+}(x',t+\zeta(x,x')) \\ &+ \big(\beta + \mathbb{B}\big)v^{-}(x',t+\zeta(x,x')) + (\partial_{x'}\zeta(x,x'))\partial_t v^{+}(x',t+\zeta(x,x')),\end{aligned} \tag{11.5.8}$$

where the operators $\mathbb{A}$ and $\mathbb{B}$ are defined by the convolution operators in (11.4.22). Furthermore, the use of (11.4.6) allows the right-hand-side of (11.5.8) to be written as

$$\big(\alpha+\gamma_-\kappa^{-1}\sqrt{\tau}\partial_t-\frac{1}{2\kappa\sqrt{\chi}}(\mathbb{I}-\mathbb{L})+\mathbb{A}\big)v^+(x',t+\zeta(x,x'))$$
$$+\big(\beta+\mathbb{B}\big)v^-(x',t+\zeta(x,x'))+(\partial_{x'}\zeta(x,x'))\partial_t v^+(x',t+\zeta(x,x')), \quad (11.5.9)$$

To proceed requires the following lemma.

Lemma 11.5.1. *If $a_i \in \mathrm{C}$, and $v \in \mathrm{C}^1$ and*

$$a_1(x)v(t)+\int_0^t a_2(x,t-s)v(s)\,ds+a_3(x)\partial_t v(t)+\int_0^t a_4(x,t-s)\partial_t v(s)\,ds=0, \quad \forall t>0,x,v, \quad (11.5.10)$$

then $a_i = 0$. That is, terms proportional to $\partial_t v^+(x,t)$, $v^+(x,t)$, and terms involving convolutions of $v^+(x,t)$ and $\partial_t v^+(x,t)$ are independent.

Proof. If we consider v to be constant, then $\partial_t v = 0$ and

$$a_1(x)+\int_0^t a_2(x,s)\,ds=0, \quad \forall t>0,x. \quad (11.5.11)$$

In particular, when $t = 0$ it follows that $a_1 = 0$ and therefore

$$\int_0^t a_2(x,s)\,ds=0, \quad \forall t>0,x, \quad (11.5.12)$$

and the continuity of a_2 then implies that $a_2 = 0$. A similar argument with $v = t$ implies that $a_3 = a_4 = 0$. □

Therefore using (11.5.5) and (11.5.6) and Lemma 11.5.1 three equations can be obtained from (11.5.9), and similar considerations of (11.5.6) yields two further equations. The first two equations are

$$\partial_{x'}P^+=\frac{1}{2\kappa\sqrt{\chi}}\big(aL+L*P^+-P^+\big)+\alpha P^++\beta P^-+aA+A*P^++B*P^-, \quad (11.5.13)$$

$$\partial_{x'}P^--2\nu\sqrt{1+\gamma^2}\partial_t P^-=\frac{1}{2\kappa\sqrt{\chi}}\big(P^--L*P^-\big)+\delta P^-+\widetilde{\gamma}P^+ +aC+D*P^-+C*P^+, \quad (11.5.14)$$

where the functional dependence of the dynamics $\{\alpha,\beta,\widetilde{\gamma},\delta\}$, on x', and $P^{\pm}(x',x;t), a(x,x')$ on x',x,t has been implicitly assumed for notational convenience.

The third equation determines the propagation time between two points x and x', which is

$$\zeta(x,x')=-\int_x^{x'}\nu(s)\gamma_-(s)\,ds=\int_x^{x'}\frac{\nu(s)}{\gamma_+(s)}\,ds,$$
$$=\int_x^{x'}\nu(s)(\sqrt{1+\gamma^2}-\gamma)\,ds. \quad (11.5.15)$$

This should be compared to the propagation time found in the case with no advection, namely just the integrated slowness (Wall and Olsson, 1997). As $0 \geq \gamma_- \geq -1$ when $\gamma > 0$, it follows that the phase velocity of the wave front is greater than $1/\nu$, as would be expected due to the additive effect of the advective velocity of the embedding medium. The function $\zeta(x, x')$ does not have an inverse, and it is convenient to define this travel time function in terms of the function

$$\zeta(x) = -\int_0^x \nu(s)\gamma_-(s)\,ds = \zeta(0, x), \tag{11.5.16}$$

with $\zeta(x, x') = \zeta(x') - \zeta(x)$. The function $\zeta(x)$ can be shown to posses an inverse through the inverse function theorem and the fact that $\nu/\gamma_+ > 0$.

The fourth equation determines the wave front attenuation/amplification factor, which has the representation

$$a(x, x') = \exp\left(-\int_x^{x'} \left(\left[2\kappa(s)\sqrt{\chi(s)}\right]^{-1} - \alpha(s)\right) ds\right), \tag{11.5.17}$$

and it is to be noted that when $x' > x$, $0 < a \leq 1$, and when $x' < x$, $a \geq 1$.

The fifth equation specifies the initial conditions for P^-, which is

$$P^-(x', x; 0) + \frac{\widetilde{\gamma} a}{2\nu\sqrt{1+\gamma^2}} = 0. \tag{11.5.18}$$

11.5.1 Forward Green Operators

The forward Green operators provide the mapping of the left-hand boundary condition, at the boundary of the propagation medium, to an interior point x' by

$$v^+(x', t + \zeta(0, x')) = \mathbb{G}_f^+(x')v^+(0, t), \quad v^-(x', t + \zeta(0, x')) = \mathbb{G}_f^-(x')v^+(0, t).$$

The forward Green operators are linear convolution operators and are related to the propagator operators by

$$\mathbb{G}_f^+(x') = \mathbb{P}^+(x', 0), \quad G^-(x) = \mathbb{P}^-(x', 0),$$

with kernels given by

$$G_f^+(x', t) = P^+(x', 0; t), \quad G_f^-(x', t) = P^-(x', 0; t).$$

The kernels $G_f^\pm(x', t)$ satisfy equations (11.5.13) and (11.5.14), but with $x = 0$. The boundary and initial conditions appropriate for the forward Green kernels are

$$G_f^+(0, t) = 0, \tag{11.5.19}$$

$$G_f^+(x', 0) = \frac{a(0, x')}{2} \int_0^{x'} \left(2A(s, 0) + \frac{L(s, 0)}{\kappa\sqrt{\chi}} - \frac{\widetilde{\gamma}\beta}{\nu\sqrt{1+\gamma^2}}\right) ds, \tag{11.5.20}$$

(11.5.21)

where equation (11.5.20) has been obtained by integrating (11.5.13) along the x-axis from $x = 0$ to x', for $t = 0$. If the semi-infinite half-space is such that all material parameters are homogeneous for $x > \ell$ then G_f^- satisfies the extra boundary value

$$G_f^-(\ell, t) = 0. \tag{11.5.22}$$

11.5.2 Transmission Green operators

The transmission Green operators provide the mapping of the transmitted field at the station $x = \ell$ in the propagation medium, to an interior point $0 \leq x' < \ell$. These operators were first introduced by He (He, 1993), where they were named *compact* Green operators, because for the non-dispersive problem he analysed their associated kernel functions had compact support. We prefer to name them *transmission* Green functions to distinguish them from the *forward* Green functions previously described.

These operators $\mathbb{G}_t^{\pm}$, are the backward operators $\mathbb{P}^{\pm}(x', \ell)$, with $x' < \ell$, and hence the transmission Green kernels are the kernels $P^{\pm}(x', \ell; t)$ and they satisfy (11.5.13) and (11.5.14), but with $x = \ell$. The boundary and initial conditions appropriate for the forward Green kernels are

$$G_t{}^+(\ell, t) = 0, \tag{11.5.23}$$

$$G_t{}^+(x', 0) = \frac{a(\ell, x')}{2} \int_\ell^{x'} \left(2A(s, 0) + \frac{L(s, 0)}{\kappa\sqrt{\chi}} - \frac{\widetilde{\gamma}\beta}{\nu\sqrt{1+\gamma^2}} \right) ds, \tag{11.5.24}$$

$$G_t{}^-(0, t) = 0, \tag{11.5.25}$$

Therefore the solutions of the first order system of partial differential equations (11.5.13) and (11.5.14) are continuous along the characteristic curves associated with the system, but may be discontinuous across these curves. From (11.5.13), it is seen that the characteristic traces are $t =$ constant for $G_t{}^+$, and as $G_t{}^+(0, t)$ is continuous for all $t > 0$, it follows that $G_t{}^+$ is continuous in the region $\{0 < x < \ell,\ 0 < t < \infty\}$. However examination of (11.5.18) shows that any discontinuity in ν, $\widetilde{\gamma}$, or γ will be propagated along the characteristic of (11.5.14). Because we have assumed that the material parameters are continuously differentiable, it follows that $G_t^-(x, 0)$ is continuous, except possibly at $x = \ell$, with a discontinuity of magnitude

$$[G_t^-](\ell, 0) = \frac{\widetilde{\gamma}(\ell) a(0, \ell)}{2\nu(\ell)\sqrt{1+\gamma(\ell)^2}}, \tag{11.5.26}$$

in the direction of increasing t. This jump in $G_t{}^-$ will propagate along the characteristic curve for $G_t{}^-$.

11.6 Signal Reconstruction

In order to reconstruct the mass concentration signal at $x = 0$, it is necessary to relate the physical variables, the concentration c and the parabolic mass flux $\partial_x c$, to the split variables $v^{\pm}$. It is seen from (11.4.4) and (11.4.11), that the right-going wave is given by

$$v^+(\ell,t) = \frac{1}{2}\left(c + \frac{\gamma}{\sqrt{1+\gamma^2}}(\mathbb{M}+\mathbb{I})c - \kappa\mathbb{K}_\chi \partial_x c\right)(\ell,t) \tag{11.6.1}$$

If we are measuring the concentration at the pipe exit, then because there is purely advective flow out the end of the pipe, it follows that $\partial_x c(\ell,t) = 0$ (Smith, 1988), and (11.6.1) reduces to

$$v^+(\ell,t) = \frac{1}{2}\left(c + \frac{\gamma}{\sqrt{1+\gamma^2}}(\mathbb{M}+\mathbb{I})c\right)(\ell,t). \tag{11.6.2}$$

However in general the derivative $\partial_x c(\ell,t)$ can be estimated in a stable manner using (11.3.26) and the method of mollification. Therefore v^+ can be readily identified from the measured concentration $c(\ell,t)$.

The propagator equations (11.5.5) and (11.5.6) form the basis of the signal reconstruction problem, which for the transmission Green kernels are

$$v^-(0,t-\zeta(\ell)) = \mathbb{G}_t{}^- \circ v^+(\ell,t), \tag{11.6.3}$$

$$v^+(0,t-\zeta(\ell)) = v^+(\ell,t)/a(0,\ell) + \mathbb{G}_t{}^+ \circ v^+(\ell,t). \tag{11.6.4}$$

From (11.4.4) it follows that $c = v^+ + v^-$, and therefore the reconstruction of the signal at $x = 0$, $c(0,t-\zeta(\ell))$, can be computed. This reconstruction is well-posed, as the solution of (11.5.13) and (11.5.14) for $\{G_t^+, G_t^-\}$ is a well-posed problem. Because we can consider τ as a regularisation parameter, then provided $\tau > 0$, it follows that we have regularised the ill-posed parabolic problem. Effectively we have approximated the ill-posed Volterra integral equation of the first kind, which is obtained from the parabolic problem, by a well-posed Volterra integral equation of the second kind, which is associated with the hyperbolic problem.

11.7 Discussion

The system splitting in (11.4.3) has not been examined in this chapter, because the splitting chosen in (11.4.2) does not appear to be ideal. A splitting which is exact when the material parameters are homogeneous is more suitable for the inverse problem considered in Section 11.6. This exact splitting includes the extra term $\kappa^{-2}\overline{v}$ in the $\mathbf{C}_{22}$ element of the operator matrix $\mathbf{C}$ in (11.4.2). For this splitting $P^- = 0$ when the material parameters are homogeneous, and therefore v^+ can be expressed purely in terms of $c(\ell,t)$, with no dependence on $\partial_x c(\ell,t)$. The associated operators for

such a splitting are very similar to the splitting operators obtained in this chapter. We note that the entry length obtained when the parameters are homogeneous in (11.3.29), appears directly in the propagator equations for such a splitting.

A discretisation similar to that in (I) will yield solutions to the propagator equations and the signal reconstruction scheme presented in Section 11.6. The propagators derived in this chapter can also be used to solve the problem of reconstructing spatially varying medium parameters such as $\kappa(x)$, $\overline{v}(x)$, and $\tau(x)$, in an advective-diffusive medium. Such problems have been considered in (I). An alternative solution approach to the signal reconstruction problem considered in this chapter is to use the space marching mollification scheme presented in Section 9.3.4. Spatially varying medium coefficients can easily be incorporated into such schemes.

Coefficient	Terms of material parameters
$\alpha(x)$	$-\frac{1}{\sqrt{1+\gamma^2}}(f(x)-j(x))+(g(x)-d(x))$
$\beta(x)$	$-\frac{1}{\sqrt{1+\gamma^2}}(f(x)-j(x))-(g(x)-d(x))$
$\widetilde{\gamma}(x)$	$\frac{1}{\sqrt{1+\gamma^2}}(f(x)-j(x))-(g(x)-d(x))$
$\delta(x)$	$\frac{1}{\sqrt{1+\gamma^2}}(f(x)-j(x))+(g(x)-d(x))$
Kernel	**Terms of material parameters**
$A(x,t)$	$-\frac{1}{\sqrt{1+\gamma^2}}((f(x)-j(x))M(x,t)-h(x)K(x,t)-d(x)e(x)J(x,t)$
$B(x,t)$	$-\frac{1}{\sqrt{1+\gamma^2}}((f(x)-j(x))M(x,t)-h(x)K(x,t)+d(x)e(x)J(x,t)$
$C(x,t)$	$\frac{1}{\sqrt{1+\gamma^2}}((f(x)-j(x))M(x,t)+h(x)K(x,t)+d(x)e(x)J(x,t)$
$D(x,t)$	$\frac{1}{\sqrt{1+\gamma^2}}((f(x)-j(x))M(x,t)+h(x)K(x,t)-d(x)e(x)J(x,t)$

Table 11.2: Identification of dynamics coefficients and kernels for hyperbolic mass transport for the second order equation (11.2.3).

Bibliography

Åberg, I. (1995). Time Domain solutions to direct and inverse scattering problems in non-stationary media. Master's thesis, Lund University, Sweden.

Åberg, I., G. Kristensson, and D. J. N. Wall (1995). Propagation of transient electromagnetic waves in time-varying media — direct and inverse scattering problems. *Inverse Problems* 11:29–49.

Åberg, I., G. Kristensson, and D. J. N. Wall (1996). Transient waves in non-stationary media. *J. Math. Phys.* 37:2229–2252.

Abou-Samra, A. B., K. J. Catt, and G. Aguilera (1987a). Calcium-dependent control of corticotropin release in rat anterior pituitary cell cultures. *Endocrinology.* 121:965–971.

Abou-Samra, A. B., J. P. Harwood, V. C. Manganiello, K. J. Catt, and G. Aguilera (1987b). Phorbol 12-myristate 13-acetate and vasopressin potentiate the effect of corticotropin-releasing factor on cyclic AMP production in rat anterior pituitary cells. *J. biol. Chem.* 262:1129–1136.

Abramowitz, M. and I. Stegun (1964). Handbook of Mathematical Functions. Dover Publications, New York.

Acar, R. and C. R. Vogel (1994). Analysis of bounded variation penalty methods for ill-posed problems. *Inverse Problems* 10:1217–1229.

Adler, M., B. S. Wong, S. L. Sabol, N. Busis, M. B. Jackson, and F. F. Weight (1983). Action potentials and membrane ion channels in clonal anterior pituitary cells. *Proc. Natl. Acad. Sci. USA* 80:2086–2090.

Aguilera, G., J. P. Harwood, J. X. Wilson, J. H. Morell, J. H. Brown, and K. J. Catt (1983). Mechanisms of action of corticotropin release in rat pituitary cells. *J. Biol. Chem.* 258:8039–8045.

Aidley, D. J. (1989). The Physiology of Excitable Cells. Cambridge University Press, Cambridge, 3rd edition.

Alberts, B., D. Bray, J. Lewis, M. Kaff, K. Roberts, and J. D. Watson (1983). Molecular Biology of the Cell. Garland, New York, 1st edition.

Alexander, S. L., C. H. G. Irvine, J. H. Liversey, and R. A. Donald (1988). The effect of isolation stress on the concentrations of arginine vasopressin, α-melanocyte-stimulating hormone and

ACTH in the pituitary venous effluent of the normal horse. *J. Endocr.* 116:325–334.

Allbritton, N. L., T. Meyer, and L. Stryer (1992). Range of messenger action of calcium ion and inositol 1,4,5-triphosphate. *Science.* 258:1812–1815.

Allen, C. M. and E. A. Taylor (1923). The salt velocity method of water measurement. *Trans. Amer. Soc. Mech. Engrs.* 45:285–341.

Amundson, J. and D. Clapham (1993). Calcium waves. *Current Opinion in Neurobiology* 3:375–382.

Antoni, F. A. (1986). Hypothalmic control of adrenocorticotropin secretion: Advances since the discovery of 41-residue corticotropin releasing factor. *Endocr. Rev.* 7:351–378.

Aris, R. (1953). On the dispersion of a solute in a fluid flowing through a tube. *Proc. Roy. Soc. Lond. Ser. A* 235:67–77.

Arnold, V. I., V. S. Afrajmovich, Y. S. Il'yashenko, and L. P. Shil'nikov (1994). Dynamical Systems V, chapter 4.4. Encyclopaedia of Mathematical Sciences. Springer-Verlag, New York.

Arrowsmith, D. K. and C. M. Place (1990). An introduction to Dynamical Systems. Cambridge University Press.

Atkinson, K. E. (1974). Existence theorem for Abel integral equations. *SIAM J. Math. Anal.* 5:729–736.

Atkinson, K. E. (1989). An introduction to Numerical Analysis. John Wiley & Sons, Inc, New York, 2nd edition.

Atri, A., J. Amundson, D. E. Clapham, and J. Sneyd (1993). A single-pool model for intracellular calcium oscillations and waves in the *Xenopus laevis* oocyte. *Biophys. J.* 65:1727–1739.

Backus, G. E. and J. F. Gilbert (1968). The resolving power of gross earth data. *Geophysical Journal of the Royal Astronomical Society* 16:169–205.

Backx, P. H., P. P. de Tombe, J. H. K. V. Deen, B. J. M. Mulder, and H. E. D. J. ter Keurs (1989). A model of propagating calcium-induced calcium release mediated by calcium diffusion. *J. Gen. Physiol.* 93:963–977.

Baer, S. M., T. Erneux, and J. Rinzel (1989). The slow passage through a Hopf bifurcation: delay, memory effects, and resonance. *SIAM. J. Appl. Math.* 49:55–71.

Baillie, R. and M. L. King (1996). Fractional differencing and long memory processes. *Journal of Econometrics* 73:1–324.

Barletta, A. and E. Zanchini (1997). Unsteady heat conduction by internal-energy waves in solids. *Phys. Rev. B* 55:14208–14213.

Batchelor, G. K. (1967). An introduction to Fluid Dynamics. Cambridge University Press, Cambridge.

Berker, A. R. (1963). Intégration des équations du mouvement d'un fluide visqueux incompressible.

Encyclopedia of Physics 8:1–384.

Berntsson, F. (1999). A spectral method for solving the sideways heat equation. *Inverse Problems* 15:891–906.

Berridge, M. J. (1997). Elementary and global aspects of calcium signalling. *J. Physiol. (Lond).* 499:291–306.

Berridge, M. J., M. D. Bootman, and P. Lipp (1998). Calcium– a life and death signal. *Nature* 395:645–648.

Bertram, R., M. J. Butte, T. Kiemel, and A. Sherman (1995). Topological and phenomenological classification of bursting oscillations. *Bulletin of Mathematical Biology* 57:413–439.

Bertram, R. and A. Sherman (1998). Population dynamics of synaptic release sites. *SIAM J. Appl. Math.* 58:142–169.

Bertram, R., A. Sherman, and E. F. Stanley (1996). Single-domain/bound calcium hypothesis of transmitter release and facilitation. *J. Neurophysiology* 75:1919–1931.

Bezprozvanny, I., J. Waltras, and B. E. Ehrlich (1991). Bell-shaped calcium-response curves of ins(1,4,5)P_3- and calcium-gated channels from endoplasmic reticulum of cerebellum. *Nature(Lond)* 351:751–754.

Bilezikjian, L. M., A. L. Blount, and W. W. Vale (1987). The cellular actions of vasopressin on corticotrophs in the anterior pituitary: resistance to glucocorticoid action. *Mol. Endocrinology* 1:451–460.

Bilezikjian, L. M. and W. W. Vale (1983). Glucocorticoids inhibit corticotropin releasing factor induced production of cAMP in cultured anterior pituitary cells. *Endocrinology.* 113:657–662.

Billger, D. V. J. and D. J. N. Wall (1999). A time domain algorithm for the reflection of waves on a viscoelastically supported Timoshenko beam. *Q. J. Mech. appl. Math.* 52:211–236.

Broeck, C. V. D. (1990). Taylor dispersion revisited. *Physica A* 168:667–696.

Brunner, H. and P. J. van der Houen (1986). The numerical solution of Volterra equations. Elsevier Science Publishers, The Netherlands.

Burden, R. L. and J. D. Faires (1993). Numerical Analysis. PWS Publishing Company, Boston, 5th edition.

Burgoyne, R. D. and A. Morgan (1993). Regulated exocytosis. *Biochem. J.* 293:305–316.

Carafoli, E. (1994). Biogenesis: plasma membrane calcium ATPases: 15 years of work on the purified enzyme. *FASEB J.* 8:993–1002.

Carslaw, H. S. and J. C. Jaeger (1967). Conduction of Heat in Solids. Oxford University Press, London, 2nd edition.

Carson, E. R., C. Cobelli, and L. Finkelstein (1983). The Mathematical modeling of metabolic and endocrine systems. John Wiley & Sons, Inc.

Carvallo, P. and G. Aguilera (1988). Protein kinase C mediates the effect of vasopressin in pituitary corticotrophs. *Soc. Neurosci.* 14:442.

Cattaneo, C. (1948). Sulla conduzione de calore. *Atti del Semin. Mat. e Fis. Univ. Modena* 3:3.

Censor, Y. and G. T. Herman (1987). On some optimisation techniques in image reconstruction from projections. *Applied Numerical Mathematics* 3:365–391.

Charm, S. E. and G. S. Kurland (1965). Viscometry of human blood for shear rates of 0-100,000 sec^{-1}. *Nature* 206:617–618.

Chay, T. R. (1997). Effects of extracellular calcium on electrical bursting and intracellular and luminal calcium oscillations in insulin secreting pancreatic β-cells. *Biophysical Journal* 73:1673–1688.

Chay, T. R. and Y. S. Fan (1995). Bursting, spiking, chaos, fractals, and universality in biological systems. *Int. J. Bif. Chaos* 5:595–635.

Childs, G. V. (1993). Structure-function correlates in the corticotropes of the anterior pituitary. *Frontiers in Neuroendocrinology* 13:271–317.

Clapham, D. E. (1995a). Calcium signaling. *Cell* 80:259–268.

Clapham, D. E. (1995b). Replenishing the stores. *Nature* 375:634–635.

Connolly, T. J. and D. J. Wall (1997). On some inverse problems for a nonlinear transport equation. *Inverse Problems* 13:283–295.

Connolly, T. J. and D. J. N. Wall (1990). On Fréchet differentiability of some nonlinear operators occurring in inverse problems: an implicit function theorem approach. *Inverse Problems* 6:949–966.

Corcuff, J. B., N. C. Guérineau, P. Mariot, B. T. Lussier, and P. Mollard (1993). Multiple cytosolic calcium signals and membrane electrical events evoked in single arginine vasopressin-stimulated corticotrophs. *J. Biol. Chem.* 268:22313–22321.

Corcuff, J. B., N. C. Guérineau, A. Tabarin, and P. Mollard (1995). Tumor-related selection of calcium signals in vasopressin-stimulated human adenomatous corticotrophs. *American J. Physiology* 269:E451–E457.

Corones, J. P., G. Kristensson, P. Nelson, and D. L. Seth, editors (1992). Invariant Imbedding and Inverse Problems. SIAM, New York.

Craig, I. J. D. and J. C. Brown (1986). Inverse problems in astronomy. Adam Hilger, Bristol.

Dautray, R. and J.-L. Lions (1988). Mathematical Analysis and Numerical Methods for Science and Technology, volume 2. Springer-Verlag.

Day, W. A. (1997a). A note on the propagation of temperature disturbances. *Quarterly of Applied Mathematics* LV:565–572.

Day, W. A. (1997b). On rates of propagation of heat according to Fourier's theory. *Quarterly of*

Applied Mathematics LV:127–138.

de Vries, G. (1998). Multiple bifurcations in a polynomial model of bursting oscillations. *J. Nonlinear Sci.* 8:281–316.

De Young, G. W. and J. Keizer (1992). A single pool model IP_3-receptor based model for agonist stimulated Ca^{2+} oscillations. *Proc. Natl. Acad. Sci. USA* 89:9895–9899.

Dean, W. R. (1927). The streamline motion of a fluid in a curved pipe. *Phil. Mag.* 7:208–220.

Denbigh, K. G. (1971). The principles of chemical equilibrium. Cambridge University Press, Cambridge, 3rd edition.

DiMagno, L., N. Dascal, N. Davidson, H. A. Lester, and W. Schreibmayer (1996). Serotonin and protein kinase C modulation of a rat brain inwardly rectifying K^+ channel expressed in *Xenopus* oocytes. *Pflügers Archiv European Journal of Physiology* 431:335–340.

Doedel, E. (1981). A program for the automatic bifurcation analysis of autonomous systems. *Congr. Numer.* 30:265–484.

Dufour, J. F., I. M. Arias, and T. J. Turner (1997). Inositol 1,4,5-triphosphate and calcium regulate the calcium channel function of the hepatic inositol 1,4,5-triphosphate receptor. *The Journal of Biological Chemistry* 272:2675–2681.

Edelstein-Keshet, L. (1988). Mathematical Models in Biology. Random House, New York.

Eldén, L. (1987). Approximations for a Cauchy problem for the heat equation. *Inverse Problems* 3:263–273.

Eldén, L. (1988). Hyperbolic approximations for a Cauchy problem for the heat equation. *Inverse Problems* 4:59–70.

Ellis, M. J., R. S. Morgan, M. J. Evans, and R. A. Donald (1994). The effects of corticotrophin-releasing hormone, arginine vasopressin and their agonists on ACTH release from perifused horse anterior pituitary cells. *J. Endocr.* 143:85–93.

Evans, M. J. (2000). Personal communication.

Evans, M. J., J. T. Brett, R. P. McIntosh, J. E. A. McIntosh, J. L. McLay, J. H. Livesey, and R. A. Donald (1988). Characteristics of the ACTH response to repeated pulses of corticotropin-releasing factor and arginine vasopressin *in vitro*. *J. Endocr.* 117:387–395.

Evans, M. J., J. T. Brett, R. P. McIntosh, J. E. A. McIntosh, H. K. Roud, J. H. Livesey, and R. A. Donald (1985). The effect of various corticotropin-releasing factor trains on the release on the release of adrenocorticotropin, β-endorphin, and β-lipoprotein from perfused pituitary ovine pituitary cells. *Endocrinology* 117:893–899.

Evans, M. J., N. E. Kitson, J. H. Liversey, and R. A. Donald (1993a). The effect of cortisol on the secretion of ACTH by anterior pituitary cells of the horse in culture. *J. Endocr.* 137:403–412.

Evans, M. J., A. G. Marshall, N. E. Kitson, K. Summers, J. H. Liversey, and R. A. Donald

(1993b). Factors affecting ACTH release from perifused equine anterior pituitary cells. *J. Endocr.* 137:391–401.

Feller, W. (1957). An Introduction to Probability Theory and its Applications, volume 1. Wiley, New York, 1st edition.

Feller, W. (1966). An Introduction to Probability Theory and its Applications, volume 2. Wiley, New York, 1st edition.

Finch, E. A., T. J. Turner, and S. M. Goldin (1991). Calcium as a coagonist of inositol 1,4,5-triphosphate-induced calcium release. *Science.* 252:443–446.

Fujita, H., H. Kurihara, and J. Miyagawa (1983). Ultrastructural aspects of the effect of calcium ionophore A23187 on incubated anterior pituitary cells of rats. *Cell Tissue Res.* 229:129–136.

Gall, D. and I. Susa (1999). Effect of Na/Ca exchange on plateau fraction and $[Ca]_i$ in models for bursting in pancreatic β-cells. *Biophysical Journal* 77:45–53.

Gibbs, D. M. (1985). Inhibition of corticotropin release during hypothermia: the role of corticotropin releasing factor, vasopressin, and oxytocin. *Endocrinology.* 116:723–727.

Gill, W. N. and K. Benson (1985). Elution curves with double peaks in mixed convective horizontal flows. *AIChE J.* 31:161–164.

Gill, W. N. and R. Sankarasubramanian (1970). Exact analysis of unsteady convective flow. *Proc. Roy. Soc. Lond. A* 316:341–350.

Gillies, G. E., E. A. Linton, and P. J. Lowrey (1982). Corticotropin-releasing activity of the new CRF is potentiated several times by vasopressin. *Nature* 299:355–357.

Gorenflo, R., G. D. Fabritiis, and F. Mainardi (1999). Discrete random walk models for symmetric lévy-feller diffusion processes. *Physica A* 269:78–89.

Gorenflo, R. and F. Mainardi (1998a). Fractional calculus and stable probability distributions. *Archive of Mechanics* 50:377–388.

Gorenflo, R. and F. Mainardi (1998b). Random walk models for space-fractional diffusion processes. *Fractional Calculus and Applied Analysis* 1:167–191.

Gorenflo, R. and F. Mainardi (1999). Approximation of lévy-feller diffusion by random walk. *J. Analysis and its Applications* 18:231–246.

Groetsch, C. W. (1980). Elements of applied functional analysis. Marcel Dekker, New York.

Groetsch, C. W. (1993). Inverse problems in the mathematical sciences. Vieweg.

Gromperts, B. D. (1990). G_E: A GTP-binding protein mediated exocytosis. *Annu. Rev. Physiol.* 52:591–606.

Grynkiewicz, G. and R. Y. Tsien (1985). A new generation of Ca^{2+} indicators with greatly improved fluorescence properties. *J. Biol. Chem.* 260:3440–3450.

Guckenheimer, J., R. Harris-Warrick, J. Peck, and A. Willms (1997). Bifurcation, bursting, and

spike frequency adaption. *J. Computational Neuroscience* 4:257–277.

Guérineau, N. C., X. Bonnefont, L. Stoeckel, and P. Mollard (1998). Synchronized spontaneous Ca^{2+} transients in acute anterior pituitary slices. *J. Biol. Chem.* 273:10389–10395.

Guérineau, N. C., J. B. Corcuff, A. Tabarin, and P. Mollard (1991). Spontaneous and corticotropin-releasing factor-induced cytosolic calcium transients in corticotrophs. *Endocrinology.* 129:409–420.

Guo, L., D. A. Murio, and C. Roth (1990). A mollified space marching finite differences algorithm for the inverse heat conduction problem with slab symmetry. *Computers Math. Applic.* 19:75–89.

Hale, J. K. and H. Kocak (1991). Dynamics and Bifurcations, chapter 6. Springer-Verlag, New York.

Halili-Manabat, C., Y. Oki, K. Iino, M. Iwabuchi, H. Morita, and T. Yoshima (1995). The role of sodium in mediating adrenocorticotropin secretion by perfused rat anterior pituitary cells. *Endocrinology.* 136:2937–2942.

Hào, D. H. (1994). A mollification method for ill-posed problems. *Numer. Math.* 68:469–506.

Hào, D. N. (1996). A mollification method for a noncharacteristic Cauchy problem for a parabolic equation. *J. Math. Anal. and Appl.* 199:873–909.

Hào, D. N. and H.-J. Reinhardt (1997). On a sideways parabolic equation. *Inverse Problems* 13:297–309.

Happel, J. and H. Breener (1965). Low Reynolds Number Hydrodynamics. Prentice-Hall Inc., London.

Harden, T. K. (1983). Agonist-induced desensitization of the β-adrenergic receptor-linked adenylate cyclase. *Pharmacological Reviews* 35:5–26.

He, S. (1992). Factorization of a dissipative wave equation and the Green function technique for axially symmetric fields in a stratified slab. *J. Math. Phys.* 33:953–966.

He, S. (1993). A compact Green function approach to the time domain direct and inverse problems for a stratified dissipative slab. *J. Math. Phys.* 34:4628–4645.

Heinze, K., R. W. Keener, and A. R. Midgley (1998). A mathematical model of luteinizing hormone release from ovine pituitary cells in perifusion. *Am. J. Physiol.* 275:E1061–E1071.

Henry, P., W. L. Pearson, and C. G. Nichols (1996). Protein kinase C inhibition of cloned inward rectifier (HRK1/KIR2.3) K^+ channels expressed in Xenopus oocytes. *JP* 495:681–688.

Herrera, L. and N. Falcón (1995). Convection theory before relaxation. *Astrophysics and Space Science* 234:139–152.

Hille, B. (1992). Ionic Channels of Excitable Membranes. Sinauer, Sunderland, MA., 2nd edition.

Hodgkin, A. L. and A. F. Huxley (1952). A quantitative description of membrane current and its

application to conduction and excitation in nerve. *J. Physiol. (Lond).* 117:500–544.

Hodgkin, A. L., A. F. Huxley, and B. Katz (1952). Measurement of current-voltage relations in the membrane of the giant axon of Loligo. *J. Physiol. (Lond).* 116:424–448.

Holden, L. and T. Erneux (1993). Slow passage through a Hopf bifurcation: from oscillatory to steady state solutions. *SIAM J. Appl. Math.* 53:1045–1058.

Huckaba, C. E. and A. W. Hahn (1968). A generalized approach to the modelling of arterial blood flow. *Bull. Math. Biophys.* 30:645–662.

Irving, M., J. Maylie, N. L. Sizto, and W. K. Chandler (1990). Intracellular diffusion in the presence of buffers. *Biophys. J.* 57:717–721.

Izhikevich, E. M. (2000). Neural excitability, spiking, and bursting. *International Journal of Bifurcation and Chaos* 10:In Press.

Jafri, M. S. and J. Keizer (1995). On the roles of Ca^{2+} diffusion, Ca^{2+} buffers, and the endoplasmic reticulum in IP_3 induced Ca^{2+} waves. *Biophys. J.* 69:2139–2153.

Jafri, M. S., S. Vajda, P. Pasik, and B. Gillo (1992). A membrane model for the cytosolic calcium oscillations. *Biophys. J.* 63:235–246.

Jijun, L. and W. Yuanming (1997). On uniqueness of an inverse problem for a 1-D wave equation from transmission data. *SIAM J. Appl. Math.* 57:195–204.

Jones, M. T. and B. Gillham (1988). Factors involved in the regulation of adrenocorticotropic hormone/β-lipotropic hormone. *Physiol. Rev.* 68:743–818.

Kao, R. R. (1989). Mathematical models of perifusion column experiments. Master's thesis, University of Guelph, Ontario, Canada.

Karlsson, A. (1996). Wave propagators for transient waves in one-dimensional media. *Wave Motion* 24:85–99.

Karlsson, A. and S. Rikte (1998). The time-domain theory of forerunners. *J. Opt. Soc. Amer.* 15:487–502.

Keener, J. and J. Sneyd (1998). Mathematical Physiology. Springer-Verlag, New York.

Keller-Wood, M. E. and M. F. Dallman (1984). Corticosteroid inhibition of ACTH release. *Endocr. Rev.* 5:1–24.

King, A. C., D. J. Needham, and N. H. Scott (1998). The effects of weak hyperbolicity on the diffusion of heat. *Proc. Roy. Soc. Lond. A* 454:1659–1679.

King, M. S. and A. J. Baertschi (1990). The role of intracellular messengers in adrenocorticotropin secretion in vitro. *Experientia* 46:26–40.

Knudsen, J. G. and D. L. Katz (1958). Fluid Dynamics and Heat Transfer. McGraw-Hill, New York.

Kondo, J. (1991). Integral Equations. Kodansha, Tokyo.

Kress, R. (1989). Linear Integral Equations. Springer-Verlag.

Kristensson, G. and D. J. N. Wall (1998). Direct and inverse scattering for transient electromagnetic waves in nonlinear media. *Inverse Problems* 14:113–137.

Krueger, R. J. and R. L. Ochs (1989). A Green's function approach to the determination of internal fields. *Wave Motion* 11:525–543.

Kurpisz, K. and A. J. Nowak (1995). Inverse Thermal Problems. Computational Mechanics Publications, Southampton.

Kuryshev, Y. A., G. V. Childs, and A. K. Ritchie (1995a). Corticotropin-releasing hormone stimulation of Ca^{2+} entry in corticotrophs is partially dependent on protein kinase A. *Endocrinology.* 136:3925–3935.

Kuryshev, Y. A., G. V. Childs, and A. K. Ritchie (1995b). Three high threshold calcium channel subtypes in rat corticotrophs. *Endocrinology.* 136:3916–3924.

Kuryshev, Y. A., G. V. Childs, and A. K. Ritchie (1996). Corticotropin-releasing hormone stimulates Ca^{2+} entry through L- and P-type Ca^{2+} channels in rat corticotrophs. *Endocrinology.* 137:2269–2277.

Kuryshev, Y. A., L. Haak, G. V. Childs, and A. K. Ritchie (1997). Corticotropin releasing hormone inhibits an inwardly rectifying potassium current in rat corticotrophs. *J. Physiol. (Lond).* 502.2:265–279.

Kuznetsov, Y. A. (1998). Elements of Applied Bifurcation Theory. Springer-Verlag, New York, 2nd edition.

Labrie, F., V. Giguere, L. Proulx, and G. Lefevre (1984). Interactions between CRF, epinephrine, vasopressin and glucocorticoids in the control of ACTH secretion. *J. Steroid Biochem.* 20:153–160.

Labrie, F., R. Vielluex, G. LeFerve, D. H. Coy, J. Sueiras-Diaz, and A. V. Schally (1982). Corticotropin-releasing factor stimulates accumulation of adenosine 3',5'-monophosphate in rat pituitary corticotrophs. *Science.* 216:1007–1008.

Lacerda, A. E., D. Rampe, and A. M. Brown (1988). Effects of protein kinase C activators on cardiac Ca^{2+} channels. *Nature* 335:249–254.

Landau, L. D. and E. M. Lifshitz (1959). Fluid Mechanics, volume 6 of *Course of Theoretical Physics*. Pergamon Press, Oxford.

Lane, R. G. and T. J. Connolly (1997). Gradient methods for superresolution. In *Proceedings of The International Conference on Image Processing*, Santa Barabara. IEEE Image Processing Society.

Larsen, J., H. Lund-Andersen, and B. Krogsaa (1983). Transient transport across the blood-retina barrier. *Bull. Math. Biol.* 45:789–758.

LeBeau, A. P. and D. R. Mason (1994). The effects of a chemically diverse range of calcium channel antagonists on the AVP-stimulated ACTH response in ovine corticotrophs. *Cell Calcium* 16:47–58.

LeBeau, A. P. and D. R. Mason (1998). Interaction between arginine vasopressin- and raised extracellular potassium-stimulated pathways in adrenocorticotropin secretion. *Life Sciences* 63:2233–2242.

LeBeau, A. P., A. B. Robson, A. E. McKinnon, R. A. Donald, and J. Sneyd (1997). Generation of action potentials in a mathematical model of corticotrophs. *Biophys. J.* 73:1263–1275.

LeBeau, A. P., A. B. Robson, A. E. McKinnon, and J. Sneyd (1998). Analysis of a reduced model of corticotroph action potentials. *J. theor. Biol.* 192:319–339.

LeBeau, A. P., D. I. Yule, G. E. Groblewski, and J. Sneyd (1999). Agonist-dependent phosphorylation of the inositol 1,4,5-trisphosphate receptor. A possible mechanism for agonist-specific calcium oscillations in pancreatic acinar cells. *J. Gen. Physiol.* 113:851–871.

Lechleiter, J. D. and D. E. Clapham (1992). Molecular mechanisms of intracellular calcium excitability in X. laevis oocytes. *Cell* 69:283–294.

Lee, A. K. and A. Tse (1997). Mechanism underlying corticotropin-releasing hormone (CRH) triggered cytosolic Ca^{2+} rise in identified rat corticotrophs. *J. Physiol. (Lond).* 504.2:367–378.

Leong, D. and M. D. Thorner (1991). A potential code of LHRH-induced calcium ion responses in the regulation of luteinizing hormone secretion among individual gonadotrophs. *J. Biol. Chem.* 266:9016–9022.

Li, Y., J. Rinzel, J. Kiezer, and S. Stojilković (1994). Calcium oscillations in pituitary gonadotrophs: Comparison of experiment and theory. *Proc. Natl. Acad. Sci* 91:58–62.

Li, Y., J. Rinzel, L. Vergara, and S. Stojilković (1995). Spontaneous electrical and calcium oscillations in unstimulated pituitary gonadotrophs. *Biophys. J.* 69:785–795.

Li, Y., S. Stojilković, J. Keizer, and J. Rinzel (1997). Sensing and refilling calcium stores in an excitable cell. *Biophys. J.* 72:1080–1091.

Linz, P. (1979). Theoretical Numerical Analysis. John Wiley & Sons, Inc, New York.

Linz, P. (1985). Analytical and Numerical Methods for Volterra Equations. SIAM, Philadelphia.

Loechner, K. J., R. M. Kream, and K. Dunlap (1996). Calcium currents in a pituitary cell line (AtT-20): differential roles in stimulus-secretion coupling. *Endocrinology* 137:1429–1437.

Luini, A., D. Lewis, S. Guild, D. Corda, and J. Axelrod (1985). Hormone secretagogues increase cytosolic calcium by increasing cAMP in corticotropin-secreting cells. *Proc. Natl. Acad. Sci. USA* 82:8034–8038.

Lundblad, J. R. and J. L. Roberts (1988). Regulation of proopiomelanocortin gene expression in the pituitary. *Endocrine Reviews* 9:135–158.

Lundstedt, J. and S. He (1994). Signal restoration after transmission through a nonuniform *LCRG* line. *IEEE Trans. Microwave Theory Tech.* 42.

Lundstedt, J. and S. He (1997). Time-domain direct and inverse problems for a nonuniform *LCRG* line with internal sources. *IEEE Trans. Electromagn. Compatibility* 39:79–88.

Lytton, J., M. Westlin, S. E. Burk, G. E. Shull, and D. H. Maclennan (1992). Functional comparisons between isoforms of the sacroplasmic or endoplasmic reticulum family of calcium pumps. *J. Biol. Chem.* 267:14483–14489.

Mainardi, F., P. Paradisi, and R. Gorenflo (1999). Probability distributions generated by fractional diffusion equations. In J. Kertesz and I. Kondor, editors, *Econophysics: an Emerging Science*, volume In Press. Kluwer.

Majó, G., F. Aguado, J. Blasi, and J. Marsal (1998). Synaptobrevin isoforms in secretory granules and synaptic-like microvesicles in anterior pituitary cells. *Life Sciences* 62:607–616.

Mansvelder, H. D. and K. S. Kits (1998). The relation of exocytosis and rapid endocytosis to calcium entry evoked by short repetitive depolarizing pulses in rat melanotropic cells. *J. Neurosci.* 18:81–92.

Marchetti, C., G. V. Childs, and A. M. Brown (1987). Membrane currents of identified isolated rat corticotropes and gonadotrophs. *Am. J. Physiol.* 252:E340–E346.

Marshall, I. C. B. and C. W. Taylor (1993). Biphasic effects of cytosolic Ca^{2+} on Ins(1,4,5)P_3-stimulated Ca^{2+} mobilization in hepatocytes. *J. Biol. Chem.* 268:13214–13220.

Mason, D. R. (2000). Personal communication.

Massey, B. S. (1991). Mechanics of Fluids. Chapman and Hall, 6th edition.

Matveev, A. N. (1985). Molecular Physics. Mir publishers, Moscow.

McDonald, D. A. (1974). Blood flow in arteries. The Camelot Press Ltd, Southhampton, 2nd edition.

McFerran, B. W. and S. B. Guild (1996). The roles of adenosine 3',5'-cyclic monophosphate-dependent protein kinase A and protein kinase C in stimulus-secretion coupling in AtT-20 cells. *J. Mol. Endocrinology* 16:133–140.

McIntosh, J. E. A. and R. P. McIntosh (1983). Influence of the characteristics of pulses of gonadotrophin releasing hormone on the dynamics of luteinizing hormone release from perifused sheep pituitary cells. *J. Endocr.* 98:411–421.

McIntosh, J. E. A., R. P. McIntosh, and R. J. Kean (1984). Microcomputer-controlled device for delivering hormone stimulation to cell suspensions in perifusion: release of luteinising hormone from sheep pituitary cells. *Medical & Biological Engineering & Computing* 259–262.

McKenzie, A. and J. Sneyd (1998). On the formation and breakup of spiral waves of calcium. *Int. J. Bif. Chaos.* 8:2003–2012.

Meldolesi, J. and T. Pozzan (1998). The endoplasmic reticulum Ca^{2+} store: a view from the lumen. *TIBS* 23:10–14.

Merchenthaler, I., M. A. Hynes, S. Vigh, A. V. Schally, and P. Petrusz (1984). Corticotropin releasing factor (CRF): Origin and course of afferent pathways to the median eminence (ME) of the rat hypothalamus. *Neuroendocrinology* 39:296–306.

Meyer, T. and L. Stryer (1991). Calcium spiking. *Annu. Rev. Biophys. Biophys. Chem.* 20:153–174.

Mironov, S. (1990). Theoretical analysis of Ca wave propagation along the surface of intracellular stores. *J. theor. Biol.* 146:87–97.

Mitchell, A. R. and D. F. Griffiths (1980). The Finite Difference Methods in Partial Differential Equations. John Wiley & Sons Ltd.

Miyawaki, A., J. Llopis, R. Heim, J. M. McCaffery, J. A. Adams, M. Ikura, and R. Y. Tsien (1997). Fluorescent indicators for Ca^{2+} based on green fluorescent proteins and calmodulin. *Nature* 388.

Mollard, P., N. Guérineau, J. Audin, and B. Dufy (1989). Measurement of Ca^{2+} transients using simultaneous dual-emission microspectrofluorimetry and electrophysiology in individual pituitary cells. *Biochem. Biophys. Res. Commun.* 164:1045–1052.

Mollard, P., J. M. Theler, N. C. Guérineau, P. Vacher, C. Chiavaroli, and W. Schlegel (1994). Cytosolic Ca^{2+} of excitable pituitary cells at resting potentials is controlled by steady state Ca^{2+} currents sensitive to dihydropyridines. *The Journal of Biological Chemistry* 269:25158–15164.

Mollard, P., P. Vacher, J. Guerin, M. A. Rogawski, and B. Dufy (1987). Electrical properties of cultured human adrenocorticotropic-secreting adenoma cells: effects of high K^+, corticotropin-releasing factor, and angiotensin II. *Endocrinology.* 121:395–405.

Morgan, A. J. and R. Jacob (1994). Ionomycin enhances Ca^{2+} influx by stimulating store-regulated cation entry and not by a direct action on the plasma membrane. *Biochemical J.* 300:665–672.

Morse, P. M. and H. Feshbach (1953). Methods of Theoretical Physics, volume 1. McGraw-Hill Book Company, New York.

Mundiña-Weilenmann, C., J. Ma, E. Ríos, and M. M. Hosey (1991). Dihydropyridine-sensitive skeletal muscle Ca channels in polarized planer bilayers. *Biophys. J.* 60:902–909.

Murio, D. A. (1989). The mollification method and the numerical solution of the inverse heat conduction problem by finite differences. *Computers Math. Applic.* 17:1385–1396.

Murio, D. A. (1993). The Mollification Method and the Numerical Solution of Ill-Posed Problems. John Wiley & Sons, Inc, New York.

Murio, D. A. and C. Roth (1988). An integral solution for the inverse heat conduction problem

after the method of Weber. *Computers Math. Appl.* 15:39–51.

Murray, J. D. (1989). Mathematical Biology. Springer-Verlag, New York.

Nargeot, J., J. M. Nerbonne, J. Engels, and H. A. Lester (1983). Time course of the increase in the myocardial slow inward current after a photochemically generated concentration jump of intracellular cAMP. *Proc. Natl. Acad. Sci. USA* 80:2395–2399.

Neher, E. and G. J. Augustine (1992). Calcium gradients and buffers in bovine chromaffin cells. *J. Physiol. (Lond).* 450:273–301.

Norman, A. W. and G. Litwack (1997). Hormones. Academic Press, San Diego, 2nd edition.

Oldham, K. R. and J. Spanier (1974). The Fractional Calculus. Academic Press, New York.

Ostwald, W. and R. Auerbach (1926). Uber die viskositat kolloider hosungen im struktur-laminar und turbulezgebiet. *Kolloid-Z.* 38:261–280.

Parys, J. B., S. W. Sernett, S. DeLisle, P. M. Snyder, M. J. Walsh, and K. P. Campbell (1992). Isolation, characterisation, and localisation of the inositol 1,4,5-triphosphate receptor protein in *Xenopus laevis* oocytes. *J. Biol. Chem.* 267:18776–18782.

Phillips, C. G. and S. R. Kaye (1996). A uniformly asymptotic approximation for the development of shear dispersion. *J. Fluid. Mech.* 329:413–443.

Phillips, C. G. and S. R. Kaye (1997). The initial transient of concentration during the development of Taylor dispersion. *Proc. Roy. Soc. Lond. A* 453:2669–2688.

Plotsky, P. M., T. O. Bruhn, and W. W. Vale (1985). Evidence for multifactor regulation of the adrenocorticotropin secretory response to hemodynamic stimuli. *Endocrinology.* 116:633–639.

Plotsky, P. M. and P. E. Sawchenko (1987). Hypophysial-portal plasma levels, median eminence content, and immunohistochemical staining of corticotropin-releasing factor, arginine vasopressin, and oxytocin after pharmacological adrenalectomy. *Endocrinology.* 120:1361–1369.

Powell, J. O. (1995). Two coefficient reconstruction via a trace formulae in a one-dimensional inverse scattering problem. *Inverse Problems* 11:275.

Putney, J. W. and G. J. Bird (1993). The inositol phosphate-calcium signaling system in nonexcitable cells. *Endocrine Reviews* 14:610–631.

Raymond, V., P. C. K. Leung, R. Veileux, and F. Labrie (1985). Vasopressin rapidly stimulates phosphatidic acid-phospatidylinositol turnover rate in rat anterior pituitary cells. *FEBS Lett.* 182:196–200.

Regińska, T. and L. Eldén (1997). Solving the sideways heat equation by a wavelet-Galerkin method. *Inverse Problems* 13:1093–1106.

Reisine, T., G. Rougon, and J. Barbet (1986). Liposome delivery of cyclic AMP-dependent protein kinase inhibitor into intact cells: Specific blockade of cyclic AMP-mediated adrenocorticotropin release from mouse anterior pituitary tumor cells. *J. Cell Biol.* 102:1630–1637.

Rinzel, J. (1985). Bursting oscillations in an excitable membrane model. In B. Sleeman and R. Jarvis, editors, *Proc. 8th Dundee Conference on the Theory of Ordinary and Partial Differential Equations*. Springer-Verlag, New York.

Rinzel, J. (1987). A formal classification of bursting mechanisms in excitable systems. In E. Teramoto and M. Yamaguti, editors, *Mathematical Topics in Population Biology, Morphogenesis and Neurosciences*, volume 71 of *Lecture Notes in Biomathematics*. Springer-Verlag, Berlin.

Rinzel, J., J. Keizer, and Y. Li (1996). Modeling plasma membrane and ER excitability in pituitary cells. *TEM* 7:388–393.

Rinzel, J. and Y. S. Lee (1986). On different mechanisms for membrane potential bursters. In H. Othmer, editor, *Nonlinear Oscillations in Biology and Chemistry*, volume 66 of *Lecture Notes in Biomathematics*. Springer-Verlag, New York.

Rinzel, J. and Y. S. Lee (1987). Dissection of a model for neuronal parabolic bursting. *Journal of Mathematical Biology* 25:653–675.

Ritchie, A. K., Y. A. Kuryshev, and G. V. Childs (1996). Corticotropin-releasing hormone and calcium signaling in corticotrophs. *TEM* 7:365–369.

Rivier, C. L. and P. M. Plotsky (1986). Mediation by corticotropin releasing factor (CRF) of adenohypophysial hormone secretion. *Ann. Rev. Physiol.* 48:475–494.

Rivier, C. L. and W. W. Vale (1983a). Interaction of corticotropin-releasing factor and arginine vasopressin of adrenocorticotropin secretion *in vivo*. *Endocrinology*. 113:939–942.

Rivier, C. L. and W. W. Vale (1983b). Modulation of stress-induced ACTH release by corticotropin-releasing factor, catecholamines and vasopressin. *Nature* 305:325–327.

Roth, G. (1989). An integral solution approach for the inverse heat conduction problem. Ph.D. thesis, University of Cincinnati.

Rudin, L. I., S. Osher, and C. Fu (1992). Nonlinear total variation based noise removal algorithms. *Physica* 60:259–268.

Rush, M. E. and J. Rinzel (1994). Analysis of bursting in a thalamic neuron model. *Biological Cybernetics* 71:281–291.

Salles, J., J. F. Thovert, R. Delannay, L. Prevors, J. L. Auriault, and P. M. Adler (1993). Taylor dispersion in porous media. Determination of the dispersion tensor. *Phys. Fluids A* 5:2348–2376.

Schecter, S. (1987). The saddle node seperatrix loop. *SIAM J. Math. Anal.* 18:1142–1156.

Schiesser, W. (1994). Computational Mathematics in Engineering and Applied Sciences: ODE's, DAE's, PDE's. CRC Press, Boca Raton, FL.

Schlichting, H. (1960). Boundary Layer Theory. McGraw-Hill Book Company, New York, 4th edition.

Scholz, K. P., L. J. Cleary, and J. H. Byrne (1988). Inositol 1,4,5-triphosphate alters bursting pacemaker activity in *Aplysia* neurons: voltage-clamp analysis of effects of calcium currents. *J. Nuerophysiology* 60:86–104.

Sculptoreanu, A., T. Scheuer, and W. Catterall (1993). Voltage-dependent potentiation of L-type Ca^{2+} channels due to phosphorylation by cAMP-dependent protein kinase. *Nature* 364:240–243.

Segel, L. A. (1977). Mathematics Applied to Continuum Mechanics. Macmillan Publishing Co., Inc., New York.

Seidman, T. I. and L. Eldén (1990). An 'optimal filtering' method for the sideways heat equation. *Inverse Problems* 6:681–696.

Shangold, G. A., S. N. Murphy, and R. J. Miller (1988). Gonadotropin-releasing hormone-induced Ca^{2+} transients in single identified gonadotrophs require both intracellular Ca^{2+} mobilisation and Ca^{2+} influx. *Proc. Natl. Acad. Sci. USA* 85:6566–6570.

Shipston, M. J., J. S. Kelly, and F. A. Antoni (1996). Glucocorticoids block protein kinase A inhibition of calcium-activated potassium channels. *J. Biol. Chem.* 271:9197–2000.

Shorten, P. R., A. P. LeBeau, A. B. Robson, A. E. McKinnon, and D. J. N. Wall (1999). A role of the endoplasmic reticulum in a mathematical model of corticotroph action potentials. Technical Report 173/1-21/(1999), University of Canterbury, New Zealand. Available at <http://www.math.canterbury.ac.nz/reports.shtml>.

Shorten, P. R., A. B. Robson, A. E. McKinnon, and D. J. N. Wall (2000). CRH-induced electrical activity and calcium signalling in pituitary corticotrophs. *J. theor. Biol.* 206:395–405.

Shorten, P. R. and D. J. N. Wall (1998). Signal restoration for a mass transport problem involving shear dispersion. *Inverse Problems* 14:1021–1032.

Shorten, P. R. and D. J. N. Wall (2000). A Hodgkin–Huxley model exhibiting bursting oscillations. *Bull. Math. Biol.* 62:695–715.

Shukla, J. B., R. S. Parihar, and B. R. P. Rao (1980). Effects of stenosis on non-Newtonian flow in an artery. *Bull. Math. Biol.* 42:283–294.

Smith, R. (1988). Entry and exit conditions for flow reactors. *IMA J. Appl. Math.* 41:1–20.

Smith, V. A. (1992). Scattering and ACTH secretion. Ph.D. thesis, University of Canterbury, Christchurch, New Zealand.

Smith, W. R. and G. C. Wake (1990). Mathematical analysis: An inverse problem arising in convective-diffusive flow. *IMA J. Appl. Math.* 45:225–231.

Smith, W. R., G. C. Wake, J. E. A. McIntosh, R. P. McIntosh, M. Pettigrew, and R. Kao (1991). Mathematical model of perifusion data: models predicting elution concentration. *Am. J. Physiol.* 261:R247–R256.

Sneddon, I. N. (1951). Fourier Transforms. McGraw-Hill Book Company, New York.

Sneddon, I. N. (1972). The use of Integral Transforms. McGraw-Hill Book Company, New York.

Sneyd, J., P. D. Dale, and A. Duffy (1998). Traveling waves in buffered systems: applications to calcium waves. *SIAM J. Appl. Math.* 58:1178–1192.

Sneyd, J. and L. V. Kalachev (1994). A profile analysis of propagating calcium waves. *Cell Calcium* 15:289–296.

Sneyd, J., J. Keizer, and M. Sanderson (1995). Mechanisms of calcium oscillations and waves: a quantitative analysis. *the FASEB Journal* 9:1463–1472.

Sneyd, J. and J. Sherratt (1997). On the propagation of calcium waves in an inhomogeneous medium. *SIAM J. Appl. Math.* 57:73–94.

Spencer, A. J. M. (1980). Continuum Mechanics. Longman, London.

Stakgold, I. (1979). Greens functions and boundary value problems. John Wiley and sons, Inc, Canada.

Streeter, V. L. (1968). Fluid Mechanics. McGraw-Hill, 4th edition.

Strikwerda, J. C. (1989). Finite difference schemes and partial differential equations. Wadsworth, Inc., California.

Takano, K., P. R. Stanfield, S. Nakajima, and Y. Nakajima (1995). Protein kinase C-mediated inhibition of an inward rectifier potassium channel by substance P in nucleus basalis neurons. *Neuron* 14:999–1008.

Takano, K., J. Yasufukutakano, A. Teramoto, and T. Fujita (1996). Corticotropin-releasing hormone excites adrenocorticotrophic-secreting human pituitary adenoma cells by activating a nonselective cation current. *J. Clin. Invest.* 98:2033–2041.

Taylor, G. I. (1953). Dispersion of soluble matter in solvent flowing slowly through a tube. *Proc. Roy. Soc. Lond. Ser. A* 219:186–203.

Taylor, G. I. (1954a). Conditions under which dispersion of a solute in a stream of a solvent can be used to measure molecular diffusion. *Proc. Roy. Soc. Lond. Ser. A* 225:473–477.

Taylor, G. I. (1954b). The dispersion of matter in turbulent flow through a pipe. *Proc. Roy. Soc. Lond. Ser. A* 223:446–468.

Taylor, M. E. (1981). Pseudodifferential Operators. Princeton Mathematical Series No. 34. Princeton University Press, Princeton, New Jersey.

Thomas, P., P. L. Mellon, J. L. Turgeon, and D. W. Waring (1996). The LβT2 clonal gonadotrope: A model for single cell studies of endocrine cell secretion. *Endocrinology* 137:2979–2989.

Tian, L., J. A. C. Philp, and M. J. Shipston (1999). Glucocorticoid block of protein kinase C signalling in mouse pituitary corticotroph AtT20 D16:16 cells. *Journal of Physiology* 516:757–768.

Tikhonov, A. N. (1963). Solution of incorrectly formulated problems and the regularisation method. *Soviet Mathematics Doklady* 4:1035–1038.

Titchmarsh, E. C. (1948). Theory of Fourier Integrals. Oxford University Press, London, 2nd edition.

Todd, K. and S. L. Lightman (1987). Vasopressin activation of phosphatidylinositol metabolism in rat anterior pituitary *in vitro* and its modification by changes in the hypothalmo-pituitary-adrenal axis. *Neuroendocrinology* 45:212–218.

Tomei, L. D. and F. O. Cope (1991). Apoptosis : the molecular basis of cell death. Plainview, N.Y : Cold Spring Harbor Laboratory Press.

Tse, A. and A. K. Lee (1998). Arginine vasopressin triggers intracellular calcium release, a calcium-activated potassium current and exocytosis in identified rat corticotrophs. *Endocrinology.* 139:2246–2252.

Tse, A. and F. W. Tse (1998). α-Adrenergic stimulation of cytosolic Ca^{2+} oscillations and exocytosis in identified rat corticotrophs. *Journal of Physiology* 512:385–393.

Tse, A., F. W. Tse, and B. Hille (1994). Calcium homeostasis in identified rat gonadotrophs. *J. Physiol. (Lond).* 477.3:511–525.

Tse, A., F. W. Tse, and B. Hille (1995). Modulation of Ca^{2+} oscillation and apamin-sensitive, Ca^{2+}-activated K^+ current in rat gonadotropes. *Pflugers Arch* 430:645–652.

Tsien, R. W. and R. Y. Tsien (1990). Calcium channels, stores and oscillations. *Annu. Rev. Cell Biol.* 6:715–760.

Tsunoda, Y. (1991). Oscillatory Ca^{2+} signaling and its cellular function. *The New Biologist* 3:3–17.

Vasin, V. V. (1973). The stable evaluation of a derivative in space $C(-\infty, \infty)$. *U.S.S.R. Computational Math. and Math. Phys.* 13:16–24.

Veldhuis, J. D. (1991). Temporal architecture of in vivo endocrine glandular signaling: obtaining a secretory blueprint by deconvolution analysis. *Molecular and Cellular Endocrinology* 77:C63–C71.

Veldhuis, J. D., M. L. Carlson, and M. L. Johnson (1987). The pituitary gland secretes in bursts: Appraising the nature of glandular secretory impulses by simultaneous multiple-parameter deconvolution of plasma hormone concentrations. *Proc. Natl. Acad. Sci. USA* 86:7686–7690.

Veldhuis, J. D., M. L. Johnson, and M. Dufau (1989). Physiological attributes of endogenous bioactive luteinizing hormone secretory bursts in man. *Am. J. Physiol.* 256:E199–E207.

Vogel, C. R. (1986). Optimal choice of truncation level for the truncated SVD solution of linear first kind integral equations when the data are noisy. *SIAM Journal of Numerical Analysis* 23:109–117.

Vogel, C. R. (1987). An overview of numerical methods for nonlinear ill-posed problems. In H. W. Engl and C. W. Groetsch, editors, *Inverse and Ill-Posed Problems*, 231–245. Academic Press, Orlando.

Vogel, C. R. (1992). Wave splitting for some nonhyperbolic time-dependent PDEs. In J. P. Corones, G. Kristensson, P. Nelson, and D. L. Seth, editors, *Invariant Imbedding and Inverse Problems*. SIAM.

Wagner, J. and J. Keizer (1994). Effects of rapid buffers on Ca^{2+} diffusion and Ca^{2+} oscillations. *Biophys. J.* 67:447–456.

Wall, D. J. and J. Lundstedt (1998). Inverse source problems involving the one-way wave equation: Source function reconstruction. *Wave Motion* 27:55–77.

Wall, D. J. N. (1997). Signal restoration after transmission through a diffusive medium. In B. J. Noye, M. D. Teubner, and A. W. Gill, editors, *Computational Techniques and Applications: CTAC97*, 711–718, Singapore. World Scientific.

Wall, D. J. N. and J. Lundstedt (1999). Inverse problems involving the one way wave equation: medium function reconstruction. *Mathematics and Computers in Simulation* 50:489–510.

Wall, D. J. N. and P. Olsson (1997). Invariant imbedding and hyperbolic heat waves. *J. Math. Phys.* 38:1723–1749.

Wang, X. J. (1993a). Genesis of bursting oscillations in the Hindmarsh-Rose model and homoclinicity to a chaotic saddle. *Physica D* 62:263–274.

Wang, X. J. (1993b). Ionic basis for intrinsic 40 Hz neuronal oscillations. *NeuroReport* 5:221–224.

Wang, X. J. (1998). Calcium coding and adaptive temporal computation in cortical pyramidal neurons. *J. Neurophysiology* 79:1549–1566.

Washburn, E. W. (1926). International critical tables of numerical data, physics, chemistry and technology. volume 5, 63–70. McGraw-Hill, New York.

Watanabe, T., Y. Oki, and N. Orth (1989). Kinetic actions and interactions of arginine vasopressin, angiotensin-II, and oxytocin on adrenocorticotropin secretion by rat anterior pituitary cells in the microperifusion system. *Endocrinology* 125:1921–1931.

Watanabe, T. and D. N. Orth (1987). Detailed kinetic analysis of adrenocorticotropin secretion by dispersed rat anterior pituitary cells in a microperifusion system: Effects of ovine corticotropin-releasing factor and arginine vasopressin. *Endocrinology* 121:1133–1145.

Watt, S. D. and A. J. Roberts (1995). The accurate dynamic modeling of contaminant dispersion in channels. *SIAM J. Appl. Math.* 554:1016–1038.

Weast, R. C. (1999). CRC handbook of chemistry and physics. CRC Press, Cleveland, Ohio, 80th edition.

Weber, C. F. (1981). Analysis and solution of the ill-posed inverse heat conduction problem. *Int.*

J. Heat Mass Transfer 24:1783–1792.

Wessells, N. K. and J. L. Hopson (1988). Biology. Random House, New York.

Westlund, K. N., G. Aguilera, and G. V. Childs (1985). Quantification of morphological changes in pituitary corticotrophs produced by *in vivo* corticotropin-releasing factor stimulation and adrenalectomy. *Endocrinology.* 116:439–445.

Weston, V. H. (1988). Factorisation of the dissipative wave equation and inverse scattering. *J. Math. Phys.* 29:2205–2218.

Whitnall, M. H., E. Mezey, and H. Gainer (1985). Co-localization of corticotropin-releasing factor and vasopressin in median eminence neurosecretory cells. *Nature* 317:248–250.

Widmaier, E. P. and M. F. Dallman (1984). The effects of corticotropin-releasing factor on adrenocorticotropin secretion from perfused pituitaries *in vivo*: Rapid inhibition by glucocorticoids. *Endocrinology.* 115:2368–2374.

Wiener, N. (1933). Fourier Integral. Dover Publications, Inc., New York.

Won, J. G. S., Y. Oki, and D. N. Orth (1990). Roles of intracellular and extracellular calcium in the kinetic profile of adrenocorticotropin secretion by perfused rat anterior pituitary cell. II. arginine vasopressin, oxytocin, and angiotensin-II stimulation. *Endocrinology.* 126:858–868.

Won, J. G. S. and D. N. Orth (1995). Role of inositol triphosphate-sensitive calcium stores in the regulation of adrenocorticotropin secretion by perfused rat anterior pituitary cells. *Endocrinology.* 136:5399–5408.

Wong, M. W. (1991). An introduction to Pseudo-differential operators. World Scientific, Singapore.

Woods, N. M., K. S. R. Cuthbertson, and P. H. Cobbold (1986). Repetitive transient rises in cytoplasmic free calcium in hormone-stimulated hepatocytes. *Nature* 319:600–601.

Wu, N. (1997). The maximum entropy method. Springer-Verlag, Berlin.

Appendix A

Sobolev spaces

Consider the space C[a, b] with inner product

$$\langle u, v \rangle = \int_a^b u(\xi) v(\xi) d\xi. \tag{A.0.1}$$

This space is not complete. L^2[a, b], the space of square-integrable functions, is the completion of C[a, b] with respect to the inner product (A.0.1). A complete inner product space is called a Hilbert space. The Sobolev space H^s[a, b] is another useful Hilbert space. H^s[a, b] is the completion of C^s[a, b], the space of s continuously differentiable functions, with respect to the norm

$$\|u\|_s = \Big[\sum_{j=0}^{s} \|u^{(j)}\|_0^2 \Big]^{1/2}. \tag{A.0.2}$$

where $\|\cdot\|_0$ is the L^2 norm. Note that H^0[a, b] = L^2[a, b]. However the above definition of H^s[a, b] is only valid for $s \in \mathbb{N}$. We can alternatively define $H^s(\mathbb{R})$ as the space of functions satisfying a certain decay in their Fourier transform (Dautray and Lions, 1988, p96) or Fourier coefficients (Kress, 1989, p108). For $s \in \mathbb{R}$, $H^s(\mathbb{R})$ is the the space of functions u such that

$$(1 + |\xi|^2)^{s/2} \widehat{u}(\xi) \in L^2(\mathbb{R}), \quad \xi \in \mathbb{R} \tag{A.0.3}$$

where

$$\widehat{u}(\xi) = \frac{1}{2\pi} \int_{\mathbb{R}} e^{-ix\xi} u(x) dx, \tag{A.0.4}$$

is the Fourier transform of u. The associated inner product for this Hilbert space is given by

$$\langle u, v \rangle_s = \int_{\mathbb{R}} (1 + |\xi|^2)^s \widehat{u}(\xi) \overline{\widehat{v}(\xi)} d\xi, \tag{A.0.5}$$

with the norm

$$\|u\|_s = \int_{\mathbb{R}} (1 + |\xi|^2)^s |\widehat{u}(\xi)|^2 d\xi. \tag{A.0.6}$$

Appendix B

Compact operators

A linear operator $L : X \to Y$, from a normed linear space X into a normed linear space Y, is called a compact linear operator if it maps bounded sets to relatively compact sets (i.e., $\overline{L(X)}$ is compact). In other words for each bounded sequence $u_n \in X$, the sequence Lu_n contains a convergent subsequence. It follows that because compact sets are bounded, a compact operator is a bounded operator. Linear combinations of compact operators are also compact, hence the space of compact operators forms a linear space. The composition $L_1 L_2$ of two bounded linear operators L_1, and L_2 is compact if one of the operators is compact. Interestingly the identity operator $I : X \to X$ is compact if and only if $\dim X < \infty$. The proof of this relies on Riesz Lemma (Kress, 1989), (p 19). The nice properties of compact sets in finite dimensional spaces implys that a bounded linear operator L, with $\dim L(X) < \infty$ is compact.

Theorem B.0.1. *The inverse of a compact operator $L : X \to Y$ with $\dim X = \infty$ is an unbounded operator.*

If L^{-1} was bounded then the composition $L^{-1}L = I$ would also be compact, but since $\dim X = \infty$ the identity operator I is not compact, a contradiction. Hence L^{-1} is an unbounded operator.